Aspects of Atmospheric C_T^2 Turbulence related to Scintillometry

Miranda Braam

Thesis committee

Promotor
Prof. Dr A.A.M. Holtslag
Professor of Meteorology
Wageningen University

Co-promotors
Dr F. Beyrich
Head of the Boundary-Layer Processes Group
Meteorologisches Observatorium Lindenberg – Richard-Aßmann-Observatorium
Deutscher Wetterdienst, Lindenberg, Germany

Dr A.F. Moene
Assistant professor, Meteorology and Air Quality Group
Wageningen University

Other members
Prof. Dr R. Uijlenhoet, Wageningen University
Prof. Dr S. Raasch, Leibniz-Universität Hannover, Germany
Prof. Dr B.J.J.M. van den Hurk, VU University Amsterdam
Dr B.J.H. van de Wiel, Eindhoven University of Technology

This research was conducted under the auspices of the Graduate School for Socio-Economic and Natural Sciences of the Environment (SENSE).

Aspects of

Atmospheric Turbulence

related to

Scintillometry

Miranda Braam

Thesis

submitted in fulfilment of the requirements for the degree of doctor
at Wageningen University
by the authority of the Rector Magnificus
Prof. Dr M.J. Kropff,
in the presence of the
Thesis Committee appointed by the Academic Board
to be defended in public
on Wednesday 28 May 2014
at 1:30 p.m. in the Aula.

Miranda Braam
Aspects of atmospheric turbulence related to scintillometry
vi + 154 pages.

PhD-thesis, Wageningen University, Wageningen, NL (2014)
With references, with summaries in Dutch and English

ISBN 978-94-6173-938-4

Contents

1 Introduction

The lower part of the atmosphere, where people and animals spend their lives and plants are growing, is known as the atmospheric boundary layer (ABL). The ABL can be defined as 'the part of the troposphere that is directly influenced by the presence of the earth's surface, and responds to surface forcings with a time scale of about an hour or less' (Stull, 1988). Within the ABL, **atmospheric turbulence** causes heat and matter (water vapour, smoke and other substances) to be efficiently transported from the earth's surface up to a kilometre or more. This transport can be indirectly measured with so-called **scintillometers**. In the following section, we introduce atmospheric turbulence and the use of scintillometers for ABL research.

1.1. Atmospheric turbulence and scintillometry

Atmospheric turbulence is the irregular, chaotic movement of air parcels within the atmosphere, which is the main vertical transport mechanism in the ABL. Within the ABL, turbulence is produced in two ways: by friction of the wind with obstacles near the surface (shear production, mechanical turbulence), or by density differences between air parcels (buoyancy production, convective turbulence). Convective turbulence results essentially from heating of the earth's surface by solar radiation. The heated surface does not only heat the soil below, but also the air near the surface will become warmer and more moist. The air will become more moist, as part of the solar energy is used to evaporate water within the soil, vegetation or at the surface. The warmer and more moist air parcels are less dense and more buoyant than the air around it, because air containing water vapour is less dense than dry air. The more buoyant parcels will be replaced by denser and less buoyant parcels from above. The chaotic three dimensional movement of air parcels going up and down is called eddy motion. Buoyancy can also destroy turbulence. During the night the surface cools, which makes the air near the surface cooler than above. This causes a temperature inversion near the surface and thus less turbulence.

The turbulent transport of these "warm and moist" and "cold and dry" air parcels is in most cases too fast to be felt by human beings. It can, however, be observed by eye:

for example the chaotic movement of smoke from a chimney or dancing air over asphalt during hot summer days are indirect observations of atmospheric turbulence. The latter can be explained with some background on electromagnetic radiation. Generally, a light beam (which is electromagnetic radiation) that travels through media with different densities changes direction each time it moves from one to another medium, i.e. the light beam is refracted. The strength of refraction depends on the contrast in density and is expressed as the refractive index. For a light beam that travels through the atmosphere, the turbulent transport of air parcels with different densities causes variations in the refractive index of the air (n) along the path. Now we have this knowledge, we can go back to observations of the appearance of a 'dancing' asphalt during a hot summer day. On such a day the turbulent transport is strong over the asphalt. Consequently, density differences among the air parcels are large, and therefore variations of the refractive index of air too. As a result, each time when the light beam from the asphalt reaches the eye of the observer, it has been refracted differently. It therefore seems as if the light beam is coming from somewhere else: the asphalt appears to be 'dancing'.

Because the amount of solar radiation depends on the location on earth, date, time of the day, and cloudiness, the strength of the turbulence within the ABL also varies strongly in time and space. The strength of turbulence has a clear diurnal cycle with a minimum during the night and a maximum during the day, and as a consequence the ABL is typically deeper during day than during night (Stull, 1988). The partitioning of solar energy between heating the soil, heating the air or evaporating water varies spatially, too. Above a lake or a wet grassland more energy is used to evaporate water than above asphalt or a dry wheat field. As a consequence, the amount of heat and water vapour that are transported from the surface into the atmosphere varies between these different surfaces. In physics, the amount of energy that is transferred per unit of time across a reference plane is called flux density, mostly abbreviated as flux. In meteorology, the energy flux related to the amount of heat transported into the atmosphere is called the sensible heat flux (H) and the energy flux related to the amount of water vapour transported into the atmosphere the latent heat flux (LE).

The area-averaged values of H and LE over natural landscapes are of interest for many meteorological applications, for instance to evaluate mesoscale numerical weather models and satellite-based retrieval algorithms (see for a extensive overview Beyrich et al. 2012). Furthermore, knowledge of the latent heat flux is also important for water budget studies and for active water management because it is a measure of the amount of evaporation. Nowadays, the surface heat fluxes are often measured with eddy-covariance (EC) systems (Lee et al., 2004; Foken, 2008). An EC system consists of a fast response anemometer, a fast response thermometer, and a fast response hygrometer. It is important to have fast response instruments, in order to resolve the high-frequency fluctuations. From the measured high-frequency fluctuations, the covariances with the vertical wind speed are calculated that are a measure of the surface fluxes. Because EC systems are located at one point, they are very suitable to determine

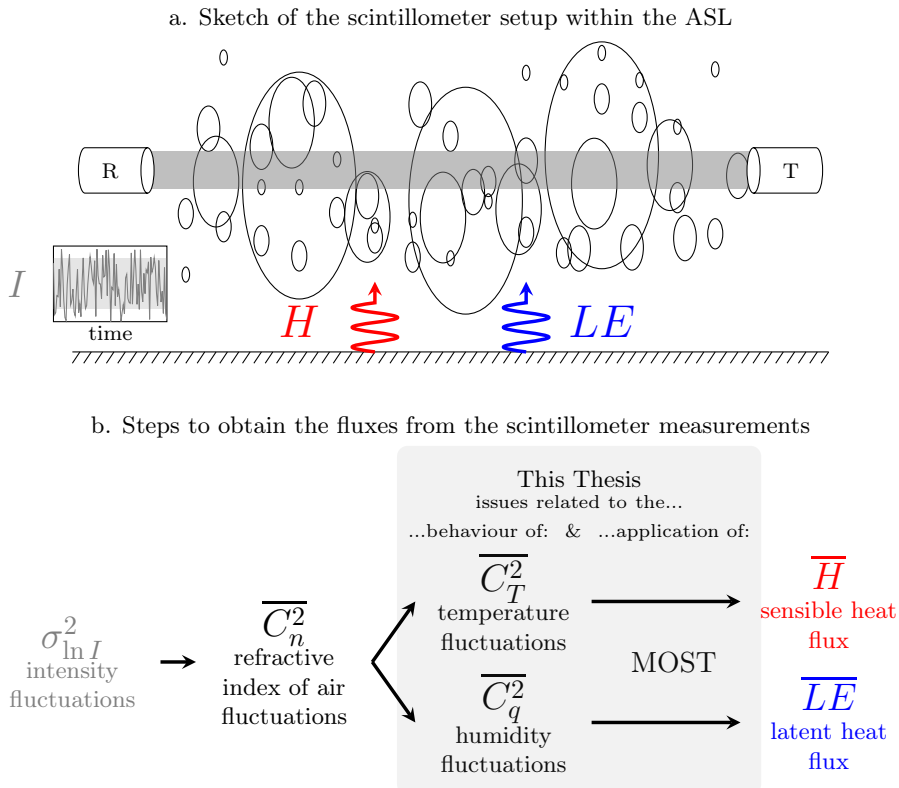

Fig. 1.1. Sketch of the scintillometer setup (a), and the steps to obtain fluxes from the scintillometer output (b).

the fluxes locally or representative over a homogeneous landscape. Natural landscapes are, however, mostly heterogeneous, and the surface heat fluxes differ among fields. As a consequence, a point measurement such as the EC method is not suitable to determine area-averaged fluxes in such a case.

Scintillometry deals with the use of scintillometers to measure the fluxes indirectly using the characteristics of atmospheric turbulence. In contrast to the EC method, scintillometry has proven to be a reliable method for determining the spatially averaged fluxes over heterogeneous surfaces (e.g. Green et al., 2001; Meijninger et al., 2002b, 2006; Evans et al., 2012). Figure 1.1 schematically shows the setup of a scintillometer system and the steps to obtain the fluxes. A scintillometer system consists of an electromagnetic beam transmitter at one end and a receiver at the other end of a path, which is in the order of 1 up to 5 km for the scintillometers used in this study. As explained before, turbulent eddies along the propagation path of an electromagnetic beam cause variations in the refractive index of air. These in turn cause variations in the received intensity of the electromagnetic radiation beam, also called scintillations. The magnitude of these intensity fluctuations ($\sigma^2_{\ln I}$) is proportional to the path-averaged structure parameter of the refractive index of air (C_n^2), which is the basic parameter that can be

derived from the scintillometer data. As fluctuations in the refractive index of air are caused by the air parcels going up and down with different temperature (T) and humidity (q), C_n^2 can be expressed through the structure parameters of temperature (C_T^2) and humidity (C_q^2). The relative contributions of C_T^2 and C_q^2 to C_n^2 depend on the wavelength emitted by the scintillometer and on the ratio between H and LE. Optical scintillometers, e.g. the large aperture scintillometer (LAS, operating at wavelengths in the visible and the near-infrared), are mainly sensitive to temperature fluctuations, while for microwave scintillometers (MWS, operating at millimetre wavelengths) the temperature and humidity fluctuations are equally important (Hill et al., 1992; Ward et al., 2013). The structure parameters of temperature and humidity are a measure of turbulent fluctuations of temperature and humidity and can therefore be linked to the surface sensible and latent heat fluxes. The method that links them is called Monin-Obukhov Similarity Theory (MOST, Monin and Obukhov, 1954; Wyngaard, 1973; Hill et al., 1992, among others).

Despite the reliable results of scintillometry to obtain surface averaged fluxes, there are still a number of open issues that require further research. The issues discussed in this thesis are related to the behaviour of the structure parameter within the atmosphere and to the applicability of MOST (indicated with the grey block in Fig. 1.1). Therefore, before going into detail within these issues, some background information on the structure parameter –the basic parameter used in scintillometry– (Sect. 1.2.1), and MOST –the method to obtain the fluxes from the structure parameters– (Sect. 1.2.2) is given in the next section.

1.2. The structure parameter and MOST

1.2.1. The structure parameter

As explained before, the structure parameter of an atmospheric scalar s (C_s^2) is a measure of the intensity of fluctuations of that scalar caused by turbulence. To allow for a better understanding and a more precise definition, this section starts with some more details about turbulence.

Turbulence is one of the unsolved problems within classical physics. Turbulence is characterized by:

- deterministically chaotic: it is not reproducible in detail and can only be described in a statistical sense and by similarity approaches,
- diffusive: it is an effective mechanism to mix energy, heat and matter,
- dissipative: its kinetic energy is converted into heat,
- three dimensional: it is characterized by rotating vortices called eddies at different scales. The kinetic energy of the eddies (turbulent kinetic energy) is produced at the largest scales, which have the size of the ABL depth. These eddies are broken into smaller eddies and they are dissipated at the smallest scales at about a few mm. This process is called the energy cascade.

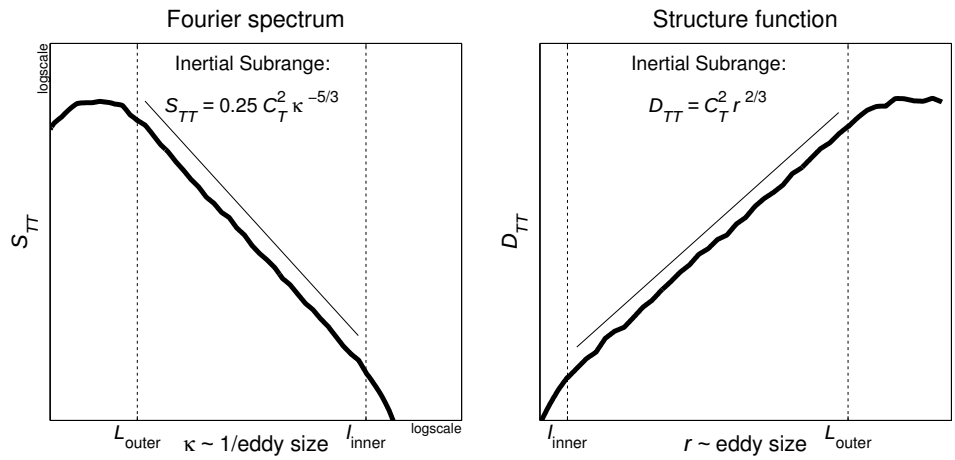

Fig. 1.2. A schematic picture of a temperature spectrum (left, on a double logarithmic scale) and of the structure function (right) as could be found in the atmosphere. κ is the wave number, and r is the separation distance. Within the temperature spectrum, the area below the plot is proportional to the variance ($\overline{T'^2}$), and the level of the line within the inertial subrange to the structure parameter (C_T^2).

Because turbulence is chaotic, its behaviour can only be described through statistics such as variances and covariances. In statistics, the variance is a measure of the spread of data. In the analysis of turbulence, it can be interpreted as a measure of fluctuations of an atmospheric quantity (s), and is denoted as: $\overline{s'^2}$. Here, s' is defined by Reynolds decomposition as the deviation of an atmospheric quantity (at a certain moment and a certain location) from its mean: $s' = s - \overline{s}$, where the overbar indicates averaging. Instead of the variance, often the standard deviation ($\sqrt{\overline{s'^2}}$) is used because it has the same dimension as s.

In statistics, the covariance is a measure of how much two variables correlate. In the analysis of turbulence, the covariance is denoted as: $\overline{s'_a s'_b}$, in which s_a and s_b are two different atmospheric quantities. In the atmosphere, turbulence is the main mechanism to transport heat, momentum and matter from the earth surface into the atmosphere –vertical transport–, which makes the covariance between the vertical windspeed fluctuations (w') and other quantities important. For instance, the covariance between w' and the temperature fluctuations (T') is a measure of the amount of sensible heat that is transported upward (if $\overline{w'T'} > 0$) or downward (if $\overline{w'T'} < 0$).

Within the turbulent motion, eddies with different scales are involved, and therefore it is worthwhile to investigate the variance or covariance associated with a particular scale instead of investigating the total variance and covariance. This can be achieved by calculating the turbulent spectrum with Fourier analysis. The left hand side of Fig. 1.2 shows a schematic picture of a temperature spectrum as it can be typically found in the ABL. In this figure we can observe three regimes. The borders of the centre regime are the outer scale L_{outer}, which has the size of ≈ 0.4 times the measurement height, and inner scale l_{inner}, which has the size of only a few mm. At the smallest

wavenumbers (largest eddies, eddy size $> L_{\text{outer}}$), temperature fluctuations are generated by turbulence (production range). At the largest wavenumbers (smallest eddies, eddy size $< l_{\text{inner}}$), temperature fluctuations are dissipated (dissipation range). The regime between the production range and the dissipation range is called the inertial subrange ($l_{\text{inner}} <$ eddy size $< L_{\text{outer}}$). In this regime, temperature fluctuations are neither produced nor dissipated, but they are transferred from the largest to the smallest scales. The decrease of spectral energy of temperature fluctuations with increasing wavelength is uniform and follows the $-5/3$ power law of Kolmogorov (Kolmogorov, 1962):

$$S_{TT} = 0.25 C_T^2 \kappa^{-5/3} \tag{1.1}$$

This relationship leads to a more precise definition of the structure parameter (for humidity fluctuation it is similar). According to Eq. 1.1 the structure parameter is the measure of the turbulent fluctuations within the inertial subrange (level of the spectrum line where it follows the $-5/3$ power law). In contrast the variance is the measure for the total amount of fluctuations, which is proportional to the area below the spectrum line.

Another way to decompose the amount of fluctuations of an atmospheric quantity by eddy size is by using the second order structure function (D_{ss}). The spatial structure function $D_{ss,x}$ describes the relation of a quantity s at a location (x) compared to its value at a location further away ($x+r$, with r the separation between the two locations), viz,

$$D_{ss} = \overline{[s(x+r) - s(x)]^2} \tag{1.2}$$

The right hand side of Fig. 1.2 shows a schematic picture of the structure function of temperature versus the separation. In this figure again the three regimes can be distinguished, and the behaviour in the inertial subrange is uniform:

$$D_{TT} = C_T^2 r^{2/3} \tag{1.3}$$

From the relation of the structure function in the inertial subrange, the nomenclature of the structure parameter becomes clear. A parameter is a "constant or variable term in a function that determines the specific form of a function"[1] - in this case a parameter used in the structure function.

The reason why the structure parameter is used in scintillometry, instead of for instance the variance, is that the intensity fluctuations of the electromagnetic beam as measured by the receiver are related to eddies within a typical range of length scales. This range depends on the scintillometer type that is used. For the LAS the typical range is an order of a few decimeters, in the order of the size of the aperture D. For the MWS, it is about a few meters, in the order of the first Fresnel zone ($\sqrt{\lambda L}$, in which λ is the wavelength and L the path length). For both instruments the ranges of scales

[1] http://dictionary.reference.com, Dec 2013

are located within the inertial subrange, and therefore $\sigma^2_{\ln I}$ can be related to C_n^2.

The exact relation between $\sigma^2_{\ln I}$ and the path averaged structure parameter ($\overline{C_n^2}$) is described with a complex mathematical expression that integrates over the typical range of eddy scales, and over the scintillometer path (see among others Beyrich et al., 2012; Van Kesteren, 2012; Hartogensis, 2006). In this thesis, we confine ourselves to a more convenient form of this relation, which specifies that the contribution of C_n^2 to the scintillometer signal varies with location along the path:

$$\sigma^2_{\ln I} \propto \int_0^{L_{\text{path}}} C_n^2(x) W(x) \mathrm{d}x \propto \overline{C_n^2} \tag{1.4}$$

in which L_{path} is the total distance of the path, and $W(x)$ is the path weighting function. The shape of $W(x)$ depends on the scintillometer type, but it closely resembles a bell-shape curve. This means that the scintillometer is not sensitive to fluctuations near the transmitter ($x = 0$) and the receiver ($x = L_{\text{path}}$), and most sensitive to fluctuations in the centre of the path ($x = L_{\text{path}}/2$).

1.2.2. Monin-Obukhov Similarity Theory

In order to describe the behaviour of turbulence often the Buckingham Π-theorem (Buckingham, 1914) is used. In the context of scintillometry Monin-Obukhov Similarity Theory (MOST) is an important framework (Monin and Obukhov, 1954). MOST links the surface fluxes with other turbulent quantities, such as mean gradients, standard deviations or structure parameters[2]. MOST assumes that the dimensionless turbulent quantity is fully determined by four parameters:

1. the kinematic surface heat flux (sensible or latent)
2. the observation height above the surface,
3. the friction velocity as a proxy of the mechanical turbulence at the surface, and
4. the buoyancy flux as a measure of the convective turbulence at the surface.

Within MOST two dimensionless groups can be formed. The first dimensionless group is the dimensionless height: z/L, in which z is the observation height and L is the Obukhov length. The Obukhov length can be interpreted as the height of the sub-layer of dynamic turbulence (Monin and Obukhov, 1954). Here, z/L is a measure of the stability and is defined as follows[3]:

$$\frac{z}{L} = -\frac{z\kappa g}{\overline{T_v}} \frac{\overline{w'T_v'}}{u_*^3} \tag{1.5}$$

[2]Note that Monin and Obukhov (1954) derived only the flux-based dimensional analysis for wind and temperature gradient for non-neutral flows. Obukhov (1960), however, was the first to derive the similarity relations for structure parameters, independent of the Monin-Obukhov similarity framework (Foken, 2006). However, because in literature the term Monin-Obukhov similarity is commonly used for surface flux-based scaling in general, we use the term here for the similarity relationships of structure parameters as well.

[3]In thesis we focus on processes near the surface instead of the entire ABL, therefore, we assume that temperature variations due to changes in height (pressure altitudes) can be neglected. In other words, we use the normal temperature (T) instead of the potential temperature (θ).

in which u_* is the friction velocity, $\overline{w'T'_v}$ is the buoyancy flux, $\kappa = 0.4$ is the von-Kármán constant, and $g = 9.81$ m s^{-2} is the acceleration due to gravity. Stability can be considered as a measure of the effect of buoyancy relative to shear in the production of turbulence. Three stability regimes are defined:

- the near-neutral regime: the effect of buoyancy is small, turbulence is mainly produced by shear ($\overline{w'T'_v} \approx 0$, $u_* >> 0$, so that $z/L \approx 0$).
- the unstable regime: the effect of buoyancy is large, turbulence is mainly produced by buoyancy (day time conditions: $\overline{w'T'_v} > 0$, $u_* \approx 0$, so that $z/L < 0$).
- the stable regime: the effect of buoyancy is large, but now turbulence is suppressed by buoyancy and only produced by shear (night time conditions: $\overline{w'T'_v} < 0$, $u_* \approx 0$, so that $z/L > 0$).

In this thesis we focus on atmospheric observations that are obtained during unstable conditions.

The second dimensionless group is the dimensionless mean turbulent quantity of interest, e.g. the dimensionless gradient, dimensionless variance or dimensionless structure parameter. In scintillometry, the dimensionless structure parameter ($\widetilde{C_s^2}$) is of interest. Using MOST, the structure parameter is made dimensionless as follows:

$$\widetilde{C_s^2} = \frac{C_s^2 z^{2/3}}{s_*^2} \tag{1.6}$$

Then the universal relation $f_s\left(\frac{z}{L}\right)$ between the $\widetilde{C_s^2}$ with z/L is empirically determined using experimental data. The most commonly used expression for unstable conditions of this relation is as follows:

$$\widetilde{C_s^2} = f_s\left(\frac{z}{L}\right) = c_{s1}(1 - c_{s2} z/L)^{-2/3} \tag{1.7}$$

Equation 1.7 shows that the mean C_s^2 decreases with height and instability in terms of z/L. This decrease with height is non-linear: it is larger close to the surface than at larger heights. For free convection conditions, buoyancy strongly dominates over friction (i.e. $-z/L$ is large), so that the decrease of C_s^2 is $\sim z^{-4/3}$.

MOST is restricted to the part of the ABL close to the surface. This layer is called the atmospheric surface layer (ASL, with depth z_{ASL}). In the ASL, turbulence is controlled by surface processes, whereas processes that occur in the rest of the ABL, such as entrainment, are neglected. Entrainment, in this context, is the mixing of air parcels from the layer above the ABL (the free atmosphere) within the ABL. A rough estimate of the depth of the ASL is about 10 % of the ABL depth (see for a more precise definition Chapter 2). As the ABL depth grows during the day, the ASL depth is not constant. At midday, when turbulent transport is strong, the ABL can be as deep as 1 km in summer time, and the ASL depth has the order of 100 m. During night, when turbulence is destroyed and the ABL depth has the order of 100 m or even less, the ASL is only around 10 m deep.

Another restriction for the use of MOST is that it is defined for stationary and homogeneous conditions only. To be able to describe the structure of the turbulent boundary layer over heterogeneous surface (i.e. differences in H and LE between patches of different surface characteristics), several concepts have been developed. The first concept is that MOST is only valid above a certain level (the so-called blending height: z_{b}), where the influence of the individual patches is not visible anymore due to turbulent mixing. In case of scintillometry, this level has to be located in the ASL, because otherwise MOST is questionable. In literature, different z_{b} for various quantities can be found. When measuring at levels below z_{b}, the heterogeneous surface along the scintillometer path becomes important. Therefore, in the second concept, it is necessary to consider the relative influences of the patches within the area that are "seen" by the instrument. This area is called 'effective fetch', 'footprint' or 'source area' (Schmid, 2002). Meijninger et al. (2002b) calculated the relative influences of the different patches with a footprint analysis, and combined this with a land-use map to obtain path-averaged surface fluxes from local EC measurements above patches of different land use. They used these path-averaged fluxes as a reference to validate the fluxes from the scintillometers.

1.3. Open issues discussed in this thesis

With the background explanation of the structure parameter and MOST, we can now address the issues discussed in this thesis. The first two issues are related to the applicability of MOST, whereas the second two are related to measuring C_s^2 over a heterogeneous surface.

1.3.1. The applicability of MOST

It appears that the theory behind the LAS is only valid for the weak scattering regime. In case of stronger scattering, the upper limit of scintillations that can be measured is reached: the signal gets saturated. In order to reduce the total amount of scintillations and therefore to prevent saturations, the LAS can be installed over a shorter path or at a higher level. The latter solution considers that the magnitude of the structure parameter decreases with height, as discussed in Sect. 1.2.2. However, a disadvantage of installing the LAS at an elevated level is that this level could be above the ASL if the ASL is shallow. This is especially the case during the morning when the ABL is shallow. Because MOST is only defined for the ASL, the use of MOST is not justified in these cases. The first research question studied in this thesis is therefore related to the depth of the ASL:

Question 1 - To what extent can the sensible heat flux be determined from the structure parameter of temperature observed at elevated levels, particularly during the morning period when the measurement level is situated above the atmospheric surface layer?

The second question is related to the large variety of the Monin-Obukhov similarity functions (f_s) that are reported in literature (Wyngaard, 1973; Wesely, 1976b; Andreas,

1988; Hill et al., 1992; Thiermann and Grassl, 1992; de Bruin et al., 1993; Li et al., 2012; Maronga, 2014). This suggests that the dimensionless function seems not to be a universal relation. Reasons for these large variations are likely related to differences between the studies in: a) the regression approaches to determine f_s, b) the stability ranges covered by the data, c) the measurement heights (z), d) the instrumentation, e) the data processing, and f) the characteristics of the underlying surface with respect to surface heterogeneity and soil moisture conditions. Because most of the effects vary simultaneously between the studies, it is difficult to separate the effect of one aspect from the effects of others. Therefore, here we will investigate the behaviour of f_s *within one dataset* for unstable conditions, so that we can assume uniform data processing, instrumentation and the surface characteristics. The related research question is:

Question 2 - To what extent is the expression for the dimensionless structure parameter influenced by specific regression approaches, stability ranges and observation levels?

1.3.2. C_s^2 over a heterogeneous surface

Information about the variability of the structure parameter is important for the validation of scintillometry over heterogeneous surfaces. Results of Petenko and Shurygin (1999); Cheinet and Siebesma (2009), and Cheinet and Cumin (2011) showed that C_s^2 varies over several orders of magnitude (local variability of C_s^2), when C_s^2 is obtained at one point (variation in time) or above a homogeneous surface (variation in space). This means that one observes variations in C_s^2 for two reasons if C_s^2 is measured along a path over a heterogeneous surface (see the sketch in Fig. 1.3). The path-averaged C_s^2 varies due to the local variability at each point along the path (black line in Fig. 1.3), but it also varies due to surface heterogeneity. The variability due to surface heterogeneity, in contrast to the local variability, would be relatively constant in time and near zero above a single patch (dark gray line in Fig. 1.3). In order to describe the relation between heterogeneous surface fluxes and the (path-averaged) scintillometer signal, a better understanding of the different types of variability in C_s^2 along the path is needed. To identify the variability in C_s^2 related to heterogeneity, one needs to know the magnitude of the local variability.

Therefore, the third research question of this thesis is related to the local variability of C_s^2. If the local variability of C_s^2 is known over a range of conditions (height, stability etc.), it can be considered as a kind of "background noise" superimposed on the variability caused by surface heterogeneity. Consequently, a measure of the local variability of C_s^2 can be used to assess whether observed spatial differences in C_s^2 along a path can be attributed to surface heterogeneity or have to be considered to lie within the range of local variability.

Question 3 - What determines the local variability of the structure parameter within the atmospheric surface layer at different heights and under different stability regimes?

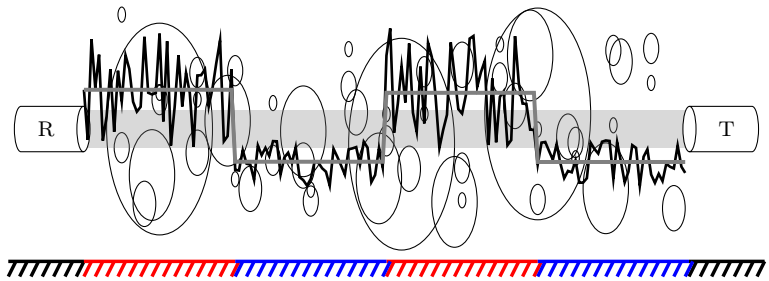

Fig. 1.3. Sketch of the scintillometer setup over a heterogeneous surface. The red patches correspond to areas with higher sensible heat flux and the blue ones to areas with lower sensible heat flux. The black line is the local C_T^2 observed along the path, and the grey line is the averaged C_T^2 over each patch.

The fourth question is related to the surface heterogeneity along the scintillometer path. In literature, the validation of scintillometer measurements over heterogeneous surfaces is usually performed by comparing the scintillometer-based fluxes with fluxes from aggregated EC measurements (Meijninger, 2003; Beyrich et al., 2006; Meijninger et al., 2006), whereas a direct validation of the path-averaged structure parameters against independent measurements is still missing. A direct validation is needed, because the relation between structure parameters and fluxes is non-linear. This non-linear relation results in an overestimation of the flux obtained from a LAS compared to fluxes from aggregated EC measurements (Meijninger, 2003; Meijninger et al., 2006). Therefore, it is necessary to validate the path-integrated structure parameter from the scintillometers with other independent data sources, such as airborne measurements or Large Eddy Simulation (LES) model results. This was the main goal of the LITFASS-2009 experiment[4]. In this context the abbrevation LITFASS can be understood as LIndenberg-To-Falkenberg Aircraft Scintillometer Study. During this field experiment, several EC stations were set-up at different patches along a 5 km LAS path and an unmanned aircraft (the meteorological mini aerial verhicle, M^2AV) was flown along the same path in order to obtain independent path averaged structure parameters (see Fig. 1.4). Here we focus on the comparison of the LAS with the M^2AV, which brings us to the last research question:

Question 4 - To what extent are the path-averaged structure parameters of large aperture scintillometers in agreement with the structure parameters obtained with an unmanned aircraft?

1.4. Research strategy

In order to answer the above research questions, data of three experiments are used. As said before, the use of MOST is restricted to homogeneous surface conditions. Therefore, data from two sites with relatively homogeneous surface conditions are analysed to answer the first two research questions related to the applicability of MOST (Cabauw,

[4]The LITFASS-2009 experiment was carried out within DFG-NWO project 'Turbulent Structure Parameters over Heterogeneous Terrain - Implications for the Interpretation of Scintillometer Data' of which this PhD-project was a part.

the Netherlands for question 1, and Leon, Kansas, USA for question 4). For the last two questions we use data collected during LITFASS-2009 and LITFASS-2010 (Lindenberg, Germany), which is characterised by a moderately heterogeneous surface.

In this section we briefly describe the research strategy related to each question including some background information about the experiments. Before, we note that whereas a better understanding of the scintillometer signal is the primary motivation of our study, we chose to determine C_s^2 using other instruments (mainly EC systems) to answer the first three research questions. One reason for this is that in that case the footprint of C_T^2 is similar as other measurements needed in the analysis (e.g. MOST, point measurements).

Question 1 is answered using data from the Cabauw tower, which is located in the western part of the Netherlands. Between the Cabauw Tower and the TV tower of IJsselstein an eXtra Large Aperture Scintillometer (XLAS Kipp & Zonen) has been set-up at a height of 60 m. Therefore, in Chapter 2, data from an EC system installed at 60 m at the Cabauw Tower is used. The research question has been accentuated as follows: How should H be determined from C_T^2 obtained at 60 m under unstable conditions, particularly during the morning period when the depth of the ASL is smaller than 60 m. To answer this question, we compare results from two proposed theoretical concepts. In the first concept, we assume that MOST applies at 60 m during the entire day and C_T^2 therefore scales with the surface flux. In the second concept, C_T^2 at 60 m is scaled with the sensible heat flux at the same level, rather than with the surface flux. To obtain the surface heat flux a correction for the flux divergence in the column below the level of observation has to be applied.

Question 2 is answered using data from the Cooperative Atmosphere-Surface Exchange Study (CASES-99, Poulos et al., 2002). This experiment was performed in October 1999 near Leon, Kansas, U.S.A. During CASES-99, 32 thermocouples were mounted along a 50 m tower. This offers a very useful dataset covering a wide range of observation heights (z) in addition to a wide range of stabilities ($1/L$). The study in Chapter 3 can be split in two parts: In the first part, we investigate the impact on f_s of applying a certain regression approach using the entire dataset (from all measurement levels and for all stability classes). In the second part we investigate the impact on f_s of measuring within different stability ranges and at different heights. Therefore, we divide the dataset into eight height classes and eight stability classes. For each class the regression coefficients are determined using the regression approach selected in part 1. Finally, the results of the different classes are compared to each other and to the results of the entire dataset.

Question 3 and 4 are answered using data from the LITFASS-2009 experiment (Beyrich et al., 2012). The study area is moderately heterogeneous with a mixture of farmland patches, forest, small lakes and small villages (Fig. 1 in Beyrich et al. (2012)). The vegetation of the farmland patches mainly consists of maize, sunflowers, colza, barley, and triticale. During the experiment several measurement techniques were

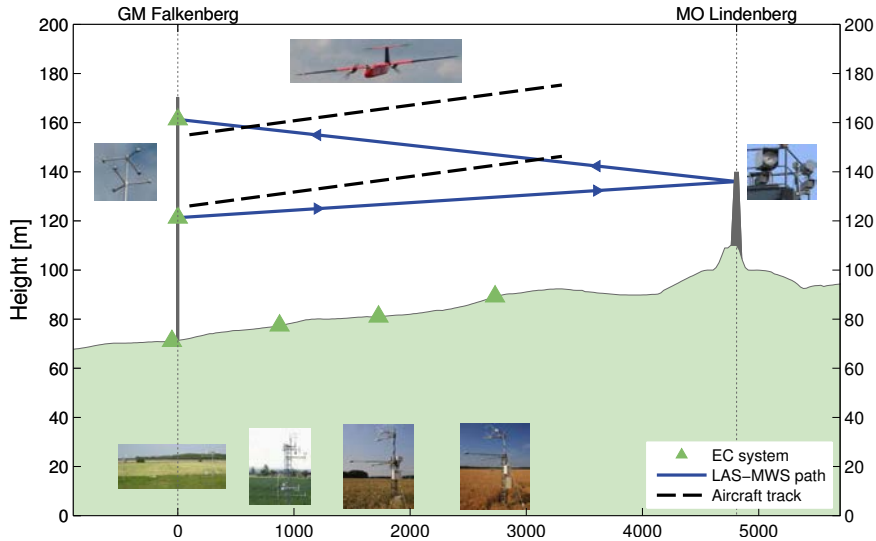

Fig. 1.4. Setup of the LITFASS-2009 experiment

employed, namely eddy covariance, unmanned aircraft and scintillometers (see Fig. 1.4 for an overview).

Question 3 is answered by determining C_T^2 and C_q^2 from EC systems. To investigate the height dependence of the local variability, we used the EC data from three levels: 2.5 m (surface station above triticale), 50 m, and 90 m (along the 99 m tower above grass). The stability dependence is investigated by dividing the data into thirteen stability classes. First, we investigate the shape of the probability density functions (PDF) of C_s^2. Second, we quantify how the variability of C_s^2 depends on the size of averaging window. Finally, we discuss implications for the interpretation of path-integrated structure parameters over heterogeneous surfaces.

To answer **question 4**, we finally focus on data obtained from scintillometer measurements. Because the meteorological conditions were unfavourable to measure a complete diurnal cycle with the unmanned aicraft, M^{2}AV, during the LITFASS-2009, we also use data from an additional flight campaign (LITFASS-2010). A first comparison of C_T^2 presented in Beyrich et al. (2012) using LAS and M^{2}AV from just one flight day (13 July 2009) shows that the afternoon decrease of C_T^2 obtained by the M^{2}AV and LAS is consistent, but the values of C_T^2 from the M^{2}AV are systematically larger than from the LAS. One reason for this difference could be that for this first comparison C_T^2 from the two systems were processed using a standard procedure, not taking into account different averaging times and the LAS path weighting function (Eq. 1.4) when analysing the M^{2}AV data. Therefore, we accentuate the last research question as follows: Can similar differences be found on the other days, and can these differences be reduced or explained through a more elaborate processing of either or both the LAS and the M^2 AV data?

1.5. Thesis outline

The research questions presented in Sect. 1.3 will be answered in chapters 2 to 5. These chapters were independently prepared for publication in Boundary-Layer Meteorology. Chapter 2 has been published in 2012, Chapter 3 has been accepted for minor revisions in March 2014, Chapter 4 has been published in 2014, and Chapter 5 is in preparation for submission. The chapters are presented in the article form. As a consequence, some repetition will occur, mainly in the sections were the theory, data or methods are described. The summary of the entire thesis is given in Chapter 6. In the final chapter the general discussion and recommendations are presented.

In the appendix, a validation of C_n^2 obtained by two LAS built by the Meteorology and Air Quality group (MAQ) of Wageningen University is given, which has been published as an internal report of MAQ. The motivation for this study was the fact that for the LITFASS-2009 experiment the signals from the two LAS were processed in different ways. Moreover, one of these LAS, which has been in operational use for more than ten years, was recalibrated after the experiment. We therefore investigated the differences in data processing and the effect of the calibration on C_n^2 obtained from the two LAS.

2 Monin-Obukhov scaling in and above the atmospheric surface layer: the complexities of elevated scintillometer measurements

2.1. Introduction

The area-averaged surface flux of sensible heat is of interest for many meteorological and hydrological studies, e.g. to evaluate mesoscale numerical models or satellite-based retrieval algorithms. Over homogeneous terrain, the eddy-covariance method or other local point measurement techniques can be used to determine this flux (Lee et al., 2004; Foken, 2008). Over heterogeneous terrain, however, point measurements are not suitable. During recent years, the use of scintillometers has proven to be a reliable method for measuring the spatially-averaged flux over heterogeneous surfaces under daytime conditions (e.g. Meijninger et al., 2002b; Beyrich et al., 2005; Kohsiek et al., 2006). To obtain the sensible heat flux from the scintillometer signal several steps are involved. From the scintillometer data the structure parameter of the refractive index of air is determined, which is used to calculate the structure parameter of temperature (C_T^2). Then, the surface sensible heat flux is derived by applying Monin-Obukhov similarity theory (MOST, Wyngaard, 1973; Meijninger, 2003; Moene et al., 2004), which is valid for the atmospheric surface layer, where fluxes are assumed to vary little with height.

One limitation of the scintillometer is that it has an upper limit on scintillations that can be measured, due to the saturation of the scintillometer signal (Kohsiek et al., 2002, 2006). One way to prevent saturation is to install a scintillometer at an elevated level, since the magnitude of the structure parameter of temperature decreases with height. However, a consequence of a greater height is that the observations are not always located in the atmospheric surface layer and the application of MOST is in principle not justified. This situation particularly occurs in the morning when the boundary layer is relatively shallow.

This chapter is published as Braam M, Bosveld FC, Moene AF (2012) On Monin-Obukhov scaling in and above the atmospheric surface layer: The complexities of elevated scintillometer measurements. Boundary-Layer Meteorol 144:157–177

In order to obtain the surface sensible heat flux from the structure parameter of temperature at elevated levels under unstable conditions, two different theoretical concepts are proposed. In the first concept, we assume that MOST still applies at levels just above the atmospheric surface layer and that C_T^2 still scales with the surface flux. In the second concept, the structure parameter of temperature at elevated levels has to be scaled with the local sensible heat flux, rather than with the surface flux. To obtain the surface heat flux a correction for the flux divergence in the column below the level of observation has to be applied.

Whereas the scintillometer is the motivation of our study, we chose to evaluate the two proposed concepts with data from a sonic anemometer/ thermometer (sonic) installed on the Cabauw tower, the Netherlands, about 60 m above the surface. The footprint of the path-averaged C_T^2 obtained by the scintillometer differs from the footprint of the sensible heat fluxes (point measurements), which are calculated from sonic data. Consequently, the main question is how the surface sensible heat flux should be determined from the structure parameter of temperature determined at 60 m under unstable conditions, particularly during the morning period when the level of 60 m is situated above the atmospheric surface layer. Since several MOST relationships are proposed in the literature (see, Moene et al., 2004), we perform an analysis of the relationships of Andreas (1988); Hill et al. (1992); and de Bruin et al. (1993, hereafter referred to A88, H92 and DB93, respectively) before comparing the two concepts, to investigate which similarity relationship is most suitable for our dataset.

The paper is structured as follows: in Sect. 2.2 the theory behind MOST and the two proposed concepts are described. Information about the experimental set-up, dataset and the applied corrections can be found in Sect. 2.3. Section 2.4 provides a description of the boundary-layer structure, a similarity study of the MOST relationships with the data observed in the atmospheric surface layer is presented, and the two proposed concepts are compared. In the final section the conclusions are given.

2.2. Theory

Monin-Obukhov similarity theory applies to the atmospheric surface layer (ASL, with depth z_{ASL}) under stationary and horizontally homogeneous surface conditions (e.g. Businger et al., 1971). In the ASL, turbulence is controlled by surface processes, whereas processes in the rest of the atmospheric boundary layer (with depth z_{i}), such as entrainment, play a less important role. For this reason, the only height in the dimensional analysis that is taken into account is the observation height (z). This holds if $z << z_{\mathrm{i}}$, which is operationalized as $z < 0.1\ z_{\mathrm{i}}$. If we assume a linear sensible heat-flux profile and no entrainment at the top of the boundary layer then surface-layer fluxes do not differ by more than 10 % from the surface flux ($\overline{w'T'}_{\mathrm{s}}$) within the surface layer, as is illustrated in Fig. 2.1 by the solid line. Therefore, the surface layer is often referred to the constant-flux layer. However, in the case of dry air entrainment, the variation in the heat flux is more than 10 % over the depth of the ASL (0.1 z_{i}, Fig. 2.1). The

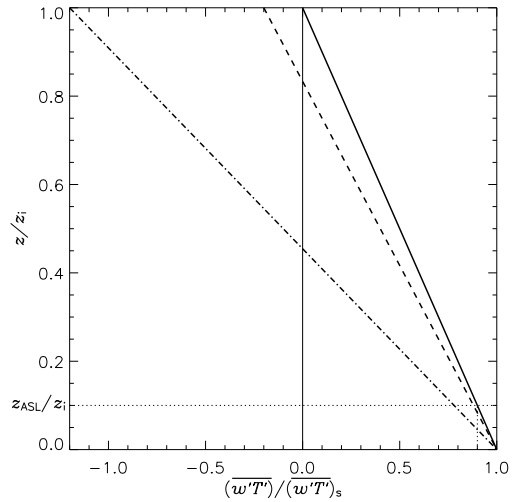

Fig. 2.1. Three sketches of the linear turbulent sensible heat-flux profile in the boundary layer. Solid line: without an entrainment flux ($\overline{w'T'}_e = 0$). Dashed line: free-convection situation ($\overline{w'T'}_e = -0.2\overline{w'T'}_s$). Dash-dotted line: early morning situation ($\overline{w'T'}_e = -1.2\overline{w'T'}_s$).

dashed line represents a case for the free convection situation with an entrainment flux ($\overline{w'T'}_e$) that amounts to $-0.2\overline{w'T'}_s$ of the surface flux (Tennekes, 1973). In that case the fluxes across the surface layer do not vary that much: 12 %. During the morning period however, when the entrainment flux is large (dash-dotted line) the fluxes within the ASL can differ much more. From our dataset we find an entrainment ratio of -1.2, two hours after sunrise. This gives a flux variation of 22 % across the atmospheric surface layer. Consequently, the application of MOST at elevated levels is questionable in the morning period for two reasons: (a) the relative height z/z_i of a certain observation level can easily be larger than 0.1 if the boundary layer is shallow, and (b) the flux divergence in the surface layer can be larger than 10 % when (the absolute value of) the entrainment ratio is large. Kohsiek (1988) used mixed-layer scaling to scale structure parameters at levels up to 200 m under convective conditions. This approach may be also questionable in the early morning when the boundary layer is not yet well-mixed.

MOST is based on the observation that the statistics of turbulence in the surface layer are fully determined by four parameters: the surface flux of the scalar under consideration, the friction velocity u_*, the buoyancy flux $(g/T)\overline{w'T'_v}$ and the height above the surface z (Wyngaard, 1973; Stull, 1988; Meijninger, 2003; Moene et al., 2004). Applying this to the structure parameter of temperature we obtain:

$$\frac{C_T^2 z^{2/3}}{T_*^2} = f\left(\frac{z}{L}\right) \tag{2.1}$$

with the Obukhov length $L = Tu_*^2/(\kappa g T_{v*})$, the temperature scale $T_* = -H/(\rho c_p u_*)$ and the friction velocity $u_* = \sqrt{\tau_0/\rho}$, in which T is the temperature, T_v the virtual temperature, $\kappa = 0.4$ is the von-Kármán constant, $g = 9.81$ m s^{-2} is the gravity

Table 2.1. Expressions for the similarity relationships ($f(z/L) = c_1 (1 - c_2 z/L)^{-2/3}$) under unstable conditions. Note that the similarity relationship of A88 is a modification of Wyngaard (1973) with $\kappa = 0.4$.

c_1	c_2	d	Observation level [m]	Stability range	Reference
4.9	6.1	1.46	5.66, 11.3 and 22.6	scatter cloud $-z/L < 1.1$ 6 points: $1.1 < -z/L < 2.5$	Andreas (1988)
8.1	15.0	1.33	3.95	50 % of data: $0.1 < -z/L < 0.5$	Hill et al. (1992)
4.9	9.0	1.13	11.3	scatter cloud: $-z/L < 3$ 6 points: $3 < -z/L < 100$	de Bruin et al. (1993)

acceleration, H is the surface sensible heat flux, ρ is the density, c_p is the specific heat at constant pressure and τ_0 is the surface shear stress. Several expressions for $f(z/L)$ exist in the literature for stable and unstable conditions (for an overview see Moene et al., 2004). Since we focus our research on unstable conditions only, the formulations of H92, A88 and DB93 are evaluated (Table 2.1). The relationships all have the form:

$$f\left(\frac{z}{L}\right) = c_1 \left(1 - c_2 \frac{z}{L}\right)^{-2/3} \tag{2.2}$$

in which the coefficients (c_1 and c_2) have been empirically determined with near-surface data by varying L. The coefficient c_1 is the asymptotic value of $f(z/L)$ for the neutral limit. On the other hand, $1/c_2$ is a measure of stability (z/L) at which the neutral limit transits into the free convection limit. The exponent $-2/3$ ensures the correct behaviour in the free convection limit. The fourth and fifth columns in Table 2.1 display the observation level and the stability range for the datasets on which the relationships are based. For near-neutral conditions the H92 relationship gives the highest values, due to the high value of c_1. The similarity relationships of DB93 and A88 have the same value of c_1. However, since c_2 is much higher for DB93, the transition point from neutral to unstable conditions occurs at a lower stability. As a result, the similarity relationship of DB93 shows the lowest values. Under very unstable conditions the three show quite similar results. In the free convection limit Eq. 2.2 reduces to $f(z/L) = d(-z/L)^{-2/3}$ in which $d = c_1 c_2^{-2/3}$; d is also given in Table 2.1 showing that A88 gives largest and DB93 gives lowest values in the free convective range.

As discussed above, MOST might not be expected to be valid at the measurement height during the morning period due to the shallow surface layer and the large entrainment flux. In order to obtain the surface sensible heat flux from the structure parameter of temperature at elevated levels, two different concepts are proposed.

In the first concept (MOSTs, s for surface), the structure parameter of temperature at 60 m is scaled with the surface flux. Although the surface flux may not affect the turbulence outside the ASL directly, it does so indirectly. The surface heat flux is the cause of the temperature contrast over the depth of the atmospheric boundary layer, and as such is the primary source of turbulent temperature fluctuations. Therefore the structure parameter, which is a measure of temperature fluctuations, will scale on

the surface flux. Consequently, we hypothesize that MOST can be applied at higher levels as well. In the second concept (MOSTl, l for local level), the structure parameter is scaled with the local-level fluxes. The assumption is that there is a local relation between vertical heat transport and the smaller scale temperature fluctuations in the turbulent cascade towards the dissipation range. This use of MOST is comparable with the local scaling hypothesis that is often used in the stable boundary layer (Nieuwstadt, 1984). In order to obtain the surface flux, a correction for the flux divergence between the surface and the observational level needs to be applied when using this concept.

2.3. Research strategy & Methods

The data have been collected at the Cabauw tower (52°58.22' N 4°55.57' E), which is located in the western part of the Netherlands. The area around the tower is open pasture terrain for 400 m; for a detailed description of the site area see van Ulden and Wieringa (1995). At first sight the surroundings of Cabauw have quite homogeneous surface characteristics, though on closer inspection a distinction has to be made between the regional characteristics and those close to the tower. First, the near-tower aerodynamic roughness length ($z_{0\,\mathrm{m}}$) is smaller than the regional value (grassland, $z_{0\,\mathrm{m}} \approx 0.03$ m and scattered rows of trees, $z_{0\,\mathrm{m}} \approx 0.15$ m, respectively). For a given geostrophic wind, the near-tower friction velocity will be different from the regional value. Second, we find a distinction between the near-tower and regional Bowen ratios (see Sect. 2.4.1). Since we investigate data from elevated levels that have a larger footprint area than surface observations, the regional surface characteristics are relevant for this study. Notice that, in this manuscript, the adjective near-tower (in contrast to regional) refers to the local horizontal area that influences the sonic measurements. This is done, because the adjective local-level (in contrast to surface) is already used to specify the local vertical measurement level used for scaling.

The analyzed period covers 4 May 2008 till 11 May 2008, a period chosen because it consists of cloud-free days, and the synoptic weather conditions show only little variation. Due to this small variation we are able to use a composite of the eight days for part of the analyses using 30-min averaged data.

This section starts with a description of the main steps in the analysis, which is supported by Fig. 2.2. Subsequently the methods of calculating fluxes and C_T^2 from the sonic anemometer/thermometer (sonic) data (Sect. 2.3.2) and the determination of C_T^2 from the scintillometer data are outlined (Sect. 2.3.3).

2.3.1. Research Strategy

This research can be split into two steps. In the first step we evaluate which of the proposed similarity relationships is valid for our dataset, while the second step evaluates the validity of the MOSTs and MOSTl concepts.

In both steps an independent measure of the structure parameter of temperature is needed (row 1, Fig. 2.2). In step 1 we need the independent C_T^2 as input to compare

the two dimensionless groups (z/L and $C_T^2 z^{2/3}/T_*^2$) in MOST. In step 2 the independent C_T^2 are used to validate the 60-m structure parameter of temperature calculated with the two different MOST concepts ($C_{T\,60\,\mathrm{mMOSTs}}^2$ and $C_{T\,60\,\mathrm{mMOSTl}}^2$). Ideally, we would use the scintillometer to determine the independent structure parameter, because the scintillometer measurements at elevated levels are the motivation behind our study. However, the MOST-scaling variables (row 2, Fig. 2.2) that are used in the validation cannot be obtained from the scintillometer but are available from the sonic measurements. So, then the footprints of the MOST-scaling variables (sonic: point measurements) will differ from the one of the independent structure parameter (scintillometer: path measurements). Furthermore, the scintillometer does not measure C_T^2 directly, but it is obtained from C_n^2. Therefore, we decided to analyze the directly observed C_T^2 from the sonic instead of C_T^2 derived from the scintillometer. Another advantage of using the sonic is that data are also available at 3, 100 and 180 m. In other words, in this research the concepts are solely analyzed with sonic data (see Sect. 2.3.3 for details about the determination of C_T^2 from the sonic), whereas the scintillometer is our motivation. Therefore, scintillometer output is only used to compare the path-averaged C_T^2 with the point measured C_T^2, in order to ensure that our conclusions are relevant for scintillometer data as well.

Furthermore, both steps also need MOST scaling variables as input data (row 2, Fig. 2.2). Strictly speaking, the temperature scale and the friction velocity are calculated from the surface fluxes (see Sect. 2.2), but in practice H and τ_0 cannot be measured. Instead, the fluxes are derived from the turbulence fluxes measured with the sonic. For the scaling related to the 3-m data it is assumed that there is no vertical flux divergence so that the observed turbulence fluxes are equal to the near-tower surface fluxes (column 1 of row 2, Fig. 2.2). As said before a difference was found between the near-tower and the regional fluxes around Cabauw, therefore in the scaling related to the 60 m we use the regional fluxes. For the local-level scaling (MOSTl) this means that we are using the regional local-level friction velocity and the regional local-level turbulent heat flux. For the surface scaling (MOSTs), it is assumed that there is only flux divergence for the sensible heat flux. Hence, the regional surface sensible heat flux is derived from the observed flux at 60 m with a correction for the flux divergence. This correction is based on the time rate of change of the temperature as observed along the mast, and where advection is neglected. Furthermore, in MOSTs we used $u_{*60\,\mathrm{m}}$ for the momentum flux. Consequently, the difference between MOSTl and MOSTs corresponds to the use of the regional local-level heat flux and the regional surface heat flux, respectively (column 2 and 3 of row 2, Fig. 2.2).

In order to evaluate which of the proposed similarity relationships (see Table 2.1) is valid for our dataset, we determine the similarity relationships for the 3-m data and the 60-m data (step 1, Fig. 2.2). In this analysis we focus on ASL data only, where MOST can be expected to be valid. As indicated in the previous section, the surface-layer depth is defined as 10 % of the boundary-layer depth. The boundary-layer

depth is determined from a wind profiler (LAP 3000) following Beyrich and Görsdorf (1995) and Klein Baltink and Holtslag (1997). At 3 m (located in the ASL the entire time) all data under unstable conditions are selected ($\overline{w'T'}_{3\,\mathrm{m}} > 0$). For the 60-m level we consider only the unstable data where 60 m is located within the surface layer ($\overline{w'T'}_{\mathrm{ll},60\,\mathrm{m}} > 0 \wedge z_{\mathrm{ASL}} > 60$ m). Both MOSTs and MOSTl are used; due to the small variation of the flux with height within the surface layer MOSTs and MOSTl should show similar results.

The second step (Fig. 2.2) is to determine the validity of the MOSTs and MOSTl concepts at 60 m. We calculate the 60-m structure parameter of temperature with the two different MOST concepts ($C^2_{T\,60\,\mathrm{mMOSTs}}$ and $C^2_{T\,60\,\mathrm{mMOSTl}}$), and compare them with the directly observed values from the sonic ($C^2_{T\,60\,\mathrm{msonic}}$). Note that the label sonic refers to the directly measured C_T^2 without scaling, in contrast to the labels MOSTs and MOSTl that refers to C_T^2 derived from sonic data by applying the scaling relation. The reason to use MOST in the reverse way (to obtain C_T^2 from observed fluxes) is that we are interested in the different processes that act on the structure parameter of temperature rather than the flux itself. In our analysis all the data under unstable conditions are considered ($\overline{w'T'}_{\mathrm{ll},60\,\mathrm{m}} > 0$). In addition, the unstable data are split into two other groups. The first group contains data where 60 m is located in the atmospheric surface layer ('ASL', $z_{\mathrm{ASL}} > 60$ m), whereas the second group consists of data obtained above the surface layer (during the early morning period, 'NASL', which represents non-atmospheric surface layer, $z_{\mathrm{ASL}} < 60$ m).

2.3.2. The sonic anemometer/thermometer

The sonic anemometer/thermometer (Gill Solent R3, sample frequency: 10 Hz) is used (a) to obtain the directly measured structure function of temperature ($C^2_{T\mathrm{sonic}}$), and (b) to determine the turbulent fluxes that are used to calculate the MOST scaling parameters. The sonic path has a length of 0.15 m. Sonics are installed at 3, 60, 100 and 180 m height, with the sonic at 3 m is positioned on a small mast approximately 200 m north of the main tower. The others are placed on the south-east booms of the tower. With easterly winds, as is in the case for the period analyzed here, no significant flow obstruction occurs.

The structure parameter of temperature

The structure parameter of temperature within the inertial subrange can be defined by (Stull, 1988; Bosveld, 1999; Moene et al., 2004):

$$C_T^2 = \frac{D_{TT_x}(r)}{r^{\frac{2}{3}}} = \frac{\overline{[T(x+r) - T(x)]^2}}{r^{\frac{2}{3}}} \tag{2.3}$$

in which D_{TT_x} is the spatial (x) structure function, r is the spatial separation, $T(x)$ and $T(x+r)$ are the temperatures at location x and $x+r$. However from point observations (e.g. sonic data), only the temporal structure function of temperature (D_{TT_t}) can be

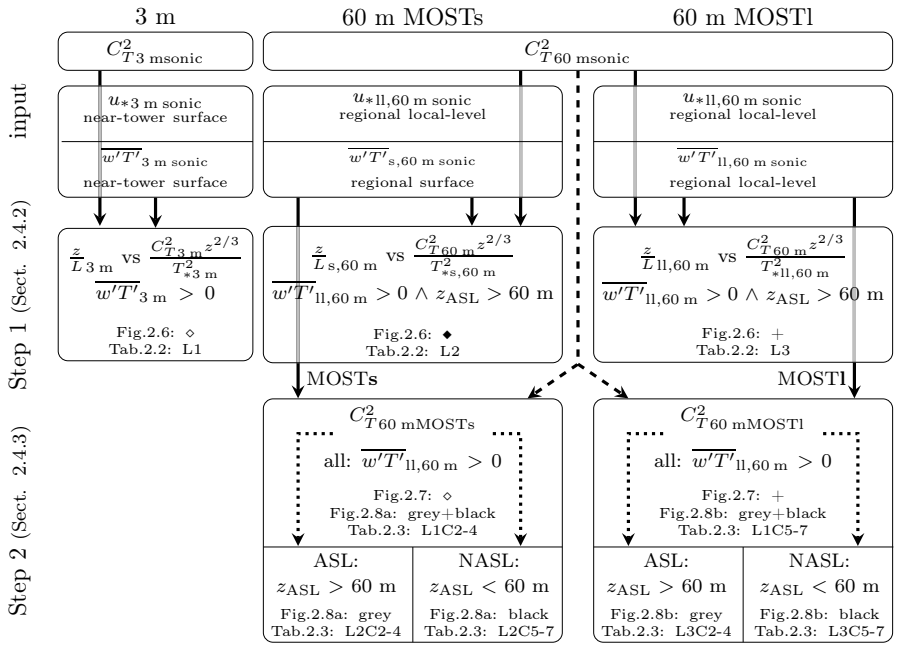

Fig. 2.2. Sketch of the research strategy. The first two rows represent the input data (the first the directly measured C_T^2 and the second the combinations of friction velocity and turbulent sensible heat flux used in MOST). The second two rows show the output (first line), with which condition the data are filtered (second line) and in which figure and table the analysis is shown (last lines). Solid arrows mean 'is input of', the dashed arrows mean 'will be used to validate' and the dotted ones 'will be split into'. The abbreviation 'ASL' stands for surface-layer data, 'NASL' for non-atmospheric surface-layer data, 'L' for line and 'C' for column.

derived:

$$D_{TT_t}(\tau) = \overline{[T(t+\tau) - T(t)]^2} \tag{2.4}$$

in which the subscript t indicates that it is the temporal structure function, $T(t)$ and $T(t+\tau)$ are the temperatures at times t and $t+\tau$, and τ is the temporal separation. Lumley (1965) and Wyngaard and Clifford (1977) derive the conversion from the wavenumber to the frequency domain. Here we are concerned with the conversion from the time to space domain and follow Bosveld (1999). The conversion is performed by (a) assuming stationary and horizontally homogeneous conditions, (b) applying Taylor hypothesis, and (c) assuming that the turbulent variation of the wind vector has a three-dimensional Gaussian distribution:

$$D_{TT_x}(r) = \frac{D_{TT_t}(r/\overline{U})}{1 - \frac{1}{9}\frac{\sigma_u^2}{\overline{U}^2} + \frac{1}{3}\frac{\sigma_v^2}{\overline{U}^2} + \frac{1}{3}\frac{\sigma_w^2}{\overline{U}^2}} \tag{2.5}$$

in which, σ_x^2 is the variance of x, where x can be the wind component in the u, v and w direction respectively and $\overline{U}$ is the averaged length of the horizontal wind vector ($\sqrt{\overline{u(t)}^2 + \overline{v(t)}^2}$). The variance in the three directions and the wind speed itself are determined with the sonic anemometer/ thermometer. In this study we use fixed time

lags, consequently, the spatial separation ($r = \tau\overline{U}$) varies in time. After investigating the width of the inertial subrange by spectral analysis (Braam, 2008), we chose a time lag of 0.2 s for the sonic at 3 m and of 1.8 s for the other levels.

The temperature data from the sonic anemometer/ thermometer are determined from the speed of sound. In the conversion from the so-called sonic temperature to the air temperature, the former is corrected for wind speed and humidity (Schotanus et al., 1983; Liu et al., 2001). The wind-speed correction is already done internally in the instrument (Gill Instruments Ltd., 2002). Essential variables in the humidity correction are specific humidity and mean temperature. Since the sonic cannot measure the absolute value of the temperature very accurately, we used the mean air temperature ($\overline{T}$) measured with KNMI Pt500-elements at 200, 140, 80, 40, 20, 10 and 1.5 m in the humidity correction. To determine the mean temperature at the height of the sonics, a linear interpolation between the two nearest levels is done. Based on the correction for temperature fluctuations (first part of Eq. 6 of Schotanus et al. 1983 and Eq. 10 of Liu et al. 2001), the temporal structure function corrected for humidity becomes:

$$\overline{\left[T_{\mathrm{cor}}(t+\tau) - T_{\mathrm{cor}}(t)\right]^2} = \overline{\left[T_{\mathrm{son}}(t+\tau) - T_{\mathrm{son}}(t) + 0.51\overline{T}(q(t) - q(t+\tau))\right]^2} \qquad (2.6)$$

in which the subscript 'cor' indicates the corrected value and 'son' the sonic measurements. The specific humidity fluctuations are derived from open-path gas analyzers (LiCor-7500) placed at the same height as the sonics.

A disadvantage of using sonics to determine the structure parameter is that the temperature fluctuations smaller than the path length are not taken into account. To correct for these spectral losses, the correction of Hartogensis et al. (2002) for the deviation of the measured spectrum from the inertial subrange is used.

Turbulent heat fluxes

The turbulent fluxes are obtained from the sonic data, and in order to correct the turbulent heat flux for humidity, we use the first part of Eq. 12 of Liu et al. (2001). A tilt correction is applied as well. Streamline tilt is estimated by a linear regression between the mean vertical wind on mean horizontal wind for wind-direction bins of 20 degrees and for wind speeds > 3 m s^{-1}. Fluxes are corrected given this wind-direction dependent mean streamline tilt. The turbulent fluxes are corrected for low frequency loss due to a finite averaging period. The correction is based on calculation of low-frequency contributions from standard surface layer cospectra (Bosveld, 1999), extended to levels above the atmospheric surface layer by Schalkwijk et al. (2010).

2.3.3. The scintillometer

An eXtra Large Aperture Scintillometer (XLAS Kipp & Zonen) has been set-up between the Cabauw Tower and the TV tower of IJsselstein (52°00.72' N. 5°03.23' E). The XLAS transmits a light beam with a near infra-red wavelength of 880 nm. The aperture diameter is 0.328 m. The distance between the two towers is 9.8 km. The terrain

around Cabauw is flat and the height of the optical path above the surface is 59.9 m, which is the average of the receiver (61.7 m) and transmitter height (62.1 m) minus 2 m, which accounts for the earth's curvature along the path (Kohsiek et al., 2002).

To calculate the structure parameter of temperature from the structure parameter of the refractive index of air (C_n^2) (the primary output of the scintillometer), the following approximation can be used (Wesely, 1976a; Moene, 2003):

$$C_T^2 = C_n^2 \frac{T^2}{A_T^2} \left(1 + \frac{0.03}{\beta}\right)^{-2} \tag{2.7}$$

in which β is the Bowen ratio and $A_T \approx -0.78 \times 10^{-6} p/T$ where p is the surface pressure. The Bowen ratio is determined from the turbulent fluxes at 60 m observed with the sonic and the LiCor. For the temperature we use the 10-m temperature. The Bowen-ratio correction ($(1 + 0.03/\beta)^{-2}$), which is a correction for humidity-related scintillations) is not applied for $\beta \approx -0.03$ ($-0.04 < \beta < -0.02$), since C_T^2 becomes numerically unstable when β approaches -0.03.

2.4. Results

2.4.1. The structure of the boundary layer

In order to understand the relationship between surface fluxes, local-level fluxes and the observed temperature structure parameters, we first need to study the dynamics of the boundary layer and the different fluxes separately. In this section first the depth of the boundary layer is discussed. Next, the temporal evolution of the friction velocity, an important variable in MOST, is studied. Finally, the turbulent heat fluxes and the measured C_T^2 at the four different levels are investigated.

The development of the boundary layer is quite similar for the eight days studied. The boundary layer starts growing around sunrise (0600 UTC) with its depth reaching 600 m between 0930 UTC and 1030 UTC. Thus only in the early morning is the 60-m level not located in the surface layer. Then, the boundary layer grows rapidly: between 1000 UTC and 1100 UTC the boundary layer reaches 1000 m in depth. A few hours before sunset, the boundary-layer depth reaches its maximum around 2000 m.

The composite diurnal cycle of the friction velocity is plotted in Fig. 2.3. During the night, the friction velocity is relatively small between 0.1 and 0.2 m s^{-1}, whereas during the day higher values are observed. It is remarkable that $u_{*\mathrm{ll,60\,m}}$ is almost twice that of $u_{*3\,\mathrm{m}}$, around 0.55 and 0.3 m s^{-1}, respectively. This is caused by the difference between the near-tower roughness and the regional roughness (see Sect. 2.3.1). In the early morning a flux divergence in turbulent stress is observed between 60, 100 and 180 m. This is a result of a deceleration of the flow when the rising convective boundary layer entrains air from the free troposphere that has been accelerated during the night when air aloft was decoupled from surface friction.

Figure 2.4a presents the time evolution of the local-level turbulent heat fluxes at

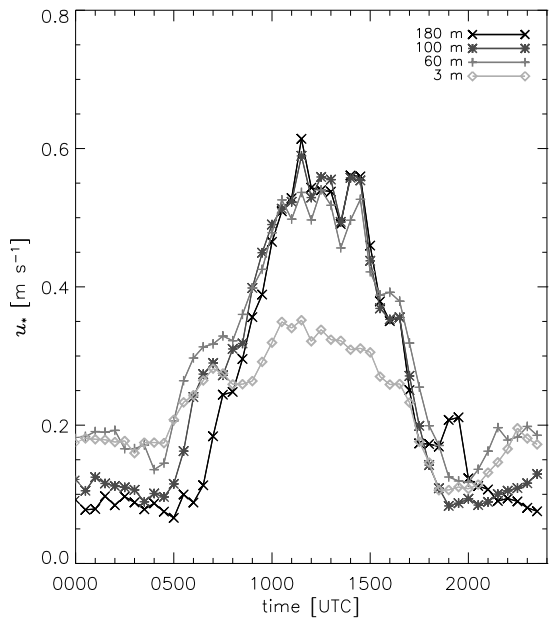

Fig. 2.3. The temporal evolution averaged over the eight days of the friction velocity ($u_{*\mathrm{ll}}$) at 3 m ($\diamond$), 60 m ($+$), 100 m ($*$) and 180 m ($\times$).

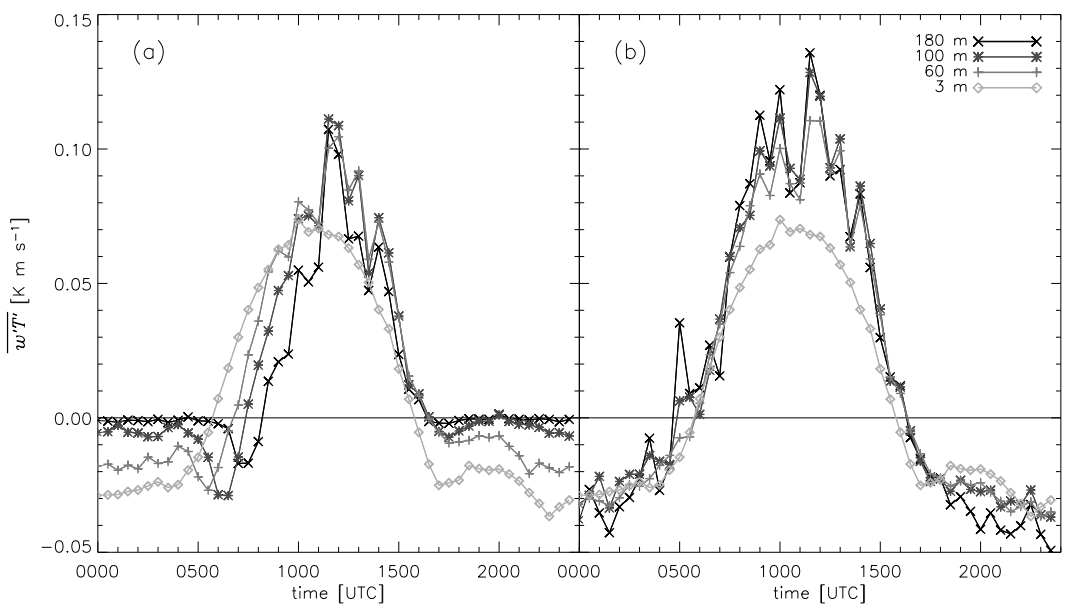

Fig. 2.4. The temporal evolution averaged over the eight days of (a) the local-level turbulent heat flux ($\overline{w'T'}_{\mathrm{ll}}$) at 3 m ($\diamond$), 60 m ($+$), 100 m ($*$) and 180 m($\times$) and (b) as in (a) but corrected for atmospheric storage below the sensor level ($\overline{w'T'}_s$).

the four levels averaged over the eight days. As can be seen, the fluxes decrease with height in the morning period until 1100 UTC. The fluxes at the elevated levels deviate

more than 10 % from the 3-m flux, as a result of the shallow surface layer and a large entrainment flux. For instance, at 0800 UTC the boundary-layer depth is almost 400 m, resulting in a surface-layer depth of 40 m. The entrainment flux could be estimated as almost -0.06 K m s^{-1}, by assuming a linear flux profile and using $\overline{w'T'}_{180\,\mathrm{m}} \approx 0$ and $\overline{w'T'}_{3\,\mathrm{m}} \approx 0.05$ K m s^{-1}. In other words, in the morning period the flux divergence is large and the application of MOST is questionable. On the other hand, after 1100 UTC the fluxes at different levels are more comparable. The values and the pattern of the 60-m and 100-m fluxes are almost the same. The 180-m flux shows a comparable pattern. However, the values are almost 20 % lower from 1100 until 1500 UTC. From 1530 until 1700 UTC, when for most days the boundary layer was deeper than 1800 m, the 180-m flux had the same values as the 60-m and 100-m fluxes.

The flux at 3 m is less variable than that at the other three levels. At 3 m the turbulent structures are much smaller than at the elevated levels. As a consequence more structures pass the sensor during the averaging time, resulting in statistically more stable values. Surprisingly, in the afternoon the 3-m flux is lower than the 60-m and 100-m fluxes, and after 1400 UTC even lower than the 180-m flux. This deviation of the 3-m flux can also be observed in Fig. 2.4b. Figure 2.4b shows the 3-m flux together with the fluxes of the other levels, corrected for flux divergence. The corrected fluxes at 60, 100 and 180 m are quite comparable, especially in the afternoon from 1200 until 1800 UTC. The 3-m flux on the other hand is much lower during the entire day. A possible reason for the differences between the 3-m flux and those at the other levels might be that the instrument at 3 m measures a different footprint. Probably the soil of the surroundings is drier than the soil just around the tower, which leads to smaller latent heat flux and larger sensible heat flux at the elevated level when compared to 3 m. This is confirmed by further observations that show that the four levels give about the same total heat flux, where the 3-m level shows a different distribution of available energy over the latent and sensible heat fluxes (figure not shown). Thus, the near-tower terrain does evaporate more then the surrounding region. Hence, in Cabauw a distinction has to be made between the near-tower and regional Bowen ratios. In order to ensure comparable footprints between the surface flux and the local-level flux, in MOSTs the regional surface flux ($\overline{w'T'}_{\mathrm{s,60\,m}}$) is used.

Figure 2.5 shows the temporal evolution of the structure parameter of temperature at the four selected levels computed from the sonic data. C_T^2 decreases with height, e.g. the values at 3 m are a factor of 10 larger than those at 60 m. The structure parameter of temperature has a clear diurnal cycle with a minimum observed in the morning and evening transition periods. In the morning sharp minima are observed around 0530 and 0700 UTC at the 3-m and 60-m levels respectively, whereas at 100 and 180 m the minimum is less pronounced (0800 and 1000 UTC). In the evening the minima are found at 1600 UTC for the 3-m observations and at 1700 UTC at the other levels. Those minima are related to the minimum in temperature fluctuations under neutral conditions. Consequently the turbulent heat flux crosses zero at the same time (Fig.

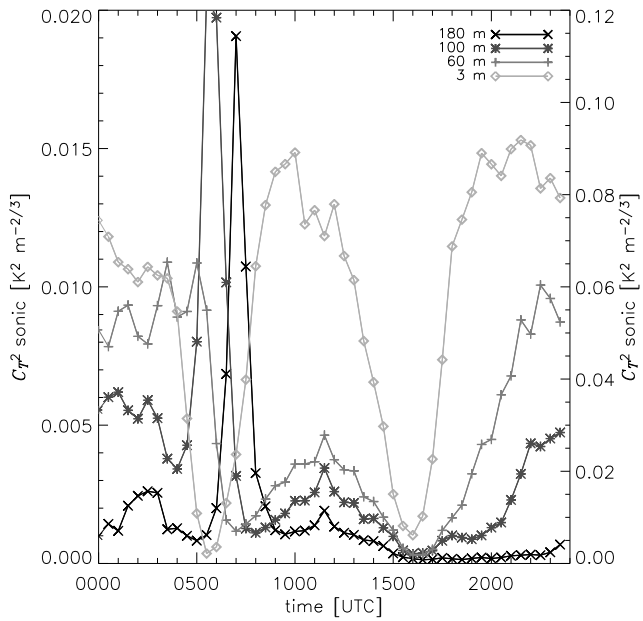

Fig. 2.5. The temporal evolution averaged over the eight days of the direct measured structure parameter of temperature with sonics at 3 m ($\diamond$, right x-axis) and at 60 m ($+$), 100 m ($*$) and 180 m ($\times$) (all left-axis).

2.4). At higher levels the minima in C_T^2 correspond to the zero local-level turbulent heat flux and not to the surface flux at that moment, which by then already has a significant positive value (Fig. 2.4).

At 100 and 180 m the structure parameters have a large peak before they reach their minimum around 0600 and 0700 UTC, respectively. The observations at 60 m do not really show a peak, but still the C_T^2 has a maximum at the end of the night (0500 UTC). Those maxima indicate strong temperature fluctuations, which occur at the moment that the particular level is located inside the entrainment zone. This is supported by the fact that the maxima at a specific level are observed at the moment when the turbulent heat flux at that level reaches its most negative value (Fig. 2.4a).

The early morning minima of C_T^2 have larger values than the afternoon minima: around 1×10^{-3} and 2×10^{-4} K^2 m$^{-2/3}$ respectively. This is probably related to the non-stationarity of the morning transition. The large temperature variances that are created during the passage of the rising entrainment layer continue to influence C_T^2, even though the local stratification is close to neutral. Thus during and just after the morning transition a direct relation between C_T^2 and the sensible heat flux is not guaranteed.

These first results indicate that the structure parameter of temperature at a specific level shows a stronger relationship with the turbulent flux at that level than with the surface flux. This is in favour of the second concept: MOSTl.

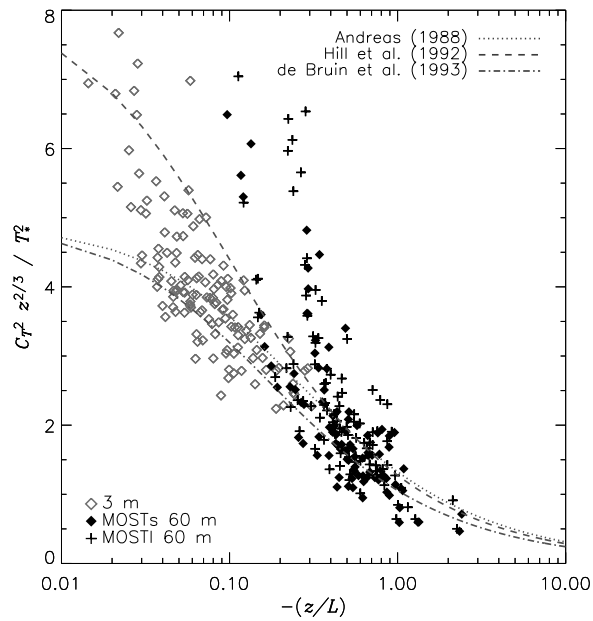

Fig. 2.6. The similarity relationship obtained from the turbulent heat flux and the friction velocity at 3 m, ($\diamond$), at 60 m with MOSTs ($+$), at 60 m with MOSTl ($\blacklozenge$), and three similarity relations proposed in the literature (lines). For the 3-m data, unstable conditions are selected: $\overline{w'T'}_{3\,\mathrm{m}} > 0$. For the 60-m data only data within the ASL are taken into account ($\overline{w'T'}_{60\,\mathrm{m}} > 0 \wedge z_{\mathrm{ASL}} > 60$). Data with $C_T^2 z^{2/3}/T_*^2 > 8$ occur but are not shown for clarity (11 data points for 3 m and 6 data points for 60 m).

2.4.2. The proposed similarity relationships in the surface layer, step 1

In this section we analyze the similarity relationships with (a) the 3-m data, and (b) the ASL data observed at 60 m from MOSTs and MOSTl (step 1, row 3, Fig. 2.2). Figure 2.6 shows the similarity relation between z/L and $C_T^2 z^{2/3}/T_*^2$ for all unstable 30-min observations as well as the relationships proposed in the literature.

The 3-m data cover a stability range from $0.015 < -z/L < 0.46$. For 60 m we observe larger values for $-z/L$ ranging between 0.09 and 3. This is lower than a factor 20 (60/3), because apart from the difference in z we also use a different u_* and $\overline{w'T'}$ for the two measuring levels (see Sect. 2.3.1). During the day, $u_{*60\,\mathrm{m}}$ is around 1.6 to 1.8 times larger than $u_{*3\,\mathrm{m}}$ (see Fig. 2.3) and $\overline{w'T'}_{60\,\mathrm{m}}$ is a factor 1.5 larger than $\overline{w'T'}_{3\,\mathrm{m}}$ (see Fig. 2.4). All these differences imply that $-z/L$ is 6-9 times larger at 60 m than at 3 m.

Most scatter is found in the neutral region for both the 3-m data ($-z/L < 0.06$) and the 60-m data ($-z/L < 0.3$). For the 60-m data, even the relationship of H92 underestimates the measured values. Note that all the data points where $C_T^2 z^{2/3}/T_*^2$ is higher than 8 are also located in the near-neutral range. The neutral data are observed during the morning and the late afternoon transition period, when (a) the turbulent heat flux is small and temperature fluctuations are non-zero, and (b) the friction velocity is low. In other words, we do not observe neutral conditions because of a high wind speed,

Table 2.2. Values of the coefficient c_2 in the similarity relationships ($f\,(z/L) = c_1\,(1 - c_2 z/L)^{-2/3}$) obtained from a fit through the ASL data with an orthogonal distance regression method (ODRPack Boggs et al., 1987). Fit 1 with a fixed c_1 of 8.1 as proposed by H92 ($c_{2\,\mathrm{H92}} = 15$) and fit 2 with a fixed c_1 of 4.9 as in the relationships from A88 ($c_{2\,\mathrm{A88}} = 6.1$) and DB93 ($c_{2\,\mathrm{DB93}} = 9$).

Dataset	Fit 1: $c_1 = 8.1$				Fit 2: $c_1 = 4.9$				
				H92				A88	DB93
	$c_{2\,\mathrm{fit}}$	$c_{2\,\mathrm{Tol}}$	$\frac{c_{2\,\mathrm{Tol}}}{c_{2\,\mathrm{fit}}}$	$\frac{c_{2\,\mathrm{fit}}-15}{15}$	$c_{2\,\mathrm{fit}}$	$c_{2\,\mathrm{Tol}}$	$\frac{c_{2\,\mathrm{Tol}}}{c_{2\,\mathrm{fit}}}$	$\frac{c_{2\,\mathrm{fit}}-6.1}{6.1}$	$\frac{c_{2\,\mathrm{fit}}-9}{9}$
3 m	24.95	0.80	0.032	0.66	8.01	0.34	0.042	0.31	-0.11
60 m MOSTs	20.12	0.89	0.045	0.34	8.64	0.44	0.051	0.42	-0.04
60 m MOSTl	17.14	0.82	0.048	0.14	7.26	0.42	0.058	0.19	-0.19

but because of a low sensible heat flux. The low heat flux means that the absolute error in the scaled structure parameter could be relatively large, which makes the neutral data more uncertain. Similar effects around near-neutral conditions for the relation between variances and fluxes mentioned by Weaver (1990). On the other hand, our neutral data points are clustered above the similarity relationships from the literature, which is an indication that the error is a bias rather than a random error. Furthermore, DB93 found also a higher scatter and a slight overestimation during near-neutral conditions (see their Fig. 2). In order to further investigate the similarity relation under near-neutral conditions, observations are needed with a combination of large friction velocity and a larger sensible heat flux than those observed in our data.

Under unstable conditions ($-z/L > 0.06$), the 3-m data are centred around the similarity relationships of DB93 and A88, with H92 as the upper limit. The 60-m data are more centred around the similarity relationship of DB93. Moreover, a small difference between MOSTs and MOSTl is observed, since in spite of evaluating only ASL data the sensible heat flux at the two levels differ slightly (see Fig. 2.7a), with the values of MOSTl being marginally higher.

In order to investigate more systematically which of the proposed similarity relations we have to use with our dataset, the relationship $f\,(z/L) = c_1\,(1 - c_2 z/L)^{-2/3}$ is fitted to the data with an orthogonal distance regression method. Due to the limited range of z/L in our dataset, especially under neutral conditions, it is impossible to fit both coefficients simultaneously. We decide to fix c_1 because our dataset does not contain many near-neutral observations and those are also more uncertain than the unstable ones (see above). We tried two fits, the first with $c_1 = 8.1$ as proposed by H92 and the second with $c_1 = 4.9$ as in A88 and DB93.

Table 2.2 shows c_2 and their tolerance obtained from the two fits for the different ASL datasets. Furthermore, the relative deviation of our fitted coefficient ($c_{2\mathrm{fit}}$) from that obtained from the literature is given (columns 5 , 9 and 10). We observe that $c_{2\,\mathrm{fit1}}$ varies from 17 to 25. The c_2 of our datasets is thus between 14 % and 66 % larger than 15 observed by H92. The values of these deviations are quite high compared with the observed tolerance ranging between the 0.03 and 0.05. For $c_{2\,\mathrm{fit2}}$ we find a variation

between 7.2 and 8.6.

In order to distinguish between fit 1 and fit 2, we calculate the relative difference in c_2 between the 3-m and 60-m dataset ($(c_{2,\,3\mathrm{m}} - c_{2,\,60\mathrm{m}})/\overline{c_2}$). We make this comparison, because in the framework of MOST a variation of z/L through a variation in z should yield the same similarity relationship as when L is varied (as is normally done). We observe a larger difference for fit 1 than for fit 2 (using MOSTs for 60 m: 0.21 and -0.07, for fit 1 and fit 2 respectively, and using MOSTl: 0.37 and 0.10). Consequently, it seems that for our data $c_1 = 4.9$ is more consistent between the two levels than $c_1 = 8.1$. This can also be observed from Fig. 2.6: we observe a larger overestimation of the H92 relationship for the more neutral 3-m data than for the more unstable 60-m data. Further, the high values of $(c_{2\,\mathrm{fit}} - c_{2\,\mathrm{H92}})/c_{2\,\mathrm{H92}}$ compared with DB93 and A88 indicate that the relation of H92 is not the best similarity relationship to use for our dataset.

If we compare $(c_{2\,\mathrm{fit}} - c_{2\,\mathrm{A88}})/c_{2\,\mathrm{A88}}$ with $(c_{2\mathrm{fit}} - c_{2\,\mathrm{DB93}})/c_{2\,\mathrm{DB93}}$, we observe first that the fitted coefficient is larger than that of A88 and smaller than that of DB93. In other words, our fit is situated between A88 as an upper limit and DB93 as a lower limit. For the 60-m MOSTl dataset, $c_{2\,\mathrm{fit2}}$ is exactly located between the two proposed coefficients. Second, in general the overestimation of our fit compared with A88 is much larger than the underestimation compared with DB93. We conclude that our data best follows the relationship of DB93, and so we use this similarity relationship in the following section.

2.4.3. The two concepts evaluated at 60 m, step 2

Figure 2.7a presents a composite diurnal cycle of the 60-m regional surface heat flux ($\overline{w'T'}_{\mathrm{s,60\,m}}$) and the 60-m regional local-level heat flux ($\overline{w'T'}_{\mathrm{ll,60\,m}}$). Note that the heat flux is the only difference in the scaling between MOSTs and MOSTl (see row 2, Fig. 2.2). Figure 2.7b shows the composite diurnal cycle of the structure parameter of temperature measured directly from the sonic and the scintillometer and calculated with MOSTl and MOSTs using the similarity relationship of DB93.

Before evaluating the two concepts, we shortly compare the directly observed structure parameter of the scintillometer and the sonic, since the former is our motivation and the latter is used in our analysis. The two structure parameters show a quite comparable variation with time. Both instruments show a minimum at 0700 UTC of 1.2×10^{-3} K^2 m$^{-2/3}$ and at 1600 UTC of 0.3×10^{-3} K^2 m$^{-2/3}$. When comparing the original 30-min data a coefficient of determination (r^2) is found of 0.71, which is quite large. The good comparison between the two instruments can be attributed to the relatively homogeneous surface around Cabauw. One difference is that the XLAS gives much smoother results, caused by the path averaging (Hartogensis et al., 2002). Furthermore, the XLAS shows sligthly larger values than the sonic, which could be caused by surface inhomogeneity combined with different footprints for the two methods. But it could also suggest that the linear error (called high-C_n^2) found by Van Kesteren and Hartogensis (2011) not only affects the Kipp & Zonen LAS but also the Kipp & Zo-

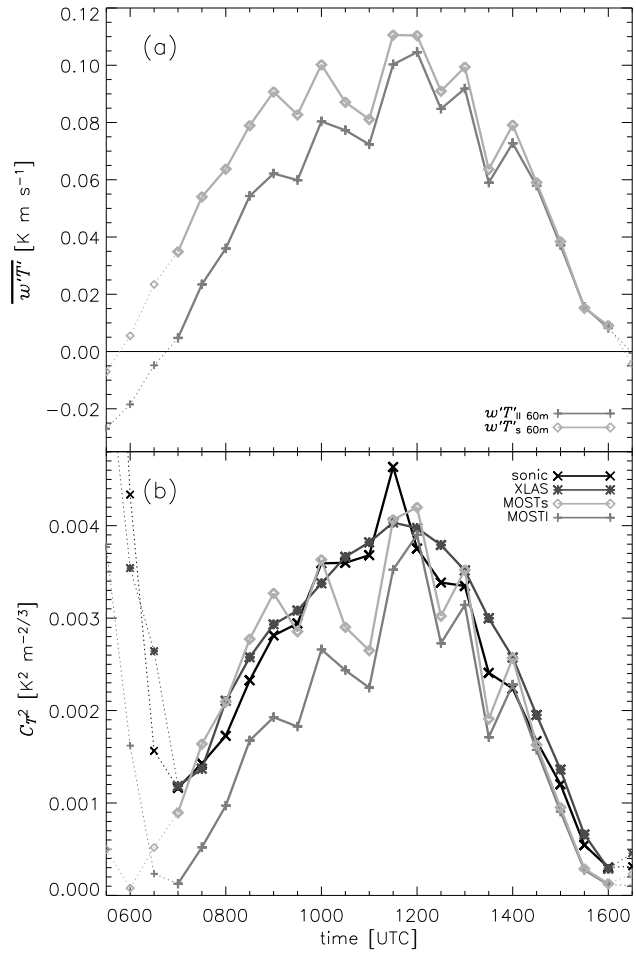

Fig. 2.7. The temporal evolution of (a) $\overline{w'T'}_{\mathrm{s},60\,\mathrm{m}}$ ($\diamond$) and $\overline{w'T'}_{\mathrm{ll},60\,\mathrm{m}}$ ($+$) and (b) C_T^2 measured with the sonic ($\times$) and the XLAS ($*$) and calculated with MOSTs ($\diamond$) and MOSTl ($+$) averaged over the eight days. In MOST the similarity relationship of DB93 is used, note that for $-z/L < 0$ (thin lines) the relationship for stable conditions is used.

nen XLAS. Nevertheless, to be consistent in our investigation we further only analyze the observations of the sonic, because the MOST-scaling variables are obtained from the sonic. Furthermore, the quite high level of agreement between the sonic and the scintillometer suggest that the conclusion of the coming analysis will be valid for the scintillometer data as well.

First, we investigate the concept MOSTs, since here MOST is applied in a standard way. By evaluating the ASL data (afternoon period) we observe (Fig. 2.7b) that the calculated structure parameter of temperature is comparable to the directly measured one. This observation is confirmed by the scatter plot of Fig. 2.8a. Figure 2.8a shows C_T^2 determined with MOSTs against the one directly measured with the sonic. The coefficients of the best linear fit, the coefficient of determination (r^2) and the coefficient of variation of the RMSD (CV) are shown in Table 2.3. The coefficient of determination

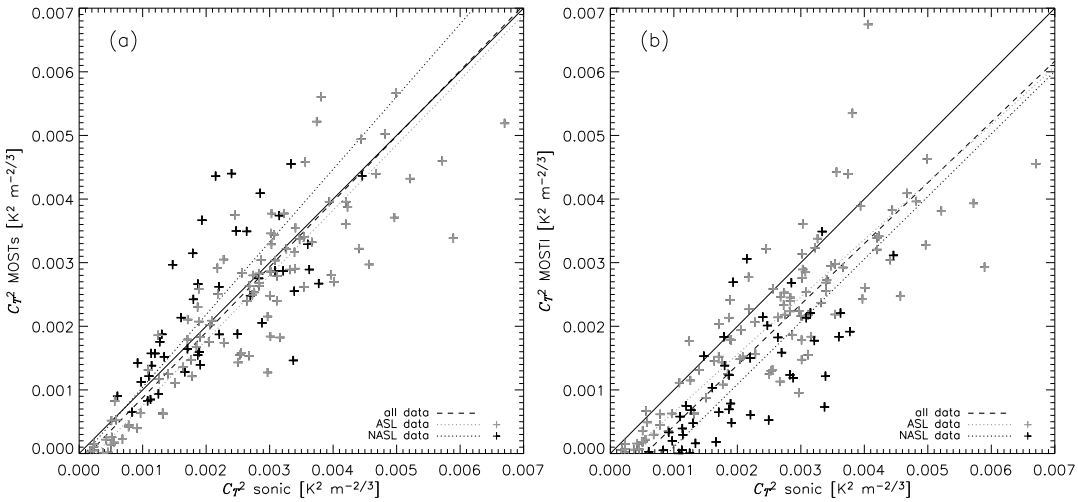

Fig. 2.8. The directly measured C_T^2 from the sonic against the calculated C_T^2 from MOSTs in (a) and MOSTl in (b) for observation inside (grey) and outside the surface layer (black). The dashed line represents the best fit through all the data, whereas the dotted grey line represents the best fit through the data inside the surface layer and the dotted black line outside the surface layer (see Table 2.3 for the functions). The solid black line is the 1:1-line.

Table 2.3. The equations of the best linear fit through the 60-m data in Fig. 2.8 together with the coefficient of determination (r^2) and the coefficient of variation of the RMSD (CV). x is C_T^2 from the sonic and y is C_T^2 from MOST (similarity relationship of DB93).

	MOSTs			MOSTl		
	equation	r^2	CV	equation	r^2	CV
all data	$y = 1.03x - 1.5 \times 10^{-4}$	<u>0.70</u>	0.32	$y = 0.96x - 5.2 \times 10^{-4}$	0.69	0.40
ASL data	$y = 1.02x - 2.7 \times 10^{-4}$	<u>0.77</u>	0.29	$y = 0.90x - 2.5 \times 10^{-4}$	0.73	0.35
NASL data	$y = 1.14x - 1.0 \times 10^{-4}$	0.46	0.40	$y = 0.98x - 8.8 \times 10^{-4}$	<u>0.52</u>	0.54

is a measure of the correlation, whereas CV indicates how much the data deviates from the 1:1-line. Notice that for this figure single data points are used instead of the composite of the eight days. The linear fit for the ASL data is located near the 1:1-line, indicating that within the surface layer MOSTs gives reliable results. Furthermore, we observe that for small values ($C_{T\,\mathrm{sonic}}^2 < 1 \times 10^{-3}$ K^2 m$^{-2/3}$) MOSTs underestimates the observed values. These data correspond to the neutral conditions during the evening transition (as a consequence of a low sensible heat flux instead of a high u_*).

Analyzing the NASL data (morning period) Fig. 2.7 shows that $C_{T\,\mathrm{MOSTs}}^2$ has a minimum at 0600 UTC when $\overline{w'T'}_{\mathrm{s,60\,m}}$ approached zero (Fig. 2.7a). This is one hour before the minimum in $C_{T\,\mathrm{sonic}}^2$. Moreover, from 0700 until 1000 UTC MOSTs overestimates the observations. From Fig. 2.8a we observe that the overestimation is almost 14 %. From 0600 to 0700 UTC MOSTs underestimates $C_{T\,\mathrm{sonic}}^2$. This underestimation is not visible in the scatter plot of Fig. 2.8a, since in that plot only unstable data are shown.

Notice that it is therefore important to plot a diurnal cycle as well, rather than to show scatter plots only. The coefficient of determination is 40 % lower for NASL data than for ASL data. Furthermore, the coefficient of variation of the RMSD (CV) is higher for NASL data, indicating that for the ASL data the values of MOSTs is closer to the observations than for NASL data. All in all, we can conclude that the surface sensible heat is not the correct scaling parameter for NASL data. Therefore, the second step is to evaluate MOSTl.

In this analysis we again make a distinction between the ASL data and NASL data. For the ASL data, we obtained from the composite diurnal cycle that $C^2_{T\mathrm{MOSTl}}$ is similar to $C^2_{T\mathrm{sonic}}$. The difference with MOSTs is relatively small. However, MOSTl shows slightly lower values because the local-level sensible heat flux is slightly lower than the regional surface sensible heat flux (see Fig. 2.7a). The small underestimation is also obtained from the scatter plot. The underestimation is around 10 % (the slope of the fit is 0.90). Consequently, the CV is also slightly higher than for MOSTs. In the end, we observe for MOSTl a relatively high r^2 of 0.73, similar to the value obtained for MOSTs.

Figure 2.7 shows that the $C^2_{T\mathrm{MOSTl}}$ has a minimum at 0700 UTC, as observed by $C^2_{T\mathrm{sonic}}$ as well. This is a first indication that the local-level sensible heat flux is a better scaling variable than the surface sensible heat flux in the transition morning period. Furthermore, the coefficient of determination and therefore the correlation is larger for MOSTl than MOSTs (0.52 and 0.46, respectively) for the NASL data during this morning period.

However, in spite of the comparable pattern during the morning transition, MOSTl underestimates the measured structure parameter by a factor of ten ($C^2_{T\mathrm{MOSTl}} = 1.26 \times 10^{-4}$ K^2 m$^{-2/3}$ and $C^2_{T\mathrm{sonic}} = 1.16 \times 10^{-3}$ K^2 m$^{-2/3}$ at 0700 UTC. This can also be seen in the group of data points in Fig. 2.8b where $C^2_{T\mathrm{sonic}}$ lies between 0.5×10^{-3} and 1.5×10^{-3} K^2 m$^{-2/3}$ whereas $C^2_{T\mathrm{MOSTl}} \approx 0$. The structure parameter obtained with MOSTl shows a deep minimum due to the near-zero value of the local-level sensible heat flux. Therewith it misses the finite value of $C^2_{T\mathrm{sonic}}$ that is probably due to ongoing transfer of temperature variance, previously produced within the entrainment zone (non-stationarity). Notice that MOSTs does not show the clustered data points in Fig. 2.8, but for the wrong reason. In Fig. 2.8 only unstable data are taken into account (see the solid lines in Fig. 2.7). Therefore the minimum of MOSTs, which is as low as the one for MOSTl, is not present in Fig. 2.8. During the rest of the morning period (0730 - 1100 UTC), MOSTl is in general 1×10^{-3} K^2 m$^{-2/3}$ lower than the observations (see the offset in the linear fit equation). The coefficient of variation of RMSD is also 36 % higher than for MOSTs (0.54 instead of 0.40). This suggest that MOSTs is on average closer to the observations than MOSTl, and the overestimation of MOSTs is smaller than that of MOSTl.

Overall, outside the surface layer neither of the two concepts provides a useful relationship between C^2_T and the sensible heat flux.

2.5. Discussions and Conclusions

We investigate whether MOST can be used to obtain the surface sensible heat flux from elevated structure parameter data (in our case at 60 m). In this analysis two time periods are distinguished: the early morning and the afternoon. During the afternoon the 60-m level is located in the atmospheric surface layer (assumed to be the lowest 10 % of the boundary layer) and MOST is valid. During the morning the application of MOST is not always justified for two reasons. First, the observation height can be larger than 0.1 of the boundary-layer depth. Second, the divergence of the turbulent heat flux within the ASL can be considerably higher than in the afternoon due to relatively strong entrainment. Therefore, the strict definition of the surface-layer depth ($z_{\mathrm{ASL}} = 0.1 z_{\mathrm{i}}$) does not imply that below that level the fluxes differ less than 10 % (constant-flux layer). For instance, in the free convection limit (entrainment ratio of -0.2) or during the morning, when entrainment is strong (e.g. entrainment ratio of -1.2) the fluxes differ 12 % or 22 %, respectively, within this layer. In other words, in our study the definition of the atmospheric surface layer is stretched and the fluxes could vary by more than 10 % in that layer.

Two theoretical concepts are proposed and compared. In the first concept (MOSTs), we assume that C_T^2 at 60 m scales with the surface flux. In the second concept (MOSTl) C_T^2 is scaled with the local-level sensible heat flux. Stability in the two concepts is also based on the surface and local-level sensible heat flux respectively. On the other hand, both concepts share the same friction velocity in the formulation of stability, in this case based on the stress measured at the 60-m level.

First, we analyzed 3-m and 60-m surface-layer data (ASL data) only, in order to investigate which of the MOST relationships proposed in the literature (DB93, H92 or A88) is suitable. We find an overestimation of our data with respect to the three relationships under low-heat-flux neutral conditions during the morning and evening transition. The data points are clustered indicating that the overestimation is a bias rather than a random error. However, since our dataset contain only low-heat-flux neutral data the scaling of C_T^2 under near-neutral conditions could not fully be investigated. Therefore, we would recommend to further investigate the MOST relationships under high-wind-speed neutral conditions.

With an orthogonal distance regression method a MOST relationship of the form $f\left(z/L\right) = c_1 \left(1 - c_2 z/L\right)^{-2/3}$ is fitted to the data. First, we fixed c_1 with a value 8.1 and 4.8 based on the relationships found in the literature. Then, the values for c_2 are compared with the coefficients of DB93, H92 and A88. In general the deviation is the smallest for DB93, and so we use the DB93 similarity relationship.

Second, we compare the pattern of C_T^2 obtained from sonic observations, at the four levels. In the early morning when the observation level is in or close to the entrainment zone, the sonic observations show a remarkable behaviour in C_T^2. First, when the elevated level is located in the entrainment zone, observations at 100 and 180 m show a peak in C_T^2 before they reach their minimum. Second, the minimum in C_T^2 occurs when

the local-level flux crosses zero, whereas the surface flux is already positive. Finally, the evening transition shows deeper minima of C_T^2 than in the morning. These three observations suggest that temperature variations in the entrainment layer influence the structure parameter during the morning transition, which indicates that the surface flux is not the sole parameter that determines C_T^2 at higher levels.

Finally, the observed C_T^2 from a sonic is compared with C_T^2 calculated from the two concepts. Comparing the two concepts during the morning (NASL data), both methods show a low correlation with the observed C_T^2. We observe that the minimum C_T^2 of MOSTs occurs indeed one hour before the observations, whereas that for MOSTl occurs at the same moment. However, the minimum value of MOSTl is much lower than the observations. In other words, the pattern of C_T^2 obtained from MOSTl is closer to that of the observations than that of MOSTs, but the values of MOSTl are too low. This indicates that, during the transition zone, additional temperature fluctuations are present that do have no relation with the scaling theory. The values of $C^2_{T\mathrm{MOSTs}}$ are more similar to $C^2_{T\mathrm{sonic}}$; we found a slight overestimation. For ASL data both concepts agree with the observations.

As stated before, we use the relationship of DB93, because for ASL data the deviations of our fits are in general a minimum for DB93. However, for MOSTl the deviations of the fitted c_2 relative to the literature values are similar for the different similarity relations (see Table 2.2). Some of the above results may differ if another similarity relationship (instead of DB93) is used. If using the relationship of H92 or A88, the structure parameter obtained from MOST becomes larger. This will improve the results of MOSTl, since the underestimation becomes less. As a consequence, for H92 and A88 the coefficient of variation of the RMSD (CV) of MOSTl is smaller than MOSTs. Other observations such as (a) the time when the $C^2_{T\mathrm{minimum}}$ is observed, (b) the large underestimation of $C^2_{T\mathrm{minimum}}$ obtained by MOSTl compared to the observations, and (c) the values for the coefficients of determination all give similar results for the proposed similarity relationships (see also Table 2.4 in the Appendix). In other words, the main conclusions do not significantly change when using these other relationships.

To conclude, neither MOSTs nor MOSTl is the final answer to the question of how to calculate the surface flux from the structure parameter at elevated levels. When the elevated level is located within the surface layer, MOSTs and MOSTl perform equally well. But in the morning hours neither works well: MOSTs does not have the correct temporal behaviour, whereas MOSTl does not provide the correct value (probably due to the strong instationarity).

Acknowledgements

We thank Frank Beyrich (Deutscher Wetterdienst) and Bert Holtslag (Wageningen University) and the anonymous reviewers for reading the manuscript and providing valuable comments. Further, we thank Henk Klein Baltink (Royal Netherlands Meteorological Institute) for providing the data of the boundary-layer depth and Eddy Moors (Alterra) for the use of the 100-m turbulent data. This work has been supported financially in part by the German Research Foundation in the framework of the project: 'Turbulent Structure Parameters over Heterogeneous Terrain - Implications for the Interpretation of Scintillometer Data'. Further financial support

was provided in the framework of the project 'Integrated observations and modelling of Greenhouse Gas budgets at the national level in the Netherlands', part of the program 'Climate changes Spatial Planning'.

2.A. Statistics of the two concepts using another similarity relationship

The results, and therefore the conclusions, from Sect. 2.4.3 could change by using another similarity relationship. Table 2.4 shows the same statistics as in Table 2.3 but now for the three proposed similarity relationships (A88, H92 and DB93). Notice that, for completeness, we include the information of DB93, which is a repetition from Table 2.3.

Table 2.4. As Table 2.3 but than for A88, H92 and DB93.

	MOSTs			MOSTl		
	equation	r^2	CV	equation	r^2	CV
A88						
all data	$y = 1.28x - 2.0 \times 10^{-4}$	0.69	0.44	$y = 1.18x - 6.6 \times 10^{-4}$	0.69	0.37
ASL data	$y = 1.27x - 3.6 \times 10^{-4}$	0.76	0.38	$y = 1.12x - 3.4 \times 10^{-4}$	0.73	0.34
NASL data	$y = 1.44x - 1.3 \times 10^{-4}$	0.46	0.61	$y = 1.23x - 1.1 \times 10^{-3}$	0.52	0.48
H92						
all data	$y = 1.26x - 1.7 \times 10^{-4}$	0.70	0.42	$y = 1.18x - 6.3 \times 10^{-4}$	0.69	0.36
ASL data	$y = 1.26x - 3.0 \times 10^{-4}$	0.77	0.37	$y = 1.11x - 2.8 \times 10^{-4}$	0.74	0.32
NASL data	$y = 1.38x - 1.2 \times 10^{-4}$	0.46	0.55	$y = 1.19x - 1.1 \times 10^{-4}$	0.52	0.48
DB93						
all data	$y = 1.03x - 1.5 \times 10^{-4}$	0.70	0.32	$y = 0.96x - 5.2 \times 10^{-4}$	0.69	0.40
ASL data	$y = 1.02x - 2.7 \times 10^{-4}$	0.77	0.29	$y = 0.90x - 2.5 \times 10^{-4}$	0.73	0.35
NASL data	$y = 1.14x - 1.0 \times 10^{-4}$	0.46	0.40	$y = 0.98x - 8.8 \times 10^{-4}$	0.52	0.54

3 Monin-Obukhov relations for C_T^2: dependence on regression approach, observation height and stability range

3.1. Introduction

In atmospheric models and in the analysis of micro-meteorological observations (e.g. scintillometer data), Monin-Obukhov similarity theory (MOST) is typically used to link surface fluxes to other turbulent quantities, such as mean gradients, standard deviations or structure parameters. In this study we focus on the structure parameter of temperature (C_T^2) measured under unstable conditions. The structure parameter can be derived in two ways, either from fast response temperature measurements or from optical scintillation measurements. The latter can be done by optical scintillometers and as such C_T^2 is a key variable in obtaining path-averaged sensible heat fluxes. Path-averaged fluxes are of interest for many meteorological and hydrological studies and applications (Meijninger et al., 2002b; Beyrich et al., 2005, 2012, among others).

In the literature a variety of MOST functions ($f\,(z/L)$) for C_T^2 is reported (for unstable conditions see e.g. Obukhov, 1960; Wyngaard et al., 1971; Wyngaard, 1973; Wesely, 1976b; Andreas, 1988; Hill et al., 1992; Thiermann and Grassl, 1992; de Bruin et al., 1993; Li et al., 2012; Maronga, 2014). They are usually based on a regression fit through observational data measured in the atmospheric surface layer (ASL). The functional expressions and in particular the regression coefficients differ between the studies. These differences may be related to variations in the experimental design, instrumentation and data processing such as:

1. the regression approach used to determine $f\,(z/L)$;
2. the stability ranges $(-1/L)$ covered by the data;
3. the measurement heights (z);
4. the instrumentation;
5. the data processing,
6. the characteristics of the underlying surface, with respect to surface heterogeneity

This chapter is accepted with minor revisions as Braam M, Moene AF, Beyrich AAM F Holtslag Similarity relations for C_T^2 in the unstable atmospheric surface layer: Dependence on regression approach, observation height and stability range. Boundary-Layer Meteorol

and soil moisture conditions.

Generally, it is difficult to separate the effect of one aspect from the effects of the others aspects, because most of them differ simultaneously between the studies. Therefore, in this paper we investigate $f(z/L)$ *within one dataset* so that the data processing, instrumentation and the surface characteristics are as uniform as possible. Hence, we can focus on the impact on $f(z/L)$ of applying various regression approaches, and of measuring within different stability ranges and at different heights (the first three issues from the list above). The dataset used here was obtained from the 60 m tower during the CASES-99 experiment (Poulos et al., 2002). It contains data over a large range of measurement heights and stabilities. The impact of different surface characteristics on $f(z/L)$ and the MOST function for C_q^2 and ϵ, under both unstable and stable conditions, is investigated by Kooijmans (2013). They evaluate these MOST functions for 11 field experiments obtained above different surface (issue 6) by Wageningen University during the last decades. The data from these experiments are uniformly processed and obtained with the same instrumentation (issue 4 and 5).

The first part of the present research concerns the impact on $f(z/L)$ of applying a certain regression approach. In the oldest studies the regression fit was often done by eye, whereas in the more recent ones a mathematical method was usually applied (e.g. non-linear least-squares method). The application of different regression approaches may lead to differences in $f(z/L)$, because each approach uses specific definitions for the residuals, i.e. the differences between the observed and the fitted values. Furthermore, in some studies the regression analysis was performed after the data had been logarithmically transformed. We will thus answer the following questions: What are the differences in $f(z/L)$ due to the use of different regression approaches, and what are the advantages and disadvantages of these approaches?

The second part concerns the impact on $f(z/L)$ of measuring within different stability ranges (in terms of $-1/L$) and at different observation levels. The similarity functions reported in the literature are usually based on a single dataset, obtained with a given setup of observation levels and containing measurements over a certain stability range. Both the observation levels and the stability range differ between the studies, and can therefore be one of the reasons for the observed differences in $f(z/L)$. For most studies the experimental data were measured at a limited height range close to the surface. We will thus answer the following question: What is the impact on $f(z/L)$ of measuring within different stability ranges and at different heights?

The paper is structured as follows: In Sect. 3.2, background information on MOST and the similarity equations proposed in the literature is given. In Sect. 3.3 we briefly introduce the various regression approaches. Section 3.4 provides information about the CASES-99 experiment and the dataset used in this study. In Sect. 3.5 the research strategy is described. In Sect. 3.6 we present and discuss our results. In the final section conclusions are given.

3.2. Monin-Obukhov similarity Theory functions for C_T^2

3.2.1. Dimensionless analysis

MOST is a concept based on the Buckingham Π-theorem. MOST applies within the atmospheric surface layer (ASL), under the condition that turbulence is only controlled by stationary and horizontally homogeneous surface conditions. It assumes that the non-dimensionalized quantity of interest, in this case C_T^2, is fully determined by four parameters: a) the kinematic sensible surface flux at the surface ($\overline{w'T'}$), b) the height above the surface (z), c) the friction velocity (u_*) as a proxy of shear production of turbulent kinetic energy, and d) the buoyancy flux ($g/\overline{T_v})\overline{w'T_v'}$ indicating the buoyancy production or destruction of TKE (where $\overline{T}$ is the mean temperature, $\overline{w'T_v'}$ is the virtual temperature surface flux, and $g = 9.81$ m s^{-2} is the acceleration due to gravity). Using these four parameters, the MOST scaled structure parameter ($\widetilde{C_T^2}$) is a dimensionless function of z/L:

$$\widetilde{C_T^2} = \frac{C_T^2 z^{2/3}}{T_*^2} = f\left(z/L\right) \tag{3.1}$$

in which T_* is the temperature scale $T_* = -\overline{w'T'}/u_*$, and L is the Obukhov length. The Obukhov length can be interpreted as the height of the sub-layer of dynamic turbulence (Monin and Obukhov, 1954), and it is defined as:

$$L = -\overline{T}{u_*}^3/(\kappa g\overline{w'T_v'}) \tag{3.2}$$

in which $\kappa = 0.4$ is the von-Kármán constant.

We want to note that Monin and Obukhov (1954) derived only the flux-based dimensional analysis for wind and temperature gradient for non-neutral flows. Obukhov (1960), however, was the first to derive the similarity relations for structure parameters, independent of the Monin-Obukhov similarity theory framework. However, because in literature the term Monin-Obukhov similarity is commonly used for surface flux-based scaling in general, we use the term here for the similarity relationships of structure parameters as well.

3.2.2. Similarity relations

Several expressions for the Monin-Obukhov similarity relations ($f\left(z/L\right)$) under unstable conditions are reported in the literature. Because we focus on variations in regression approach, measurement height and stability ranges, here we summarize the conditions with respect to those aspects for the studies in Table 3.1.

First, Table 3.1 shows that some studies used observations from only one level, whereas others used more. But for most studies the observations were done not higher than at about 10 meters, except for the study of Wyngaard (1973, who measured up to 20 m) and Maronga (2014, who used high-resolution large eddy simulation (LES) from 14 m up to 100 m). Second, the data were measured within different stability ranges (in

Table 3.1. Background information on Monin-Obukhov similarity relations for the structure parameter of temperature under unstable conditions proposed in the literature. For the upper block Eq. 3.3 was fitted, whereas in the lower block other functions were fitted. The first part gives information about the dataset: the measurement height z, and the stability in terms of $-1/L$. The second part gives information about the regression approach: Transformation (are the data or axes transformed on a logarithmic scale), and the Regression method that is used (in which LSR means classical non-linear least-squares). The third part gives the values of the regression coefficients for the upper block. NI means no information

Reference	dataset		Regression approaches		coefficients		
	z [m]	$-1/L$ [m^{-1}]	Transformation	Regression	c_1	c_2	d
Wyngaard (1973)	5.66, 11.3, 22.6	scatter cloud: $-1/L < 1.1$ 6 points: $1.1 < -1/L < 2.5$	loglog	NI	4.9[f]	6.1[f]	1.5
Hill et al. (1992)[a]	3.95	50 % of data: $0.025 < -1/L < 0.125$	NI	NI	8.1	15.0	1.3
de Bruin et al. (1993)[b]	11.3	scatter cloud: $-1/L < 0.3$ 6 points: $0.3 < -1/L < 10$	loglog	eye	4.9	9.0	1.1
Li et al. (2012)[b]	0.9, 1.9, 2.9, 3.9	$0.0025 < -1/L < 10$	loglog	LSR	6.7	14.9	1.1
Maronga (2014)[c]	14 up to 100	$0.0025 < -1/L < 10$	loglog	LSR	6.1	7.6	1.6
Wesely (1976b)[b]	1 up to 2	$0.025 < -1/L < 1$	NI	NI	[d]		
Thiermann and Grassl (1992)[a]	2	NI	NI	NI	[e]		

a. from scintillometer measurements,
b. from eddy covariance measurements,
c. from large eddy simulation data,
d. $\left(1 + 0.45(-z/L + 1.5) + 0.01(-z/L + 1.5)^{10}\right)^2$ which is only valid for $0.05 < -z/L < 0.1$,
e. $6.37\left(1 - z/L + 75(z/L^2\right)^{-1/3}$,
f. these are the constants proposed by Andreas (1988), who modified the coefficient proposed by Wyngaard (1973) by replacing $\kappa = 0.35$ by $\kappa = 0.40$

terms of $-1/L$). The older studies were based on a smaller range of $-1/L$ than the more recent ones.

The most common shape of $f\,(z/L)$ under unstable conditions is (Wyngaard et al., 1971; Wyngaard, 1973; Andreas, 1988; Hill et al., 1992; de Bruin et al., 1993; Li et al., 2012; Maronga, 2014):

$$f\,(z/L) = c_1\,(1 - c_2 z/L)^{-2/3} \tag{3.3}$$

in which c_1 is the asymptotic value of $f\,(z/L)$ for $-z/L = 0$ and $1/c_2$ is the value of $-z/L$ where the neutral range approximately transits into the free convection range (see Fig. 3.1). This shape is first introduced by Wyngaard et al. (1971), similar to the Businger-Dyer type of functions used for dimensionless gradients. In the free convection limit ($-z/L >> 1$) Eq. 3.3 becomes $f\,(z/L) = d\,(-z/L)^{-2/3}$, where $d = c_1 c_2^{-2/3}$ is the coefficient for the free convection range. The coefficients are also listed in Table 3.1. Their values differ between the different studies. The variation between the five values in Table 3.1 is large with a relative standard deviation of 0.22 for c_1, 0.40 for c_2, and 0.17 for d. The shape of the equation in the free convection limit is similar to the similarity relation proposed by Obukhov (1960).

Because Eq. 3.3 is the most common shape and the shapes of Thiermann and Grassl (1992) and Wesely (1976b) are exceptions, and because the two coefficients can be interpreted physically, we choose to only evaluate Eq. 3.3.

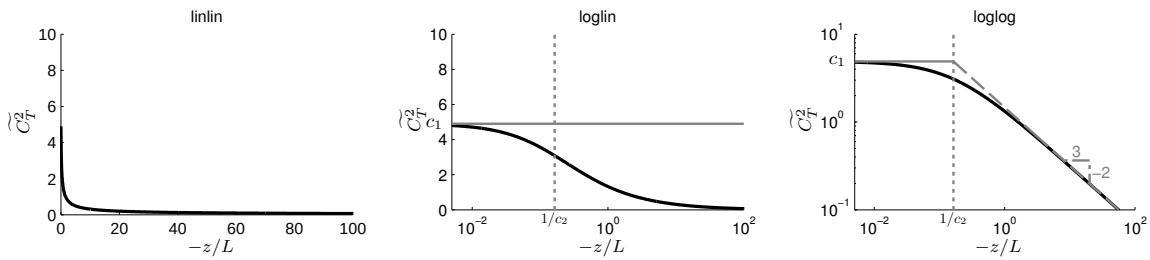

Fig. 3.1. A sketch of plotting $\widetilde{C_T^2}$ versus $-z/L$ for the three different data transformation approaches: linlin (left column), loglin (centre column), and loglog (right column). In grey the construction lines to find the regression coefficients, see also the text.

3.3. Regression approaches

The regression method used to fit an empirical relation to the data differs between the studies. In the oldest studies the regression function was determined by eye, whereas in the most recent studies often a mathematical regression method is used. The use of different mathematical regression methods can lead to differences in c_1 and c_2, because the different methods use different definitions for the residuals. A difference in the definition of the residual only impacts on the regression coefficients if the residuals are large, which is the case if the data is scattered. The latter is common in plots of C_T^2 versus $-z/L$. In the first part of our research, we evaluate regression approaches that differ in four aspects: the transformation of data, the mathematical regression methods, a weighing of the data, and the number of regression coefficients to fit. In total this leads to thirty regression approaches[1]. Each aspect is explained below.

3.3.1. Transformation of data

Often, the figures of $\widetilde{C_T^2}$ versus $-z/L$ are displayed semi-logarithmically (loglin) or double-logarithmically (loglog) instead of linearly (linlin). The advantage of using a logarithmic x-axis is that the behaviour of $\widetilde{C_T^2}$ in the neutral range and in the free convection range can be studied in the same graph, despite the large $-z/L$ range covered by the data.

The advantage of both a logarithmic x-axis and a logarithmic y-axis is that the coefficients and the exponent in Eq. 3.3 can be deduced from the plot, as seen in the sketch shown in Fig. 3.1. The coefficient c_1 and the exponent can be deduced immediately, as c_1 is defined as the level of the horizontal asymptote in the neutral range, and the exponent is defined as the slope of the oblique line in the free convection range. Furthermore, c_2 can be deduced indirectly: $1/c_2$ is defined as the transition point, which in a loglog plot coincides with the point where the extended horizontal and oblique lines cross.

The disadvantage of plotting loglin or loglog is that the regression function fitted to

[1] 30 = (3 (data transformation) × 2 (mathematical regression method) × 2 (weighting data) × 3 (fitting coefficients)) − 6 (because the values of the coefficients are the same for linlin and loglin if using LSR, see Sect. 3.3.2)

the data (linlin) does not correspond with the data that are shown. In order to be consistent, one must first transpose the data to the logarithmic values and then fit the coefficients. The relation for the loglin fit has the shape:

$$y_{\text{loglin}} = f\left(z/L\right) = c_1 \left(1 + c_2 10^{\,x_{\log}}\right)^{-2/3} \tag{3.4}$$

The relation for the loglog fit has the shape:

$$y_{\text{loglog}} = \log_{10}\left(f\left(z/L\right)\right) = \log_{10} c_1 - \tfrac{2}{3}\log_{10}\left(1 + c_2 10^{\,x_{\log}}\right) \tag{3.5}$$

with $x_{\log} = \log_{10}\left(-z/L\right)$. Using Eq. 3.4 or Eq. 3.5 instead of Eq. 3.3 results in different values for the coefficients c_1 and c_2. The choice of the transformation depends on which stability range one wants to emphasize.

3.3.2. Mathematical regression methods

The most commonly used mathematical regression method is the classical non-linear least-squares (abbreviated as LSR) method. The term 'non-linear' means that the regression function represents a non-linear combination of the model coefficients and the independent variable (x-value). 'Least-square' regression is a method that searches for a solution where the sum of the squared residuals has its minimum. In classical least square regression the residual is defined as the difference between the observed and estimated dependent variable (y-values). No uncertainties in the independent variable are assumed. Orthogonal distance regression (ODR, also called total-least-square, among others, Boggs et al., 1987; Zwolak et al., 2007) does take into account uncertainties in both the dependent and independent variables. In other words, in LSR the residuals are perpendicular to the x-axis, whereas in ODR the residuals are perpendicular to the fitted function. Because L is determined from several micro-meteorological measurements (Eq. 3.2), in MOST the x-values ($-z/L$) can have observational uncertainties, just as much as $\widetilde{C_T^2}$. Therefore, ODR is considered a more appropriate choice for fitting the similarity relations than LSR.

Notice that because the residuals are parallel to the y-axis when using LSR and only the data on the x-axis is transformed when using loglin (Eq. 3.4) instead of linlin (Eq. 3.3), the coefficients of the combination of LSR and loglog have the same value as LRS and loglin.

3.3.3. Weighting of data

When using observational data, some data points might be less reliable than others because of various reasons. If these unreliable data points are located outside of the scatter cloud (outliers) they could have a large impact on the regression. One way to overcome the problem of outliers, is to use a data filter that removes the most unreliable data points. Another way, is to minimize their impact by weighting the data by their errors. The most reliable data points obtain a larger weight in the regression than

unreliable data points. Using this approach (abbreviated as 'weight'), the regression coefficients are essentially based on the most reliable data. This makes 'weight' a more logical choice than using an unweighted dataset ('notWeight').

3.3.4. Number of regression coefficients to fit

Generally, one would prefer to fit both regression coefficients simultaneously (abbreviated as 'unfixed'), but this could be difficult if the data cover only a limited range of $-z/L$. In that case it is impossible to fit both coefficients simultaneously, and one has to choose to fix one of the two coefficients (abbreviated as 'fixed c_1' and 'fixed c_2', see also Braam et al. 2012).

3.4. Data

The data used in this study were obtained during the Cooperative Atmosphere-Surface Exchange Study (CASES-99, Poulos et al., 2002). The experiment took place in October 1999 near Leon, Kansas, U.S.A. (37.6486° N, 96.7351° W). CASES-99 focused on stable conditions, but most instruments operated also during daytime. The area is relatively flat and covered with prairie grasses with a typical roughness length ($z_{0\,\mathrm{m}}$) of about 0.03 m (Steeneveld et al., 2008).

3.4.1. Temperature data from the 60 m Tower

We calculate C_T^2 from temperature measurements with 32 thermocouples (Chromel/ Constantan, 0.0254 mm, sample frequency of 5 Hz) mounted at the 60-m tower operated by the National Center for Atmospheric Research (Burns and Sun, 2000). The thermocouples were separated vertically by 1.8 m with the lowest level at 2.3 m and the highest level at 58.1 m. The vertically highly-resolved temperature data within the atmospheric surface layer makes this dataset ideal to investigate not only the influence on $f\,(z/L)$ of variations in $-1/L$ but also of variations in z.

The dataset as available from NCAR is already processed in the sense that spikes within the time series were removed, and that the time stamp differences and mean differences between the data from the three Campbell CR2X data loggers have been corrected (Burns and Sun, 2000).

C_T^2 is calculated as the mean of the spatial structure function (D_{TT_x}) over a range of spatial separations (r) within the inertial subrange.

$$C_T^2 = \left\langle \frac{D_{TT_x}(r)}{r^{\frac{2}{3}}} \right\rangle = \left\langle \frac{D_{TT_t}(\tau)}{(\tau\overline{U})^{\frac{2}{3}}} \right\rangle = \left\langle \frac{\overline{[T(t+\tau) - T(t)]^2}}{(\tau\overline{U})^{\frac{2}{3}}} \right\rangle \tag{3.6}$$

in which D_{TT_t} is the temporal structure function, $T(t)$ is the temperature at time t and $T(t+\tau)$ the temperature at time $t+\tau$, τ $(= r/\overline{U})$ is the temporal separation, $\overline{U}$ is the mean horizontal wind speed, the overbar indicates temporal averaging (30 min), and the $\langle\rangle$ indicate the averaging over a range within the inertial subrange. This range is

estimated as $0.4s < \tau < z/\overline{U}$ ($0.4\overline{U} < r < z$). Consequently, for the lowest levels C_T^2 is not always available (i.e. in the case that $0.4\overline{U} > z$).

For the conversion from temporal into spatial structure parameter, we need U at each thermocouple level. However, the measured wind speed ($\overline{U}_{\rm meas}$) profile is not easy to use for this purpose. First, $\overline{U}_{\rm meas}$ is not always available during the selected periods. Second, $\overline{U}_{\rm meas}$ is only available at twelve levels measured with different instruments[2]. Third, the inaccuracies in $\overline{U}_{\rm meas}$ resulted in profiles that are not smooth (some levels show a large discrepancy, especially the sonic measurements at 20 m). Therefore, we decided to calculate the mean wind speed at each thermocouple level with the flux profile relation of Businger-Dyer ($\overline{U}_{\rm BD}$, Businger et al., 1971) using the surface flux and wind speed observed with the eddy covariance station (see Sect. 3.4.2). From a linear least square regression analysis over the selected available wind speed measurements at all levels[2] except for the 20 m level, we find that $\overline{U}_{\rm BD} = 0.98\overline{U}_{\rm meas} + 0.5$ m s^{-1} with the coefficient of determination (r^2) of 0.97.

3.4.2. Surface data required by MOST

Surface data are needed to determine the scaled temperature structure parameter ($\widetilde{C_T^2}$, Eq. 3.1) and the stability[3] (L, Eq. 3.2). For this we use the processed dataset from the eddy covariance station (CSAT3 sonic anemometer and a KH20 Krypton hygrometer - Campbell Scientific Inc., Logan, U.S.A.) located 300 m east-south-east of the tower at a height of 2.65 m above the surface. This eddy covariance station was operated and processed by the Meteorology and Air Quality Group of Wageningen University (Hartogensis et al., 2002). Hartogensis et al. (2002) processed the data with EC-pack (van Dijk et al., 2004) over a time window of 30-min. A number of corrections were applied in the processing of raw data to fluxes[4] and the uncertainty of the variables[5] (Δ_s) was calculated (van Dijk et al., 2004).

3.4.3. Data selection

We select only periods for which:

- local time is between 10h30 and 17h00, in order to exclude periods in which data may be too instationary (around transition) and the atmospheric boundary layer may be so shallow that parts of the mast are located above the ASL,
- the atmosphere is unstable ($-z/L > 0.00$ and $H > 0$ W m^{-2}),
- the relative uncertainties (rel$\Delta_s = \Delta_s/s$, with Δ_s obtained from EC-pack[5]) of the fluxes ($\overline{w'T'}$ and $\overline{w'q'}$) and of the friction velocity (u_*) is smaller than 0.3.

[2] sonic anemometer measurements at 1.5, 5, 10, 20, 30, 40, 50, 55 m, and cup anemometer measurements at 15, 25, 35, 45 m

[3] in which $\overline{w'T_v'} = \overline{w'T'}(1 + 0.61\overline{q}) + 0.61\overline{T}\overline{w'q'}$

[4] a) double rotation; b) the sonic temperatures are corrected for humidity (Schotanus et al., 1983; Liu et al., 2001); c) the Krypton hygrometer signal is corrected for sensitivity to oxygen fluctuations, and off-sets in the calibration caused by weathering of the instrument's magnesium fluoride window are removed; d) the time series are linearly detrended, see Hartogensis et al. (2002) for the details.

[5] $\Delta_{\overline{s}} = 2\sigma(s)/\sqrt{n_{\rm indep}}$, in which s is the variable under consideration, and $n_{\rm indep}$ is the number of independent samples (van Dijk et al., 2004)

This leaves us with a total of 190 time periods of 30 minutes.

3.5. Data Analysis

3.5.1. Part 1: Regression approaches

In part 1, we assess the regression approaches introduced in section 3.3. This part consists of three steps. The first step is to fit the entire dataset (all selected time periods and levels) using the thirty regression approaches, and determine the coefficients c_1 and c_2 for each approach. Normally, however, we are not interested in the coefficients themselves but in their impact on the sensible heat flux that was calculated from them. Therefore, the second step is to assess the impact of the regression approaches on the surface fluxes derived from observed C_T^2 and stability. Finally, in the third step we discuss the main differences between the regression approaches, based on the results of step 1 and 2. From this discussion, we select the most suitable approaches that we will apply in the second part of the research. In the sections below, the details about the strategy of step 1 and step 2 are given.

Step 1, Impact of regression approaches on the regression coefficients

The data is fitted with the Fortran95 library ODRPACK95 (Zwolak et al., 2007) using the thirty approaches as presented in section 3.3. ODRPACK95 calculates the best fit through the data according to the principles of ODR, but the option LSR is also available. The boundaries of the range for the regression coefficients can be set beforehand. For both coefficients we select a lower limit of 0 and an upper limit of 10^8.

For the option 'weight', we define the weights for x and y as one divided by the uncertainties for x ($1/\Delta_x$) and y ($1/\Delta_y$). Δ_x and Δ_y are calculated using error propagation from the uncertainties in the fluxes obtained from EC-Pack[5], and assuming a relative uncertainty in C_T^2 to be 0.1. This makes $\Delta_x = -z/L\sqrt{\left(\frac{\Delta_{\overline{w'T_v'}}}{\overline{w'T_v'}}\right)^2 + 3\left(\frac{\Delta_{u*}}{u_*}\right)^2}$, and $\Delta_y = \widetilde{C_T^2}\sqrt{2\left(\frac{\Delta_{\overline{w'T_v'}}}{\overline{w'T_v'}}\right)^2 + 2\left(\frac{\Delta_{u*}}{u_*}\right)^2 + \left(\frac{0.1}{C_T^2}\right)^2}$. The uncertainty in $x_{\log}$ is calculated as $\Delta(x_{\log}) = \Delta_x/(x\ln(10))$ and in $y_{\log}$ as $\Delta(y_{\log}) = \Delta_y/(y\ln(10))$, in which x and y are the original (non-logarithmic) data.

For the 'fixed c_1' and 'fixed c_2' procedure, we are using the coefficients of de Bruin et al. (1993): $c_1 = 4.9$ and $c_2 = 9.0$.

In addition to the estimated coefficients, ODRPACK95 gives an estimate of their uncertainty (Δ_{c_1} and Δ_{c_2}) and the Weighted Residual Standard Deviation (WRSD) of the regression. From the uncertainty we calculate the relative uncertainty ($\mathrm{rel}\Delta_c = \Delta_c/c$), which together with WRSD is used as an indicator of the quality of the fitting approach. In the determination of WRSD the weights are included. As a consequence WRSD can not be used to compare different regression approaches for which the magnitude of the weights differs, i.e. between 'weight' and 'unWeight' or between the three transforma-

Table 3.2. The range and the number of data points for the eight z classes (*left columns*) and for the eight $-1/L$ classes (*right columns*).

z classes			$-1/L$ classes				
nr	height [m]	data points	nr	$\log(-1/L)$	$-1/L$	$-L$	data points
1	2.3 - 7.7	551	1	− 2.90 - − 2.25	0.001 - 0.006	178 - 841	443
2	9.5 - 14.9	672	2	− 2.25 - − 2.00	0.006 - 0.010	100 - 178	707
3	16.7 - 22.1	665	3	− 2.00 - − 1.75	0.010 - 0.018	56 - 100	814
4	23.9 - 29.3	663	4	− 1.75 - − 1.50	0.018 - 0.032	31 - 56	754
5	31.1 - 36.5	651	5	− 1.50 - − 1.25	0.032 - 0.056	17 - 31	670
6	38.3 - 43.7	679	6	− 1.25 - − 1.00	0.056 - 0.100	10 - 17	583
7	45.5 - 50.9	668	7	− 1.00 - − 0.75	0.100 - 0.178	5.6 - 10	698
8	52.7 - 58.1	667	8	− 0.75 - 0.11	0.178 - 1.32	0.7 - 5.6	547
tot	2.3 - 58.1	5216	tot	− 2.90 - 0.11	0.001 - 1.32	0.7 - 841	5216

tions. In order to check if the behaviour in the free convection limit differs between the regression approaches, we will also evaluate d.

Step 2, Impact of regression approaches on the fluxes

In order to assess the impact of the different regression approaches on the derived surface fluxes, we calculate the surface sensible heat flux with the similarity relationship given in Eq. 3.1 using $f\,(z/L)$ according to Eq. 3.3 and the coefficients c_1 and c_2 as obtained with each regressions approach. This calculated surface flux (H_{MOST}) is compared to the observed sensible heat flux (H_{obs}) at the surface station (Sect. 3.4.2). The additional quantities needed in Eq. 3.1 and Eq. 3.3, are obtained from the surface station (Sect. 3.4.2).

For the comparison of H_{MOST} and H_{obs}, we do a linear least squares regression forced through the origin (the data are not weighted). The slope (a), the coefficient of determination (r^2) and the coefficient of variation (abbreviated as CV) are evaluated. The coefficient of determination is a measure of the strength of the correlation, and CV indicates how much each point –in a relative sense– deviates from the 1:1-line on average.

3.5.2. Part 2: Stability and height dependency

In part 2, we assess the impact of measuring within different stability ranges and at different heights within one dataset. To that end, we divide our dataset into eight $-1/L$ classes and eight z classes (Table 3.2). Splitting the 32 measurement levels in eight z classes, containing four levels each, ensures that these classes contain a comparable number of data points. In order to be consistent, the borders of the eight $-1/L$ classes are specified in such a way that the $-1/L$ classes represent a comparable number of data points too. For each class the regression coefficients are determined using the regression approach selected in part 1. The eight $-1/L$ classes represent a limited

range of $-z/L$, especially the more unstable classes 5 to 8, which makes it impossible to fit both coefficients simultaneously (see section 3.3). In part 2 we, therefore, choose to fix c_1. The value of c_1 used is the one obtained from the entire dataset in part 1, using the most suitable approach. As a consequence, we can now determine c_2 for each class or for the entire dataset.

To investigate if the differences in c_2 and d between the classes are statistically significant, we compare Δ_{c_2} (which is given from ODRPACK95) and Δ_d (which is calculated as $d\sqrt{\mathrm{rel}\Delta_{c_1}^2 + \left(\frac{2}{3}\mathrm{rel}\Delta_{c_2}\right)^2}$) *within* each class with the variation of c_2 and d *between* the classes.

Notice, that in this paper we are not in search of the best shape of $f\,(z/L)$, but we are interested in the effect of using various regression approaches and measuring within different stability ranges and at different heights on $f\,(z/L)$. Therefore, we discuss the values of the coefficients relative to other regression approaches (Part 1) and between the classes (Part 2), and do not compare the values of the coefficients with literature.

3.6. Results and Discussion

3.6.1. Part 1: Regression approaches

Step 1, impact of regression approaches on the regression coefficients

The first step of part 1 is to fit the entire dataset (all selected time periods and levels) using the thirty regression approaches, in order to assess the effect on the regression coefficients. The coefficients obtained with the different regression approaches are given in the centre part of Table 3.3 for LSR and in the centre part of Table 3.4 for ODR. Notice that for LSR, the loglin transformation is not given because the coefficients are the same as the those of the linlin transformation.

In general, we find that c_1 ranges from 3.9 (LSR, loglog, 'notWeight', 'unfixed') up to 8.5 (ODR, loglin, 'notWeight', 'unfixed') and c_2 ranges from 8.0 (LSR, loglog, 'notWeight', 'unfixed') up to 34.5 (ODR, loglin, 'notWeight', 'unfixed). For both coefficients, relΔ is small with a maximum of 4% for c_1 and 7% for c_2. The large range of coefficients in combination with the small relative uncertainty implies that the experimentally determined similarity relations depend on the details of the regression approach used.

The coefficient of the free convection approximation, d, is more comparable among the approaches (ranging from 0.81 up to 1.11) than c_1 and c_2 individually. This means that the approaches are relatively consistent in the free convection range. Consequently, we conclude that the deviations between the approaches are mainly due to data in the near-neutral range, when T_* is not well defined. Hence, as c_2 depends on c_1 through $d = c_1 c_2^{-2/3}$, an ill-defined c_1 will affect c_2. As the data used in each regression approach are identical, differences in c_1 and c_2 are thus to be related to the influence on the regression of data points in the neutral range. Another effect of the dependency of c_1 and c_2 through d, is that the value of c_1 and c_2 are positively correlated: if c_1 of a

Table 3.3. The results of the different regression approaches using classical linear least square (LSR). The centre columns show the results of the regression (Step 1): the regression coefficients (c_1, c_2 and d, all shaded to easily find them) with the corresponding relative uncertainty (relΔ) and the WRSD of the fit. The right columns show the results of the linear least square regression H_{obs} versus H_{MOST} (forced through the origin) calculated from the obtained coefficients (Step 2): the slope (a), the coefficient of determination (r^2) and the coefficient of variation (CV). The approaches differ in the following three aspects: 1. Weighting of data: 'notWeight' (first part); and 'weight' (second part), 2. Transformation of data: linlin (first block per part); and loglog (last block per part), 3. Number of coefficients to fit: 'unfixed'; (first row per block); 'fixed c_1' (second row per block); and 'fixed c_2' (third row per block).

	Step 1						Step 2		
approach	c_1	relΔ [%]	c_2	relΔ [%]	d	WRSD	a	r^2	CV
'notWeight'									
linlin									
'unfixed'	5.1	1.2	14.1	2.8	0.88	0.443	1.02	0.587	0.241
'fixed c_1'	4.9		12.7	0.9	0.90	0.443	1.00	0.592	0.234
'fixed c_2'	4.3	0.4	9.0		0.99	0.453	0.96	0.608	0.220
loglog									
'unfixed'	3.9	1.7	8.0	3.1	0.97	0.131	0.98	0.611	0.220
'fixed c_1'	4.9		12.0	0.7	0.93	0.133	0.98	0.595	0.228
'fixed c_2'	4.1	0.4	9.0		0.96	0.131	0.99	0.606	0.224
'weight'									
linlin									
'unfixed'	4.4	1.4	11.6	2.9	0.85	0.801	1.04	0.594	0.246
'fixed c_1'	4.9		14.5	0.8	0.82	0.805	1.06	0.584	0.260
'fixed c_2'	3.9	0.4	9.0		0.90	0.807	1.02	0.605	0.233
loglog									
'unfixed'	4.0	1.7	8.7	3.1	0.95	0.483	0.99	0.607	0.224
'fixed c_1'	4.9		12.4	0.7	0.91	0.488	0.99	0.593	0.232
'fixed c_2'	4.1	0.4	9.0		0.94	0.483	0.99	0.606	0.224

certain approach is larger than that of another approach c_2 will be larger too.

In order to understand the differences between the various regression approaches, Fig. 3.2 shows $\widetilde{C_T^2}$ versus $-z/L$ of the entire dataset in each of the three data transformations used in the regression analysis: linlin (left column), loglin (centre column), and loglog (right column). The first row shows the entire range of the data points. From these figures, the differences between the three transformation methods can be observed, as is described in Sect. 3.3. The range of observed $-z/L$ is from 7.5 10^{-3} up to 7.6 10^{1}. Because, at $-z/L \approx 0.005$ (the left border of the logaritmic x-axes) the regression lines are not horizontal, we conclude that the neutral asymptote is not reached yet.

The results of the several regression approaches are shown in the second up to the fourth row of Fig. 3.2. These rows show a segment of the near-neutral range, because we already analysed that the behaviour of the free convection range is similar for the various fits. In the following paragraphs, the differences between the approaches are discussed, with the focus on relΔ of c_1 and c_2, and WRSD.

1. Transformation of the data. First, we compare the coefficients from linlin (Eq. 3.3), loglin (Eq. 3.4), and loglog (Eq. 3.5). In this paragraph we start with a focus on

Table 3.4. The results of the different regression approaches using orthogonal distance regression (ODR). The centre columns show the results of the regression (Step 1): the regression coefficients (c_1, c_2 and d, all shaded to easily find them) with the corresponding relative uncertainty (relΔ) and the WRSD of the fit. The right columns show the results of the linear least square regression H_{obs} versus H_{MOST} (forced through the origin) calculated from the obtained coefficients (Step 2): the slope (a), the coefficient of determination (r^2) and the coefficient of variation (CV). The approaches differ in the following three aspects: 1. Weighting of data: 'notWeight' (first part); and 'weight' (second part), 2. Transformation of data: linlin (first block per part); loglin (second block per part); and loglog (last block per part), 3. Number of coefficients to fit: 'unfixed'; (first row per block); 'fixed c_1' (second row per block); and 'fixed c_2' (third row per block).

	Step 1						Step 2		
approach	c_1	relΔ [%]	c_2	relΔ [%]	d	WRSD	a	r^2	CV
'notWeight'									
linlin									
'unfixed'	4.8	4.0	12.8	6.8	0.88	0.156	1.02	0.591	0.240
'fixed c_1'	4.9		13.2	0.7	0.88	0.156	1.02	0.590	0.240
'fixed c_2'	3.9	0.4	9.0		0.91	0.157	1.02	0.605	0.233
loglin									
'unfixed'	8.5	2.8	34.5	4.9	0.81	0.180	1.04	0.554	0.272
'fixed c_1'	4.9		12.3	0.9	0.92	0.224	0.99	0.594	0.231
'fixed c_2'	4.8	0.4	9.0		1.11	0.247	0.89	0.611	0.231
loglog									
'unfixed'	4.3	1.7	9.8	3.2	0.95	0.115	0.99	0.603	0.226
'fixed c_1'	4.9		12.2	0.7	0.92	0.115	0.99	0.594	0.230
'fixed c_2'	4.1	0.4	9.0		0.96	0.115	0.99	0.606	0.224
'weight'									
linlin									
'unfixed'	5.4	2.2	17.1	3.8	0.82	0.560	1.06	0.578	0.264
'fixed c_1'	4.9		14.4	0.7	0.83	0.561	1.05	0.585	0.258
'fixed c_2'	3.9	0.4	9.0		0.90	0.586	1.02	0.605	0.233
loglin									
'unfixed'	6.0	1.7	20.0	3.2	0.82	0.641	1.05	0.572	0.264
'fixed c_1'	4.9		13.5	0.8	0.86	0.649	1.03	0.588	0.244
'fixed c_2'	4.1	0.4	9.0		0.95	0.679	0.99	0.606	0.224
loglog									
'unfixed'	4.4	1.7	10.2	3.2	0.93	0.436	0.99	0.601	0.226
'fixed c_1'	4.9		12.6	0.7	0.90	0.438	1.00	0.592	0.233
'fixed c_2'	4.1	0.4	9.0		0.94	0.437	0.99	0.606	0.224

ODR (Table 3.4) only, because for LSR the coefficients are the same using linlin and loglin (Sect. 3.3.2).

For the options 'notWeight' (first part of Table 3.4) and 'weight' (second part of Table 3.4), we observe the same pattern: loglin given the largest coefficients and loglog given the smallest coefficients. The tendency for loglin to show the largest coefficients is supported by Fig. 3.2, where the largest values of $\widetilde{C_T^2}$ (outliers) in the near-neutral range are better visible for loglin than linlin and loglog. In other words, outliers with large $\widetilde{C_T^2}$ in the near-neutral range have the largest influence on the coefficient when using loglin.

Comparing the relΔ_c of the approaches we observe that the smallest errors are obtained for the loglog transformation. These small values suggest that the loglog ap-

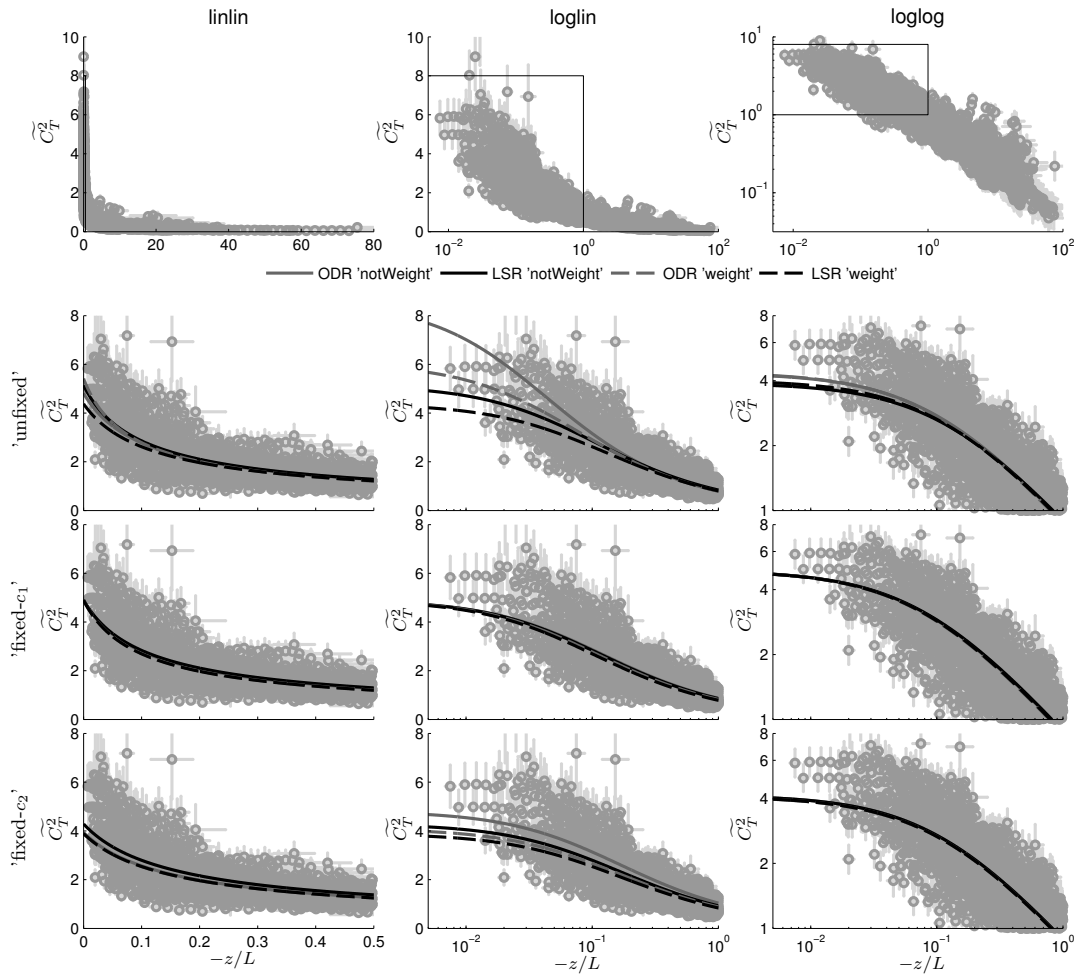

Fig. 3.2. The scaled structure parameter of temperature ($\widetilde{C_T^2}$) versus stability ($-z/L$). The *first row* shows the entire dataset for the three data transformation approaches: linlin (left column), loglin (centre column), and loglog (right column). The *second up to fourth row* show a segment in the near-neutral range (the black box in the first row), including the lines resulting from the different regression approaches. The approaches differ in the following three aspects: 1. Mathematical regression method: LSR (black lines) and ODR (grey lines), 2. Weighting of the data: 'notWeight' (solid line) and 'weight' (dashed line), and 3. Number of coefficients to fit: 'unfixed' (second row), 'fixed c_1' (third row), and 'fixed c_2' (fourth row).

proach has the most robust coefficients. Notice that for LSR (Table 3.3), the relΔ_c has larger values for loglog than for linlin, however, the differences are small.

Another way to investigate which data transformation gives the most robust regression results is to compare the regression coefficients for all approaches while keeping the data transformation constant. We therefore calculate for each transformation (linlin, loglin, and loglog) a standard deviation in c_1 and c_2 of the eight approaches. The eight approaches results from the combinations of two methods (LSR and ODR), two options ('notWeight' and 'weight') and two procedures (for c_1: 'unfixed' and 'fixed c_2', and for c_2: 'unfixed' and 'fixed c_1'). Using the eight values of c_1 gives a standard deviation in c_1 of 0.6 (linlin), 1.5 (loglin), and 0.2 (loglog). For c_2 the standard deviation is 1.7 (linlin),

7.6 (loglin), and 1.8 (loglog). For c_1, loglog has the smallest standard deviation among the approaches, and for c_2 linlin. The standard deviation of c_1 of loglog is comparable with the one of linlin. This means that the loglog transformation is the most consistent among the different approaches. This can be understood by looking to Fig. 3.2: in the neutral range the scatter is least for loglog.

2. Mathematical regression methods. Second, we compare the classical least square regression (Table 3.3) with the orthogonal distance regression method (Table 3.4). ODR yields larger coefficients than LSR for most of the approaches. Especially, when applying the loglin transformation the c_1 and c_2 are much larger. The relative uncertainties of the coefficients are smaller for LSR than for ODR in case of linlin and loglin, and similar in case of loglog, whereas the WRSD is larger for LSR than for ODR in any case. This means that the results do not show a preferred method. However, the use of LSR is not an appropriate choice, because uncertainties in $-z/L$ are not taken into account whereas for ODR they are (Sect. 3.3).

3. Weighting the data. Third, we compare the unweighted dataset with the weighted dataset (see the errorbars in Fig. 3.2). There is not a clear pattern which of these two options gives the larger coefficients This is to be expected, because the weighted dataset has to be seen as a new dataset, and the weighting ($1/\text{rel}\Delta$) differs between linlin, loglin and loglog (Sect. 3.5.1).

If the data is weighted, $\text{rel}\Delta_c$ is reduced for all the approaches compared to the unweighted dataset. This can be understood as follows: most outliers have a large uncertainty and consequently a low weight. Hence, these have a lower impact on the regression and thus the $\text{rel}\Delta_c$ is reduced.

4. Number of regression coefficients to fit. Fourth, we compare the 'unfixed' procedure with the 'fixed c_1' or 'fixed c_2' procedure. On the one hand if comparing the coefficients obtained with these procedures, we observe that using 'unfixed', the obtained coefficients are less robust as compared to 'fixed c_1' and 'fixed c_2'. This is found by comparing for each of the three procedures the standard deviation in c_1 and in c_2 of the twelve approaches, which we have by varying the three transformations (linlin, loglin and loglog), the two methods (LSR and ODR) and the two options ('notWeight' and 'weight'). The 12 values of c_1 give a standard deviation of 1.3 for 'unfixed' and 0.3 for 'fixed c_2'. The standard deviation in c_2 is 7.2 for 'unfixed' and 0.9 for 'fixed c_1'. Furthermore, the $\text{rel}\Delta_c$ of the 'unfixed' coefficients are also the largest. This reduced robustness if using 'unfixed' is to some extent trivial, because when one of the coefficients is fixed, the regression will have fewer degrees of freedom than when both are kept unfixed. On the other hand, WRSD is the smallest for the 'unfixed' procedure. However, in some cases the differences are minor. The smallest WRSD for 'unfixed' is to be expected, because this procedure obtains the optimal fit through the data.

Step 2, impact of regression approaches on the fluxes

The right parts of the Table 3.3 (LSR) and Table 3.4 (ODR) give the results of the comparison between the observed sensible heat fluxes (H_{obs}) and the calculated sensible heat fluxes (H_{MOST}). The latter are calculated from the coefficients obtained in Step 1 with Eq. 3.1 using $f\,(z/L)$ according to Eq. 3.3. However, the fluxes are the same when using Eq. 3.4 or 3.5. In other words, when knowing the coefficients a data transformation does not affect the calculations of the sensible heat flux.

In general the ratio of H_{MOST} and H_{obs} is about one, with a r^2 of about 0.60 and a CV of about 0.23. The differences between the approaches are small despite the large differences in the coefficients. This is an important result for using MOST in practice. The reason why the different approaches generally have comparable H_{MOST} can be understood as follows. A linear regression through the origin is mainly dominated by large values. These relatively large values of H correspond to large values of $-z/L$. Large values of $-z/L$ are close to the free convection limit, for which regression approaches (d) are comparable (see step 1).

Step 3, evaluation and discussion of the regression approaches

Based on the theory given in Sect. 3.3 and on the results above, we now can identify a recommended regression approach.

1. *Transformation of data:* loglog, because it shows the most robust coefficients (the smallest relΔ and the most comparable coefficient between the approaches).
2. *Mathematical regression method:* ODR, because uncertainties in $-z/L$ are taken into account as well.
3. *Weighting of data:* 'weight', because the more uncertain data points have less influences on the fit.
4. *Number of coefficients to fit:* 'unfixed' if the data cover a broad range of $-z/L$ including near-neutral data, because the WRSD has the lowest values and one does not have to chose a fixed value beforehand.

To summarize, we recommend to calculate the regression using a double logarithmic transformation, an orthogonal distance regression method, weighted data, and keeping both coefficients unfixed (provided that the $-z/L$ range is sufficiently large). This is the regression approach we like to use in Part 2, however, in that analysis the range of $-z/L$ within in one stability class is limited (Table 3.2). Therefore we choose to have a fixed value $c_1 = 4.4$, which is the value obtained with this approach over the entire dataset.

Note that if a limited $-z/L$ range makes fixing of one of the coefficients necessary, the *value* of that fixed coefficient will influence the value of the coefficient that is left free in the regression. The asymptotic value for the similarity relations as stability approaches neutral conditions is under discussion (Hill et al., 1992; Thiermann and Grassl, 1992; Van Kesteren, 2012). Hill et al. (1992) found a value of 8.1, and Thiermann and Grassl (1992) and Van Kesteren (2012) argue that c_1 has to be 6.37 based on an analysis of

Table 3.5. Results of additional regression approaches tested using ODR: the coefficients (c_1, c_2 and d) with the corresponding relative uncertainty (relΔ) and the WRSD of the fit. First part: using a 'fixed c_1' of 6.37 as argued by Thiermann and Grassl (1992); Van Kesteren (2012) (ODR, weight, 'fixed c_1'). Second part: an artificial dataset with randomized $\overline{w'T'}$ (ODR, 'notWeight', 'unfixed'). Third part: an artificial dataset with randomized u_* (ODR, 'notWeight', 'unfixed').

approach	c_1	relΔ [%]	c_2	relΔ [%]	d	WRSD
test another c_1: $c_1 = 6.37$						
linlin	6.4		22.6	0.7	0.80	0.562
loglin	6.4		22.0	0.7	0.81	0.641
loglog	6.4		19.9	0.7	0.87	0.449
test artificial data with randomized $\overline{w'T'}$						
linlin	18.0	9.5	0.0	34.1	153.44	37.583
loglin	658.1	1.0	458.0	94.2	11.08	11.656
loglog	4.3	11.7	0.3	30.4	10.36	0.817
test artificial data with randomized u_*						
linlin	5.2	7.9	15.5	13.0	0.84	0.185
loglin	52.9	34.1	567.3	51.6	0.77	0.182
loglog	6.3	4.1	18.8	6.6	0.89	0.141

the budget equations and the neutral asymptote (equal to one) for the gradient MOST relations. This value is relatively large compared to the values we found. Because c_1 and c_2 are positively correlated, using a fixed value for c_1 of 6.37 increases c_2 (up to 20). Consequently, using c_1 equal to 6.37 gives larger WRSD than using 4.9, except for the ODR-loglin approach (Table 3.5).

So far we compare the various regression approaches to fit the most common shape of $\widetilde{C_T^2}$ (Eq. 3.3). However, also different shapes have been proposed (Table 3.1). For instance Thiermann and Grassl (1992) and Wesely (1976b) used a function with more coefficients. The reason why we choose this shape is already given in Sect. 3.1. Moreover, as observed from our study, it is already difficult to fit two coefficients simultaneously, so using an extra coefficient only creates extra uncertainty.

Because the parameters plotted on the x-axis ($-z/L$) and the y-axis ($\widetilde{C_T^2}$) in MOST contain common variables (H and u_*), the observed correlation can be an artificial self-correlation. Baas et al. (2006) investigated the effect of self-correlation on the determination of flux-gradient relationships within the stable boundary layer. They generated artificial data, based on observed data, for which MOST variables (H and u_*) were randomized. To analyse the effect of self-correlation on the regression approaches for $\widetilde{C_T^2}$, we repeat the method of Baas et al. (2006) by generating two artificial datasets. In the first dataset only $\overline{w'T'}$ is randomized (the combination of C_T^2 and u_* still is the same as in the original dataset). In the second dataset only u_* is randomized. Table 3.5 shows the regression results for both artificial datasets (ODR - 'notWeight' - 'unfixed'). The coefficients obtained from the artificial dataset with the randomized $\overline{w'T'}$ are totally different from the original dataset: they even have unreasonable values (with e.g. c_2 about zero). On the other hand, the artificial dataset with the randomized

u_* gives reasonable values. This is to be expected, because in the free convection limit, when winds are calm, the surface stress and therefore u_* becomes unimportant. Hence, the intact combination of $\widetilde{C_T^2}$ and $\overline{w'T'}$ is sufficient to reproduce the correct d. For data in the free convection range perturbations in u_* will cause a displacement along the free convection relationship. This means that the behaviour of data points of the artificial dataset in the free convection range is similar as for the data points of the real dataset. In the neutral range, however, a randomly large u_* will cause an increase in $\widetilde{C_T^2}$ and a decrease in $-z/L$. This means that data points in the neutral range are located higher than data points of a real dataset. These higher values in the neutral range cause both coefficients and their relative uncertainty to become larger.

3.6.2. Part 2: Stability and height dependency

Variation of MOST relations between eight $-1/L$ classes

We start this section with analysing the impact of measuring within different stability ranges on the Monin-Obukhov similarity functions. Fig. 3.3 shows the scaled structure parameter ($\widetilde{C_T^2}$) versus the stability ($-z/L$) together with the best fit for the entire dataset and for each class separately. Fig. 3.4 shows bar charts of the values of c_2 and d, including their uncertainty (Δ), in order to investigate how c_2 and d change with increasing $-1/L$.

Three remarks have to be made related to Fig. 3.4.

1. We recall that here we use the regression approach 'fixed c_1', and therefore d is proportional to $c_2^{-2/3}$. As a consequence, an increase in c_2 results in a decrease in d and in a downward shift of the regression line given in Fig. 3.3.
2. In general Δ_{c_2} and Δ_d are smaller for each class than the variations between the classes. The standard deviation of c_2 ($\sigma(c_2)$) among the classes is 1.9 and the mean size of the uncertainty ($\overline{\Delta_{c_2}}$) is 0.21. This indicates that the differences in c_2 and d between $-1/L$ classes are statistically significant.
3. The uncertainty of d for the entire dataset is larger than that of each $-1/L$ class except for the first class. The larger Δ_d for the entire dataset occurs because there we use the regression approach 'unfixed', and c_1 is included in the calculation of Δ_d, whereas for the eight $-1/L$ classes, we use the approach 'fixed c_1', and therefore the uncertainty in c_1 is zero. The reason for the larger uncertainty in d for the first class is that in this class only near-neutral data points are included which create extra uncertainty in describing the behaviour in the free convection limit.

From Fig. 3.3, we conclude that the regression lines of the border classes are located higher than those of the centre classes, resulting in a smaller c_2 and a larger d (Fig. 3.4). Especially, the first class ($c_2 = 6.2$ and $d = 1.3$) deviates from the entire dataset ($c_2 = 10.2$ and $d = 0.9$). Notice, that the number of data points in this class is less than in the other classes resulting in a larger Δ_{c_2}. Nevertheless, Δ_{c_2} is still smaller than the differences in c_2 between the first and second class and thus c_2 is significantly different.

The higher position of the regression line of the first class implies that under neutral

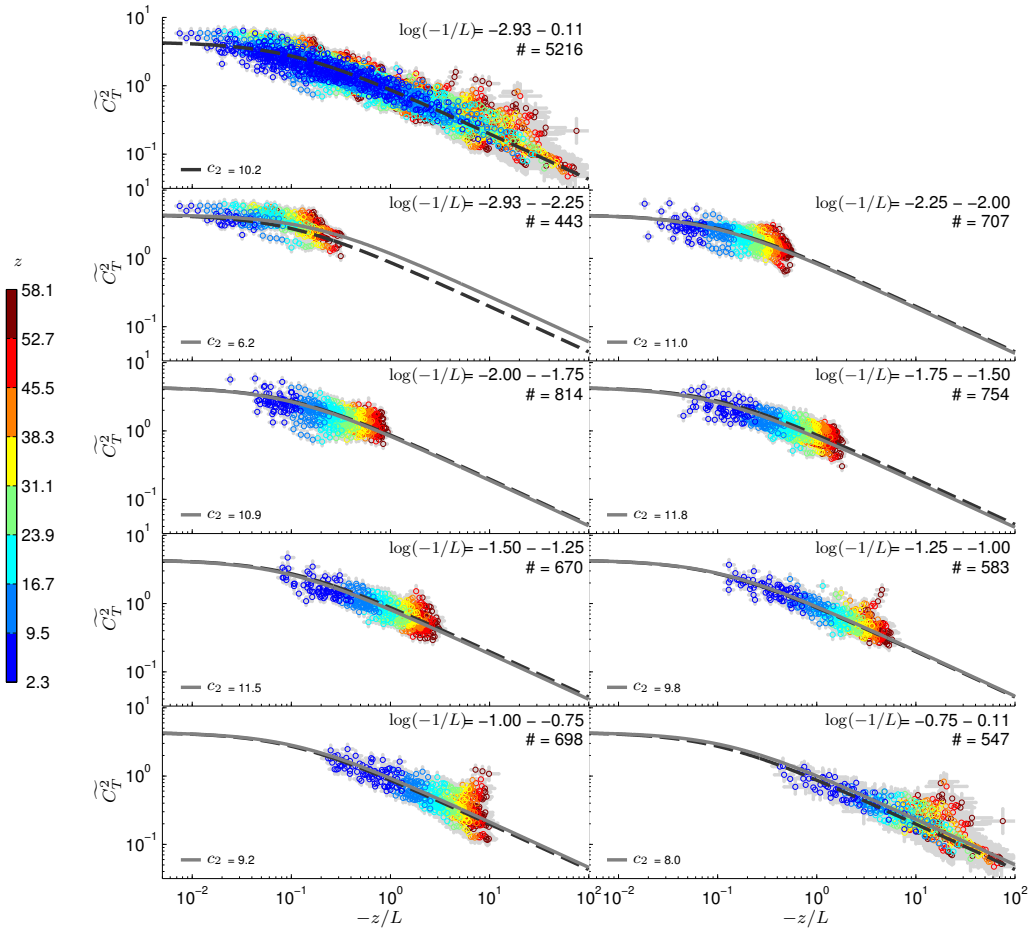

Fig. 3.3. The scaled structure parameter ($\widetilde{C_T^2}$) versus stability ($-z/L$) for all data and for the eight $-1/L$ classes. Each colour represents a different z class. The black dashed line is the fit calculated over the entire dataset (ODR-'weight'-loglog-'unfixed'), with $c_1 = 4.4$ and $c_2 = 10.2$. The grey solid line is the fit for the specific $-1/L$ class (ODR-'weight'-loglog-'fixed $c_1 = 4.4$'). In the right corner the borders of the class, and the number of data points (#) in the class are given.

conditions the observed data is located higher compared to the other classes. This is also observed in other studies. First, Hill et al. (1992) obtained a large c_1 from a dataset observed under near neutral conditions. Second, in the studies of de Bruin et al. (1993); Li et al. (2012); and Braam et al. (2012) data points in the neutral range have generally higher values compared to the regression line through the respective entire dataset.

The consistency between the studies and the relative small uncertainty (see errorbars in Fig. 3.3) indicates that in the near-neutral range the behaviour differs from that in the other ranges. However, the deviation in the first class can also be a mathematical artefact. With c_1 (the neutral asymptote) fixed we need information from more unstable data (beyond $-z/L \approx 1/c_2$, see Fig. 3.1) to be able to determine c_2. The near-neutral class contains only few points that are sufficiently unstable.

The regression fits of classes 2 up to 5 are all located below the fit of the entire dataset (c_2 is larger and d is smaller). The $-z/L$ ranges of these classes are around

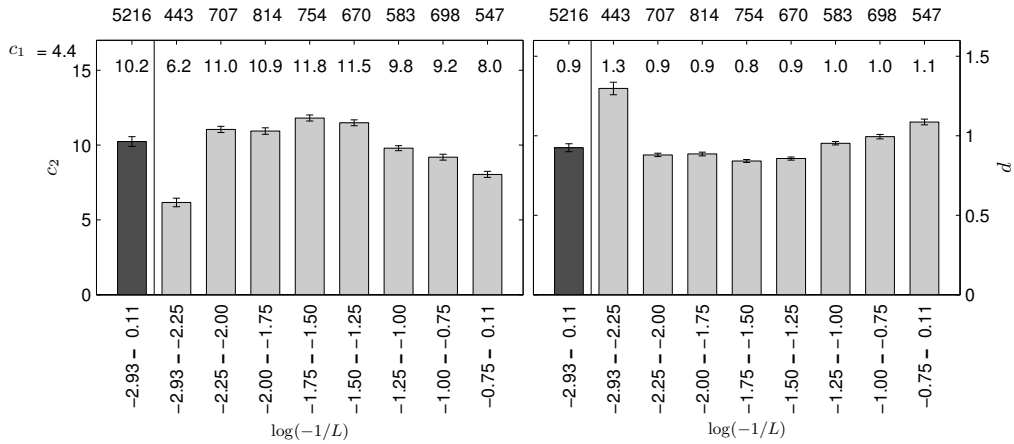

Fig. 3.4. Bar charts with errorbars of the values of c_2 (left) and d (right) for the eight $-1/L$ classes. Above the bars the value of the coefficient is given. The values above the plot are the number of data points in each class.

the transition point ($\approx 1/c_2$) where the neutral class develops into the free convection range. Furthermore, when looking in detail at the entire dataset and its regression fit (first panel in Fig. 3.3), the regression fit indeed overestimates the data in these $-z/L$ ranges. Moreover, the difference between class 2 and 3, and between class 4 and 5 is smaller than the size of the errorbar, so statistically class 2 and 3, and class 4 and 5 are not different.

For classes 6 up to 8, the regression fits of each class are located above the fit of the entire dataset (c_2 is smaller and d is larger). For class 8 the overestimation is larger than for class 6. This means that the behaviour of the free convection limit is different from that of the entire dataset.

In the end, we can conclude that measuring within different stability ranges changes the Monin-Obukhov similarity function for our dataset. The pattern we observe depends on the measured $-z/L$ range. For the most neutral and most unstable classes c_2 is smaller and d is larger than for the centre classes. This could indicate that the data in these classes are located too close to the edge of the entire dataset (in terms of $-z/L$), with a too limited range to properly apply the regression.

Variation of MOST relations between eight z classes

The analysis of the impact of measuring at different heights is based on Figures 3.5 and 3.6. Figure 3.5 shows the similarity fit for each class, and Fig. 3.6 shows the bar charts of the values of c_2 and d. Notice, that the three remarks related to the analysis of the eight $-1/L$ classes (Fig. 3.4) hold as well for the eight z classes. With respect to the second remark, we observe $\sigma(c_2) = 1.5$ and $\overline{\Delta_{c_2}} = 0.22$ among the classes, which implies that a variation in c_2 and d due to variations in observation height is also statistically significant.

For the eight z classes we find that c_2 decreases and d increases with increasing height. In other words, for the classes with a low z the regression fit is located below

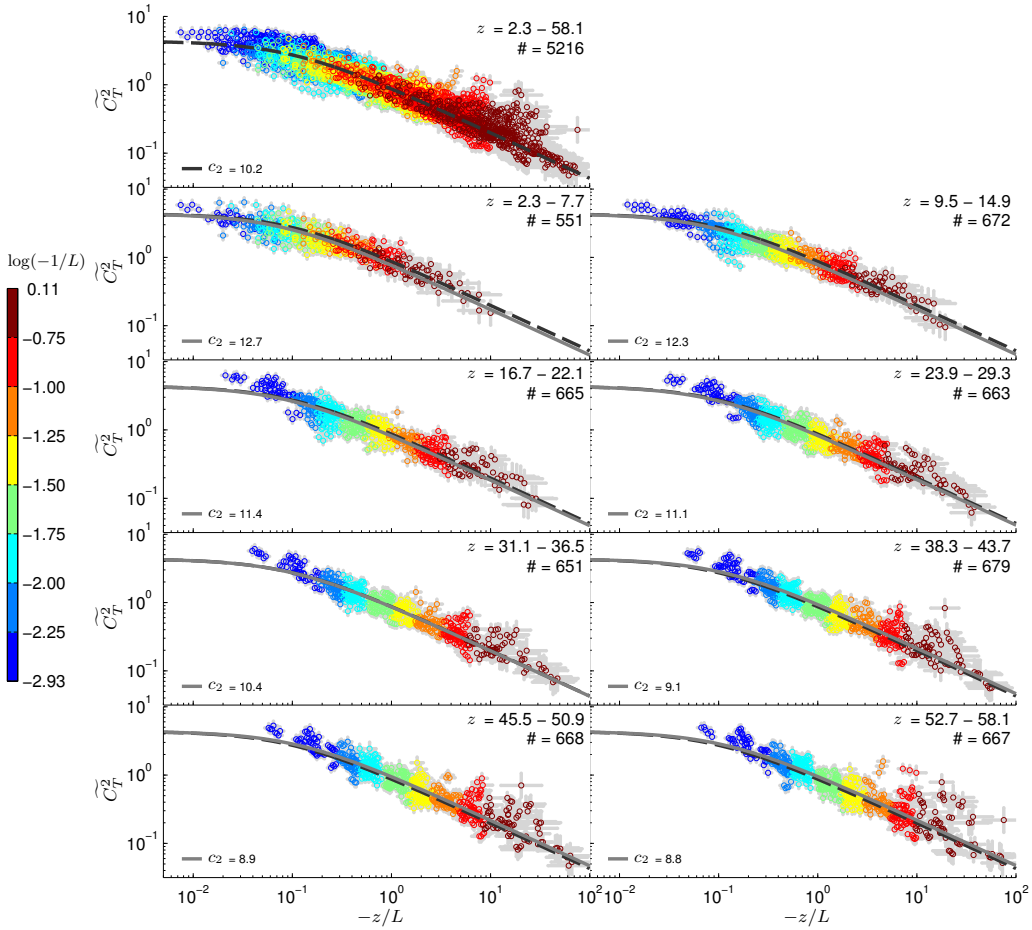

Fig. 3.5. The scaled structure parameter ($\widetilde{C_T^2}$) versus stability ($-z/L$) for all data and for the eight z classes. Each colour represents a different L class. The black dashed line is the fit calculated over the entire dataset (ODR-'weight'-loglog-'unfixed'), with $c_1 = 4.4$ and $c_2 = 10.2$. The grey solid line is the fit for the specific z class (ODR-'weight'-loglog-'fixed $c_1 = 4.4$'). In the right corner the borders of the class, and the number of data points (#) in the class are given.

the regression fit of the entire dataset and for the classes with a high z it is located above. This means that the observed pattern differs from that found for the eight $-1/L$ classes. One reason can be that the scaled structure parameter behaves differently for a given range of $-z/L$, depending on whether this range is attained by varying the height or by varying $-1/L$. This would undermine one of the basic assumptions of MOST. Another reason is related to the $-z/L$ range of each class. The $-z/L$ range of each z class is about 3 decades, which is twice as large as the range in each $-1/L$ class. This is as expected, because in our entire dataset z varies less ($\approx$ 55 m) than L ($\approx$ 840 m). The increased $-z/L$ range has two effects. First, the larger $-z/L$ range of each z class better corresponds to the $-z/L$ range of the entire dataset. Consequently, we observe a smaller $\sigma(c_2)$ for the eight z classes than for the eight $-1/L$ classes. Second, in each z class, the $-z/L$ range includes the transition point ($1/c_2$), where the neutral range develops into the free convection range. In class 1, the class with the near-neutral data,

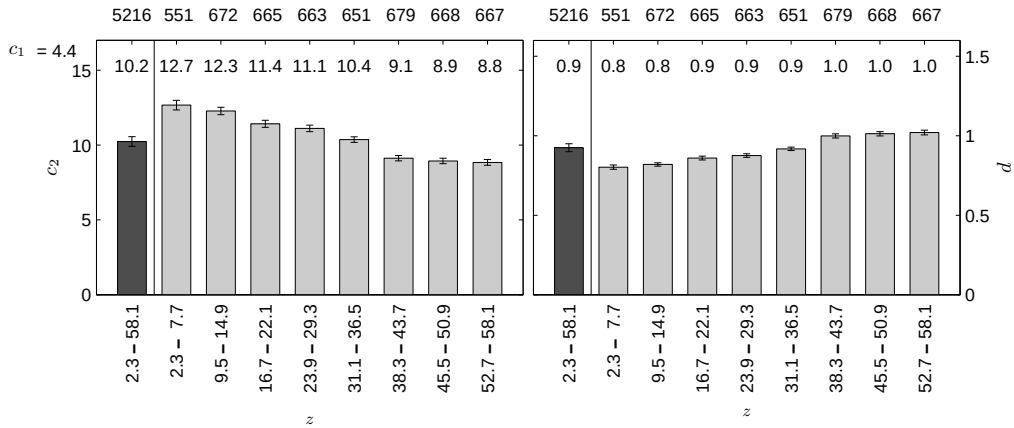

Fig. 3.6. Bar charts with errorbars of the values of c_2 (left) and d (right) for the eight z classes. Above the bars the value of the coefficient is given. The values above the plot are the number of data points in each class.

the transition point is 7.8 10^{-2} and the $-z/L$ range varies from 2.9 10^{-3} up to 10. In class 8, the class with the most unstable data, the transition point is 1.1 10^{-1} and the $-z/L$ range varies from 6.7 10^{-2} up to 75. As each z class includes the transition point, the way how the value of c_2 varies between the classes is different in shape and magnitude for the eight z classes when compared to the eight $-1/L$ classes.

Discussion

In this section we start to discuss three issues related to splitting the dataset in eight classes: First, as stated before, the size of the errorbar for c_2 within a class is smaller than the variations between the classes which makes the results statistically significant. In order to further substantiate this conclusion, an additional analysis is performed. Therefore, we divided the entire dataset into eight random classes, by assigning each data point a random number from 1 up to 8. Each class now contains data points randomly attributed to different z and different $-1/L$ values. For this dataset, c_2 is determined for each class, including the average size of the errorbar for each class ($\overline{\Delta_{c_2}}$), as well as the variability between the classes ($\sigma(c_2)$). This procedure is repeated hundred times. These hundred divisions in eight random classes have a $\sigma(c_2)$ ranging from 0.28 up to 1.01 with an average of 0.58, and a $\overline{\Delta_{c_2}}$ ranging from 0.21 up to 0.65 with an average of 0.64. In seventy out of the hundred realizations $\overline{\Delta_{c_2}}$ is larger than $\sigma(c_2)$. The difference between $\sigma(c_2)$ and $\overline{\Delta_{c_2}}$ for each division ranges from -0.36 up to 0.60 with an average of -0.05. These values are smaller than the difference between $\sigma(c_2)$ and $\overline{\Delta_{c_2}}$ for the eight $-1/L$ classes (1.7) and for the eight z classes (1.3). Thus the division in random classes gives coefficients that are statistically identical for each class. So we can conclude that the height and stability dependency in the eight $-1/L$ classes or eight z classes is statistically significant.

Second, in order to investigate if the pattern that is visible for eight classes depends on the number of classes, we repeat the analysis using four and sixteen $-1/L$ classes

and z classes (Figures not shown). For the four $-1/L$ classes we observe a similar but weaker pattern as for eight $-1/L$ classes. Again c_2 is small and d is large for the most neutral and most unstable classes. When dividing into sixteen $-1/L$ classes, the pattern is similar to that of eight $-1/L$ classes. Only the classes with the smallest number of data points deviate from the pattern, probably because the $-z/L$ range gets too small. For the four and sixteen z classes, the pattern is identical with the eight z classes: c_2 decreases and d increases with increasing z. Moreover, contrary to the $-1/L$ classes, $\sigma(c_2)$ is also similar: $\sigma(c_2)$ is 1.6 for the four and 1.5 for the sixteen classes.

Third, related to the number of classes, it is difficult to compare the behaviour of eight $-1/L$ classes and eight z classes because they have different $-z/L$ ranges. Notice, however, that it is physically impossible to have a comparable class width and a comparable number of data points per class. In our case this would mean that z would have to vary by 840 m as well, and then the highest levels are located far outside the ASL and MOST is not applicable any more.

The division of the dataset in $-1/L$ classes shows that the coefficients differ among each class. This can be related to the shape of $f\,(z/L)$. In our research we use the most common shape with two coefficients. As a consequence of using two coefficients, the data is within two regimes: the near-neutral range (described with c_1) and the free-convection range (described with d), and the transition between these two regimes is described with just one value ($1/c_2$, see also Section 3.1). However, from the results for the eight $-1/L$ classes it seems that three regimes exist (near-neutral range, transition range, and a free-convection range), which indicates that the function with two coefficients is probably not sufficiently flexible to describe $f\,(z/L)$. For turbulent quantities other than C_T^2, Kader and Yaglom (1990) also observed that the data can be separated into three regimes: the dynamic regime ($-z/L < 0.04$), the dynamic-convective regime ($0.12 < -z/L < 1.2$), and the free-convective regime ($-z/L > 5$). Notice that, because their regimes do not cover the full stability range, and Kader and Yaglom (1990) searched separate equations for the three regimes, their solution is not a practical one. Another possible solution would be to use a function with more coefficients as introduced by Wesely (1976b); Thiermann and Grassl (1992), it is however not a priori clear if each coefficient is sensitive to one particular stability regime.

The division of the dataset in z classes shows a height dependence. Here we discuss two issues related to this. First, the observation of a height dependence of MOST relations could be related to flux divergence. Under unstable conditions the flux decrease with height. Therefore, one could argue that when analysing elevated levels it is better to use the fluxes observed at that level (local level fluxes) than those observed at the surface, as was suggested for the stable boundary layer by Nieuwstadt (1984). Using local level fluxes, which are smaller than the surface fluxes, will give larger values of $\widetilde{C_T^2}$ at a certain $-z/L$ (Fig. 6 of Braam et al. 2012). This in turn would yield a increase in d and a corresponding decrease in c_2. As the data for larger z already show relatively large d and small c_2, the use of local fluxes would enhance this pattern rather than

diminish it.

Second, the height dependence can be related to the fact that the size of the footprint of the observations increases with the observation height. If sampling another footprint would be the reason for the observed decrease of c_2 and increase of d, the surface flux would have to increase with increasing distance to the tower on average. This is not likely, because, the surface around the tower is relatively homogeneous.

3.7. Conclusions

In literature different values of the coefficients (c_1 and c_2) are reported for the most common shape of Monin-Obukhov similarity relations for the structure parameter of temperature C_T^2 ($f\left(z/L\right) = c_1\left(1 - c_2 z/L\right)^{-2/3}$). These coefficients were empirically obtained by applying various regression approaches to datasets with different characteristics (e.g. stability in terms of $-1/L$ and the measurement height z). Here we investigate the impact on the numerical value of the regression coefficients of applying different regression approaches and using data from different heights and within different stability ranges. By doing this for one dataset we can exclude causes of variations due to differences in the data processing, instrumentation and the surface characteristics.

From the comparison of different regression approaches, we conclude the following:

1. Applying different regression approaches has an impact on the regression coefficients c_1 and c_2. The range of c_1 and c_2 among the approaches is large, and the differences are statistically significant. However, variations in the coefficient of the free convection limit (d) are small. Therefore, differences in c_1 and c_2 are mainly related to data in the near-neutral range. In turn, as under near-neutral conditions the sensible heat flux is relatively small, the effect of the different approaches on the sensible heat fluxes is small. When presenting similarity relations it is important to specify the regression approach used in the determination.
2. We suggest to use an orthogonal distance regression method (ODR) such that uncertainties in $-z/L$ are also taken into account, where both dimensionless groups ($\widetilde{C_T^2}$ and $-z/L$) are logarithmically transformed (loglog), the data are weighted such that unreliable data points have a smaller influence on the fit ('weight'), and both coefficients are fitted ('unfixed') simultaneously.

From the division of the dataset into eight $-1/L$ classes and into eight z classes, we obtained different coefficients for each class, therefore we conclude the following:

1. Measuring at different heights, and within different stability ranges can have an impact on the regression coefficients c_1 and c_2. The variations in the coefficients as given in literature, can thus be an effect of variations in the height and stability range between datasets (see Table 3.1). Moreover, new presented coefficients measured at another z or within a different $-1/L$ range will likely differ from previously observed regression coefficients.
2. One should thus be careful with applying the coefficients to z ranges or $-1/L$ ranges different from the dataset for which they were derived. Even if the $-z/L$

range corresponds, it does not guarantee that the coefficients are correct when z or the $-1/L$ range are very different.

3. The observed variation in the coefficients within one dataset is an first indication that the most common shape with two coefficients is not sufficiently flexible to describe $f(z/L)$. However, it is not advisable to simply use a shape with more coefficients, because we found from the comparison of the different regression approaches that it is already difficult to fit two coefficients simultaneously.
4. The $-z/L$ range has to be large enough and has to cover both near-neutral and free convection data to allow for a reliable estimation of the regression coefficients.

Acknowledgements

We thank the CASES-99 community for having their data freely accessible. Further, we thank Huug Ouwersloot and Oscar Hartogensis for the discussions, Bram van Kesteren for reading and commenting on the manuscript. Moreover, we thank the anonymous reviewers and Thomas Foken for their comments. Especially, the remarks of Thomas Fokens leading to a more accurate historical overview about similarity theory were very helpful. The research has been supported financially by the German Research Foundation (DFG) in the framework of the project: 'Turbulent Structure Parameters over Heterogeneous Terrain - Implications for the Interpretation of Scintillometer Data' (through grant BE2044/3-3) and by the Meteorology and Air Quality group of Wageningen University.

4 Variability of the structure parameters of temperature and humidity observed in the atmospheric surface layer under unstable conditions

4.1. Introduction

During recent years, scintillometers have been proven to be reliable instruments for determining the path-averaged sensible and latent heat fluxes over different terrain and surface types (e.g. Green et al., 2001; Meijninger et al., 2002b, 2006; Evans et al., 2012). A scintillometer system consists of an electromagnetic beam transmitter at one end and a receiver at the other end of a path. The received electromagnetic signal varies in intensity due to fluctuations in the refractive index of air (scintillations) caused by turbulent eddies along the propagation path. The variance of these fluctuations is proportional to the path-averaged structure parameter of the refractive index of air (C_n^2), which is the basic atmospheric parameter derived from scintillometer data. From C_n^2 the structure parameter of temperature (C_T^2), humidity (C_q^2) and the cross-structure parameter of temperature and humidity (C_{Tq}) can be obtained (provided multiple scintillometers or additional meteorological observations are available, e.g. Hill et al., 1992; Moene, 2003). C_s^2 and C_q^2 are measures of the turbulent fluctuations in temperature and humidity and can be used to calculate path-averaged surface sensible and latent heat fluxes using Monin-Obukhov similarity theory (MOST) (Monin and Obukhov, 1954; Wyngaard, 1973; Hill et al., 1992, inter alia). Scintillometers operating at optical wavelengths (e.g. in the near-infrared) are basically sensitive to temperature fluctuations, while for scintillometers operating at microwave wavelengths the contributions of temperature and humidity fluctuations are equally important. Thus an optical scintillometer can be used to derive the sensible heat flux, while a combination of an optical and a microwave scintillometer is necessary to derive both the sensible and latent heat

This chapter is published as Braam M, Moene AF, Beyrich F (2014) Variability of the structure parameters of temperature and humidity observed in the atmospheric surface layer under unstable conditions. Boundary-Layer Meteorol 150:339-422

fluxes.

The scalar structure parameter (now denoted as C_s^2 for a generic scalar s) is a measure of the magnitude of fluctuations in space or time of a turbulent quantity s within the inertial subrange of turbulence. C_s^2 has a log-normal distribution in time and space (Kolmogorov, 1962). From sodar and large-eddy simulation (LES) data, Petenko and Shurygin (1999), Cheinet and Siebesma (2009), and Cheinet and Cumin (2011) (hereafter denoted as PS99, CS09 and CC11, respectively) found a large width of the probability density function (PDF) of $\log(C_s^2)$, which indicates a variability of C_s^2 over several orders of magnitude. Furthermore, they found a bimodal distribution of $\log(C_s^2)$, which is caused by differences in C_s^2 between upward and downward motions.

In PS99, CS09 and CC11, the variability of C_s^2 is described for heights of several decametres above the ground at one point (in the case of the sodar) or above a homogeneous surface and one specific surface forcing (in the case of LES). Both approaches characterize the local variability of C_s^2 of a turbulent field. If, however, C_s^2 is measured along a path over a heterogeneous surface, the averaged C_s^2 may vary in time due to the local variability at each point along the path, but may vary in addition due to surface heterogeneity (i.e. differences in the surface sensible and latent heat fluxes between patches of different surface characteristics). The variability due to surface heterogeneity, in contrast to the local variability, would be relatively constant in time and about zero above a single patch. The separation of these two effects is still an open research question relevant for scintillometry. In order to describe the relation between heterogeneous surface fluxes and the (path-averaged) scintillometer signal, a better understanding of the different types of variability in C_s^2 along the path is needed. To identify the variability in C_s^2 related to heterogeneity, one needs to know and reduce the influence of the local variability. One way to achieve this could be averaging. For example, van den Kroonenberg et al. (2012) used repeated flights over the same path for this purpose, and in this way they identified patterns in C_s^2 that were more or less constant in time. Another way to decompose the effect of the local variability and the variability caused by surface heterogeneity on the path-averaged C_s^2 could be to determine the local variability of C_s^2 over a range of conditions (height, stability etc.). This variability could then be considered as the background noise superimposed on the variability caused by surface heterogeneity. Subsequently, this measure of the local variability can be used to assess whether observed spatial differences in C_s^2 along a path can be attributed to surface heterogeneity or have to be considered to lie within the range of local variability.

The aim of this study is thus to quantify the local variability of C_s^2 at a given point for a range of heights and stabilities. For this, we use eddy-covariance (EC) measurements obtained at three heights in the atmospheric surface layer (ASL) during the LITFASS-2009 experiment (Beyrich et al., 2012). The analysis is restricted to unstable conditions. There are two reasons to use EC measurements to investigate the local variability of C_s^2: first, the use of EC measurements instead of sodars (PS99) or LES (CS09 and

CC11) has the advantage of covering the lowest part of the ASL. Second, the use of EC measurements instead of LES has the advantage that EC measurements are direct observations rather than model simulations, obtained during different atmospheric conditions rather than representing a single, ideal situation. By using one month of observations it is possible to describe the variability over a range of different stability classes (representing different weather conditions). To the authors' knowledge it is the first time that the variability of C_s^2 is evaluated from EC measurements obtained over a long period (one month) at different heights in the ASL.

In order to identify the behaviour of C_s^2 in general, and to quantify the variability of $\log(C_s^2)$, we investigate the mean, the probability density function and the variances of $\log(C_s^2)$ in the ASL, and answer the following two research questions:

- What is the shape of the probability density function of $\log(C_s^2)$ at several heights in the ASL?
- What determines the variance of $\log(C_s^2)$ at these heights?

4.2. Theory

4.2.1. Definition of the structure parameter

The scalar (subscript s) structure parameter is defined within the inertial subrange as (Stull, 1988; Bosveld, 1999),

$$C_s^2 = \frac{D_{ss,x}(r)}{r^{\frac{2}{3}}} = \frac{\langle [s(x+r) - s(x)]^2 \rangle}{r^{\frac{2}{3}}} \tag{4.1}$$

in which $D_{ss,x}$ is the spatial (x) structure function, $s(x)$ and $s(x+r)$ are scalar observations at locations x and $x+r$, r is the spatial separation, and the angle brackets indicate spatial averaging over x. The distance over which the averaging takes place is one of the topics discussed herein, later referred to as 'window size'.

4.2.2. Mean structure parameter

The behaviour of the mean C_s^2 in the ASL under unstable conditions is discussed for temperature by e.g. Wyngaard (1973); Andreas (1988); Hill et al. (1992) and Li et al. (2012), and for humidity by Li et al. (2012). The dependence of the mean C_s^2 on height and instability within the ASL is described using Monin-Obukhov similarity theory (MOST) scaling, which is valid under stationary conditions and over horizontally homogeneous surface. Using MOST C_s^2 can be made dimensionless, and the scaled structure parameter is denoted as $\widetilde{C_s^2}$,

$$\widetilde{C_s^2} = \frac{C_s^2 z^{2/3}}{s_*^2} = f_s\left(\frac{z}{L}\right) = c_{s1}(1 - c_{s2} z/L)^{-2/3} \tag{4.2}$$

with the observation height z, the Obukhov length $L = \overline{T_v} u_*^2/(\kappa g T_{v*})$, the scalar scale $s_* = -\overline{w's'}_0/(u_*)$ and the friction velocity $u_* = \sqrt{\tau_0/\overline{\rho}}$, in which T is the temper-

ature, T_v* is the virtual temperature scale, $\kappa = 0.4$ is the von-Kármán constant, $g = 9.81 \quad \mathrm{m\,s^{-2}}$ is the acceleration due to gravity, ρ is the air density, τ_0 is the surface shear stress, and $\overline{w's'}_0$ is the surface flux of scalar s. The overbar indicates time averaging. The right-hand side of Eq. 4.2 is the most commonly used expression for $f\,(z/L)$ for unstable conditions. Several values for the empirical constants (c_{s1} and c_{s2}) have been proposed in the literature, and in this study we use the set of Andreas (1988) with $c_{s1} = 4.9$ and $c_{s2} = 6.1$, who modified the original MOST relation of Wyngaard (1973) by replacing $\kappa = 0.35$ by $\kappa = 0.40$. The similarity relation in Eq. 4.2 shows that the mean $\widetilde{C_s^2}$ decreases with height and instability in terms of $-z/L$; the decrease of the mean $\widetilde{C_s^2}$ with height is non-linear. It is larger close to the surface than at larger heights in the ASL; for free convection conditions the decrease of C_s^2 is $\sim z^{-4/3}$.

4.2.3. Variability of the structure parameter

Although the mean C_s^2 has been studied extensively, less is known about the variability of C_s^2. Kolmogorov (1962) assumed that C_s^2 has a log-normal distribution. A property of a log-normally distributed random variable is that the standard deviation is proportional to the mean (Wilks, 2006), and is the main reason to study the variability of the logarithm of the structure parameter ($\log(C_s^2)$) rather than that of C_s^2. Furthermore, PS99, CS09 and CC11 also focussed their analysis on $\log(C_s^2)$; their results already provide two insights into the shape of the PDFs of $\log(C_s^2)$ and so into the variability of the structure parameter.

Insight 1: Deviation from a log-normal distribution

The PDFs of $\log(C_s^2)$ deviate from the normal distribution under some circumstances and this deviation varies with height. The PDF is flatter than that of a normal distribution or even bimodal, due to differences in C_s^2 between upward and downward motions. PS99 suggest that the PDFs of $\log(C_s^2)$ of the upward and downward motions separately are log normal leading to a total PDF that is flatter or bimodal.

In upward motions (air from a lower level) C_s^2 is larger than in the downward motions (air from a higher level), because the mean C_s^2 decreases with height (Sect. 4.2.2). Differences in C_s^2 between upward and downward motions increase with increasing height (sketch in the left panel of Fig. 4.1 and the right lowest two panels of Fig. 5 of CS09).

This can be understood by considering and combining two concepts:

- The decrease of C_s^2 with height is larger at lower levels (Sect. 4.2.2). Consequently, C_s^2 in air from a lower level (upward motions) differs more from the C_s^2 at the observation level than for air from a higher level (downward motions).
- The distance over which the air is transported (δz) increases with height and instability (Moene and Schüttemeyer, 2008).

Both concepts combined explain that the differences in C_s^2 between upward and downward motions are larger at higher levels than at lower levels. Note that this model does not take into account differences in δz for upward motion and downward motion.

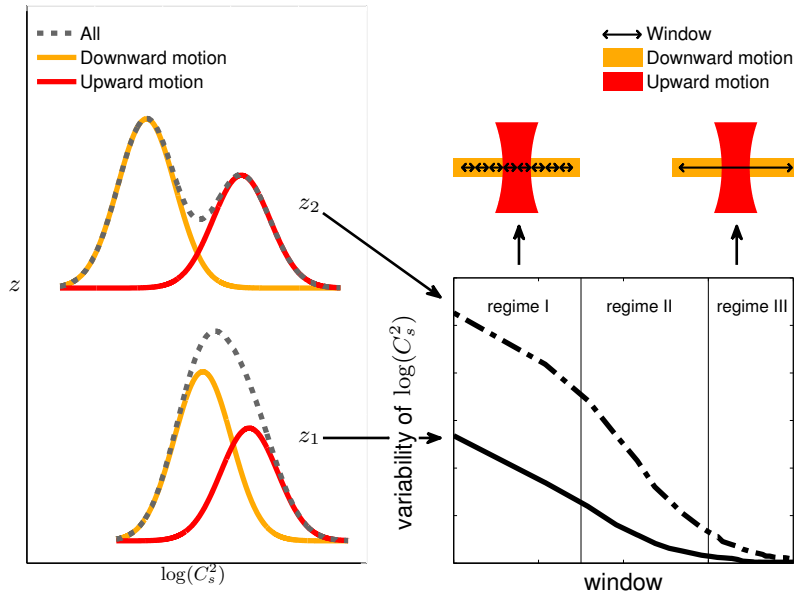

Fig. 4.1. *Left panel*: sketch of the PDFs of $\log(C_s^2)$ at two heights, z_1 near the surface and z_2 at a larger height in the ASL (total: grey dashed, upward motions: red, and downward motions: orange). *Right bottom panel*: the variability of $\log(C_s^2)$ versus the window size for the two heights (z_1: solid, z_2: dash-dotted) separated into three regimes (based on Fig. 8 of CS09). *Right upper panel* a sketch of the window size (indicated with $\leftrightarrow$) within the atmosphere with upward motions in red and downward motions in orange for regime I and regime III. Regime II can be seen as the transition regime. *Left sketch*: one window ($\leftrightarrow$) covers either a part of the upward motions or a part of the downward motions (regime I); *right sketch*: the window ($\leftrightarrow$) covers the entire domain including both upward and downward motions (regime III).

For the two lowest levels used in CS09 (80 m and 310 m), δz can be estimated as 56 m at $z = 80$ m and 270 m at $z = 310$ m (using the similarity functions for the variance of de Bruin et al. (1993) and the similarity functions for the mean gradient of Businger et al. (1971) with $L = -15.3$ m). The differences in $\log(C_T^2)$ between the upward and downward motions can be estimated as 1.0 at $z = 80$ m and as 1.5 at $z = 310$ m ($\log(C_T^2)_{+\delta z} - \log(C_T^2)_{-\delta z} = -\frac{2}{3}\log\left([z_{+\delta z} - c_{s2}z_{+\delta z}^2/L]/[z_{-\delta z} - c_{s2}z_{-\delta z}^2/L]\right)$). The increase of differences in C_s^2 between upward and downward motions with height causes the width of the total PDF, and hence the variance, to increase (Fig. 2 in CS09 and Fig. 1 in CC11).

In conclusion, if the total PDFs of $\log(C_s^2)$ deviate from a log-normal distribution and are flatter or even bimodal, this can be explained by the contrast in C_s^2 between upward and downward motions.

Insight 2: Variation of variability with averaging window size

The variability of C_s^2 depends on the averaging window size (the spatial averaging in Eq. 4.1). The variability of C_s^2 decreases if the averaging window size increases, because an increasing part of the variability is averaged out. CS09 showed the effect of the averaging window size on the variability of C_s^2 for a horizontal slab of a LES run (their Fig. 8 and the lower right panel of our Fig. 4.1). They found that the rate of decrease

of variance with window size is height-dependent and can be split into three regimes. The variation of that dependence with height can be explained by differences between upward and downward motions (see also the text on p 1011 of CS09).

In regime I, where the window size is small, the rate of decrease of the variance with window size ('slope') is moderate and similar for each height. The window covers either a part of the upward motion or a part of the downward motion (left sketch in the upper right panel of Fig. 4.1). Hence, the variance is mainly due to the contrast in C_s^2 between upward motion and downward motion. The variability of C_s^2 for the smallest window (the 'offset') increases with height, because differences in C_s^2 between upward and downward motions increase with height. In regime II (transition regime), where the window covers parts of both the upward and the downward motions, the slope is enhanced, because differences between upward and downward motions are mixed in the averaging process and variability is lost with increasing window size. In regime III, where the window covers almost the entire LES domain (right sketch in the upper right panel of Fig. 4.1), the slope is moderate again and the variances reach an asymptotic value of zero. Because, the offset of regime I increases with height the slopes in regime II and III increase with height as well.

4.3. Data and Research Strategy

4.3.1. The LITFASS-2009 experiment

The data used in this study have been collected during the LITFASS-2009 experiment in the area around the Meteorological Observatory Lindenberg - Richard-Aßmann-Observatory (MOL-RAO) of the Deutscher Wetterdienst (DWD, German Meteorological Service), about 60 km south-east of Berlin. One main objective of LITFASS-2009 was to better understand the influence of a heterogeneous surface along a scintillometer path on the scintillometer signal. During the experiment several measurement techniques were employed, e.g. eddy covariance, unmanned aircraft and scintillometers. For a detailed description of the experimental set-up and the instrumentation see Beyrich et al. (2012). The surface in the study area is moderately heterogeneous with a mixture of farmland patches, forest, small lakes and small villages (Fig. 1 in Beyrich et al., 2012). The patches mainly consists of maize, sunflowers, colza, barley and triticale, with the typical dimension of the patches varying between 300 m and 1000 m.

Here, we used observations from three EC systems at effective heights of 2.5 m, 50 m, and 90 m. The effective height was calculated as $z_{\mathrm{eff}} = z_{\mathrm{m}} - d$, in which z_{m} is the observation height, and d is the zero-plane displacement estimated as 2/3 of the vegetation height. At each height the instrumentation consisted of a combination of a sonic anemometer/thermometer (sonic) and an infrared hygrometer (LiCor), see Table 4.1. The 2.5-m observations were performed above triticale. The 50-m and 90-m observations were obtained above grass, from the 99-m tower located at GM Falkenberg (where GM stands for Grenzschichtmessfeld, the German translation of boundary-layer

Table 4.1. Characteristics of the three EC systems. l_{p} is the path length, z_{eff} ($= z_{\mathrm{m}} - d$) is the effective height

	triticale	tower 50 m	tower 90 m
Sonic	CSAT-3	USA-1	USA-1
	Campbell Sci., UK	METEK GmbH, Germany	METEK GmbH, Germany
$l_{\mathrm{p\,Sonic}}$ (m)	0.116	0.18	0.18
Hygrometer	LI7500	LI7500	LI7500
	LiCor Inc., U.S.	LiCor Inc., U.S.	LiCor Inc., U.S.
$l_{\mathrm{p\,LiCor}}$ (m)	0.125	0.125	0.125
z_{eff} (m)	2.5	50	90
boom orientation	160°	190°	190°

field site). Furthermore, we used data from the standard operational measurement systems at MOL-RAO:

- pressure, measured at 1 m (PTB220, Vaisala Oy, Finland). The pressure at 50 m and 90 m was estimated by assuming a linear decrease of 12.5 Pa m^{-1},
- precipitation, measured with a weighing precipitation gauge (Pluvio, Ott GmbH, Germany),
- temperature and humidity profiles, measured on a 10-m tower (at 0.5, 1, 2, 4 m) and the 99-m tower (at 10, 20, 40, 60, 80 m, HMP245, Vaisala Oy, Finland)
- boundary-layer depth, deduced from simultaneous sodar/RASS (DSDPA 90-64/ MERASS, METEK GmbH, Germany), windprofiler/RASS (TWP16000, Radian Cop, USA) and ceilometer (CHM 15k Jenoptik GmbH, Germany) measurements.

Data were collected from 26 June to 22 July 2009 (day of the year, DOY: 177-203), a period when the meteorological conditions were not very favourable to study surface-layer turbulent processes. The first three days were completely overcast, whereas the other days were intermittently cloudy; rain showers in the morning or afternoon hours occurred during 14 of the 27 days. The noontime Bowen ratio (the sensible heat flux divided by the latent heat flux) for the different surfaces was relatively constant during the experiment: around 1.2 over the forest, smaller than 0.5 for maize and grass, around 0.6 for colza, around 3 for barley, and between 1 (start of experiment) and 2 (end of experiment) for triticale. Except for the forest, these values can be found in the lower panel of Fig. 3 in Beyrich et al. (2012).

Section 4.3.2 describes the methods used to determine the input data for the subsequent analysis: scalar structure parameter (4.3.2) and the surface fluxes (4.3.2). In Sect. 4.3.3 the logic of the actual analysis is given. The text is supported by Fig. 4.2 giving an overview of the different steps of the analysis.

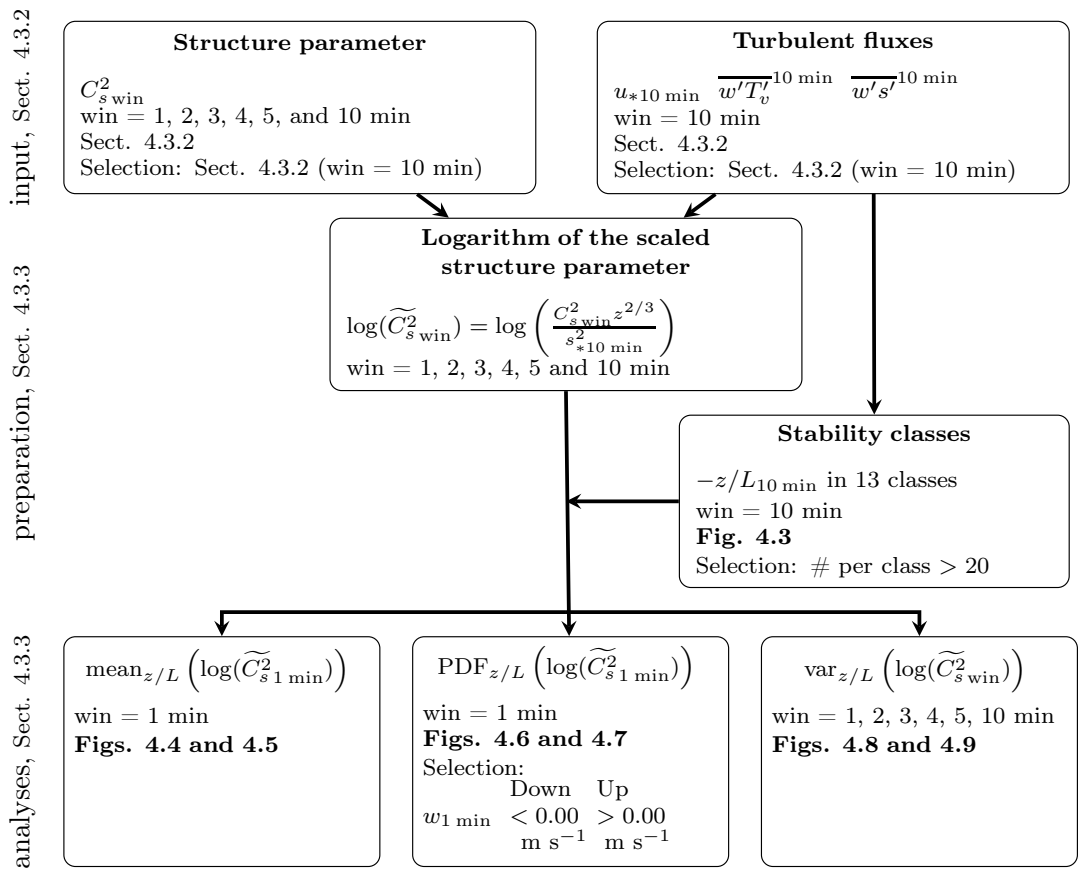

Fig. 4.2. Overview diagram of the research strategy and the analysis. *First row*: determination of the input dataset.*Second two blocks*: the further preparation of our dataset. *Last row*: the three variables that are analyzed in this paper. The lines in the blocks are structured as follows: first line: the variable, second line: the temporal averaging window size (abbreviated as 'win'), third line: the text section where the calculation method or the figures showing the results are given, last line: the selection criteria.

4.3.2. Data preprocessing

The first step in the data processing was the preparation of an input dataset for the subsequent analysis (row 1 in Fig. 4.2). This dataset consists of the scalar structure parameters for different window sizes and the turbulent fluxes averaged over 10 min. Details of the calculations are given in Sect. 4.3.2 for C_s^2 and in Sect. 4.3.2 for the turbulent fluxes.

The scalar structure parameter

Before calculating C_s^2 (left block of row 1 in Fig. 4.2) the raw 20 Hz data from the EC systems were checked and converted to physical values. Using a block length of 1200 data points, data were checked for unphysical values[1], spikes, and insufficient amplitude resolution based on Vickers and Mahrt (1997). The spikes and the data beyond physical

[1] Values that are specified as unphysical are outside the following ranges: the vertical wind speed (w): [−10, 10] m s^{-1}, the components of the horizontal wind vector (u and v): [−40, 40] m s^{-1}, the temperature signal of the sonic (T_{sonic}): [240,320] K and the humidity signal of the LiCor (ρ_v): [0, 0.025] kg m^{-3}

limits were excluded. From the amplitude resolution check we found that the PDFs of the sonic temperature of the USA-1 have more gaps than those of the CSAT-3. This is due to a combination of a higher resolution of the CSAT-3 (theoretically: 0.001 K for the CSAT-3 and 0.01 K for the USA-1) and the internal crosswind correction in the CSAT-3 (personal communication: Ulrich Weisensee, MOL-RAO, 2012). The spectra of the USA-1 do not, therefore, have a well-defined inertial subrange at small amplitudes or high frequencies.

We applied two conversions to the raw data. First, the temperature signal of the sonic and the humidity signal of the LiCor were iteratively converted to air temperature and absolute humidity (Schotanus et al., 1983; Liu et al., 2001). We applied the crosswind part of Eq. 3 of Liu et al. (2001) for the USA-1 only, because for the CSAT-3 it is already applied internally. Second, the wind components of the sonic were rotated using the planar fit method (Wilczak et al., 2001) and the coordinate system was rotated such that the x-axis is along the mean horizontal wind. The planar fit angles were calculated with EC-Pack version 2.5.23 (van Dijk et al., 2004) over the entire experiment (Sect. 4.3.2).

We calculated C_s^2 via the structure function (Eq. 4.1) that is more robust than the spectrum method (Hartogensis, 2006) for the small window sizes that were needed to determine the variability of C_s^2. Furthermore, the structure function can still be used when the dataset has gaps, whereas for the calculation of spectra a continuous data series is needed.

From EC observations only the temporal structure function ($D_{ss,t}$) can be derived,

$$D_{ss,t,\,\mathrm{win}}(\tau) = \overline{[s(t+\tau) - s(t)]^2}^{\mathrm{win_t}} \tag{4.3}$$

in which the subscript t indicates the temporal structure function, $s(t)$ and $s(t+\tau)$ are scalar observations at times t and $t+\tau$, and τ is the temporal separation with $\overline{U}$ being the mean horizontal wind speed. The overbar indicates time averaging and $\mathrm{win_t}$ the temporal window size over which the averaging is performed. We calculated C_s^2 over six window sizes varying from 1 to 10 min (win = 1, 2, 3, 4, 5, and 10 min). The conversion of $D_{ss,t}$ to $D_{ss,x}$ was done using Eq. 5 from Braam et al. (2012) following Bosveld (1999). $C^2_{s\,\mathrm{win}}$ was calculated as the mean of $D_{ss,x,\,\mathrm{win}}\ r^{-2/3}$ over a range of fixed spatial separations within the inertial subrange: $2l_\mathrm{p} < r < \kappa z_\mathrm{eff} = 0.4 z_\mathrm{eff}$ (where $2l_\mathrm{p}$ is the path length of the instrument, and the spatial separation was linked to the temporal separation as $\tau = r/\overline{U}$). Here $2l_\mathrm{p}$ is the smallest size of eddies that can be properly resolved, and κz is a measure for the neutral mixing length (Moene and Schüttemeyer, 2008); κz can be interpreted as a measure of the size of the largest eddies and hence of the scale of the production range of turbulence under neutral conditions. For unstable conditions the limit of κz is a conservative estimate for the border of the inertial subrange as can be diagnosed from the spectra of Kaimal et al. (1972, in which the inertial subrange starts at a normalized frequency of $\approx$ 1, which corresponds to a wavelength of z). The use of a range of fixed separations implies the range of time lags

to vary in time with wind speed $\overline{U}$ ($2l_\mathrm{p}/\overline{U} < \tau < \kappa z_\mathrm{eff}/\overline{U}$).

The amplitude resolution problem of the USA-1 caused the structure function to be not well-defined at small separations (that is, high frequencies). In order to ensure that our calculations were performed for a well-defined inertial subrange, we decided to increase the lower separation limit to a value of 5 m instead of $2l_\mathrm{p}$ for the USA-1 data measured at $z = 50$ m and 90 m. This decision was based on plots of $D_{TT,s}$ versus r for a series of typical situations. These plots showed a slope reasonably close to $-2/3$ for separations larger than 5 m.

A disadvantage of using EC data to determine the structure parameter is that fluctuations smaller than the path length of the sonic or LiCor instruments (Table 4.1) are not taken into account. To correct for these losses, the correction of Hartogensis et al. (2002) for the deviation of the measured spectrum from the inertial subrange was applied on Eq. 4.3.

Turbulent fluxes

As stated before, the turbulent fluxes were calculated over a 10-min averaging window. This choice was a compromise between the request to be as close as possible to the averaging window size used for calculating C_s^2 and the generally accepted lower limit for flux calculation using the EC method (Lee et al., 2004).

Turbulent fluxes (right block of row 1 of Fig. 4.2) and the corresponding tolerances were calculated with the EC-Pack flux-software package (version 2.5.23) developed by Wageningen University (van Dijk et al., 2004). The following corrections were applied: a) planar fit rotation (Wilczak et al., 2001); b) correction for density effects on the latent heat flux (Webb et al., 1980); c) humidity correction (Schotanus et al., 1983; Liu et al., 2001) for the sonic temperature; d) cross-wind correction (Schotanus et al., 1983; Liu et al., 2001) for the sonic temperature measured with the USA-1, and e) corrections for spectral loss due to path averaging and sensor separation (Moore, 1986).

MOST scaling is based on the turbulent fluxes measured near the surface. For the measurements at the tower, we did not use local surface fluxes obtained at the tower site (grass) but regional scale surface flux estimates. The reason for this is that the footprint at $z = 50$ m and 90 m covered more land-use types than simply grass, and the Bowen ratio differed between the different fields around the tower (see Sect 4.3.1). The regional surface fluxes were derived (for $z = 50$ m and 90 m separately) from the observed flux at the respective observation level corrected for the flux divergence. This correction was obtained by assuming that the time rate of change of temperature and of humidity along the tower was only determined by flux divergence, and that other processes (e.g. horizontal advection) could be neglected.

Data Selection

In order to focus on well-defined atmospheric conditions, we finally applied a filter on the dataset and selected only 10-min blocks for which:

- the ASL was unstably stratified ($-z/L > 0.001$);
- there was no rain;
- there was no flow obstruction caused by the tower. Wind directions for a sector of $\pm 45°$ around the tower orientation were filtered out (tower orientation = boom orientation $+180°$);
- the relative tolerance of $\overline{w'T'}$, u_* (in both the temperature and humidity analysis), and $\overline{w'q'}$ (in the humidity analysis only) was < 0.3, in order to exclude intervals when the fluxes were not well-defined;
- z_{eff} was located within the ASL. As a rough criterion for the latter condition, we required the measurement levels to be below 10% of the actual boundary-layer depth (Braam et al., 2012). We thus excluded the periods when the ABL depth was lower than 500 m for the 50-m level and lower than 900 m for the 90-m level. The ABL depth was estimated from the height of elevated maxima in the sodar/windprofiler backscatter intensity, and in the aerosol backscatter gradients in case of the ceilometer data.

4.3.3. Data Analysis

To investigate the variability of C_s^2, we calculated C_s^2 using averaging over six window sizes, ranging from 1 to 10 min. When the statistical properties of $\log(\widetilde{C_{s\,\text{win}}^2})$ are then evaluated over a given time period, e.g., 1 hr, this would correspond to a dataset of between 60 points (for the window size of 1 min) and 6 points (for the window size of 10 min). This would not be very robust statistically. We therefore used a different approach and calculated the statistics over stability ($-z/L$) classes rather than over given time periods. Statistics over a stability class can be considered as proxies of ensemble statistics, representing comparable atmospheric conditions within one class. The preparation of the stability classes and the scaled structure parameters is discussed in Sect. 4.3.3, whereas the methodology of the analysis of the statistics of the structure parameters is discussed in Sect. 4.3.3.

Preparation

The second step in the data processing was to calculate both the logarithm of the scaled structure parameter and $-z/L_{10\,\text{min}}$, and to split the dataset into stability classes (centre two blocks in Fig. 4.2). The logarithm of the scaled structure parameter (centre block in Fig. 4.2) was calculated in two phases: first, we calculated $\widetilde{C_{s\,\text{win}}^2}$ from C_s^2 for each of the six window sizes and scaled it with the corresponding 10-min averaged surface fluxes (see sect 4.3.2). Thus, structure parameters determined over windows shorter than 10 min have been scaled with the corresponding 10-min averaged surface flux. Second, we calculated the decadic logarithm of the scaled structure parameter ($\log(\widetilde{C_{s\,\text{win}}^2})$). We used the logarithm with base ten to retain clear information on the order of magnitude of the original data.

The stability ($-z/L_{10\,\text{min}}$) was calculated using the 10-min averaged surface flux

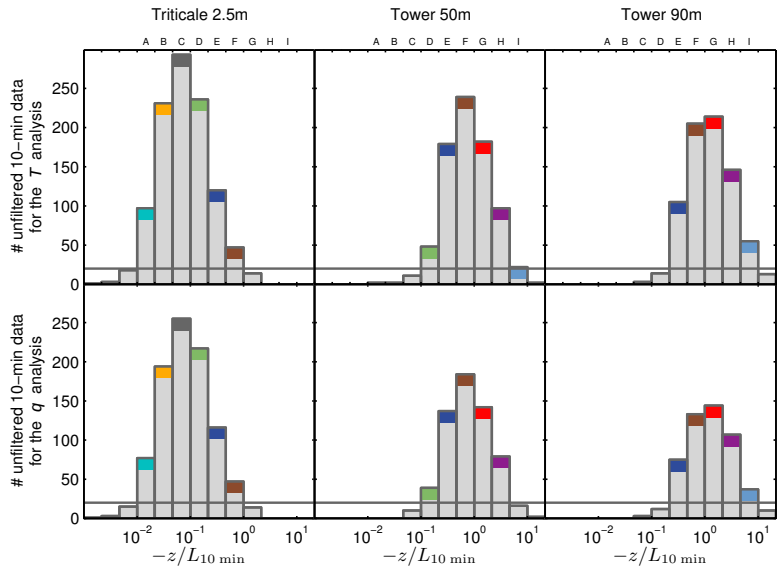

Fig. 4.3. Frequency distribution of the unfiltered 10-min data per stability class for the temperature (top) and humidity (bottom) analyses for the three heights (left: triticale $z = 2.5$ m, centre: tower $z = 50$ m, and right: tower $z = 90$ m). Only the stability classes with more than 20 data points (solid line) are further evaluated, these are indicated with the coloured top. Each colour represents a different stability class, those will be used in Fig. 4.4 through Fig. 4.9 as well.

data (see Sect. 4.3.2); then the dataset was split into classes, where we specified three stability classes per decade. The total dataset encompassed 13 classes, where the first class started with $-z/L_{10\,\mathrm{min}} = 10^{-8/3}$ and the last class ended at $-z/L_{10\,\mathrm{min}} = 10^{4/3}$.

Figure 4.3 shows the number of available 10-min periods per stability class for the three heights and for the two scalars considered. Note that the only difference in available time periods between the temperature and humidity analysis is that for humidity the relative tolerance of the humidity flux has to be < 0.3 as well (see Sect. 4.3.2). In order to have sufficient data per stability class, we only analyzed the classes with more than 20 10-min periods (marked with colours in Fig. 4.3). Each class, consequently, consists of more than 200 1-min periods and more than 20 10-min periods. With this criterion five to six stability classes remained for each height. For each level at least three stability classes contained more than 100 10-min periods.

Analysis

After determining $\log(\widetilde{C_s^2})$ and separating the data in the corresponding stability classes, we performed the analysis of the data in three different ways (Fig. 4.2, lower row). First, we analyzed $\log(\widetilde{C_{s\,1\,\mathrm{min}}^2})$ versus $-z/L_{10\,\mathrm{min}}$ for the three heights and for the two scalars (Fig. 4.2, lower row, left block). The focus was on the class-mean scaled structure parameter $(\mathrm{mean}_{z/L}\left(\log(\widetilde{C_{s\,1\,\mathrm{min}}^2})\right))$, because this gave the possibility of investigating whether the structure parameter calculated over the short 1-min window gives reasonable values (that is, comparable to published stability dependences).

Second, we analyzed the shape of the PDFs of C_s^2 and C_q^2 in the ASL (Fig. 4.2, lower row, centre block), by answering the following two questions: does the shape (width, skewness and kurtosis) of the PDF depend on the scalar (T or q), height (z is 2.5 m, 50 m or 90 m) and instability ($-z/L_{10\,\mathrm{min}}$ class), and does the bimodal shape of the PDF observed by PS99, CS09 and CC11 also exist close to the ground? To this end, we examined the PDFs of $\log(\widetilde{C_s^2}_{1\,\mathrm{min}})$ per stability class ($\mathrm{PDF}_{z/L}\left(\log(\widetilde{C_s^2}_{1\,\mathrm{min}})\right)$) for T and q at the three heights. Note that, since we had already evaluated $\mathrm{mean}_{z/L}\left(\log(\widetilde{C_s^2}_{1\,\mathrm{min}})\right)$, we could focus on the shape of the PDFs only and did not have to consider the central location. In order to answer the second question, we split our data into two groups using conditional sampling: upward motions ($w_{1\,\mathrm{min}} > 0.0$) and downward motions ($w_{1\,\mathrm{min}} < 0.0$). Note that the conditional sampling is based on the 1 min mean vertical wind speed, that is, relatively large-scale rising and sinking motions. Finally, we analyzed how the variability of $\log(\widetilde{C_s^2})$ depends on the measurement height, stability and the averaging window size (Fig. 4.2, lower row, right block).

Note that within the first two steps we used only the 1-min (smallest) window size, whereas for the last step we used all six window sizes. In this study we use the logarithm of $\widetilde{C_s^2}$, therefore the statistical moments (mean, variance, kurtosis and skewness) were determined by first calculating $\log(\widetilde{C_s^2})$ of each observation and by subsequently estimating the statistical moment for each stability class. Consequently, the resulting statistics should not be interpreted as statistical properties of the structure parameter itself.

4.4. Results and Discussion

4.4.1. Stability-class mean $\log(\widetilde{C_s^2})$

We start with the analysis of the stability dependence of the logarithm of the scaled structure parameters for temperature (Fig. 4.4) and humidity (Fig. 4.5) for the three heights. The range of $\log(\widetilde{C_s^2}_{1\,\mathrm{min}})$ values is broader than observed in other studies (cf. Fig. 2 in de Bruin et al. 1993, Fig. 1 in Li et al. 2012, or Fig. 6 in Braam et al. 2012). This is a logical consequence of the fact that we used a 1-min averaging window, as opposed to typical 15-min to 30-min windows used in other studies.

As stated before, the class mean $\log(\widetilde{C_s^2}_{1\,\mathrm{min}})$ was determined by first calculating the logarithm of each observation and subsequently averaging over the stability class. We followed this procedure for consistency reasons with our analysis below where we consider the PDF and the variance of $\log(\widetilde{C_s^2})$. Moreover, this way of averaging is consistent with plotting on a logarithmic y-axis. The procedure differs from e.g. Li et al. (2012), who averaged C_s^2 instead of $\log(C_s^2)$. Applying our procedure gives a lower class mean than if averaging is done before taking the logarithm. A small underestimation, therefore, compared to the similarity relation proposed by Andreas (1988) had to be expected. Note that the difference between these two procedures increases with increasing scatter, and hence are smaller if using a 10-min window.

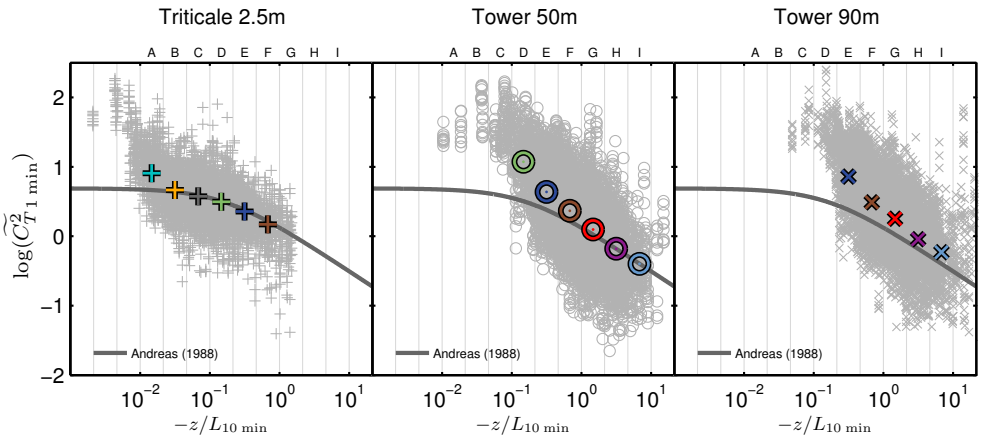

Fig. 4.4. Scatterplot of $\log(\widetilde{C}^2_{T\,1\,\mathrm{min}})$ versus stability for the three heights (left, +: triticale $z = 2.5$ m; centre, ○: tower $z = 50$ m; right, ×: tower $z = 90$ m). The points for individual 1-min intervals are plotted in light grey. The coloured symbols represent the stability-class mean values ($\mathrm{mean}_{z/L}\left(\log(\widetilde{C}^2_{T\,1\,\mathrm{min}})\right)$). The dark grey line is the similarity relation proposed by Andreas (1988).

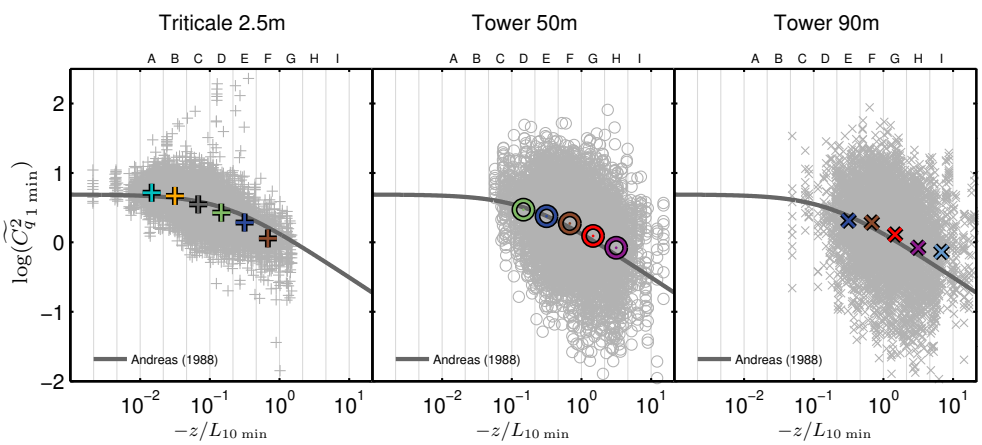

Fig. 4.5. Scatterplot of $\log(\widetilde{C}^2_{q\,1\,\mathrm{min}})$ versus stability for the three heights (left, +: triticale $z = 2.5$ m; centre, ○: tower $z = 50$ m; right, ×: tower $z = 90$ m). The points for individual 1-min intervals are plotted in light grey. The coloured symbols represent the stability-class mean values ($\mathrm{mean}_{z/L}\left(\log(\widetilde{C}^2_{q\,1\,\mathrm{min}})\right)$). The dark grey line is the similarity relation proposed by Andreas (1988).

Discussing the results in Figs. 4.4 and 4.5, we first compare the observed class mean $\log(\widetilde{C}^2_{s\,1\,\mathrm{min}})$ at $z = 2.5$ m with the similarity relation proposed by Andreas (1988). In general, the observations follow the similarity relation. For temperature, the observed class mean $\log(\widetilde{C}^2_{T1\,\mathrm{min}})$ in class A is larger than described by the similarity relation proposed by Andreas (1988). This deviation in the near-neutral range was also observed by Braam et al. (2012). For near-neutral conditions, the sensible heat fluxes are small whereas temperature fluctuations may still be finite (but uncorrelated to the vertical wind speed). This may cause an overestimation in $\log(\widetilde{C}^2_{T1\,\mathrm{min}})$ (Braam et al., 2012).

Furthermore, the relative error in the sensible heat fluxes is large, which makes the value of $\log(\widetilde{C^2_{T\,1\,\mathrm{min}}})$ more uncertain for near-neutral conditions than for unstable conditions. For humidity, the observed $\mathrm{mean}_{z/L}\left(\log(\widetilde{C^2_{q\,1\,\mathrm{min}}})\right)$ in class A is comparable to the corresponding values from the similarity relation of Andreas (1988). The reason for the difference in near-neutral behaviour for temperature and humidity can be related to the size of the sensible heat flux and moisture flux under near-neutral conditions. If the near-neutrality is caused by a small heat flux (rather than a large shear stress), the sensible heat flux is by definition close to zero, whereas the latent heat flux can still be substantial.

Second, we analyze the other two levels. In general, for both the temperature and humidity the observed $\mathrm{mean}_{z/L}\left(\log(\widetilde{C^2_{s\,1\,\mathrm{min}}})\right)$ at $z = 50$ m and at $z = 90$ m also follow the similarity relation of Andreas (1988) except for the most neutral classes. Furthermore, it seems that the $\mathrm{mean}_{z/L}\left(\log(\widetilde{C^2_{s\,1\,\mathrm{min}}})\right)$ increases with height, resulting in a small overestimation compared to the similarity relation proposed by Andreas (1988) at larger heights. One cause for this overestimation could be that the fluxes used to non-dimensionalize C_s^2 and z (via s_* and L) were too small, due to the short averaging interval of 10 min (low frequency loss). Bosveld (1999) estimated this low frequency loss due to a finite averaging time as a function of wind speed and stability. After applying his suggested correction to our dataset, we found that the $\mathrm{mean}_{z/L}\left(\log(\widetilde{C^2_{s\,1\,\mathrm{min}}})\right)$ is more comparable with the similarity relation of Andreas (1988) (figure not shown). For some data points with very low wind speeds, however, the correction causes unrealistic values, which will have an effect on $\widetilde{C^2_{s\,1\,\mathrm{min}}}$, and therefore the variability of $\log(\widetilde{C^2_{s\,1\,\mathrm{min}}})$. Becaus the focus here is on the variability rather than on the mean value, we did not correct our data for low frequency losses in the fluxes.

4.4.2. Shape of $\log(\widetilde{C_s^2})$ histograms per stability class

Analysis

Next we consider the shape and width of the PDFs of $\log(\widetilde{C^2_{s\,1\,\mathrm{min}}})$ for the different stability classes. The results are shown in Fig. 4.6 for temperature and Fig. 4.7 for humidity. First, the total PDFs (upward and downward motions together) for both $\log(\widetilde{C^2_{T\,1\,\mathrm{min}}})$ and $\log(\widetilde{C^2_{q\,1\,\mathrm{min}}})$ at different heights are discussed. At first sight, the PDFs show a distribution that does not deviate much from a log-normal distribution. In particular, we do not observe a bimodal distribution as did PS99 and CS09. The PDFs for $\log(\widetilde{C^2_{s\,1\,\mathrm{min}}})$ of the most neutral and most unstable classes contain fewer data points and are therefore less smooth. Because $\log(\widetilde{C^2_{s\,1\,\mathrm{min}}})$ decreases with instability (see also Fig. 4.4 and Fig. 4.5), the PDFs shift from right to left if instability increases. With increasing height, we observe that the width of the PDFs, which is a measure of the variability of $\log(\widetilde{C^2_{T\,1\,\mathrm{min}}})$, increases slightly for temperature. For humidity however, the PDFs observed at $z = 50$ m and at $z = 90$ m are much wider than at $z = 2.5$ m.

PDFs of $\log(\widetilde{C^2_{T\,1\,\mathrm{min}}})$ that deviate from the normal distribution can be a first in-

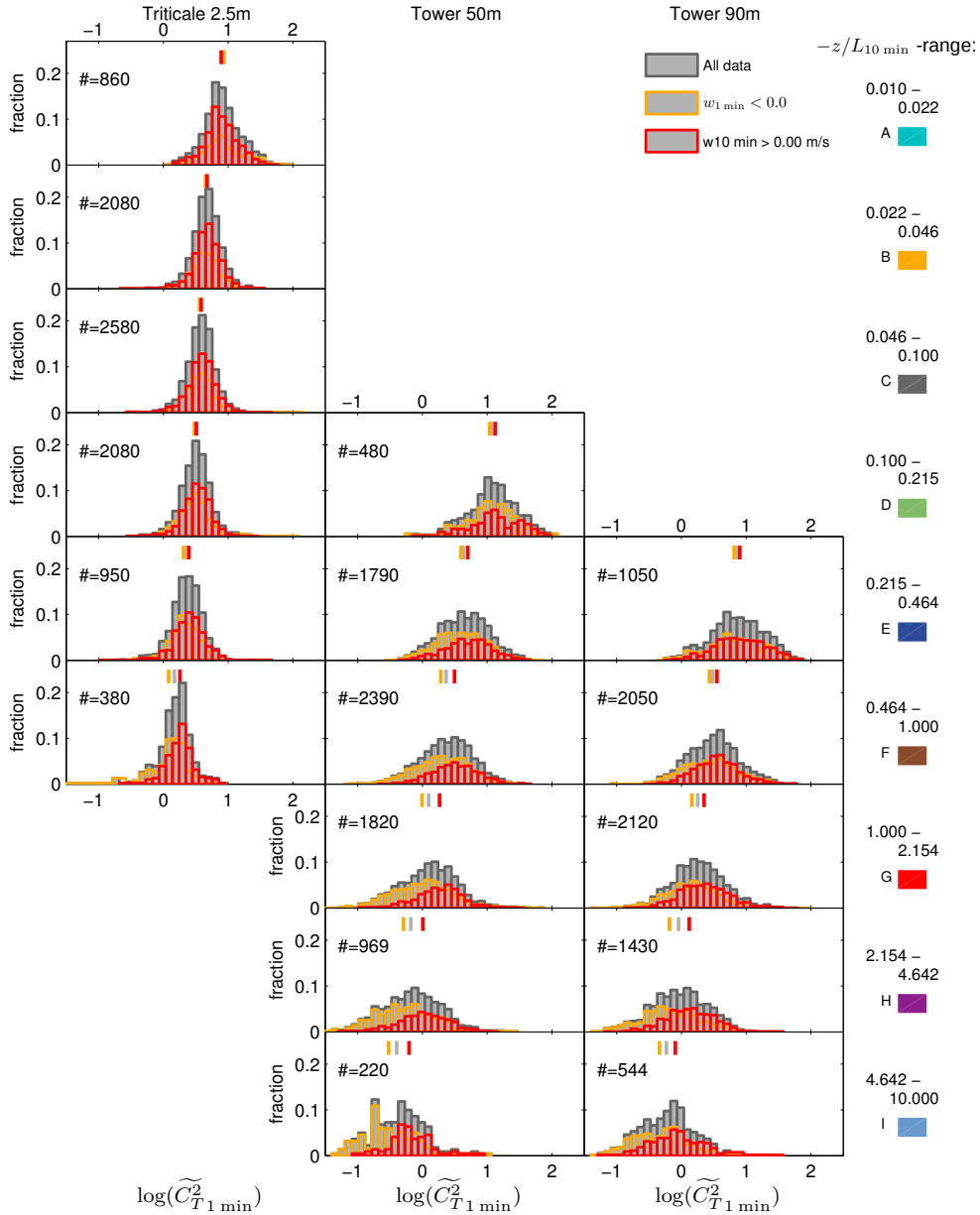

Fig. 4.6. Histograms of $\log(\widetilde{C}^2_{T\,1\,\mathrm{min}})$ for each observation level (columns) and each stability class (rows). Top row: most neutral class, and bottom row: most unstable class, see right legend for the stability ranges, in which the letters and colours corresponds to the nomenclature introduced in Fig. 4.3. Left column: triticale z = 2.5 m, centre column: tower z = 50 m, and right column: tower z = 90 m). Grey: the total dataset, red: the upward motions ($w_{1\,\mathrm{min}} > 0.0$), and orange: downward motions ($w_{1\,\mathrm{min}} < 0.0$). The histograms range from -1.5 up to 2.5 divided in 40 bins. The vertical lines at the top of the graphs show the mean value for the entire dataset (grey), the upward motions (red), and the downward motions (orange). The number of data points that are taken into account is given in the upper left part of each graph.

dication of the impact of differences between upward and downward motions (see Sect. 4.2.3). Therefore, we here look at the variation of the higher-order moments

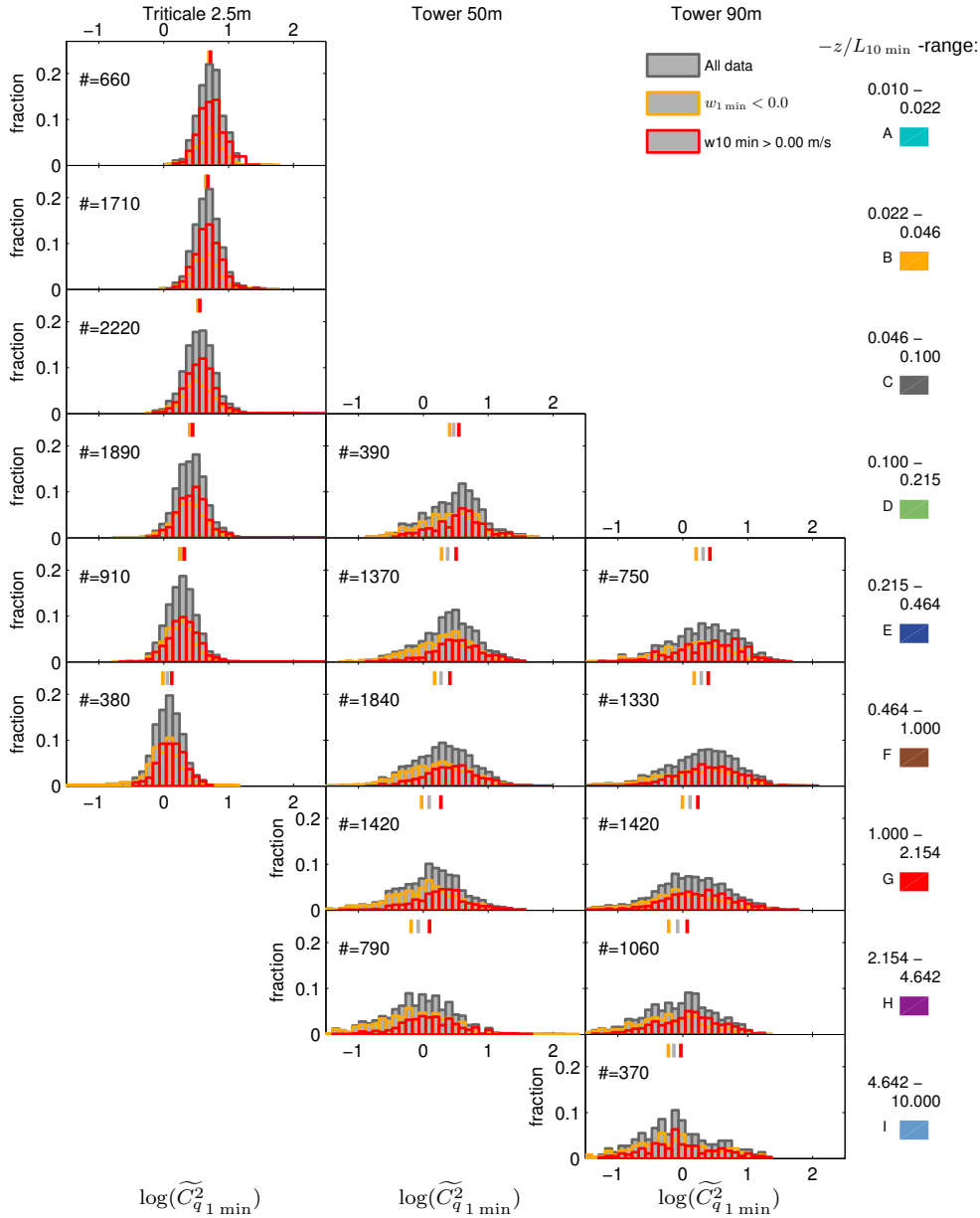

Fig. 4.7. Histograms of $\log(\widetilde{C}^2_{q\,1\,\mathrm{min}})$ for each observation level (columns) and each stability class (rows). Top row: most neutral class, and bottom row: most unstable class, see right legend for the stability ranges, in which the letters and colours corresponds to the nomenclature introduced in Fig. 4.3. Left column: triticale $z = 2.5$ m, centre column: tower $z = 50$ m, and right column: tower $z = 90$ m). Grey: the total dataset, red: the upward motions ($w_{1\,\mathrm{min}} > 0.0$), and orange: downward motions ($w_{1\,\mathrm{min}} < 0.0$). The histograms range from -1.5 up to 2.5 divided in 40 bins. The vertical lines at the top of the graphs show the mean value for the entire dataset (grey), the upward motions (red), and the downward motions (orange). The number of data points that are taken into account is given in the upper left part of each graph.

of $\log(\widetilde{C}^2_{s\,1\,\mathrm{min}})$ with height and instability. In most cases the skewness is slightly negative, and the traditional kurtosis is close to 3 (normal distribution). Both higher-order

moments do not show a regular behaviour with changing height or instability. This confirms the results of PS99, who stated that they did not find a "definite regularity in the time and height behaviour" of the higher-order moments.

Despite the fact that we do not find a bimodal distribution, it is still of interest to investigate the impact of differences between upward and downward motions on the PDF for $\log(\widetilde{C_{s\,1\,\mathrm{min}}^2})$ for the different scalars, stability classes and heights. The conditional PDFs of the upward (red) and downward motions (orange) for $\log(\widetilde{C_{s\,1\,\mathrm{min}}^2})$ are shown in Fig. 4.6 and Fig. 4.7. We focus on differences in the mean for the upward and downward motions (vertical lines at the top of the panels). We observe that the difference in the mean of $\log(\widetilde{C_{s\,1\,\mathrm{min}}^2})$ between upward and downward motions is enhanced with increasing instability. At $z = 2.5$ m in class A up to D (less unstable conditions) the means of $\log(\widetilde{C_{s\,1\,\mathrm{min}}^2})$ for the upward and downward motions nearly overlap. However, under more unstable conditions, the mean value of $\log(\widetilde{C_{s\,1\,\mathrm{min}}^2})$ for upward motions is located at higher values compared to that for the downward motion. At $z = 50$ m and at $z = 90$ m, this feature becomes more pronounced.

For the two stability classes E and F ($0.215 < -z/L_{10\,\mathrm{min}} < 1$) for which data from all three heights can be considered, we examine how the PDF for $\log(\widetilde{C_{s\,1\,\mathrm{min}}^2})$ between upward and downward motions depend on height. We do not find a clear tendency in the differences between upward and downward motions with increasing height. For temperature, the separation between the mean of $\log(\widetilde{C_{T\,1\,\mathrm{min}}^2})_{\mathrm{up}}$ and $\log(\widetilde{C_{T\,1\,\mathrm{min}}^2})_{\mathrm{down}}$ does not differ substantially between the levels. For humidity, we observe that at $z = 50$ m and at $z = 90$ m the distance between $\mathrm{mean}_{z/L}\left(\log(\widetilde{C_{q\,1\,\mathrm{min}}^2})_{\mathrm{up}}\right)$ and $\mathrm{mean}_{z/L}\left(\log(\widetilde{C_{q\,1\,\mathrm{min}}^2})_{\mathrm{down}}\right)$ is larger than at $z = 2.5$ m.

All together, we only found an instability dependence (in terms of $-z/L_{10\,\mathrm{min}}$) for the differences in C_s^2 between upward and downward motions and not a height dependence as described in CS09. As a consequence, the increase in total variability with increasing height cannot be explained by the different behaviour between upward and downward motions. The reason why we found an instability dependence only can be explained by combining the two concepts introduced in Sect. 4.2.3. There we showed that δz increases with instability and as a consequence $\log(C_s^2)_{+\delta z} - \log(C_s^2)_{-\delta z}$ also increases. Furthermore, we showed that $\log(C_s^2)_{+\delta z} - \log(C_s^2)_{-\delta z}$ is smaller at lower levels for a fixed L. But in our analysis we did not compare the differences between upward and downward motions for a fixed L, but for a fixed stability class $-z/L$ (that is: one row in Figs 4.6 or 4.7). If determining $\log(C_s^2)_{+\delta z} - \log(C_s^2)_{-\delta z}$ at different heights in the same way as in Sect. 4.2.3, but using a fixed $-z/L$ instead of a fixed L, $\log(C_s^2)_{+\delta z} - \log(C_s^2)_{-\delta z}$ would be identical for each height (consistent with what was observed in Figs 4.6 and 4.7). In other words, our results do not contradict the results of CS09. CS09 analyzed just one LES case ($L = -15.3$ m) and their observed height dependence is a result of increasing $-z/L$ with height.

In analyzing the conditional PDFs, we have up to this point only focussed on the mean

values, which changed with stability, but not with height. If we, however, investigate the widths of the conditional PDFs we do observe a height dependence within a given stability class (class E and F). With increasing height the width of the conditional PDFs increase slightly for $\log(\widetilde{C^2_{T\,1\,\mathrm{min}}})$ and considerably for $\log(\widetilde{C^2_{q\,1\,\mathrm{min}}})$. This has the effect that the width of the total PDFs increase as well, as we observed above. Thus, apart from a stability effect on the variance of $\log(\widetilde{C^2_{s\,1\,\mathrm{min}}})$, there also appears to be a height effect. The reason for the increase of the width of the conditional PDFs with height is still unclear.

Discussion

We would like to note that these general results do not depend on the specific choice of the threshold that separates upward and downward motions. Instead of using the fixed threshold of $w_{1\,\mathrm{min}} = 0.00$, we also tried to separate downward and upward motions by introducing a 'buffer' range ($w_{1\,\mathrm{min}} < w_{\mathrm{down}}$ and $w_{1\,\mathrm{min}} > w_{\mathrm{up}}$ m s^{-1}), with several thresholds for w_{down} and w_{up}. Using such a 'buffer' range changed the location of $\mathrm{mean}_{z/L}\left(\log(\widetilde{C^2_{s\,1\,\mathrm{min}}})\right)_{\mathrm{up}}$ and $\mathrm{mean}_{z/L}\left(\log(\widetilde{C^2_{s\,1\,\mathrm{min}}})\right)_{\mathrm{down}}$, however, it did not change our basic findings related to the height and stability dependence. Still, the distances between $\mathrm{mean}_{z/L}\left(\log(\widetilde{C^2_{s\,1\,\mathrm{min}}})\right)_{\mathrm{up}}$ and $\mathrm{mean}_{z/L}\left(\log(\widetilde{C^2_{s\,1\,\mathrm{min}}})\right)_{\mathrm{down}}$ stayed similar with increasing height and increased with increasing instability (figures not shown).

4.4.3. Variability of $\log(\widetilde{C^2_s})$ as a function of window size and stability

Analysis

In this section, we quantify the variance of $\log(\widetilde{C^2_s})$ and discuss its dependence on the window size as was also done by CS09. The top panels of Fig. 4.8 and Fig. 4.9 show how $\mathrm{var}_{z/L}\left(\log(\widetilde{C^2_{s\,\mathrm{win}}})\right)$ varies with the window size for temperature and humidity (compare with Fig. 8 from CS09). In these figures the window size is normalized by a time scale of 1 sec to make the argument of the logarithm dimensionless. For each scalar, height and stability class $\mathrm{var}_{z/L}\left(\log(\widetilde{C^2_{s\,\mathrm{win}}})\right)$ decreases with increasing window size as was also found by CS09. The slope of this decrease depends on stability, and it is smaller at $z = 2.5$ m than at $z = 50$ m and at $z = 90$ m, especially for humidity.

We want to quantify how the decrease depends on the observed scalar, measurement height and stability. Therefore, a simple linear regression was applied to the points in the top panels of Figs 4.8 and 4.9, viz.

$$\mathrm{var}_{z/L}\left(\log(\widetilde{C^2_{s\,\mathrm{win}}})\right) = -a_s \log(win) + b_s \tag{4.4}$$

in which $-a_s$ is the slope and b_s is the offset, where the subscript s indicates the scalar being investigated. The bottom panels of Fig. 4.8 and Fig. 4.9 show a_s and b_s as a function of stability. As the upper panels of the figures are a part of the larger picture describing the dependence of $\mathrm{var}_{z/L}\left(\log(\widetilde{C^2_{s\,\mathrm{win}}})\right)$ on window size (sketched in

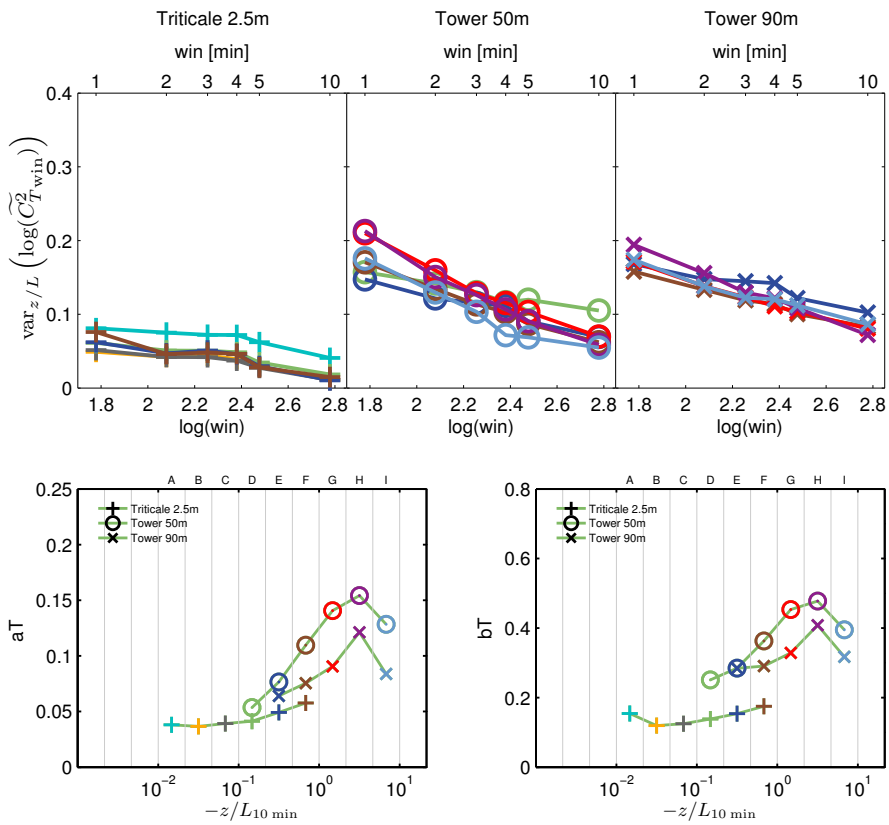

Fig. 4.8. *Top panel*: The variances of $\log(\widetilde{C_T^2})$ versus the logarithm of the window size normalized by 1 sec for different stability classes indicated by the different colours for the three heights (left: triticale $z = 2.5$ m, centre: tower $z = 50$ m and right: tower $z = 90$ m). *Bottom panels*: a_T, the negative slope (left) and b_T, the offset (right) of a simple linear regression ($y = -a_T x + b_T$) through the data of the top panel versus stability for the three heights. The points have been assigned to the centre of each stability class.

Fig 4.1), it is relevant to assess which regime or regimes our window sizes cover. For the determination of the regimes we convert our window size to the spatial window of CS09. In the conversion we assume frozen turbulence and an observed mean wind speed of 2.5 m s^{-1} for the triticale dataset at $z = 2.5$ m, and of 5 m s^{-1} for the tower dataset at $z = 50$ m and $z = 90$ m. Hence, the temporal window sizes used here (1 min $< win_t <$ 10 min) translate into spatial window sizes (win_x) of 150 m up to 1500 m for triticale and of 300 m up to 3000 m for the tower. From Fig. 8 in CS09 we estimate the boundary between regimes I and II to be located at approximately 180 m and that between regimes II and III at 500 m (with $win_x = 2r'$, where r' is the radius of the averaging disk in CS09). This places our window sizes in regimes II and III.

For the temperature observations (bottom panels of Fig. 4.8), a_T ranges from 0.04 (z = 2.5 m: class A) up to 0.15 (z = 50 m: class H). The slope increases with instability, except for the most unstable case both at $z = 50$ m and at $z = 90$ m. The reason for the fact that the most unstable class shows a smaller decrease of $\mathrm{var}_{z/L}\left(\log(\widetilde{C_{s\,\mathrm{win}}^2})\right)$ with window size than the neighbouring class at $z = 50$ m and at $z = 90$ m is still unclear. However, the deviation could be due to the relatively small number of data points in

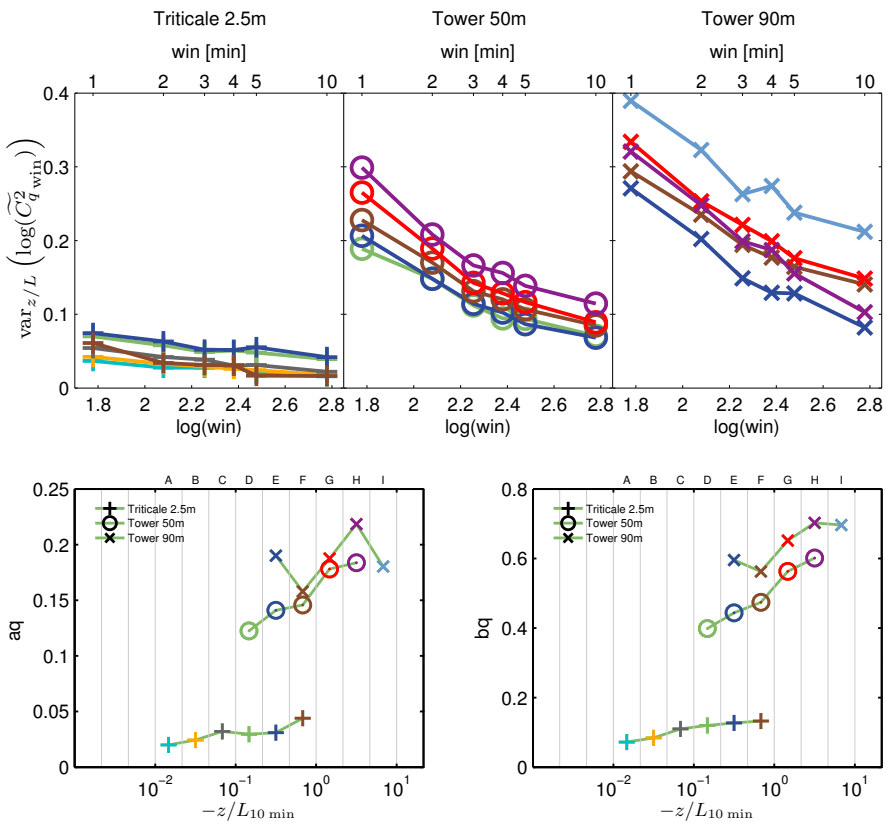

Fig. 4.9. *Top panel*: The variances of $\log(\widetilde{C}_q^2)$ versus the logarithm of the window size normalized by 1 sec for different stability classes indicated by the different colours for the three heights (left: triticale $z = 2.5$ m, centre: tower $z = 50$ m and right: tower $z = 90$ m). *Bottom panels*: a_q, the negative slope (left) and b_q, the offset (right) of a simple linear regression ($y = -a_q x + b_q$) through the data of the top panel versus stability for the three heights. The points have been assigned to the centre of each stability class.

this class compared to other stability classes at these heights. The largest values of a_T are observed at $z = 50$ m, but the three heights show similar results for the two overlapping classes. The offset, b_T, also increases with instability except for the most unstable case both at $z = 50$ m and at $z = 90$ m. The offset ranges from 0.12 ($z = 2.5$ m: class B) up to 0.48 ($z = 90$ m: class H). For the offset the two overlapping classes shows a clear distinction between the data at $z = 2.5$ m and the data at $z = 50$ m and 90 m.

Comparing the temperature and humidity data (Fig. 4.8 with Fig. 4.9), we find that at $z = 2.5$ m the offset and the slope are comparable. At $z = 50$ m and at $z = 90$ m, however, the offset and the slope are larger for humidity than for temperature. Comparison of the humidity data between the three levels shows that for the overlapping classes D-F the slope and the offset at $z = 50$ m and at $z = 90$ m are different from those at 2.5 m. It is still unclear, why a_q and b_q at $z = 50$ m and at $z = 90$ m are larger than at $z = 2.5$ m, and larger than a_T and b_T at the corresponding heights. One could suspect that surface heterogeneity in the footprint area of the $z = 50$-m and 90-m measurements might have caused the larger variability. But we have not been

able to find a relation between the variance and either wind direction or Bowen ratio (both variables can be seen as indicators for source areas with different characteristics). Furthermore, the 1-min time series of C_q^2 and C_T^2 show similar variations at each level at the tower.

The increase in a_s and b_s with increasing instability could be explained as follows. Differences in $\log(\widetilde{C_s^2})$ between upward and downward motions increase with increasing instability (Sect. 4.4.2). As a consequence, if the window is sufficiently small such that it represents either a part of the upward or downward motions (regime I), $\mathrm{var}_{z/L}\left(\log(\widetilde{C_s^2})\right)$ would increase (see also right upper panel of Fig. 4.1). Moreover, a_s and b_s are an estimate of the variability of $\log(\widetilde{C_s^2})$ in regime I despite our window sizes being located in regime II and III. This is because regime II connects the variability of regime I with regrime III (where the variability reaches the asymptotic value of zero), and an increase in $\mathrm{var}_{z/L}\left(\log(\widetilde{C_s^2})\right)$ at small window sizes will lead to an increase of the offset and slope in regime II and III.

We would like to compare our results on the window-size dependence of $\log(\widetilde{C_{T\,1\,\mathrm{min}}^2})$ to those of CS09. However, their type of data and analysis differ from ours, hence the comparison can only be a rough indication. CS09 calculated the variance of $\ln(C_T^2)$ over a horizontal slab in their LES domain. First, they calculated at each grid point a disk average of $\ln(C_T^2)$ using disks with different radii (r'). Subsequently, they calculated the variance over all these disk-averaged $\ln(C_T^2)$ within a horizontal slab. In order to compare the results of CS09 to ours, we need to convert the radius of their spatial disk to a time window assuming frozen turbulence and also to convert $\ln(C_T^2)$ into $\log(\widetilde{C_{T\,1\,\mathrm{min}}^2})$. The wind speed needed for the conversions is calculated with the similarity functions for the mean gradient of Businger et al. (1971) and $z_0 = 0.05$ m. In regimes II and III at $z = 80$ m, CS09 found that the variance of $\ln(C_T^2)$ is between 0.4 for $\ln(r') = 5$ and zero for $\ln(r') = 7$. This corresponds to $\mathrm{var}_{z/L}\left(\log(\widetilde{C_T^2})\right)$ 0.08 for a window size of 1 min and zero for a window size of 7.3 min (using $-z/L = 5.2$ and $U_{80\,\mathrm{m}} = 5.1$ m s^{-1}). A simple linear regression gives a_T is 0.04 and b_T is 0.26. Compared to our results CS09 found a lower slope and therefore a lower variance of $\ln(C_T^2)$. The reason is probably that CS09 determined the variances over a disk (two-dimensional averaging) and plotted it against the radius of the disk (one dimension), whereas we determine the variance over a time series (one-dimensional averaging) and plot it against the length of the time series (one dimension). The two-dimensional averaging will automatically lead to a lower variance for a given window (or disk) size.

Discussion

One limitation of the LITFASS data is that observation were not made under very favourable weather conditions. The intermittent cloudy situations ensured that the incoming radiation did not follow a smooth diurnal cycle. The net radiation at the surface forces the turbulence in the ASL, and therefore it is possible that extra variability of C_s^2 is produced by the variable forcing on cloudy days. In order to investigate if

our results are reasonable despite the cloudy days, we look at data obtained on seven clear-sky days during the BLLAST campaign 2011 (Lannemezan, France, see Lothon and Lenschow (2010)). We use data observed at $z = 2.5$ m above grass at the "edge site" (DOY: 170, 171, 176, 178, 182, 183 and 186, van de Boer et al., 2012). The data were processed in the same way as the LITFASS data. The BLLAST data show a similar slope as the LITFASS data at $z = 2.5$ m: $0.022 < a_T < 0.055$, and $0.021 < a_q < 0.054$ for class D - G. The offset is lower: $0.09 < b_T < 0.17$ and $0.07 < b_q < 0.16$ for class D - G. If the intermittently cloudy days during BLLAST are included as well (DOY: 166 - 186), the results do not change essentially. For class D - G, the slopes are $0.022 < a_T < 0.051$ and $0.023 < a_q < 0.049$, and the offsets are $0.10 < b_T < 0.16$ and $0.08 < a_T < 0.14$. This leads us to conclude that the intermittent cloudy days during LITFASS probably did not introduce extra variability in C_s^2.

Having quantified $\mathrm{var}_{z/L}\left(\log(\widetilde{C_s^2})\right)$ within the ASL, we now give an example of how this estimate can be used to assess the contribution of surface heterogeneity to the total variability of C_s^2 along a flight or scintillometer path. If one measures $\log(\widetilde{C_T^2})$ with an aircraft over a heterogeneous surface, the choice of the spatial window size is a compromise between a small window such that individual patches can be distinguished, and a large window such that the sampling uncertainty is reduced. The pragmatic solution is to choose the spatial window to have the same size as the typical patch size. Let us assume a heterogeneous surface with a patch size of around 300 m. Furthermore, the atmospheric conditions are unstable with $-z/L = 0.8$ (class G) and the wind speed is 5 m s^{-1}. When C_s^2 is determined from aircraft data, a spatial window instead of a temporal window is used (assuming that the ground speed is sufficiently large). The spatial window size is 300 m, which corresponds to a temporal window size of 60 s, assuming Taylor's frozen-turbulence hypothesis. With the given $-z/L$, $a_T \approx 0.1$, and $b_T \approx 0.35$ (Fig. 4.8), which makes $\mathrm{var}_{z/L}\left(\log(\widetilde{C_{T1\ \mathrm{min}}^2})\right) \approx -0.1\log(60) + 0.35 \approx 0.2$. This estimate indicates the level of local turbulent variability of $\log(\widetilde{C_T^2})$ to be expected under given atmospheric conditions. Differences in $\log(\widetilde{C_T^2})$ between patches of different land use along a flight path must thus exceed a value of $\sqrt{0.2}$ in order to be attributed to surface heterogeneity.

Despite the fact that the slope and offset are an indication of the variance in regime I, it is not advisable to use the linear regression results for window sizes outside the range considered in this study (1 min $< win_t <$ 10 min), where one would enter regime I or the tail of regime III. In these ranges the approximate linearity of the decrease of the variance with an increase of window size can no longer be assumed (Fig. 4.1).

4.5. Summary and Conclusions

In this study we quantified the local variability of the logarithm of the Monin-Obukhov scaled structure parameter of temperature ($\log(\widetilde{C_T^2})$) and humidity ($\log(\widetilde{C_q^2})$) where the structure parameters were determined over a range of averaging windows. To achieve

this, we examined $\log(\widetilde{C_s^2})$ determined from EC data measured at different heights (one surface system above triticale at 2.5 m, and two tower systems at $z = 50$ m and at $z = 90$ m) obtained within one month during the LITFASS-2009 experiment.

Before investigating the local variability, the mean values of the scaled structure parameters determined over a 1-min window were examined. At $z = 2.5$ m class mean $\log(\widetilde{C_{T\,1\,\mathrm{min}}^2})$ and $\log(\widetilde{C_{q\,1\,\mathrm{min}}^2})$ both follow the similarity relation proposed by Andreas (1988). At $z = 50$ m and at $z = 90$ m, in contrast, $\mathrm{mean}_{z/L}\left(\log(\widetilde{C_{T\,1\,\mathrm{min}}^2})\right)$ is slightly larger than the similarity relation suggests. This overestimation could be an effect of an underestimation of the surface fluxes, which might be explained by missing flux contributions due to the short averaging interval of fluxes used for the scaling (10 min).

From the probability density functions (PDFs) of $\log(\widetilde{C_{s\,1\,\mathrm{min}}^2})$ per stability class (in terms of $-z/L_{10\,\mathrm{min}}$), we found increasing differences in $\log(\widetilde{C_{s\,1\,\mathrm{min}}^2})$ between upward (large values of C_s^2) and downward motions (small values of C_s^2) with increasing instability ($-z/L$). However, these differences are not sufficiently large to produce a bimodal overall PDF. Moreover, within a given stability class, the differences in $\log(\widetilde{C_{s\,1\,\mathrm{min}}^2})$ between upward and downward motions do not depend on height.

The variance of $\log(\widetilde{C_s^2})$ decreases with an increase in the averaging window size (win) over which C_s^2 was determined. The magnitude of this decrease seems to be dependent on instability. We made a rough quantification of the decrease by fitting a simple linear regression between $\mathrm{var}_{z/L}\left(\log(\widetilde{C_{s\,\mathrm{win}}^2})\right)$ and log(win). Generally it appeared that both the offset and (the absolute value of) the slope increased with instability: the variance becomes increasingly sensitive to the averaging window size as instability increases. The explanation is that, at larger instability, the differences between upward and downward motions cause larger variances if the window size is sufficiently small. For temperature, the offset and slope are similar at the three heights. For humidity, however, at 2.5 m the offset and the slope are the same as for temperature, whereas at $z = 50$ m and at $z = 90$ m the offset and the slope for humidity are larger than for temperature.

The offset and the slope of the linear regression of $\mathrm{var}_{z/L}\left(\log(\widetilde{C_{s\,\mathrm{win}}^2})\right)$ versus $\log(win)$, can be used to quantify the local variability of C_s^2 for averaging times down to about 1 min for a given stability. In the context of the spatial sampling over a heterogeneous surface, this estimate of the local variability can be used to assess whether differences in C_s^2 along a scintillometer or flight path might be attributed to surface heterogeneity.

This observational study provides for the first time information on the variability of structure parameters of temperature and humidity in the ASL at different heights under different stability conditions. However, a number of problems remain. The differences in the variances between C_s^2 and C_q^2 are still unexplained; furthermore, the apparent discontinuity between the data at $z = 2.5$ m and those at $z = 50$ m and at $z = 90$ m calls for an investigation using data with a more gradual spacing in the vertical.

Acknowledgements

We thank Ulrich Weisensee and Jens P. Leps (both from Meteorological Observatory Lindenberg, DWD) for the discussions and extra analysis of the tower EC data. Further, we thank Anneke van de Boer and the BLLAST community for the use of their data for extra validation. In the end, we thank the anonymous reviewer for his thorough comments on two earlier versions of the manuscript, which really helped to improve the manuscript. The LITFASS-2009 experiment and part of the research has been supported financially by the German Research Foundation (DFG) in the framework of the project: 'Turbulent Structure Parameters over Heterogeneous Terrain - Implications for the Interpretation of Scintillometer Data' (through grant BE2044/3-1 and BE2044/3-3) and by the Meteorology and Air Quality group of Wageningen University.

5 On the discrepancy in simultaneous observations of C_T^2 by scintillometers, sonics and unmanned aircraft during LITFASS-2009 and LITFASS-2010

5.1. Introduction

During the past twenty years, large aperture scintillometers (LAS) have proven to be reliable instruments for providing area-averaged surface fluxes over natural landscapes (among others Green et al., 2001; Meijninger et al., 2002b, 2006). These measurements are important for validation of numerical models and satellite-based retrieval algorithms (see for an extensive literature review Beyrich et al., 2012, hereafter denoted as B12).

A scintillometer does not measure the area-averaged surface fluxes directly, and obtaining fluxes from scintillation measurements involves several steps (Moene et al., 2004). From the scintillation measurements the path-averaged structure parameter of the refractive index of air (C_n^2) is determined. Large aperature scintillometers are operating at optical wavelengths for which C_n^2 is basically determined by temperature fluctuations. Hence C_n^2 is subsequently used to derive the path averaged structure parameter of temperature (C_T^2, e.g. Hill et al., 1992; Ward et al., 2013). Finally, the area-averaged sensible heat flux can be derived from C_T^2 by applying Monin-Obukhov similarity theory (MOST, Monin and Obukhov, 1954; Wyngaard, 1973; among others).

Until now, the validation of LAS measurements over heterogeneous surfaces has been performed by comparing the scintillometer-based fluxes with fluxes from aggregated eddy-covariance (EC, Meijninger et al., 2002a,b, 2006) or from airborne measurements (Beyrich et al., 2006; Moene et al., 2006). However a direct validation of the path-averaged structure parameters against independent measurements is still missing. Such a direct validation is needed, because the relation between structure parameters and fluxes is non-linear. This non-linear relation results in a consistent overestimation of the flux obtained from a LAS compared to an aggregated flux of a number of EC systems when measuring above heterogeneous terrain (Meijninger, 2003; Meijninger et al., 2006).

Beyrich et al. (2005) were among the first to validate C_T^2 from the scintillometer with

This chapter is in preparation for submission to Boundary Layer Meteorology

independent measurements; however, they compared path-averaged LAS-based C_T^2 with EC measurements which are point measurements. Maronga et al. (2013) validate C_T^2 of the LAS with data obtained from a large eddy simulation (LES) and aircraft data obtained during the RECAB campaign near Cabauw in the Netherlands. This study extends beyond Beyrich et al. (2005) and considers a path averaged C_T^2, but it is limited to two case studies over a relatively homogeneous terrain. Furthermore, the lowest flight level of the aircraft was located at about twice the height of scintillometer path.

It was the aim of the LITFASS-2009 and LITFASS-2010 experiments to validate C_T^2 from the LAS with independent measurements over a moderately heterogeneous surface (B12, van den Kroonenberg et al., 2012, hereafter denoted as vdK12). Therefore, C_T^2 was derived from data of the unmanned meteorological mini aerial vehicle (M^2 AV, Spiess et al., 2007) that flew along the path of a LAS over a distance of several kilometres.

B12 show a first comparison for one flight day (13 July 2009). The 30-min and path-averaged C_T^2 derived from the LAS was compared with the mean of the flight-track C_T^2 from the M^{2}AV within the 30-min interval. B12 observed that the decrease with time of C_T^2 in the afternoon is consistent between M^{2}AV and LAS (Fig. 5 in B12), but the values of C_T^2 from the M^{2}AV are systematically larger than those from the LAS (Fig. 6 in B12). For this preliminary validation, the data of both systems were processed using a standard procedure, which is not optimal for such a comparison. The question arises whether the processing could explain (part of) the observed differences. For instance, the temporal averaging differs: thirty minutes for the LAS compared to about two minutes for the M^{2}AV. Moreover, despite the fact that the M^{2}AV flew along the scintillometer path, the spatial averaging differs: the path-averaged C_T^2 from the LAS has a bell-shaped weighting function (Wang et al., 1978), whereas the flight-track C_T^2 from the M^{2}AV was obtained from the leg as a whole.

During LITFASS-2009 the meteorological conditions were unfavourable to perform measurements over a complete undisturbed diurnal cycle with the M^{2}AV. Therefore a second small flight campaign was performed on 11 and 12 July 2010 (vdK12). So far, the M^{2}AV data of LITFASS-2010 have only been compared with EC data. Both systems show good agreement in the morning and in the afternoon, but C_T^2 from the M^{2}AV is larger than that from EC around noon (Fig. 4 in vdK12), which might be caused by a difference in the footprint of both observations.

The present study tries to improve on the studies of B12 and vdK12 by answering the following research questions:

1. Are the differences between LAS and M^{2}AV (initially found for 13 July 2009) also found for the other days during LITFASS-2009 and LITFASS-2010?
2. Can the differences be reduced or explained by a more elaborate processing of either or both the LAS and the M^{2}AV data?

Such a more elaborate processing includes:

a. the normalization of measured C_T^2 values to a reference height for both systems

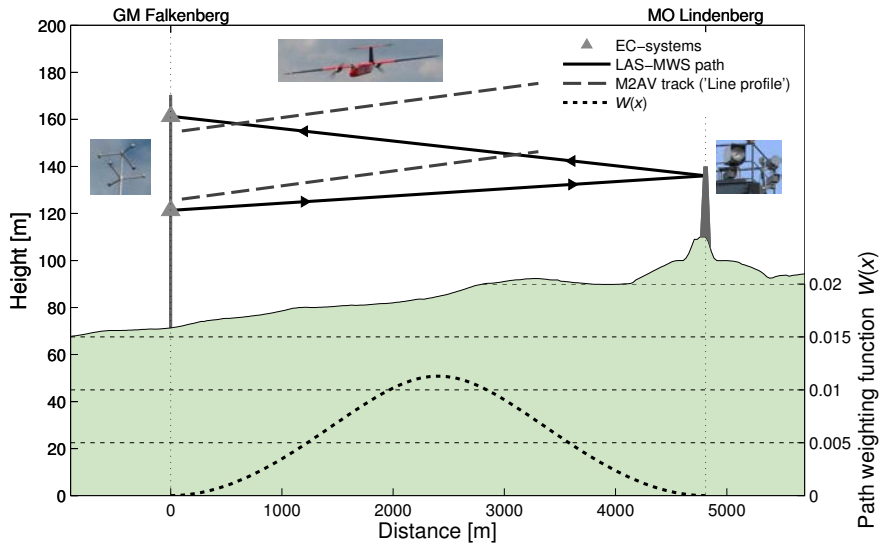

Fig. 5.1. Overview of the instrumental set-up of LITFASS-2009 and LITFASS-2010 experiments as used in this paper. In the lower part of the figure the path weighting function $W(x)$ of the LAS is shown.

taking into account stability,

b. the consideration of possible saturation effects on the LAS data (also called saturation correction),
c. proper treatment of the effect of humidity fluctuations on C_n^2 in deriving C_T^2 with the LAS (also called humidity correction),
d. the reduction of the LAS averaging time to the flight leg duration,
e. the use of alternative mathematical methods to determine the structure parameters from M^{2}AV data,
f. the proper weighing of the M^{2}AV data by taking into account the scintillometers path-weighting function.

A side-effect of applying such an elaborate data processing is that for each step of the data processing different options can be compared. This brings us to the last research question,

3. What is the influence on C_T^2 of applying the various options in the data processing for the two measurement systems?

5.2. Data and Methods

The LITFASS-2009 and LITFASS-2010 experiments (where LITFASS stands for LIndenberg-To-Falkenberg Aircraft Scintillometer Study) were performed in the area around the Meteorological Observatory Lindenberg – Richard-Aßmann-Observatory (MO Lindenberg) of the German Meteorological Service (Deutscher Wetterdiens, DWD). The surface in the so-called LITFASS-area (Beyrich et al., 2002) is moderately heterogeneous with a mixture of farmland, forest, small lakes and small villages (see Fig. 1 in B12 for a map of the different land-use types during LITFASS-2009). The vegeta-

Table 5.1. The scintillometers operating during the two experiments, where z_{eff} is the effective height of the scintillometer above the surface (Beyrich et al., 2012)

system	location receiver	z_{eff}	datalogger	freq
LITFASS-2009				
WURLAS98005-MWUB	Lindenberg	43 m	CR9000	500 Hz
WURLAS98005			G2	10 min
WURLAS98006	Falkenberg	63 m	CR9000	500 Hz
LITFASS-2010				
WURLAS98005	Lindenberg	43 m	G2	10 min
BLS900	Falkenberg	63 m		10 min

tion of the farmland mainly consists of maize, sunflowers, colza, barley and triticale. The typical dimensions of the crop fields vary between 300 m and 1000 m. Fig. 5.1 shows a schematic overview of the instrumental setup during the two experiments along the LAS-path. The weather conditions during the two experiments differed. During LITFASS-2009 (29 June - 24 July 2009) cloudless conditions never lasted longer than a few hours. Rain occurred on more than 50 % of the days. The wind speed at 10 m frequently exceeded 6 m s^{-1} preventing safe operation of the M^{2}AV (B12). During LITFASS-2010 (11 and 12 July 2010) the sky was mostly cloud-free, and during day time the wind speed at 10 m was between 2 and 5 m s^{-1} (vdK12).

In the sections below we present the methodology of how C_T^2 is calculated from data of the three measurement systems.

5.2.1. C_T^2 from LAS

During the two experiments two scintillometers were operated at an effective height (z_{eff}) of 43 m and 63 m over a path of $\approx$ 4800 m between the 99 m tower at GM-Falkenberg (see Fig. 5.1, where GM stands for" Grenzschichtmessfeld", German translation for boundary-layer field site) and a 26 m tower at MO-Lindenberg. Note that the lower path is almost parallel to the slanted surface, while the height above ground decreases from Falkenberg to Lindenberg for the upper path. The scintillometer signal was sampled in several ways (see Table 5.1).

During LITFASS-2009, the data of two LAS systems (WURLAS98005, z_{eff} = 43 m, and WURLAS98006, z_{eff} = 63 m, Meijninger et al., 2000, built at Wageningen University, the Netherlands) were sampled and stored with a frequency of 500 Hz on a Campbell CR9000 datalogger. The WURLAS98005 is in long-term operation at DWD. Its internal data logger routinely stores data as well (G2 datalogger with a storage interval of 10 min). Furthermore, it was combined with a microwave scintillometer built by the University of Bern (MWUB, logged on the CR9000). For a more detailed setup of the scintillometers we refer to B12, and for a comparison of data obtained from the two dataloggers to chapter A.

During LITFASS-2010, the WURLAS98005 was routinely operated with the G2 datalogger. Moreover, at $z_{\text{eff}} = 63$ m a BLS900 (Scintec AG, 2006, Scintec, Germany) was operated and stored data with a sampling interval of 10 min (replacing the WURLAS98006 used in 2009).

Data from the systems were processed with an averaging time of 10 min. In addition, for LITFASS-2009 the WURLAS98005 and WURLAS98006 data were processed over the exact time window of the flight legs as well (see item d of the elaborate processing list in Sect. 5.1). This was not posible for LITFASS-2010, because for that second experiment no raw data of the LAS were available.

From the scintillometer signal to C_n^2

The first step when analysing LAS data is to obtain the path averaged C_n^2 from the variance of the logarithmic signal amplitude ($\sigma^2_{\ln(I)}$). Because for the G2-logger (Meijninger et al., 2000) and the BLS900 (Scintec AG, 2006) this step was already applied internally, it had to be applied for the raw data logged on the CR9000 only. For the 500 Hz data, the following relation was used:

$$C_n^2 = \frac{\sigma^2_{\ln(I)}}{4b(D,L)} \tag{5.1}$$

in which the constant b was obtained from the scintillometer equation (compare Eq. 1 in B12), depending on the aperture size D and the path lenth L. For both WURLAS instruments $b \approx 20.60 \times 10^{12}$. The CR9000 datalogger at Falkenberg used to log the signal of WURLAS98006 did not have a stable calibration. Therefore a correction for each day was applied (see chapter A).

Saturation correction

One issue related to scintillometry is the limitation of the theory to a weak scattering regime. In case of stronger scattering C_n^2 is no longer linearly proportional to $\sigma^2_{\ln(I)}$: the signal gets saturated. While it is better to prevent saturation (by reducing the path length or increasing the observation level), one can also correct the C_n^2 signal. From an extensive comparison of different saturation correction methods, Kleissl et al. (2010) recommended the Clifford correction method (Clifford et al., 1974). For both the WURLAS and BLS, the saturation correction factor $m = C^2_{n\text{cor}}/C^2_{n\text{uncor}}$ was calculated for seven values[1] of $C^2_{n\text{uncor}}$. Afterwards a linear interpolation method was used to obtain $C^2_{n\text{cor}}$ for each time interval. In order to be consistent between the WURLAS and the BLS, we decided to apply this saturation correction also to the BLS900 data, instead of using the correction that is implemented in the Scintec software (Scintec AG, 2006).

[1] $C^2_{n\,\text{uncor}} = (0.1,\ 0.5,\ 1.0,\ 2.5,\ 5.0,\ 7.5,\ 10,\ 25,\ \text{and}\ 50) \times 10^{-15}\ \text{m}^{-2/3}$

From C_n^2 to C_T^2- correction for humidity contribution

The structure parameter of the refractive index of air is related to C_T^2, C_q^2 and C_{Tq} via (Hill, 1989; Lüdi et al., 2005; Ward et al., 2013):

$$C_n^2 = \frac{A_T^2}{\overline{T}^2} C_T^2 + \frac{A_T A_q}{\overline{T}\,\overline{q}} C_{Tq} + \frac{A_q^2}{\overline{q}^2} C_q^2 \tag{5.2}$$

in which A_T and A_q are the partial derivatives of the refractive index of air with respect to temperature (T) and humidity (q), respectively, and the overbar indicates averaging. For the WURLAS98005-MWUB system, which measured C_n^2 at two wavelengths, C_T^2 was explicitly solved. In literature, two methods can be found to obtain C_T^2 from a two-wavelength scintillometer system, by using either

1. the covariance between the signal of the two instruments ($cov_{\ln(I\mathrm{LAS}),\ln(I\mathrm{MWS})}$, see Lüdi et al., 2005; Ward et al., 2013), or
2. the correlation coefficient between T and q (R_{Tq}, see Hill, 1989).

For the systems that measured C_n^2 at an optical wavelength only, the humidity contribution to C_n^2 (the second and third term in Eq. 5.2) had to be estimated from other meteorological measurements. This reduces Eq. 5.2 to:

$$C_n^2 = \frac{A_T^2}{\overline{T}^2} C_T^2 \; c_{q\mathrm{con}} \tag{5.3}$$

in which $c_{q\mathrm{con}}$ is a correction for humidity contribution that can be estimated in three different ways (see Moene, 2003, hereafter denoted as M03), from A_q, A_T, $\overline{q}$, $\overline{T}$ and:

3. R_{Tq} and the standard deviation of temperature and humidity (σ_T and σ_q) using Eq. 8 of M03,
4. R_{Tq} and the Bowen ratio (β, the ratio of the sensible to the latent heat flux) using Eq. 11 of M03, or
5. β using Eq. 12 of M03, which is comparable with the Eq. 10 of Wesely (1976b).

M03 has shown that the relative error for the last three methods is smaller than 1% if $|\beta| > 1$. For $|\beta| < 1$, the deviation of the three methods is larger, using method 3 gives errors of less than 3%, whereas method 5 gives errors of 5-40 % (his Fig. 8). Because his analysis was based on EC-data, he did not include the methods of the two-wavelength scintillometers in his analysis (method 1 and 2).

5.2.2. C_T^2 from the M²AV

The M²AV is an unmanned aircraft built by the Institute of Aerospace Systems of the Technische Universität Braunschweig (TU-BS, Spiess et al., 2007; Martin et al., 2011, vdK12). The wind direction and wind speed are obtained using a 5-hole probe, an inertial navigation unit and a GPS receiver. Temperature is measured with a Vaisala HMP 50 (response frequency of 1 Hz) and a custom-made thermocouple (10 Hz). The final temperature data is a combination of those two instruments using complementary filtering with a cut-off frequency of 0.02 Hz (vdK12).

During the two experiments different flight patterns were flown (B12, vdK12). In this study, we only analyse the 'line profile' and 'scintillometer profile' data (both called leg in vdK12) where the aircraft flew at different levels below 110 m along the scintillometer path either parallel to the surface or parallel to the LAS beam. These patterns were flown on 7 days: 5 days in 2009 (7, 12, 13, 17 and 21 July), and 2 days in 2010 (11, 12 July). Both patterns covered only the southern part of the scintillometer path (3.3 km $\approx 70\%$), because it was not allowed to fly above the village of Lindenberg. The mean ground speed was about 24 m s^{-1}. Consequently a leg took between two and three minutes. In Fig. 5.1 a schematic example of the line profile is given.

Related to the data of the M^{2}AV two remarks have to be made. First, after the experiments it appeared that the temperature of the Vaisala HMP 50 (slow thermometer) showed a dependency on solar exposure (personal communication: Sabrina Martin, TU-BS, 2010). Second, on some flights during the LITFASS-2009 experiment the height above the surface was not well measured. For these flights the average height was estimated as the level pre-set when programming the flight mission. This is a reasonable estimate as proven for those flights where the altimeter worked properly.

Different methods to calculate $C^2_{T\,\mathrm{M^2AV}}$

The first method to calculate C_T^2 from the aircraft data employs the traditional way using the structure function ($D_{TT} = \overline{[T_i - T_{i-\Delta i}]^2}$, in which i is the temperature measurement at a certain location or time and Δi is the separation). Here we follow the methods described in vdK12. The 100 Hz temperature data observed with the M^{2}AV is considered as a time series, from which the temporal structure function is calculated over a range of separations. Then the conversion of the temporal to the spatial structure function is done by applying Taylor hypothesis using the mean ground speed. In the end C_T^2 is calculated as the mean of D_{TT} times the separation to the power $-2/3$ over a range of spatial separations within the inertial subrange (IS, $C_T^2 = \overline{D_{TT}\Delta i^{-2/3}}^{\mathrm{IS}}$). In the present dataset, the inertial subrange exists for separations between 2.5 and 25 m (vdK12). First, we calculated D_{TT} and C_T^2 over the leg as a whole as was done in B12 and vdK12. Second, following vdK12 we calculated D_{TT} over a moving window to obtain the spatial series for applying the LAS path-weighting function. The length of the window was about 300 m.

The second method to calculate C_T^2 is via the Fourier spectrum using the routines as described in Hartogensis et al. (2002). Within this routine, the inertial subrange is automatically determined. Here again the 100 Hz data was analysed as a time series and the mean ground speed was used in the conversion from temporal to spatial data.

The third method to calculate C_T^2 is using wavelet spectrum as described in Maronga et al. (2013). Using the geo-location of the 100 Hz data, we converted the time series of temperature along the leg to an equidistant space series (linear interpolation was used). The spatial resolution was equal to the mean spatial resolution of the original time series (approximately 0.25 meter). Next, the wavelet spectrum was calculated for

each point in the spatial series. The wavelet function was the Morlet wavelet with a nondimensional frequency of 6. C_T^2 was derived from Eq. 14 in Maronga et al. (2013) and it was subsequently spatially averaged over a running window of 300 m around each measurement point and stored for every 2 meter along the flight leg. Spectral averaging was applied over a range of scales from 2.5 to 25 m.

Applying the path-weighting function

In B12 $C_{T\mathrm{M^2AV}}^2$ is obtained over the leg as a whole. In order to obtain spatial averaging similar to that of the scintillometers, we also applied the LAS path weighting function ($W(x)$, Wang et al., 1978) to the spatial series obtained with the M^{2}AV. This procedure consists of four steps:

1. $W(x)$ is determined for different x along the scintillometer path;
2. the grid of the spatial series of C_T^2 is projected on the scintillometer path (x in meters, note that because the M^{2}AV did not fly exactly parallel to the scintillometer path Δx varies). This gives us $C_T^2(x)$;
3. for each location x, the path weighting function $W(x)$ is obtained using interpolation;
4. the mean C_T^2 along the path including the path weighting function of the LAS ($C_{TW(x)\mathrm{LAS}}^2$) is calculated:

$$C_{TW(x)\mathrm{LAS}}^2 = \sum C_T^2(x) W(x) \Delta x \tag{5.4}$$

5.2.3. C_T^2 from sonic measurements at the tower

In order to have an independent validation, C_T^2 was also determined from two sonic anemometer/ thermometers (USA-1, METEK GmbH, Germany) located at 50 m and at 90 m on the 99 m tower of GM-Falkenberg. We calculated C_T^2 from the temporal structure function of temperature over the same time window as the LAS (10 min), following the procedure described in (Braam et al., 2014). Because the C_T^2 from the USA-1 is only an extra validation, we do not repeat details of the method to calculate C_T^2 here[2].

5.2.4. Normalizing C_T^2 to one reference level

The mean structure parameter decreases with height in the ASL. The scintillometers, M^{2}AV and the sonics measured C_T^2 at different levels (z_m), which makes it difficult to compare C_T^2 between the instruments. Therefore, we normalized all C_T^2 data to a common reference level of 50 m ($C_{T50\mathrm{m}}^2$). For this we used Monin-Obukhov similarity theory (MOST) scaling. The normalization of the structure parameter at the observation level

[2]The raw 20 Hz data were checked for unphysical values, spikes, and insufficient amplitude resolution based on Vickers and Mahrt (1997), converted to physical values (Schotanus et al., 1983; Liu et al., 2001), and wind components were rotated using the planar fit method (Wilczak et al., 2001) and the x-axis is along the mean horizontal wind. The conversion of the temporal structure function into the spatial structure function was done with Eq. (5) from Braam et al. (2012) following Bosveld (1999). To correct for fluctuations smaller than the path length, the correction of Hartogensis et al. (2002) for the deviation of the measured spectrum from the inertial subrange was applied.

($C^2_{T\,z_\mathrm{m}}$) to 50 m is, for unstable conditions (subscript un), given by:

$$C^2_{T\mathrm{un50m}} = C^2_{T\,z_\mathrm{m}} \frac{z_\mathrm{m}^{2/3}\left(1 - c_{2\mathrm{un}} z_\mathrm{m}/L\right)^{2/3}}{50^{2/3}\left(1 - c_{2\mathrm{un}} 50/L\right)^{2/3}} \tag{5.5a}$$

and for stable conditions (subscript st) by:

$$C^2_{T\mathrm{st50m}} = C^2_{T\,z_\mathrm{m}} \frac{z_\mathrm{m}^{2/3}\left(1 + c_{2\mathrm{st}}\left(z_\mathrm{m}/L\right)^{2/3}\right)}{50^{2/3}\left(1 + c_{2\mathrm{st}}\left(50/L\right)^{2/3}\right)} \tag{5.5b}$$

in which L is the Obukhov length ($L = \overline{T_v}{u_*}^2/(\kappa g T_{v*})$ with T_v being the mean virtual temperature, u_* the friction velocity, $\kappa = 0.4$ the von-Kármán constant, $g = 9.81$ m s^{-2} the acceleration due to gravity, and T_{v*} the virtual temperature scale); c_2 is the second regression coefficient used in the most common expression of MOST. In this study, we used the regression coefficients of Andreas (1988), who modified the original MOST relation of Wyngaard (1973) by replacing $\kappa = 0.35$ with $\kappa = 0.40$: $c_{2\mathrm{un}} = 6.1$ and $c_{2\mathrm{st}} = 2.2$. The Obukhov length needed in the normalization was obtained from the fluxes measured with the EC system at 50 m (see the first item in the list of Sect. 5.2.5).

5.2.5. Other data

For the humidity correction and the height normalization additional data are needed:

- R_{Tq}, σ_T, σ_q, β and L were obtained from data measured with the USA-1 together with a LI7500 infrared hygrometer (LiCor Inc., U.S.) at 50 m and at 90 m. They were calculated with the EC-Pack flux-software package (version 2.5.23) developed by Wageningen University (van Dijk et al., 2004) over a 10 min window (Braam et al. 2014[3]). The influence of unreliable data points and data gaps in the time series is minimized, to reduce possible errors if applying the corrections. We, therefore, excluded in the 10-min time series of each variable spikes (following the method of Vickers and Mahrt, 1997) and the data points with a relative uncertainty > 0.3. Afterwards, all gaps in the 10-min time series were filled using linear interpolation and the dataset was smoothed using a running average of 2 data points. Moreover, the third humidity contribution correction was not applied if $\beta \approx \frac{A_q}{\overline{q}} \frac{\overline{T}}{A_T} \frac{c_p}{L_v} \approx -0.03$, because then C^2_T becomes numerically ill-defined[4].
- pressure, measured at 1 m (PTB220, Vaisala Oy, Finland). The pressure at 50 m and 90 m was estimated by assuming a linear decrease of 12.5 Pa m^{-1},
- precipitation, measured with a weighing precipitation gauge (Pluvio, Ott GmbH, Germany),

[3]The following corrections were applied by Braam et al. (2014): a) planar fit rotation (Wilczak et al., 2001); b) correction for density effects on the latent heat flux (Webb et al., 1980); c) humidity and cross wind correction (Schotanus et al., 1983; Liu et al., 2001) for the sonic temperature; and d) corrections for spectral loss due to path averaging and sensor separation (Moore, 1986).

[4]Range of rejected Bowen ratios: $-0.4\frac{A_q}{\overline{q}} \frac{\overline{T}}{A_T} \frac{c_p}{L_v} < \beta < -1.6\frac{A_q}{\overline{q}} \frac{\overline{T}}{A_T} \frac{c_p}{L_v}$

5.3. Research Strategy

This research consist of three parts. In all these parts, we use linear least square regressions forced through the origin abbreviated as LLSRO. With LLSRO we evaluate the slope (a), the coefficient of determination (r^2) and the coefficient of variation (abbreviated as CV). The coefficient of determination is a measure of the strength of the correlation, and CV indicates how much each point deviates from the 1:1-line on average.

For the comparison of the LAS and the sonic and the different data processing methods of the LAS, we analyse the data measured on the flight days between 0500 UTC and 1800 UTC (local summer time is UTC + 2 h). Furthermore, we mainly focus on $C_{T50\mathrm{m}}^2$. To simplify notation, we remove the subscript 50 m throughout the rest of the paper. As an effect $C_{T\mathrm{LAS43m}}^2$ refers to the 50-m normalized structure parameter obtained from the LAS with $z_{\mathrm{eff}} = 43$ m.

In part 1, we answer our first research question and compare C_T^2 obtained with the LAS and M^{2}AV for all the days. For this, we calculate $C_{T\mathrm{LAS}}^2$ and $C_{T\mathrm{M^2AV}}^2$ as follows (see also Table 5.5): $C_{T\mathrm{LAS}}^2$ is not corrected for saturation, it is corrected for humidity using Eq 12 of M03, and it is averaged over 10 min. $C_{T\mathrm{M^2AV}}^2$ is calculated directly over the entire leg, using the method as proposed by vdK12.

In part 2, we focus on the last research question: the impact on C_T^2 of applying different options from the elaborate data processing list (see Sect. 5.1). The C_T^2 obtained with the different options as suggested above are therefore compared to each other. In this part we evaluate the LAS (part 2a) and M^{2}AV (part 2b) separately.

The weather conditions differed between LITFASS-2009 and LITFASS-2010. This can have an effect on the corrections. Therefore, we analyse the two experiments separately. During LITFASS-2009 conditions were more moist than for LITFASS-2010. The noontime Bowen ratio (determined with the EC system data at 50 m and averaged between 1000 and 1500 UTC) is 0.78 for LITFASS-2009 and 3.15 for LITFASS-2010.

In part 3, we investigate if the elaborate data processing done in the analysis can reduce and explain the deviations between LAS and M^{2}AV as found in B12 (research question 2).

5.4. Results and Discussion

5.4.1. Part 1: Comparison of C_T^2 for all flight days

The bottom panel of Fig. 5.2 shows the daytime evolution of C_T^2 obtained with the various instruments during the days where the M^{2}AV flew the line profile or the scintillometer profile at a height smaller than 110 m.

Validation of the height normalization (item a)

We start to compare C_T^2 derived from the different observation levels for the LAS and the sonic to evaluate the method to normalize C_T^2 to 50 m. It can be seen that for both

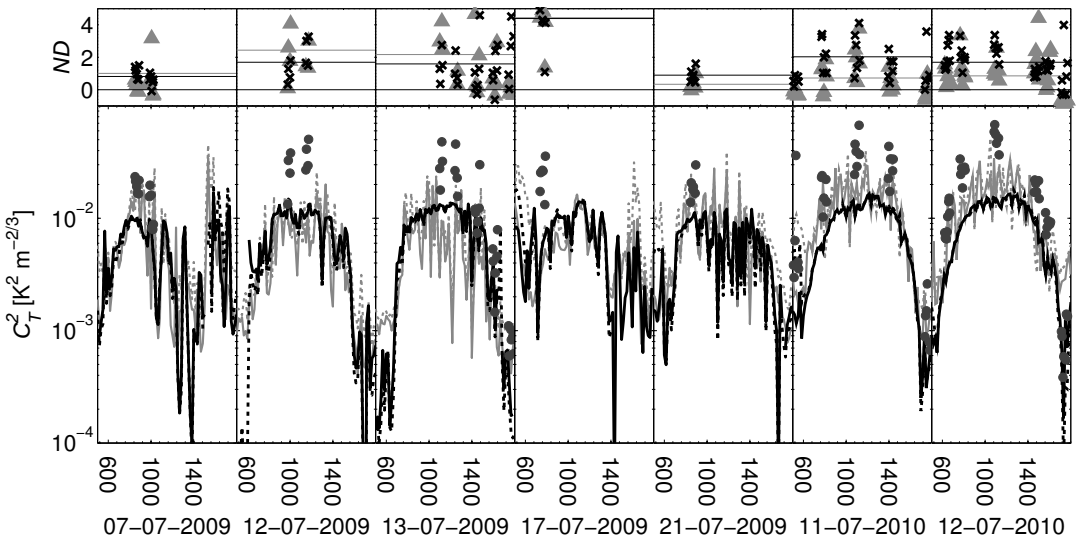

Fig. 5.2. The daytime evolution of $C^2_{T\mathrm{LAS43m}}$ (solid black line), $C^2_{T\mathrm{LAS63m}}$ (dashed black line), $C^2_{T\mathrm{M^2AV}}$ (grey circles), $C^2_{T\mathrm{sonic50m}}$ (solid grey line), and $C^2_{T\mathrm{sonic90m}}$ (dashed grey line) during the flight days of LITFASS-2009 and LITFASS-2010 experiments (see Sect. 5.3 and Table 5.5 for the applied methods and corrections to obtain C_T^2). The top panel shows the normalized differences ($ND_{\mathrm{M^2AV,LAS}}$, see Eq. 5.6) between $C^2_{T\mathrm{M^2AV}}$ and the other instruments for each leg ($\times$ $ND_{\mathrm{M^2AV,LAS}}$ and $\triangle$ $ND_{\mathrm{M^2AV,sonic}}$) and their daily averaged value (black lines $ND_{\mathrm{M^2AV,LAS}}$, and grey lines $ND_{\mathrm{M^2AV,sonic}}$).

systems normalized C_T^2 obtained at the two levels are comparable. LLSRO between C_T^2 obtained at the higher level versus C_T^2 obtained at the lower level gives $a = 1.00$ and $r^2 = 0.92$ for the LAS, and $a = 1.11$ and $r^2 = 0.70$ for the sonic. We observe a better comparison between the two levels for the LAS than for the sonic, because the two levels of the LAS are closer to each other and centred around 50 m. The largest deviation is found during the evening transition. Separation of the data by stability shows that, for unstable conditions ($z/L < 0$), $a = 0.99$ and $r^2 = 0.98$ for the LAS, and $a = 1.08$ and $r^2 = 0.76$ for the sonic. For stable conditions ($z/L > 0$), $a = 1.40$ and $r^2 = 0.71$ for the LAS, and $a = 1.78$ and $r^2 = 0.59$ for the sonic. These deviations for stable conditions illustrate the limited applicability of MOST at several decameters above ground (see also Braam et al. 2012). Because most of the flight data were obtained during unstable conditions, we conclude that the method to normalize C_T^2 to 50 m is justified to compare the M^{2}AV data with the LAS.

Comparison of C_T^2 obtained with LAS, M^{2}AV and sonic

Comparing C_T^2 obtained from the three instruments to each other, we observe that $C^2_{T\mathrm{M^2AV}}$ is in generally higher than $C^2_{T\mathrm{LAS}}$ and $C^2_{T\mathrm{sonic}}$. This is also visible in the top panel of Fig. 5.2, which shows the normalized difference (abbreviated as ND) between $C^2_{T\mathrm{M^2AV}}$ and C_T^2 of the other instrument (subscribt other) defined as:

$$ND_{\mathrm{M^2AV,other}} = \frac{C^2_{T\mathrm{M^2AV}} - C^2_{T\mathrm{other}\overline{z}}}{C^2_{T\mathrm{other}\overline{z}}} \tag{5.6}$$

in which, $C^2_{T\mathrm{other}\overline{z}}$ is the average C_T^2 of the normalized values from the two measurement levels. In general ND is located around one or two, as also observed in B12 and vdK12. Most of the time $ND_{\mathrm{M^2AV,LAS}}$ is larger than $ND_{\mathrm{M^2AV,sonic}}$, especially during LITFASS-2010; for these data $C^2_{T\mathrm{sonic}}$ is typically larger than $C^2_{T\mathrm{LAS}}$. From LLSRO between $C^2_{T\mathrm{LAS}\overline{z}}$ and $C^2_{T\mathrm{sonic}\overline{z}}$, we observe an overestimation of 17% with an r^2 of 0.49. The underestimation of the LAS can be explained by the notion that the saturation correction is not applied, this will be discussed in more depth in the next section. Another possible reason for the deviation may be the difference in the footprints of the two instruments. The relatively small value for r^2 is attributed to the smoother curve of the LAS when compared to the sonic (Figure 5.2), caused by the path averaging (Hartogensis et al., 2002).

Despite of the general tendency that ND is larger than zero (which implies $C^2_{T\mathrm{M^2AV}} > C^2_{T\mathrm{other}}$), there are also a few flight legs when they are smaller ($C^2_{T\mathrm{M^2AV}} < C^2_{T\mathrm{other}}$). Figure 5.2 suggests that these situations basically occur in the early morning or late afternoon. These exceptions indicate that there could be a physical reason for the overestimation of $C^2_{T\mathrm{M^2AV}}$ compared C_T^2 of the other methods. Therefore, we compared ND against different meteorological variables, such as mean wind speed, mean cross wind, wind direction, R_{Tq}, z/L, β. However, scatter plots between ND and these variables did not give any clear indication of a relation between one of those variables and ND (figures not shown, $r^2 < 0.05$).

In addition, we investigated the dependence of $ND_{\mathrm{M^2AV,LAS}}$ on the flight level and flight direction (more or less north-south or south-north), but for both we did neither find and clear relationship (figures not shown). The flight direction was considered because, first, one possible reason for the overestimation of C_T^2 from the M²AV could be errors in the temperature measurements due to solar heating of the temperature sensor. Note that the dependency on solar heating of the Vaisala HMP 50 cannot be the reason. That is because this temperature is only used for the low frequency range (< 0.02 Hz), whereas $C^2_{T\mathrm{M^2AV}}$ is calculated over a range of scales between 2.5 and 25 m (corresponding to 9.6 and 0.96 Hz, assuming a mean ground speed of 24 m s^{-1}). It is possible, however, that the thermocouple shows a dependency on solar heating too. Second, another reason could be the use of the mean ground speed instead of the true airspeed in the calculation of $C^2_{T\mathrm{M^2AV}}$. Differences in $C^2_{T\mathrm{M^2AV}}$ using these two air speeds would likely be opposite for the two flight directions. Extra temperature fluctuations (higher C_T^2) due to intermittent cloudy situations along the flight leg could also not be the reason for the large ratios, because an overestimation by M²AV is also observed during LITFASS-2010 that was characterized by cloud-free situations.

To conclude, we cannot explain the differences in C_T^2 between the instruments by a clear relation to atmospheric conditions or flight parameters. Therefore we investigate if a more elaborate data processing can reduce and explain the differences.

Table 5.2. Comparison of $C^2_{T\mathrm{LAS}}$ corrected for humidity (y) relative to uncorrected for humidity (x, $y = ax$) for the WURLAS98006 ($z_{\mathrm{eff}} = 43$m), together with the coefficient of determination (r^2) and the coefficient of variation (CV)

	correction method	reference	LITFASS-2009, $\beta = 0.78$			LITFASS-2010, $\beta = 3.15$		
			a	r^2	CV	a	r^2	CV
Using LAS-MWS								
1	$cov_{\ln(I\mathrm{LAS}),\ln(I\mathrm{MWS})}$	Ward et al. (2013)	0.959	0.995	0.067			
2	R_{Tq}	Hill (1989)	0.942	0.998	0.078			
Using LAS only								
3	$R_{Tq} + \sigma_T + \sigma_q$	Eq. 8 of M03	0.949	0.989	0.095	0.974	1.000	0.032
4	$R_{Tq} + \beta$	Eq. 11 of M03	0.945	0.991	0.094	0.981	1.000	0.024
5	β	Eq. 12 of M03	0.910	0.957	0.176	0.975	0.999	0.037

5.4.2. Part 2a: Evaluation of the determination of C_T^2 from LAS measurements

Saturation correction (item b)

The applied saturation correction only depends on the measured C_T^2. The correction factor m is largest if C_T^2 is large. Because C_T^2 decreases with height, the correction has a larger influence on C_T^2 obtained at 43 m than at 63 m. On average the values of C_T^2 obtained during LITFASS-2009 and LITFASS-2010 are comparable, so the effect of the correction between the two experiments will be comparable as well; during LITFASS-2009, m is on average 1.16 for $C^2_{T\mathrm{LAS43m}}$, and 1.11 for $C^2_{T\mathrm{LAS63m}}$, and during LITFASS-2010, m is 1.15 for $C^2_{T\mathrm{LAS43m}}$, and 1.10 for $C^2_{T\mathrm{LAS63m}}$. If only the flight times are taken into account, the correction is even somewhat larger (LITFASS 2009: 1.18 for 43 m and 1.12 for 63 m, LITFASS-2010: 1.17 for 43 m and 1.11 for 63 m).

The saturation correction of $C^2_{T\mathrm{LAS}}$ improves the comparison of C_T^2 obtained from the LAS and the sonic. LLSRO between $C^2_{T\mathrm{LAS}\overline{z}}$ and $C^2_{T\mathrm{sonic}\overline{z}}$ now gives a slope of 1.03 (before it was 1.17), taking both experiments together.

From C_n^2 to C_T^2- correction for humidity contribution, item c

The effect on C_T^2 of applying the various correction methods for the humidity contribution to C_n^2 is given in Table 5.2. We choose to focus on 43 m for two reasons. First, method 1 and 2 could be validated at 43 m only, because a MWS was not available at 63 m. Second, for the last three methods the corrections are identical, because we had to use the data obtained with the sonic at 50 m for the corrections at both levels.

The table shows that the correction for the humidity contribution to C_n^2 is larger for LITFASS-2009 (within 10 %) than for LITFASS-2010 (within 3%). This is expected, because the LITFASS-2009 experiment was characterized by more humid conditions. During LITFASS-2009 the noontime Bowen ratio is in the range for which M03 found the highest relative error between method 3-5 ($|\beta| < 1$). Note that M03 compared C_T^2 obtained from the three correction methods with the real value based on EC data, whereas we compare it with the uncorrected value from the LAS. As a consequence, the a we found does not give the error as is given in Fig. 8 of M03. During LITFASS-2009,

Table 5.3. Comparison of $C^2_{T\,\mathrm{M^2AV}}$ calculated using Fourier spectrum or Wavelet spectrum (y) relative to $C^2_{T\,\mathrm{M^2AV}}$ calculated using the structure function over the entire leg (x, $y = ax$), together with the coefficient of determination (r^2) and the coefficient of variation (CV)

method	a	r^2	CV
Fourier	0.96	0.98	0.14
Wavelet	0.75	0.98	0.37

the deviations between the methods are large. The correction is largest for method 5, and smallest for method 2. The two methods using the LASMWS combination (method 1 and 2) give a similar correction. The two methods of M03 based on R_{Tq} are also in this range (method 3 and 4). This indicates that the humidity correction should be approximately 5% during LITFASS-2009.

During LITFASS-2010, the deviation between the three methods is much smaller. This is to be expected, because under dry conditions (β= 3.15) the influence of humidity is negligible and the error in the three methods is similar (M03).

We conclude that C_T^2 is underestimated within about 4-5 %, by the traditional Bowen ratio method (method 5) as used in the first validation in B12 and in Fig. 5.2. In Part 3, we will therefore use method 3, because it shows similar results as the methods obtained via the LASMWS, and it has the smallest error according to M03.

Synchronizing averaging times (item d)

In order to investigate the effect of taking a different time window for the LAS data than for the M²AV, we calculate $C^2_{T\mathrm{LAS}}$ exactly over the time intervals of the flights of the M²AV during LITFASS-2009 from the 500 Hz data available. LLSRO between the $C^2_{T\mathrm{LAS}\overline{z}}$ (y) based on the 10-min interval compared to $C^2_{T\mathrm{LAS}\overline{z}}$ (x) based on the flight interval gives a slope of 0.97, $r^2 = 0.83$ and $CV = 0.21$. These results indicate that $C^2_{T\mathrm{LAS}}$ differs when measuring at shorter intervals. However, the comparison does not show a bias, which means that flight intervals of the M²AV are not systematically related to intervals with large C_T^2.

5.4.3. Part 2b: Evaluation of the determination of C_T^2 from the M²AV data

Different methods to calculate C_T^2 (item e)

Because $C^2_{T\,\mathrm{M^2AV}}$ deviates from both the C_T^2 obtained with other systems, we extensively checked the methodology and its implementation to calculate $C^2_{T\,\mathrm{M^2AV}}$. Table 5.3 shows the comparison of the three methods (see section 5.4.3) to calculate $C^2_{T\,\mathrm{M^2AV}}$. We note that the method via D_{TT} and via Fourier spectrum give similar results, which is expected because they are mathematically equivalent. Differences occur, because the first method averaged over a predefined inertial subrange between 5 and 25 m, whereas the latter takes only points within the spectrum that pass the check for the $-5/3$ slope. The wavelet method gives lower values, which would better correspond to the $C^2_{T\mathrm{LAS}}$ and $C^2_{T\mathrm{sonic}}$. One difference between the wavelet method and the other

Table 5.4. Comparison of $C^2_{T\,\mathrm{M^2AV}}$ calculated from the spatial series along the path evenly weighted ($y = W(x) = c$) or applying the path-weighting function ($y = W(x)$ from LAS) relative to $C^2_{T\,\mathrm{M^2AV}}$ calculated over the leg as a whole (x, $y = ax$), together with the coefficient of determination (r^2) and the coefficient of variation (CV)

	LITFASS-2009			LITFASS-2010		
	a	r^2	CV	a	r^2	CV
$y = C^2_{T\,\mathrm{M^2AV}\,W(x)=c}$	1.04	0.96	0.10	0.96	0.99	0.32
$y = C^2_{T\,\mathrm{M^2AV}\,W(x)\mathrm{LAS}}$	1.17	0.97	0.32	0.83	0.64	0.63

methods is that the data is first converted to spatial data using the geo-location and linear interpolation, whereas the other methods use temporal data and the mean ground speed. To investigate if this explains the differences, we calculate $C^2_{T\,\mathrm{M^2AV}}$ via the spatial structure function using the spatial dataset. The differences between these two options are small: LLSRO gives a slope of 0.97 and $r^2 = 1.00$. The reason for the lower values of the wavelet method remains unclear, it might be related to the choice of the wavelet function.

Finally, because the structure function and Fourier spectrum method show comparable results, we conclude that the method and its implementation to obtain $C^2_{T\,\mathrm{M^2AV}}$ cannot explain the larger values compared to the other instruments. Therefore, in the following paragraphs we calculate $C^2_{T\,\mathrm{M^2AV}}$ via the structure function method as described in vdK12.

Applying the LAS path-weighting function (item f)

Here, we evaluate the effect of the LAS path-weighting function on the M^{2}AV data. Before doing so, we compare the $C^2_{T\,\mathrm{M^2AV}}$ obtained over the leg as a whole ($C^2_{T\,\mathrm{M^2AV\,EL}}$) with $C^2_{T\,\mathrm{M^2AV}}$ obtained as the average of the spatial series (i.e. constant weighting, $C^2_{T\,\mathrm{M^2AV}\,W(x)=c}$, first line in Table 5.4). Both methods determine $C^2_{T\,\mathrm{M^2AV}}$ via the same method (via D_{TT}) and using the same dataset. Therefore we expect the same value. However, this is not the case. For LITFASS-2009 we observe that $C^2_{T\,\mathrm{M^2AV}\,W(x)=c}$ is larger than $C^2_{T\,\mathrm{M^2AV\,EL}}$, whereas for LITFASS-2010 we find the opposite. There are three reasons for this deviation:

1. calculating D_{TT} from a smaller dataset ($\approx$ 300 m instead of $\approx$ 3000 m, in case of $C^2_{T\,\mathrm{M^2AV}\,W(x)=c}$) increases the random error.
2. calculating D_{TT} from a smaller dataset causes that at the border of each small sample (300 m) the temperature measurements is taken into account only once (via T_i or $T_{i-\Delta i}$).
3. applying the moving window causes that in the averaged $C^2_{T\,\mathrm{M^2AV}\,W(x)=c}$ temperature fluctuations ($[T_i - T_{i-\Delta i}]$) in the centre of the entire leg are more frequently considered than at the borders. Consequently, turbulence at the borders of the leg has less influence on $C^2_{T\,\mathrm{M^2AV}}$.

The deviation due to the second reason drops out if first a dataset of the temperature deviations is obtained ($T' = [T_i - T_{i-\Delta i}]$) and then D_{TT} is determined using a moving

window over this new series. However, we choose to be consistent with vdK12, and determine D_{TT} using a moving window over the original temperature series.

Applying the path-weighting function of the LAS ($C^2_{T\,\mathrm{M^2AV}\,W(x)\mathrm{LAS}}$, second line in Table 5.4) gives larger values of $C^2_{T\,\mathrm{M^2AV}}$ for LITFASS-2009 and smaller values for LITFASS-2010. This indicates that surface heterogeneity can play a role, as the contribution of C_T^2 in the centre of the path is enhanced. During LITFASS-2009, the vegetation at the border of the path near Falkenberg was maize that was actively transpiring, whereas in the centre of the path it was dry triticale (in the south) and barley (in the north), both being senescent. Above barley and triticale the daily averaged C_T^2 was larger than above maize (see B12), which results in a net increase in C_T^2 when applying $W(x)$ from LAS.

During LITFASS-2010, the field at the southern border near Falkenberg was barley. The vegetation at the two centre fields was maize (in the south) and colza (in the north). Because LITFASS-2010 took place in July as well, we can assume that barley and colza were dry and senescent, while the maize was actively transpiring. Consequently, C_T^2 decreases when applying $W(x)$ from LAS.

For both experiments, the direction of the deviation of $C^2_{T\,\mathrm{M^2AV}\,W(x)=c}$ from $C^2_{T\,\mathrm{M^2AV\,EL}}$ and the one of the deviation of $C^2_{T\,\mathrm{M^2AV}\,W(x)\mathrm{LAS}}$ from $C^2_{T\,\mathrm{M^2AV\,EL}}$ is similar: an overestimation during LITFASS-2009 and an underestimation during LITFASS-2010. Moreover, as mentioned above, the deviation of $C^2_{T\,\mathrm{M^2AV}\,W(x)\mathrm{LAS}}$ from $C^2_{T\,\mathrm{M^2AV\,EL}}$ is related to the smaller contribution of the vegetation at the southern field at the border relative to fields in the centre. This indicates that the third reason in the list above has the main impact in the deviation of $C^2_{T\,\mathrm{M^2AV}\,W(x)=c}$ from $C^2_{T\,\mathrm{M^2AV\,EL}}$.

In order to investigate if C_T^2 calculated from D_{TT} based on a moving window can be used to study the effect of surface heterogeneity on C_T^2 (as done in vdK12), we compare the spatial series of C_T^2 using this method with the wavelet method (Fig. 5.3). We already observed that the averaged values of the wavelet method were lower, so we focus now on the spatial pattern of both methods. Figure 5.3 shows that the spatial pattern of the two methods is similar. This means that, while for both methods the average value differs, they can both be used to indicate the relative effect of surface heterogeneities on C_T^2 along a leg, which was the main goal of vdK12. In order to remove time varations, vdK12 normalized the spatial series of $C^2_{T\,\mathrm{M^2AV}}$ with $C^2_{T\,\mathrm{M^2AV}}$ over the entire leg. Note that for the latter only $C^2_{T\,\mathrm{M^2AV}\,W(x)=c}$ can be used, because of the differences between $C^2_{T\,\mathrm{M^2AV\,EL}}$ and $C^2_{T\,\mathrm{M^2AV}\,W(x)=c}$.

Another issue might be whether the path-weighting function should be applied before or after the height normalization. The differences between these two options are less than one percent. First applying the height normalization needs spatial information of the flight level. This is not available for the legs where the height above the surface was not well measured, therefore, we applied the path-weighting function first in our analysis.

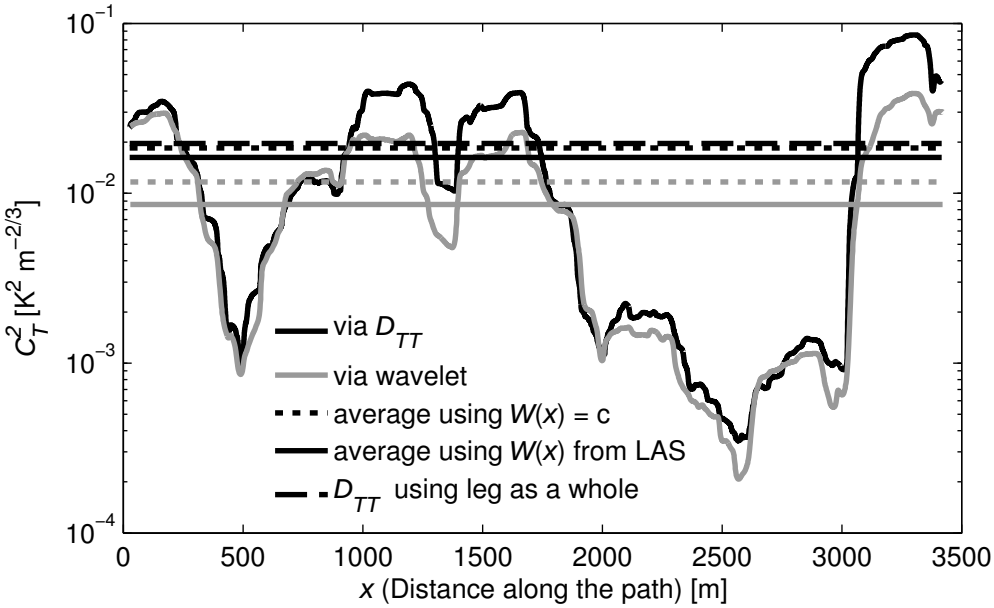

Fig. 5.3. The variation of $C^2_{T\mathrm{M^2AV}}$ along the scintillometer path during one leg for the structure function method (black lines) and for the wavelet method (grey lines). Together with the averaged values along the leg: constant weighted (dotted horizontal line, $y = W(x) = c$), applying the path-weighting function (solid horizontal line, $y = W(x)$ from LAS), and calculated over the leg as a whole via the structure function (dashed line)

5.4.4. Part 3: Effect of the elaborate data processing

In this section we investigate if the differences between $C^2_{T\mathrm{M^2AV}}$ and $C^2_{T\mathrm{LAS}}$ can be reduced or explained by applying the more elaborate data processing. The effect on C_T^2 is shown in Fig. 5.4.

We here calculate $C^2_{T\mathrm{LAS}}$ and $C^2_{T\mathrm{M^2AV}}$ as follows: $C^2_{T\mathrm{LAS}}$ is corrected for saturation, it is corrected for humidity using Eq 8 of M03, and it is both averaged over 10 min and averaged over the time window during the flight legs. $C^2_{T\mathrm{M^2AV}}$ is calculated via D_{TT} as proposed by vdK12 (item e) and applying the path-weighting function (item f). As already expected from the results of the analysis of Sect. 5.4.2 and Sect. 5.4.3 the normalized difference between $C^2_{T\mathrm{M^2AV}}$ and $C^2_{T\mathrm{other}}$ decreases, but is still substantial in most cases.

Applying the two corrections for the LAS improves the correlation between the sonic and LAS. Now, LLSRO between $C^2_{T\mathrm{LAS}\overline{z}}$ and $C^2_{T\mathrm{sonic}\overline{z}}$ has a slope of 1.00 and a r^2 of 0.47, taking data from both experiments together. The slope of 1.00 indicates that C_T^2 does not show system deviations for these datasets, although the footprints of the two instruments differ (point versus path-averaged). It is therefore unlikely that the reason for the observed differences between LAS and M^{2}AV is the fact that the M^{2}AV legs covered only the southern 70 % of the LAS path and missed the village of Lindenberg.

When comparing $C^2_{T\mathrm{LAS}}$ calculated for exactly the time intervals of the aircraft, we

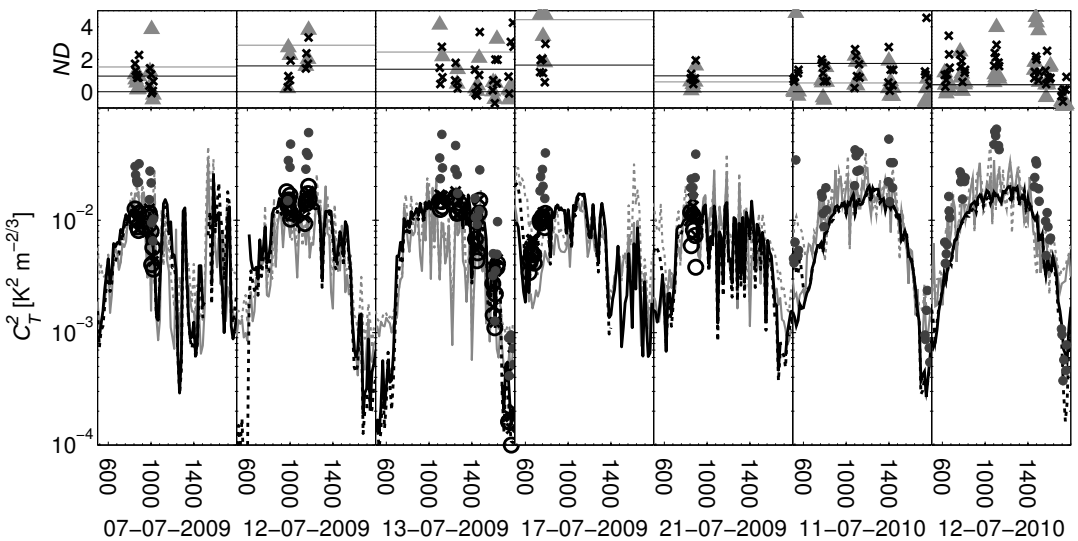

Fig. 5.4. The daytime evolution of $C^2_{T\mathrm{LAS43m}}$ (solid black line), $C^2_{T\mathrm{LAS63m}}$ (dashed black line), $C^2_{T\mathrm{M^2AV}}$ (grey circles), $C^2_{T\mathrm{sonic50m}}$ (solid grey line), and $C^2_{T\mathrm{sonic90m}}$ (dashed grey line) during the flight days of LITFASS-2009 and LITFASS-2010 experiments after applying the more elaborate data processing see Sect. 5.3 and Table 5.5 for the applied methods and corrections to obtain C_T^2. The black symbols represents $C^2_{T\mathrm{LAS}}$ during the flight legs ($\times$ is $C^2_{T\mathrm{LAS43m}}$ and $\circ$ is $C^2_{T\mathrm{LAS63m}}$). The top panel shows the normalized difference between $C^2_{T\mathrm{M^2AV}}$ and the other instruments for each leg ($\times$ $ND_{\mathrm{M^2AV,LAS}}$ and $\triangle$ $ND_{\mathrm{M^2AV,sonic}}$, in which $ND_{\mathrm{M^2AV,other}} = \left(C^2_{T\mathrm{M^2AV}} - C^2_{T\mathrm{other}\overline{z}}\right)/C^2_{T\mathrm{other}\overline{z}}$) and the daily averaged value (black lines $ND_{\mathrm{M^2AV,LAS}}$ and grey lines $ND_{\mathrm{M^2AV,sonic}}$).

refer to our conclusion in Sect. 5.4.2; namely that the time intervals of the M^{2}AV are not coincidentally related to the moments with large values of $C^2_{T\mathrm{LAS}}$ and cannot explain the differences between the two instruments.

5.5. Conclusions and Outlook

This study shows an elaborate comparison of the structure parameter of temperature, C_T^2, from two LAS, the M^{2}AV, and two sonic anemometers during the LITFASS-2009 and LITFASS-2010 experiments. It is an extension of the study of Beyrich et al. (2012), who found that the C_T^2 obtained with M^{2}AV is larger than C_T^2 from LAS for one flight day when data from LAS and M^{2}AV were processed using standard procedures.

We conclude that for the other measurement days during LITFASS-2009 and LITFASS-2010 similar differences can be found. $C^2_{T\mathrm{M^2AV}}$ overestimates both $C^2_{T\mathrm{LAS}}$ and $C^2_{T\mathrm{sonic}}$. A more elaborate data analysis did improve the agreement between $C^2_{T\mathrm{LAS}}$ and $C^2_{T\mathrm{sonic}}$, but did not substantially improve the agreement of $C^2_{T\mathrm{M^2AV}}$ on the one hand and $C^2_{T\mathrm{LAS}}$ and $C^2_{T\mathrm{sonic}}$ on the other hand.

Furthermore, from the more elaborate data analysis we learn that

- it is important to apply the saturation correction for the LAS at 43 m and 63 m along the 5 km scintillometer path between Falkenberg and Lindenberg,
- during the LITFASS-experimenst the correction for humidity should be performed,

based on the correlation between T and q and the standard deviation of T and q (method 3). The use of the Bowen ratio method underestimates the true C_T^2 during LITFASS-2009, which agrees with the study of M03,

- calculating $C_{T\mathrm{M^2AV}}^2$ with structure functions or Fourier spectrum gives similar results, whereas the wavelet method gives lower C_T^2, which might be related to the choice of the wavelet function,
- $C_{T\mathrm{M^2AV}}^2$ obtained from the structure function determined over the leg as a whole differs from the leg-averaged value obtained from a spatial series of $C_{T\mathrm{M^2AV}}^2$ values determined over sections of the leg and using a moving window,
- the spatial pattern of $C_{T\mathrm{M^2AV}}^2$ along the leg is consistent between the structure functions applying a moving window and the wavelet method.

Finally, we have to conclude that the deviations between $C_{T\mathrm{M^2AV}}^2$ on the one hand, and $C_{T\mathrm{LAS}}^2$ and $C_{T\mathrm{sonic}}^2$ on the other hand cannot be explained so far. Therefore, we recommend further experimental studies. A useful modification of the measurement strategy for any new experiment is to use multiple unmanned aircraft flying synchronously along the scintillometer path, in order to obtain statistical information on $C_{T\mathrm{M^2AV}}^2$ as well.

Another reason could be related to the determination of $C_{T\mathrm{M^2AV}}^2$ from a temperature dataset that varies in time and space. The amount of variation in time and space is related to the mean ground speed. It might be possible that $C_{T\mathrm{M^2AV}}^2$ can only be determined from a temperature dataset that varies only in space if an aircraft flies extremely fast, or from a temperature dataset that varies only in time as is the case for the sonic. In order to investigate this we propose to initiate a sensitivity analysis of C_T^2 from virtual flights in a Large Eddy Simulation model with different mean ground speeds.

Acknowledgements

We thank Sabrina Martin (Technische Universität Braunschweig) for collecting and Andreas Platis (Eberhard Karls Universität Tübingen) for processing the data of the M^{2}AV. Moreover, the discussions with Jens Bange (Eberhard Karls Universität Tübingen), Andreas Platis and Oscar Hartogensis (Wageningen University) were very helpful. Finally, we like to thank Bram van Kesteren (Deutscher Wetterdienst) for reading and commenting on the manuscript. The research has been supported financially by the German Research Foundation (DFG) in the framework of the project: 'Turbulent Structure Parameters over Heterogeneous Terrain - Implications for the Interpretation of Scintillometer Data' (through grant BE2044/3-1, BE2044/3-2, BE2044/3-3).

5.A. Overview of the options used for the data processing

Table 5.5. Overview of the options used for the elaborate data processing in this study.

	explanation method			results		
correction	Sect.	specification	references	Sect.	Fig. 5.2	Fig. 5.4
All instruments						
a normalization to one z	5.2.4	via MOST, 50 m	-	5.4.1	✓	✓
LAS	5.2.1					
b saturation	5.2.1	-	Kleissl et al. (2010)	5.4.2		✓
c humidity	5.2.1	1. $covar_{\ln(I\mathrm{LAS}),\ln(I\mathrm{MWS})}$	Ward et al. (2013)	5.4.2		
		2. R_{Tq}	Hill (1989)			
		3. R_{Tq}, σ_T, σ_q	Eq. 8 of M03			✓
		4. R_{Tq}, β	Eq. 11 of M03			
		5. β	Eq. 12 of M03		✓	
d synchronizing time	5.2.1	only LITFASS-2009	-			✓
M^{2}AV	5.2.2					
e methods C_T^2	5.2.2	1. D_{TT}	vdK12	5.4.3	✓	✓
		2. Fourier spectrum	Hartogensis et al. (2002)			
		3. Wavelet spectrum	Maronga et al. (2013)			
f applying $W(x)$	5.2.2	1. leg as a whole[1]	-	5.4.3	✓	
		2. moving window[1] - $W(x) = c$	-			
		3. moving window[1] - $W(x)$LAS	-			✓

1. using D_{TT}

6 Summary

6.1. Atmospheric turbulence and scintillometry

Atmospheric turbulence is the main vertical transport mechanism in the atmospheric boundary layer (ABL). The surface fluxes related to this turbulent transport are the sensible (H) and latent heat fluxes (LE). Their strength depends, among others, on the location on earth, date and time. One way to determine H and LE is using scintillometers. A scintillometer system consists of an electromagnetic beam transmitter at one end of a propagation path and a receiver at the other end. The length of the propagation path is of the order of 1 up to 5 km for the scintillometers used in this study. The intensity of the electromagnetic signal at the receiver varies due to fluctuations in the refractive index of air (n) caused by turbulence along the path. The magnitude of these fluctuations is proportional to the path-averaged structure parameter of the refractive index of air (C_n^2). From C_n^2 the structure parameter of temperature (C_T^2) and of humidity (C_q^2) can be derived. C_T^2 and C_q^2 are measures of the turbulent fluctuations in temperature and humidity within the inertial subrange of the turbulence spectrum. The relative contribution of C_T^2 and C_q^2 to C_n^2 depends on the wavelength emitted by the scintillometer. Large aperture scintillometers (LAS, operating at wavelengths in the visible and the near-infrared) are mainly sensitive to C_T^2, while for microwave scintillometers (MWS, operating at millimetre wavelengths) C_T^2 and C_q^2 are equally important (Hill et al., 1992; Ward et al., 2013). Finally, C_T^2 and C_q^2 are used to determine path-averaged H and LE via Monin-Obukhov similarity theory (MOST).

Monin-Obukhov similarity theory (MOST) is based on dimensional analysis (Monin and Obukhov, 1954; Foken, 2006). As such it uses universal functions to link surface fluxes to other turbulent quantities, i.e. structure parameters in case of scintillometry. MOST is restricted to homogeneous and stationary conditions and to the part of the atmosphere close to the surface: the atmospheric surface layer (ASL). Within the ASL turbulence is controlled by surface processes, whereas other processes in the ABL, such as entrainment and advection are neglected. The depth of the ASL, estimated as the lowest 10 % of the ABL, is not constant during the day. In the afternoon, when turbulence is strong, it will reach its maximum, whereas during the morning and at

night, it will be relatively shallow.

The area-averaged values of the fluxes are of interest for many meteorological applications, e.g. to evaluate mesoscale numerical weather models and satellite-based retrieval algorithms. Natural landscapes are often heterogeneous, i.e. H and LE differ among fields. This makes scintillometry a more suitable method for obtaining area-averaged fluxes over natural landscapes than traditional point measurements. During the past twenty years, scintillometry has proven to be a reliable method for determining the area-averaged flux over heterogeneous surfaces (e.g. Meijninger et al., 2002b; Beyrich et al., 2005; Kohsiek et al., 2006)). However, there are still open issues that require further research. The four questions answered in this thesis are related to the applicability of MOST (chapters 2 and 3) and to the behaviour of structure parameters over heterogeneous surfaces (chapters 4 and 5). All together, the primary motivation of this thesis is to better understand and quantify the scintillometer signal in terms of the structure parameter.

For our studies we used meteorological data of three sites. We confine ourselves to observations obtained during daytime: under unstable conditions when turbulence is mainly produced by buoyancy. Because MOST is restricted to homogeneous surface conditions, the first two questions (chapter 2 and 3) related to the applicability of MOST are answered with data measured at sites with relatively homogeneous surface conditions (Cabauw; the Netherlands, and CASES-99; Leon; Kansas; USA, in which CASES stands for Cooperative Atmosphere-Surface Exchange Study). The last two questions (chapter 4 and 5) are answered using data from two experiments with moderately heterogeneous surface conditions (LITFASS-2009 and LITFASS-2010; Lindenberg; Germany, in which LITFASS stands for LIndenberg-To-Falkenberg Aircraft Scintillometer Study). For the first three research questions we obtain C_T^2 from point measurements rather than from scintillometers, despite that understanding of the scintillometer signal is the primary motivation.

6.2. The applicability of MOST

6.2.1. On Monin-Obukhov scaling in and above the ASL

One limitation of scintillometry is that the theory behind it is only valid for the weak scattering regime, because in case of stronger scattering the signal gets saturated. One way to prevent saturation is to install the scintillometer at a higher level, because C_s^2 decreases with height. However, a disadvantage of installing the scintillometer at more elevated levels is that the observation level might be located outside the ASL if the ASL is shallow. In that case the validity of MOST can be questioned. This brings us to the first question that is answered in chapter 2:

Question 1 - To what extent can the sensible heat flux be determined from the structure parameter of temperature observed at elevated levels, particularly during the morning period when the measurement level is situated above the

atmospheric surface layer?

In order to answer this question, two concepts to determine H from C_T^2 are proposed and compared. In the first concept, MOSTs, C_T^2 scales with the *s*urface heat flux, and thus it is based on the assumption that MOST still applies at levels just above the ASL. In the second concept, MOSTl, C_T^2 scales with the *l*ocal heat flux rather than with the surface heat flux, which is comparable with the local scaling hypothesis used in the stable boundary layer (Nieuwstadt, 1984). To obtain the surface heat flux, a correction for the flux divergence in the column below the level of observation has to be applied.

We calculate C_T^2 with the two MOST concepts using flux observations (MOST in the reverse way), and compare them with C_T^2 directly derived from sonic anemometer/ thermometer (sonic) measurements at 60-m height on the Cabauw tower. In the analysis, we distinguish two time periods: the early morning and the afternoon. During the early morning, the 60-m level is located above the ASL and MOST can be questioned, whereas during the afternoon, the 60-m level is located within the ASL and MOST is likely to be valid.

In the afternoon both concepts give results that are comparable to the values of C_T^2 directly derived from sonic measurements. In the morning, our data do not unequivocally support one of the two concepts. Firstly, the peak in C_T^2 that occurs when the measurement height is located in the entrainment zone disqualifies the use of MOST at that moment. Secondly, MOSTl shows the correct temporal behaviour, the time of the zero flux corresponds with the time of the C_T^2 minimum, but underestimates C_T^2 by a factor of ten. Thirdly, a linear least squares regression shows that the slope is closer to one for MOSTl, whereas the offset is closer to zero for MOSTs. Finally, the correlation between C_T^2 observed directly and estimated with the two concepts is low and similar for MOSTl and MOSTs. For all these reasons, we conclude that MOST is not applicable for the morning hours when the observation level is located above the ASL.

6.2.2. Dependence on regression approach, observation height and stability range

The universal function that links H and C_T^2 within MOST ($f\,(z/L)$, where z is the height, and $1/L$ is a measure of the stability) needs to be determined empirically. In literature a great variety of the similarity functions can be found. One reason for this variation is that these studies differ in experimental design, instrumentation and data processing. In chapter 3 we therefore used one single dataset (CASES-99) to answer the following question:

Question 2 - To what extent is the expression for the dimensionless structure parameter influenced by specific regression approaches, stability ranges and observation levels?

The advantage of using one single dataset is that we can exclude other causes of variation, such as differences in data processing, instrumentation and surface characteristics.

We confine ourselves to the most commonly used shape of $f(z/L)$ for unstable conditions, which describes the relation by a power law and two empirical coefficients c_1 and c_2: $f(z/L) = c_1 (1 - c_2 z/L)^{-2/3}$.

In the first part of our research, we evaluate regression approaches that differ in four aspects: the logarithmic transformation of data, the mathematical regression methods, weighing of the data i.e. taking into account the measurement accuracy of each data point, and the number of regression coefficients to fit. The results show that applying various regression approaches has an impact on the regression coefficients c_1 and c_2. This means that studies always should specify the regression approach, when presenting similarity relations. We advice to use an orthogonal distance regression method, applied to the logarithmic transformation of both dimensionless groups, and weighted such that unreliable data points have a smaller influence on the fit.

Dividing the dataset in eight z and eight $1/L$ classes we show that the observation height and the stability range have an impact on the coefficients too. This implies that variations in c_1 and c_2 found in literature may result from variations in the height and stability ranges among the datasets. Furthermore, application of a given $f(z/L)$ on a dataset measured at a different height or within a different stability range has to be done with care. Finally, the variation in the coefficients between the classes indicates that the Monin-Obukhov similarity function for C_T^2 is not sufficiently described by the two-coefficient function used here.

6.3. C_s^2 over heterogeneous surfaces

Knowledge about the variability of C_s^2 over a heterogeneous surface is important, because the MOST relation between C_s^2 and the fluxes assumes homogeneous surface conditions.

6.3.1. Variability of C_T^2 and C_q^2 observed in the ASL

Whether variations in C_s^2 along a scintillometer path or aircraft flight leg are within the range of local variability in C_s^2, or whether they could be attributed to surface heterogeneity, we formulate the following question in chapter 4:

Question 3 - What determines the local variability of the structure parameter within the atmospheric surface layer at different heights and under different stability regimes?

In this study, we focus on the logarithm of the Monin-Obukhov-scaled structure parameters for temperature and humidity (denoted as $\log(\widetilde{C_s^2})$), where C_s^2 is determined over a range of averaging windows varying from 1-10 min. We use 1 month of observations from EC systems installed at 2.5 m over a triticale field and at 50 m, and 90 m at the 99-m tower in Falkenberg during the LITFASS-2009 experiment.

We find that the variability of $\log(\widetilde{C_s^2})$ is determined by stability and by the size of the averaging window over which $\log(\widetilde{C_s^2})$ is calculated. If instability increases, differences

in $\log(\widetilde{C_s^2})$ between upward motions (large C_s^2) and downward motions (small C_s^2) increase. The differences are, however, not sufficiently large to result in a bimodal overall probability density function.

If the averaging window size increases, the variance of $\log(\widetilde{C_s^2})$ decreases. A rough estimation of this decrease is made by fitting a simple linear regression between the variances of $\log(\widetilde{C_s^2})$ and the averaging window size. From this we found that for various stability classes both the offset and slope (in absolute sense) decrease with increasing instability. For temperature, the offset and slope from the three heights show comparable results. For humidity, in contrast, the offset and slope are larger at 50 m and 90 m than at 2.5 m.

The offset and slope can be used to quantify the local variability for averaging times down to 1 min for a given stability range. This in turn can give an indication if variations in C_s^2 along a scintillometer or flight path might be attributed to surface heterogeneity.

6.3.2. A comparison of C_T^2 from LAS and unmanned aircraft measurements

In the final chapter we answer the following question:

Question 4 - To what extent are the path-averaged structure parameters of large aperture scintillometers in agreement with the structure parameters obtained with an unmanned aircraft?

This study is an elaboration of the study of Beyrich et al. (2012). They compared C_T^2 obtained with the unmanned meteorological mini aerial vehicle (M^2AV) with C_T^2 obtained with the LAS for five flights on one single day during LITFASS-2009. Processing the data using standard procedures, they found that C_T^2 obtained from the M^2AV data is systematically larger than from the LAS data. Here, we investigate if similar differences can be found for other days, and if these differences can be reduced or explained through a more elaborate processing of both the LAS data and the M^2AV data.

We conclude that the difference reported in Beyrich et al. (2012) can be found for other days during LITFASS-2009 and LITFASS-2010 as well. C_T^2 obtained from the M^2 AV data is larger than from the data of the LAS and the sonic. A more elaborate data analysis does not substantially improve the results. Moreover, an exact synchronization of the LAS data with the time intervals of the M^2AV data does not eliminate the discrepancy between both datasets. Consequently, the deviation between C_T^2 from the M^2AV on the one hand and from the LAS and sonic on the other hand cannot be explained so far.

7 Discussion and Recommendations

This thesis shows four different aspects related to the behaviour of C_s^2 under conditions that are near the limits of MOST, and therefore scintillometry. There are, however, several issues that were not discussed in the thesis, and new questions that arose. In this section, our results are therefore discussed and placed in a broader perspective. We again start with the subjects presented in this thesis: applicability of MOST (Section 7.1) and C_s^2 over heterogeneous surfaces (Section 7.2). Following, we focus on subjects that were of relatively lesser importance within this thesis: the structure parameter of humidity (Section 7.3); determination of C_n^2 using LAS (Section 7.4); differences in obtaining turbulent fluxes using scintillometry or using eddy covariance methods (EC, Section 7.5).

7.1. The applicability of MOST

From the study in chapter 2 we learned that the use of MOST is not always justified when the ASL is shallow and the observation level is located above the ASL. These findings are based on data obtained during unstable conditions during the morning period. It is, however, likely that MOST has also to be questioned during stable conditions, when the ASL is very shallow and turbulence at an elevated level can be decoupled from the surface.

In our study, we used the simple estimation of the ASL depth as the lowest 10 % of the ABL. The value of 10 % has the following background. First, the heat fluxes are not allowed to diverge more than 10 % within the ASL, in order to ensure that turbulence is only controlled by surface processes. Second, if we assume –for simplicty– that there is no entrainment flux, and the flux profile is linear in the ABL, the 10 % decrease in flux corresponds to the lowest 10 % of the ABL-depth. During the morning period, however, the divergence of the sensible heat flux can be larger than 10 % over the lowest 10 % of the ABL. For instance, we observed a decrease in the flux with ≈ 22 % during the morning transition. Moreover, the entrainment ratio (the entrainment flux divided by the surface flux) of latent heat is often much larger than 0 (Maronga, 2014; van de Boer et al., 2013, see also 7.3). In such cases processes other than surface processes

play an important role even when the observation level is located within the ASL using the above simple definition.

During recent years, also other similarity relations have been proposed in order to take into account entrainment processes (Laubach and McNaughton, 2009; van de Boer et al., 2014) for turbulence quantities other than structure parameters, e.g. spectra and variances. In these studies the relevant height scale in the dimensional analysis is not only the observation height, but also the ABL depth and entrainment flux. This makes it not a practical solution for scintillometry, because it requires extra additional observations not routinely available. Moreover, it can be questioned if this is a necessary extension for C_s^2. This is because these studies show deviations of spectra at larger scales, but at scales within the inertial subrange, where C_s^2 is determined, the spectrum scales already correctly with traditional scaling parameters (Laubach and McNaughton, 2009).

The study in chapter 3 shows that in determining the functional shape of MOST, the results are affected by the regression approach, measurement height and stability range. We used the most common shape of the MOST function with two coefficients. This shape splits the data in two regimes: the near-neutral range and the free-convection range. However, our results suggest the existence of three regimes (near-neutral range, transition range, and a free-convection range), which indicates that the function with two coefficients is probably not sufficiently flexible to describe $f\,(z/L)$. Using an alternative shape with more coefficients (e.g. Wesely (1976b); Thiermann and Grassl (1992)) can be a solution. There are, however, also several disadvantages. First, the shape of Wesely (1976b) is only applicable up to $-z/L = 1$. Second, our study shows that under some conditions it is already difficult to fit two coefficients simultaneously, and using an extra coefficient would create additional uncertainty. Furthermore, it is not a priori clear whether each coefficient is sensitive to one particular stability regime.

So in the end, we conclude that the use of MOST to obtain fluxes from structure parameters is not always that straightforward and calls for further research.

7.2. C_s^2 over heterogeneous surfaces

At the end of chapter 4, we discuss how our findings on the variability of C_s^2 can give an indication if variations in C_s^2 along a scintillometer or flight path might be attributed to surface heterogeneity using an hypothetical example. It would, however, be of more interest to discuss this based on real data. Therefore, we propose to investigate if the variability in C_T^2 observed by the M^{2}AV during LITFASS-2010 as shown by van den Kroonenberg et al. (2012) can really be attributed to surface heterogeneity. This consists of two steps. First, the local variability of $\log(\widetilde{C_T^2})$ has to be estimated with the results of the simple linear regression given in chapter 4, using $-z/L_{10\,\mathrm{min}}$ obtained from e.g. EC data. This estimate indicates the local variability expected under the given atmospheric conditions. Only if differences in $\log(\widetilde{C_T^2})$ between patches of different land use exceed this value it can be attributed to surface heterogeneity. Therefore, as a second step,

the variability found by van den Kroonenberg et al. (2012) has to compared with this estimate.

There are a number of remaining issues following from the study of chapter 4. First, the difference in variability of C_T^2 and of C_q^2 is still unexplained. Second, the apparent discontinuity between the variability of C_s^2 at $z = 2.5$ m on the one hand and those at $z = 50$ m and at $z = 90$ m on the other hand calls for an investigation using data with a more dense spacing in the vertical such as the CASES-99 dataset.

In chapter 5 the path averaged C_T^2 from LAS is compared with the C_T^2 obtained with M^{2}AV during the LITFASS-2009 and LITFASS-2010 campaigns. The reason for the deviation of C_T^2 obtained with the M^{2}AV with respect to the LAS and to the sonic remains unexplained to large extent. Therefore, we would recommend to repeat the field experiments, and then to use multiple unmanned aircraft flying synchronously along the scintillometer path, in order to obtain statistical information about calculating C_T^2 from the M^{2}AV.

The ultimate goal of the LITFASS-2009 experiment[1] was to compare the path averaged C_T^2 from the LAS measured with the M^{2}AV data, LES data from the PArallelized LES Model (PALM Raasch and Schröter, 2001) and an aggregated C_T^2 obtained from the surface stations over the different fields along the path (see figure 1.4). The comparison of C_T^2 obtained with all these methods would then give a comprehensive picture of C_T^2 in the ASL. So far, only the LAS data is compared with M^{2}AV data (chapter 5).

The reason that no LES has been based on LITFASS-2009 is that during this experiment the meteorological conditions were unfavourable to simulate the daytime ABL evolution. There were no clear sky conditions during an entire day, and the geostrophic wind speed was too large. Therefore, the PALM simulations focussed on data of the LITFASS-2003 experiment (Maronga, 2014; Maronga et al., 2014). The disadvantage of using this experiment is that no airborne measurements where performed at the levels of the LAS between Falkenberg and Lindenberg. Using data from LITFASS-2010 was not an option either, because for this experiment H and LE at the different fields within the LES domain were not measured, which would be needed as input data for PALM.

The PALM studies based on LITFASS-2003 data are used to investigate the applicability of the blending height concept. This concept assumes that over heterogeneous terrain MOST is only valid above the blending height (z_b), where the influence of the individual patches is not visible anymore due to turbulent mixing. Maronga et al. (2014) showed that the influence of the individual patches over the heterogeneous surface along the LAS path between Falkenberg and Lindenberg is still present in the structure parameters up to 100-200 m. This is in agreement with another LES study (Dutch Atmospheric LES Heus et al., 2010) based on an idealized heterogeneous striped surface pattern (van Laar, 2013). Van Laar (2013) found that the blending height, ranges from 70-955 m, which is larger than the 8-15 m based on a thermal blending height

[1] DFG-NWO project 'Turbulent Structure Parameters over Heterogeneous Terrain - Implications for the Interpretation of Scintillometer Data'

expression given in Bange et al. (2006). Both studies indicate that the measurement level of the scintillometers during the LITFASS experiments is below z_b. As a consequence, the blending height concept cannot be used for the LAS between Falkenberg and Lindenberg. This is because differences in C_s^2 of individual patches along the path are visible in the path-averaged C_s^2. Moreover, the study of van Laar (2013) found that the domain-averaged C_s^2 over the heterogeneous surface differs from that over the homogeneous surface, whereas the averaged prescribed surface fluxes are identical. Both findings create extra uncertainty in the use of MOST to obtain the fluxes.

One reason why we did not consider the aggregated C_T^2 from the meteorological stations is that the inter-comparison study of different laser scintillometers (SLS, Scintec) that took place just before LITFASS-2009 showed differences in C_T^2 between the instruments (Beyrich et al., 2012). These differences were unexplained so far, but can probably be reduced with the new calibration procedure of the SLS that can be applied retroactively (Van Kesteren et al., 2013).

Moreover, there are still some open questions related to obtaining an aggregated C_T^2. An aggregated C_T^2 can be obtained using footprint models, see the examples given by Meijninger (2003); Meijninger et al. (2006). It is, however, unclear whether these footprint analyses can be applied for C_T^2 because of two reasons. First, footprint models have been formulated for measurements of concentrations and fluxes. In these analyses the distribution of the surface source and sink strength is combined with a footprint function. These functions are based on diffusion (e.g. Gaussian diffusion), advection-diffusion or dispersion equations (Schmid, 2002). C_s^2, however, is a property of a turbulent field and it is neither transported (as in case of a concentration) nor is it a direct measure of the transport (as in case of the fluxes). Second, the footprint functions differ for each atmospheric quantity, e.g. between T and q (Schmid, 2002), and have to be defined for structure parameters before they can be used to calculate aggregate values.

As a further research step, we therefore propose to evaluate if the footprint models for concentrations or fluxes can be used for structure parameters. One way to evaluate this, is to apply to C_s^2 the method used by van de Boer et al. (2013) for evaluating analytical flux footprints. They compared observed fluxes at a station on the edge of two fields to fluxes that were obtained by combining observed fluxes in the centre of those fields, using the relative contribution of the fields derived with different footprint models.

7.3. The structure parameter of humidity

Within chapters 2, 3, 5 we focussed on C_T^2 only, whereas for obtaining LE from scintillometry the MOST relation for C_q^2 is needed. The focus on C_T^2 has two reasons. First, fast response hygrometers were unavailable at the tower during the CASES-99 experiment and at the M^2AV during the LITFASS experiments. Second, the evaluation of C_q^2 had less practical need until now. To obtain C_q^2 from scintillometry, a two-wavelength

scintillometer system –a combination of a LAS and a MWS– is needed. The LAS is available commercially and is in long term operational use at several places (Beyrich et al., 2002), whereas the MWS is still in a prototype stage (only few experimental instruments exist) mainly used during research campaigns (among others Beyrich et al., 2012; Leijnse et al., 2007).

In the coming years, however, this situation is expected to change because of a successful cooperation[2] that has lead to the development of the prototype of a commercial MWS by Radiometer Physics GmbH. This would make research into the behaviour of C_q^2 also of more practical interest.

There are also other reasons why research into the behaviour of C_q^2 is important. First, its behaviour seems to be different from C_T^2 (Li et al., 2012; Maronga, 2014). This contradicts with the theory where the similarity relations for C_q^2 and C_T^2 are necessarily equal. The equality is based on the standard assumption of MOST (stationary and homogeneous conditions, turbulence is controlled by surface processes only) and that the correlation between temperature and humidity (R_{Tq}) is one. However, within the ASL R_{Tq} is observed to be smaller than one because of several reasons (Katul et al., 2008). Li et al. (2012) show that a small value of R_{Tq} leads to a deviation in the shape of the MOST relations of C_T^2 and C_q^2. Based on a sensitivity study with large-eddy simulation (LES), Maronga (2014) found that both C_T^2 and C_q^2 follow MOST if $R_{Tq} \approx 1$. If, however, $R_{Tq} < 1$, e.g. due to dry air entrainment, the behaviour of C_q^2 deviates from MOST.

The bigger impact of entrainment on C_q^2 than on C_T^2, in such cases, can cause that at a certain height the impact of surface heterogeneity is less visible for C_q^2 than for C_T^2. In other words, the level up to which surface heterogeneity is visible is lower for C_q^2 than for C_T^2, as is also observed with LES by Maronga et al. (2014) and van Laar (2013). Because this level is then an indirect effect of dry air entrainment, it is not the same as the z_b. Above this level MOST is still not valid, which has to be considered when studying the blending height concept.

Second, observations of C_q^2 can be used to investigate the behaviour of MOST within the near-neutral regime. Under near-neutral conditions $\widetilde{C_T^2}$ is sometimes unreliably large. The reason for the large values of $\widetilde{C_T^2}$ is as follows. For near-neutral conditions H is small, whereas temperature fluctuations may still be finite (but uncorrelated to the vertical wind speed). As H is small, a small error in absolute sense can be large in relative sense. Moreover, an underestimation in H results in a larger deviation in $\widetilde{C_T^2}$ than an overestimation in H. For instance, an error of 20 % in H leads to an increase in $\widetilde{C_T^2}$ of 25 % if H was underestimated, but to a decrease of 16 % if H was overestimated. In these near-neutral periods LE can be still substantial, and therefore the error in $\widetilde{C_q^2}$ is smaller.

All together, for the reasons as given above, we would propose to focus on the be-

[2] within the STW project 'WTC7484: Innovations in Scintillometry - Measuring surface fluxes of water vapour, sensible heat and momentum on field to kilometre scales'

haviour of C_q^2 in coming research.

7.4. Scintillometer measurements

Scintillometers do not measure C_s^2 directly, but C_n^2 is obtained from the variance of the logarithmic intensity $\sigma^2_{\ln I}$. As is shown in appendix A, it appears that $\sigma^2_{\ln I}$ differs between two calculation methods. The deviation between these two methods could be the reason for the underestimation of C_n^2 obtained from the LAS of scintec (BLS900) compared to those from the LAS of WUR (WURLAS), as it was found from long-term intercomparison study (personal communication: Frank Beyrich, Bram van Kesteren, MOL-RAO, 2012-2013). It was shown that the difference between BLS900 and WURLAS depends on the mean cross-wind along the path. The exact reason for this deviation is still not clear. In order to investigate if the differences between between the two instruments can be related to the differences of the two methods, we recommend to investigate if the latter does also show a cross-wind dependency. The intercomparison study and the study in appendix A, both used data along the same path (Lindenberg-Falkenberg), and therefore we propose to investigate if the deviation is also visible for other datasets.

7.5. Turbulent Fluxes

In order to validate MOST (chapter 2 and 3) and to better understand the variability of the local structure parameter (chapter 4) turbulent fluxes were used. In our case, we obtained these fluxes using EC technique. However, we would like to make some remarks related to obtaining fluxes with EC (Van Kesteren, 2012, among others):

- EC systems measure at one point, whereas scintillometers measure along a path;
- EC observations are sensitive to flow distortion by the mast or instrument, whereas scintillometer observations are not;
- In order to obtain the flux with an EC system all eddy scales relevant contributing to the flux have to be sampled, whereas scintillometers are only sensitive to eddy scales within the inertial subrange;
- In order to sample the largest eddy scales EC needs a period of stationary conditions (Lee et al., 2004), whereas scintillometers allow small flux averaging times because they combine spatial and temporal averaging;

Moreover, although EC is a direct method to determine the turbulent fluxes, afterwards several corrections have to be applied. For instance, humidity correction for the sonic temperature (Schotanus et al., 1983; Liu et al., 2001), corrections for spectral loss due to path averaging and sensor separation (Moore, 1986), and a correction for the rotation of the wind components of the sonic (Wilczak et al., 2001). A sensitivity study of Mauder et al. (2007) shows that different options in applying these corrections resulted in a deviation of 10 % for H and 15 % for LE. The uncertainty in the EC fluxes is an important issue in micro-meteorology, because it can be one of the reasons for the

non closure of the surface energy balance as it is often observed with experimental data ($Q^* + G \neq H + LE$, in which Q^* is the net radiation, and G is the soil heat flux).

While scintillometry has many advantages over EC, its disadvantage is that it is an indirect method: it uses the functional relations described in MOST or an alternative scaling method. These relations have to be empirically determined using experimental data, which are often obtained by EC-systems. This creates a vicious circle. In order to use scaling one needs the true fluxes. These fluxes could probably better be obtained by scintillometry than by EC, especially over heterogeneous surfaces. However, for obtaining these fluxes we need scaling. This brings us to one open issue in micro meteorology: How do we have to obtain the fluxes correctly? And if we can measure them correctly can this reduce the non closure of the energy balance?

Consequently, we propose to search for alternatives methods to obtain the real surface fluxes and to validate MOST or another scaling method. For the latter, the study of Maronga (2014) shows that the use of LES models running at very high resolution can be a possible solution.

Bibliography

Andreas EL (1988) Estimating C_n^2 over snow and sea ice from meteorological data. J Opt Soc 5:481–495

Baas P, Steeneveld GJ, Van de Wiel BJH, Holtslag AAM (2006) Exploring self-correlation in flux-gradient relationships for stably stratified conditions. J Atmos Sci 63:3045–3054

Bange J, Spieß T, Herold M, Beyrich F, Hennemuth B (2006) Turbulent fluxes from Helipod flights above quasi-homogeneous patches within the LITFASS area. Boundary-Layer Meteorol 121(1):127–151

Beyrich F, Görsdorf U (1995) Composing the diurnal cycle of mixing height from simultaneous sodar and windprofiler measurements. Boundary-Layer Meteorol 76:387–394

Beyrich F, DeBruin HAR, Meijninger WML, Schipper JW, Lohse H (2002) Results from one-year continuous operation of a large aperture scintillometer over a heterogeneous land surface. Boundary-Layer Meteorol 105(1):85–97

Beyrich F, Kouznetsov RD, Leps J, Lüdi A, Meijninger WML, Weisensee U (2005) Structure parameters for temperature and humidity from simultaneous eddy-covariance and scintillometer measurements. Meteorol Z 14:641–649

Beyrich F, Leps JP, Mauder M, Bange J, Foken T, Huneke S, Lohse H, Lüdi A, Meijninger WML, Mironov D, Weisensee U, Zittel P (2006) Area-averaged surface fluxes over the LITFASS region based on eddy-covariance measurements. Boundary-Layer Meteorol 121(1):33–65

Beyrich F, Bange J, Hartogensis OK, Raasch S, Braam M, van Dinther D, Gräf D, van Kesteren B, van den Kroonenberg AC, Maronga B, Martin S, Moene AF (2012) Towards a validation of scintillometer measurements: The LITFASS-2009 experiment. Boundary-Layer Meteorol 144:83–112

van de Boer A, Graf A, Moene AF, Schüttemeyer D (2012) Applying footprint models to investigate MO-dissimilarity over heterogeneous areas. In: 30th Conference on Agric For Meteorol

van de Boer A, Moene AF, Schüttemeyer D, Graf A (2013) Sensitivity and uncertainty of analytical footprint models according to a combined natural tracer and ensemble approach. Agric For Meteorol 169:1–11

van de Boer A, F MA, Graf A, , Schüttemeyer D, Simmer C (2014) Detection of entrainment influences on surface-layer measurements and extension of Monin-Obukhov similarity theory. Boundary-Layer Meteorol

Boggs P, Byrd R, Schnabel R (1987) A stable and efficient algorithm for nonlinear orthogonal distance regression. SIAM J Sci Stat Comput 8(6):1052–1078, http://epubs.siam.org/doi/pdf/10.1137/0908085

Bosveld FC (1999) The KNMI Garderen experiment: micro-meteorological observations 1988-1989. Scientific report WR 99-03, KNMI

Braam M (2008) Determination of the surface sensible heat flux from the structure parameter of temperature at 60 m height during day-time. Technical report TR-303, KNMI

Braam M, Bosveld FC, Moene AF (2012) On Monin-Obukhov scaling in and above the atmospheric surface layer: The complexities of elevated scintillometer measurements. Boundary-Layer Meteorol 144:157–177

Braam M, Moene AF, Beyrich F (2014) Variability of the structure parameters of temperature and humidity observed in the atmospheric surface layer under unstable conditions. Boundary-Layer Meteorol 150:399–422

de Bruin HAR, Kohsiek W, van den Hurk BJJM (1993) A verification of some methods to determine the fluxes of momentum, sensible heat, and water vapour using standard deviation and structure parameter of scalar meteorological quantities. Boundary-Layer Meteorol 63:231–257

Buckingham E (1914) On physically similar systems: Illustrations of the use of dimensional equations. Phys Rev 4:345

Burns SP, Sun J (2000) Thermocouple temperature measurements from the CASES-99 main tower. In: 14th Symposium on Boundary Layer and Turbulence

Businger JA, Wyngaard JC, Izumi Y, Bradley EF (1971) Flux-profile relationships in the atmospheri surface layer. J Atmos Sci 28:181–189

Cheinet S, Cumin P (2011) Local structure parameters of temperature and humidity in the entrainment-drying convective boundary layer: A large-eddy simulation analysis. J Appl Meteorol Climatol 50(2):472–481

Cheinet S, Siebesma AP (2009) Variability of local structure parameters in the convective boundary layer. J Atmos Sci 66:1002–1017

Clifford SF, Ochs GR, Lawrence RS (1974) Saturation of optical scintillation by strong turbulence. J Opt Soc Am 64(2):148–154

van Dijk, A Moene AF, de Bruin HAR (2004) The principles of surface flux physics: Theory, practice and description of the ECPACK library. Tech. rep., Meteorology and Air Quality Group, Wageningen University, Wageningen, the Netherlands

Evans JG, McNeil DD, Finch JW, Murray T, Harding RJ, Ward HC, Verhoef A (2012) Determination of turbulent heat fluxes using a large aperture scintillometer over undulating mixed agricultural terrain. Agric For Meteorol pp 221 – 233

Foken T (2006) 50 years of the Monin-Obukhov similarity theory. Boundary-Layer Meteorol 119(3):431–447

Foken T (2008) Micrometeorology. Springer

Gill Instruments Ltd (2002) Omindirection (R3) & Asymmetric (R3A) Research Ultrasonic Anemometer, User Manual,. Gill Instruments Ltd., Hampshire, United Kingdom

Green AE, Astill MS, McAneney KJ, Nieveen JP (2001) Path-averaged surface fluxes determined from infrared and microwave scintillometers. Agric For Meteorol 109(3):233–247

Hartogensis OK (2006) Exploring scintillometry in the stable atmospheric surface layer. PhD thesis, Wageningen University, Wageningen

Hartogensis OK, DeBruin HAR, Van de Wiel BJH (2002) Displaced-beam small aperture scintillometer test. Part ii: CASES-99 stable boundary-layer experiment. Boundary-Layer Meteorol 105:149–176

Heus T, van Heerwaarden CC, Jonker HJJ, Siebesma AP, Axelsen S, van den Dries K, Geoffroy O, Moene AF, Pino D, de Roode SR, Vil'a-Guerau de Arellano J (2010) Formulation and numerical studies by the Dutch Atmospheric Large-Eddy Simulation (DALES). Geoscientific Model Development 3:99–180

Hill RJ (1989) Implications of Monin-Obukhov similarity theory for scalar quantities. J Atmos Sci 46(14):2236–2244

Hill RJ, Ochs GR, Wilson JJ (1992) Measuring surface-layer fluxes of heat and momentum using optical scintillation. Boundary-Layer Meteorol 58:391–408

Kader BA, Yaglom AM (1990) Mean fields and fluctuation moments in unstably stratified turbulent boundary layers. J Fluid Mech 212(1):637–662

Kaimal J, Wyngaard J, Izumi Y, Coté O (1972) Spectral characteristics of surface-layer turbulence. Q J Roy Meteorol Soc 98(417):563–589

Katul GG, Sempreviva AM, Cava D (2008) The temperature-humidity covariance in the marine surface layer: A one-dimensional analytical model. Boundary-Layer Meteorol 126(2):263–278

Klein Baltink H, Holtslag AAM (1997) A comparison of boundary-layer heights inferred from wind profiler backscatter profiles with diagnostic calculations using regional model forecasts. In: Proceedings EURASAP Workshop, 1-3 October 1997, Risø, Denemarken, pp 51–54

Kleissl J, Hartogensis OK, Gomez JD (2010) Test of scintillometer saturation correction methods using field experimental data. Boundary-Layer Meteorol 137(3):493–507

Kohsiek W (1988) Observation of the structure parameters C_T^2, C_{TQ}, and C_Q^2 in the mixed layer over land. Appl Optics 27:2236–2240

Kohsiek W, Meijninger WML, Moene AF, Heusinkveld BG, Hartogensis OK, Hillen WCAM, DeBruin HAR (2002) An extra large aperture scintillometer for long range applications. Boundary-Layer Meteorol 105:119–127

Kohsiek W, Meijninger WML, DeBruin HAR, Beyrich F (2006) Saturation of the large aperture scintillometer. Boundary-Layer Meteorol 121(1):111–126

Kolmogorov A (1962) A refinement of previous hypotheses concerning the local structure of turbulence in a viscous incompressible fluid at high Reynolds number. J Fluid Mech 13:82–85

Kooijmans LMJ (2013) Testing the universality of Monin-Obukhov similarity functions. Master's thesis, Meteorology and Air Quality Group, Wagenigen University

van den Kroonenberg AC, Martin S, Beyrich F, Bange J (2012) Spatially-averaged temperature structure parameter over a heterogeneous surface measured by an unmanned aerial vehicle. Boundary-Layer Meteorol 142:55–77

van Laar T (2013) Surface heterogeneity: how to detect it and the effect on the spatially averaged structure parameters of temperature and humidity and on the blending height. Master's thesis, Meteorology and Air Quality Group, Wagenigen University

Laubach J, McNaughton KG (2009) Scaling properties of temperature spectra and heat-flux cospectra in the surface friction layer beneath an unstable outer layer. Boundary-Layer Meteorol 133(2):219–252

Lee X, Finigan J, Kyaw TPU (2004) Handbook of Micrometeorology, A Guide for Surface flux measurements and Analysis. Kluwer Academic Publishers, The Netherlands, Dordrecht

Leijnse H, Uijlenhoet R, Stricker JNM (2007) Hydrometeorological application of a microwave link: 1. evaporation. Water Resour Res 43(4)

Li D, Bou-Zeid E, De Bruin HAR (2012) Monin-Obukhov similarity functions for the structure parameters of

temperature and humidity. Boundary-Layer Meteorol 140:1–23

Liu H, Peters G, Foken T (2001) New equations for the sonic temperature variance and buoyancy heat flux with an omnidirectional sonic anemometer. Boundary-Layer Meteorol 100:459–468

Lothon M, Lenschow DH (2010) Studying the afternoon transition of the planetary boundary layer. Eos 91(29):253–254

Lüdi A, Beyrich F, Mätzler C (2005) Determination of the turbulent temperature–humidity correlation from scintillometric measurements. Boundary-Layer Meteorol 117(3):525–550

Lumley JL (1965) Interpretation of time spectra measured in high-intensity shear flows. Phys Fluids 9:1056–1062

Maronga B (2014) Monin-Obukhov similarity functions for the structure parameters of temperature and humidity in the unstable surface layer: results from high-resolution large-eddy simulations. J Atmos Sci 71:716–733

Maronga B, Moene AF, van Dinther D, Raasch S, Bosveld FC, Gioli B (2013) Derivation of structure parameters of temperature and humidity in the convective boundary layer from large-eddy simulations and implications for the interpretation of scintillometer observations. Boundary-Layer Meteorol 148:1–30

Maronga B, Hartogensis OK, Raasch S, Beyrich F (2014) The effect of surface heterogeneity on the structure parameters of temperature and humidity - a LES case study for the LITFASS-2003 experiment. Boundary-Layer Meteorol

Martin S, Bange J, Beyrich F (2011) Meteorological profiling of the lower troposphere using the research UAV "M^{2}AV Carolo". Atmos Meas Tech 4(4):705–716

Mauder M, Oncley SP, Vogt R, Weidinger T, Ribeiro L, Bernhofer C, Foken T, Kohsiek W, Bruin HAR, Liu H (2007) The energy balance experiment EBEX-2000. part II: Intercomparison of eddy-covariance sensors and post-field data processing methods. Boundary-Layer Meteorol 123(1):29–54

Meijninger WML (2003) Surface fluxes over natural landscapes using scintillometry. PhD thesis, Wageningen University, Wageningen

Meijninger WML, Moene AF, Hartogensis OK, de Bruin HAR, B H (2000) The Large Aperture Scintillometer - User manual and technical information. Meteorology and Air Quality Group, Wageningen University, Wageningen, the Netherlands

Meijninger WML, Green AE, Hartogensis OK, Kohsiek W, Hoedjes JCB, Zuurbier RM, deBruin HAR (2002a) Determination of area-averaged water vapour fluxes with large aperture and radio wave scinillometers over a heterogeneous surface - Flevoland Field Experiment. Boundary-Layer Meteorol 105:63–83

Meijninger WML, Hartogensis OK, Kohsiek W, Hoedjes JCB, Zuurbier RM, DeBruin HAR (2002b) Determination of area-averaged sensible heat fluxes with a large aperture scinillometer over a heterogeneous surface - Flevoland Field Experiment. Boundary-Layer Meteorol 105:37–62

Meijninger WML, Beyrich F, Lüdi A, Kohsiek W, DeBruin HAR (2006) Scintillometer-based turbulent fluxes of sensible and latent heat over a heterogeneous land surface–a contribution to LITFASS-2003. Boundary-Layer Meteorol 121(1):89–110

Moene AF (2003) Effects of water vapour on the structure function parameter of the refractive index for near-infrared radiation. Boundary-Layer Meteorol 107:635–653

Moene AF, Schüttemeyer D (2008) The effect of surface heterogeneity on the temperature–humidity correlation and the relative transport efficiency. Boundary-Layer Meteorol 129(1):99–113

Moene AF, Meijninger WML, Hartogensis OK, Kohsiek W, DeBruin HAR (2004) A review of the relation describing the signal of the large aperture scintillometer. Tech. rep., Meteorology and Air Quality Group, Wageningen University, Wageningen, the Netherlands

Moene AF, Meijninger WML, Hartogensis OK, Heusinkveld BG, de Bruin HAR (2005) The effect of finite accuracy in the manufacturing of large aperture scintillometers. Tech. rep., Meteorology and Air Quality Group, Wageningen University, Wageningen, the Netherlands

Moene AF, Meijninger WML, Kohsiek W, Gioli B, Miglietta BFC F and (2006) Validation of fluxes of an extra large aperture scintillometer at Cabauw using sky arrow aircraft flux measurements. In: Proceedings of 17th symposium on boundary layers and turbulence. American Meteorological Society, San Diego, CA, 22 - 25 May 2006

Monin AS, Obukhov AM (1954) Osnovnye zakonomernosti turbulentnogo peremesivanija v prizemnom sloe atmosfery (basic laws of turbulent mixing in the atmosphere near the ground). Trudy geofiz inst AN SSSR 24(151):163–187

Moore CJ (1986) Frequency response corrections for eddy correlation systems. Boundary-Layer Meteorol 37:17–35

Nieuwstadt FTM (1984) The turbulent structure of the stable, nocturnal boundary layer. J Atmos Sci 41:2202–2216

Obukhov AM (1960) O strukture temperaturnogo polja i polja skorostej v uslovijach konvekcii (Structure of the temperature and velocity fields under conditions of free convection). Izv AN SSSR, ser Geofiz pp 1392–1396

Petenko IV, Shurygin EA (1999) A two-regime model for the probability density function of the temperature structure parameter in the convective boundary layer. Boundary-Layer Meteorol 93(3):381–394

Poulos GS, Blumen W, Fritts DC, Lundquist JK, Sun J, Burns SP, Nappo C, Banta R, Newsom R, Cuxart J,

Terradellas E, Balsley B, Jensen M (2002) CASES-99: A comprehensive investigation of the stable nocturnal boundary layer. Bull Am Meteorol Soc 83(4):555–581

Raasch S, Schröter M (2001) PALM - a large-eddy simulation model performing on massively parallel computers. Meteorol Z 10(5):363–372

Schalkwijk J, Bosveld FC, Siebesma AP (2010) Timescales and structures in vertical transport in the atmospheric boundary layer. Tech. Rep. WR-2010-02., KNMI

Schmid HP (2002) Footprint modeling for vegetation atmosphere exchange studies: a review and perspective. Agric For Meteorol 113:159–183

Schotanus P, Nieuwstadt FTM, DeBruin HAR (1983) Temperature measurements with a sonic anemometer and its application to heat and moisture fluxes. Boundary-Layer Meteorol 26:81–93

Scintec AG (2006) BLS Manual 1.36. Scintec AG, Rottenburg, Germany

Spiess T, Bange J, Buschmann M, Vorsmann P (2007) First application of the meteorological Mini-UAV 'M^{2}AV'. Meteorol Z 16(2):159–169

Steeneveld GJ, Mauritsen T, de Bruijn EIF, Vilà-Guerau de Arellano J, Svensson G, Holtslag AAM (2008) Evaluation of limited area models for the representation of the diurnal cycle and contrasting nights in CASES99. J Appl Meteorol Climatol 47:869–887

Stull RB (1988) An Introduction to Boundary-Layer Meteorology. Kluwer, Academic Publishers, Dordrecht

Tennekes H (1973) A model for the dynamics of the inversion above a convective boundary layer. J Atmos Sci 30:558–567

Thiermann V, Grassl H (1992) The measurement of turbulent surface-layer fluxes by use of bichromatic scintillation. Boundary-Layer Meteorol 58(4):367–389

van Ulden AP, Wieringa J (1995) Atmos boundary layer research at Cabauw. Boundary-Layer Meteorol 78:39–69

Van Kesteren B (2012) Measuring water-vapour and carbon-dioxide fluxes at field scales with scintillometry. PhD thesis, Wageningen University, Wageningen

Van Kesteren B, Hartogensis OK (2011) Analysis of the systematic errors found in the Kipp&Zonen large aperture scintillometer. Boundary-Layer Meteorol 138:493–509

Van Kesteren B, Beyrich F, Hartogensis OK, Kroonenberg AC (2013) The effect of a new calibration procedure on the measurement accuracy of scintec's displaced-beam laser scintillometer. Boundary-Layer Meteorol pp 1–15

Vickers D, Mahrt L (1997) Quality control and flux sampling problems for tower and aircraft data. J Atmos Ocean Technol 14:512–526

Wang T, Ochs G, Clifford S (1978) Saturation-resistant optical scintillometer to measure C_n^2. J Opt Soc 68:334–338

Ward HC, Evans JG, Hartogensis OK, Moene AF, De Bruin HAR, Grimmond CSB (2013) A critical revision of the estimation of the latent heat flux from two-wavelength scintillometry. Q J Roy Meteorol Soc 139:1912–1922

Weaver HL (1990) Temperature and humidity flux-variance relations determined by one-dimensional eddy correlation. Boundary-Layer Meteorol 53:77–91

Webb EK, Pearman GI, Leuning R (1980) Correction of flux measurements for density due to heat and water vapour transfer. Q J Roy Meteorol Soc 106(447):85–100

Wesely ML (1976a) The combined effect of temperature and humidity fluctuations on refractive index. J Appl Meteorol 15:43–49

Wesely ML (1976b) A comparison of two optical methods for measuring line averages of thermal exchanges above warm water surfaces. J Appl Meteorol 15(11):1177–1188

Wilczak JM, Oncley SP, Stage SA (2001) Sonic anemometer tilt correction algorithms. Boundary-Layer Meteorol 99(1):127–150

Wilks DS (2006) Statistical methods in atmospheric sciences, International Geophysics, vol 91, second edition edn. Elsevier, Academic Press, London

Wyngaard J, Izumi Y, Collins J, Stuart A, et al. (1971) Behavior of the refractive-index-structure parameter near the ground. J Opt Soc 61(12):1646–1650

Wyngaard JC (1973) On surface-layer turbulence. In: Haugen DA (ed) Workshop on Micrometeorology, American Meteorological Society, pp 101–149

Wyngaard JC, Clifford SF (1977) Taylor's hypothesis and high-frequency turbulence spectra. J Atmos Sci 34:922–928

Zwolak JW, Boggs PT, Watson LT (2007) Algorithm 869: ODRPACK95: A weighted orthogonal distance regression code with bound constraints. ACM Trans Math Soft 33(4)

Validation of C_n^2 observed from two LAS during the LITFASS-2009 experiment

A.1. Research Motivation

In order to obtain the structure parameter of refractive index of air (C_n^2) from the light intensity (I) measured with the receiver of a Large Aperture Scintillometer (LAS) the following equation is used (Wang et al., 1978):

$$C_n^2 = 1.12 D^{7/3} L_{\text{path}}^{-3} \sigma_{\ln(I)}^2 \tag{A.1}$$

in which D is the diameter of the beam ($D = 0.15$ m for the WURLAS), L_{path} is the path length of the scintillometer, and $\sigma_{\ln(I)}^2$ is the variance of the logarithmic intensity.

Because the capacity of dataloggers for high frequency raw data storage used to be small, the LAS built by Wageningen University (WURLAS) processes its electronic signal internally. This analogue processing converts the demodulated signal (I) from the diode into an output voltage (V_{out}) that is directly related to C_n^2 via (Moene et al., 2005):

$$C_n^2 = 10^{-12+\overline{V_{\text{out}}}} \tag{A.2}$$

During the LITFASS-2009 experiment 500 Hz data were saved as well from two WURLAS instruments (sn98005 and sn98006). It would be of interest to investigate how well C_n^2 obtained via Eq. A.1 corresponds to C_n^2 via the processing by analogue electronics. Moreover, after the LITFASS-2009 campaign the electronics within the WURLAS from DWD (WURLAS98005) were recalibrated. This brings us to the first two questions answered in this study:

Question 1 - How good is the analogue processing of the WURLAS?
Question 2 - Does the recalibration have any effect on the results?

Table A.1. The different methods of calculating C_n^2.

name	method	equations	filtering	datalogger	variables	averaging time
Mvardirect	$\sigma^2_{\ln(I)}$ directly	A.1+A.3a	Matlab	CR9000	I	500 Hz
Mvarlognorm	$\sigma^2_{\ln(I)}$ assuming	A.1+A.3b	None	CR9000	I	500 Hz
	lognormal			CR9000	σ_I and $\overline{I}$	$\overline{\text{1min}}^{\text{10min}}$
	distribution			G2	σ_I and $\overline{I}$	10 min
MVout	V_{out}	A.2	Analogue	CR9000	$\overline{V_{\text{out}}}$	$\overline{\text{1min}}^{\text{10min}}$
				G2	$\overline{V_{\text{out}}}$	10 min

A.2. Strategy

As said above, we compare C_n^2 obtained from Eq. A.1 using the raw (500 Hz) data with C_n^2 obtained from Eq. A.2 observed from both WURLAS instruments within the LITFASS-2009 experiment.

The variance of the logarithm of the intensity ($\sigma^2_{\ln(I)}$) in Eq. A.1 can be calculated in two ways. Directly from the 500-Hz data (abbreviated as Mvardirect):

$$\sigma^2_{\ln(I)} = \frac{1}{N}\sum_{i=1}^{N}\left(\ln(I) - \overline{\ln(I)}\right)^2 \tag{A.3a}$$

but also assuming a log-normal distribution and fluctuations that are small compared to the mean value (abbreviated as Mvarlognorm):

$$\sigma^2_{\ln(I)} = \ln\left(1 + \frac{\sigma_I^2}{\overline{I}^2}\right) \tag{A.3b}$$

in which the overbar in both equations indicates the mean. The log-normal distribution assumption (Eq. A.3b) is also used in Van Kesteren and Hartogensis (2011) and in the data analysis of the BLS900 (Scintec AG, 2006, boundary layer scintillometer of Scintec). The advantage of the second method is that then Eq. A.1 can be used to calculate C_n^2 because σ_I and $\overline{I}$ can be saved using simple data logger. For instance, they are part of the standard output of the WURLAS. In order to have an indication when Eq. A.3b could be used, Fig. A.1 shows probability density functions of artificial datasets obtained with a randomized data generator, assuming a log-normal distribution with four different standard deviations. From this figure it can be concluded that the difference between the two methods (Mvardirect and Mvarlognorm) can be neglected if $\sigma_I < \overline{I}$ and start to become important if $\sigma_I >> \overline{I}$.

This brings us to the last question answered in this study:

Question 3 - What are the differences between C_n^2 calculated with the three different methods (see Table A.1)?

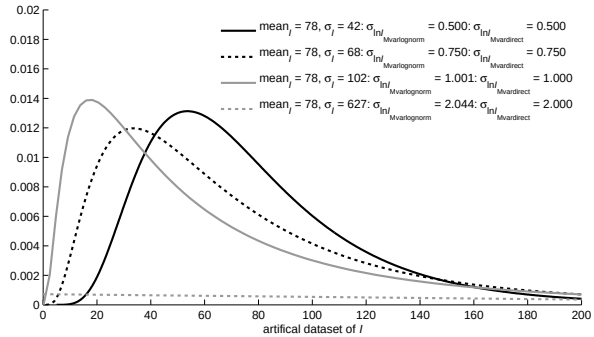

Fig. A.1. Bar charts of an artificial dataset obtained with a randomized data generator assuming a log-normal distribution with four different standard deviations in Matlab.

Table A.2. The scintillometers used in this study. The location is the location of the datalogger and receiver, z_{eff} is the effective height, G2 is the internal data logger of the WURLAS (1 Hz) and CR9000 an additional data logger used during LITFASS-2009 (500 Hz). The time window and frequency as is specified in the table indicate the saving window and frequency.

WURLAS	location	z_{eff}	G2	CR9000	
			10 min	1 min	500 Hz
98005	Lindenberg	43m	$\overline{V_{\text{out}}}$, $\sigma^2_{V_{\text{out}}}$, $\overline{I}$, σ^2_I, $\overline{C_n^2}$	$\overline{V_{\text{out}}}$, $\sigma^2_{V_{\text{out}}}$, $\overline{I}$, σ^2_I, $\overline{C_n^2}$	I
98006	Falkenberg	63m		$\overline{V_{\text{out}}}$, $\sigma^2_{V_{\text{out}}}$, $\overline{I}$, σ^2_I, $\overline{C_n^2}$	I

A.3. Data and Methods

A.3.1. Data

The scintillometers and data loggers

During LITFASS-2009, two WURLAS instruments were set-up between the Lindenberg and Falkenberg towers ($L_{\text{path}} = 4800$ m)[1]) with an effective height (z_{eff}) of 43 m (WURLAS98005) and 63 m (WURLAS98006 Beyrich et al., 2012).

The 10-min data (slow dataset) from the WURLAS98005 was logged on the internal datalogger: the G2, which is in operational use for more than 10 years (see Table A.2). Notice that within the G2, C_n^2 was internally calculated with Eq. A.2 and then averaged, which differs from calculating C_n^2 with $\overline{V_{\text{out}}}$.

The 1-min data (slow dataset) and the 500 Hz data (raw dataset) from both instruments (WURLAS98005 and WURLAS98006) were logged on a datalogger CR9000 (see Table A.2). Within the CR9000, the 1-min C_n^2 was internally calculated as in the G2. The 1-min data of the datalogger CR9000 was averaged up to 10 min in order to compare it with the data of the G2[2].

[1] $L = 4800$ m was determined with GPS and GIS after the experiment. The pot-setting P of the WURLAS98005 was set for $L = 4700$ m ($P = \left(5475.81/\left(\sqrt{4.474D^{-7/3}L^{-3}0.3314 \cdot 10^{12}} + 5.23\right)\right) - 47$, Meijninger et al., 2000. As a consequence, P had to be set to 922.2 instead of 924.5. In order to correct $C_{n\ \text{MVout}}^2$, C_n^2 was multiplied with a factor 0.939 ($(4700/4800)^3$).

[2] $\sigma^2(x)_{10\text{ min}} = \overline{\sigma^2(x)_{1\text{ min}}}^{10\text{ min}} + \sigma^2(\overline{x}^{1\text{ min}})_{10\text{ min}}$

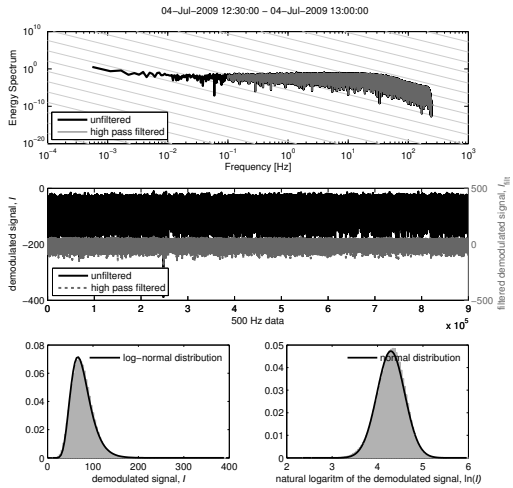

Fig. A.2. Top: Unfiltered and filtered energy spectrum of the 500 Hz data (WURLAS98005) between 1230 UTC and 1300 UTC at 4 July 2009 (doy 185). Middle: the first 10 min plotted for the unfiltered and filtered series. Below: Bar charts of the demodulated signal (left) and the logarithm of the demodulated signal (right) including a probability density function of the normal distribution.

During the LITFASS-experiment the pot-setting of the WURLAS98006 was set to 404.5 which corresponds to $L = 720$ m instead of 4800 m (Meijninger et al., 2000). Therefore, the structure parameter from the processed 1-min data needed to be corrected: $C_{n^2\mathrm{cor}} = C_{n^2\mathrm{meas}} \left(\frac{720}{4800}\right)^3 = 3.375 \times 10^{-3} C_{n^2\mathrm{meas}}$.

A.3.2. Obtaining C_n^2 using the three methods

C_n^2 via V_{out} (MVout)

To obtain V_{out}, several steps are required within the analogue electronics of the LAS. The demodulated intensity signal: a) is low-pass filtered at 400 Hz in order to exclude electronic noise, b) passes a log-amplifier, c) is amplified with a gain that depends on L and D and d) is high-pass filtered at 0.1 Hz to exclude water vapour absorption fluctuations, e) passes through a RMS-to-DB converter (Moene et al., 2005). The averaged values of the final signal (V_{out}) and C_n^2 were saved on the internal datalogger (10 min, G2 datalogger) and the CR9000 datalogger (1 min).

C_n^2 via $\sigma^2_{\ln(I)}$ directly calculated (Mvardirect)

To obtain C_n^2 using Eq. A.1, and Eq. A.3a or Eq. A.3b from the 500-Hz data, four steps were taken with Matlab: a) Data points corresponding to a demodulated signal of zero are removed, b) $\ln(I)$ and I are high-pass filtered at 0.1 Hz using Fourier spectrum. This is done in order to exclude the absorption fluctuations from the raw signal. The upper part of Fig. A.2 shows an example of the filtered and unfiltered spectrum at 4 July 2009 (1230 UTC, local summer time is UTC + 2 h) of I. These data will not be low-pass filtered at 400 Hz, because the Fourier spectrum has a cut-off at 250 Hz to avoid aliasing. c) From the Fourier spectrum over a 10-min window, $\sigma^2_{\ln(I)}$ or σ_I is

calculated, in order to easily compare it with the analogue processed data from the G2 datalogger. d) The 10 min averaged C_n^2 is calculated using Eq. A.1.

This method differs from MVout in i) the raw data is not low-passed filtered, ii) a different high-pass filter is used, and iii) possible errors within calibration of the analogue processing do not influence the raw data.

C_n^2 via $\sigma^2_{\ln(I)}$ assuming log normal distribution (Mvarlognorm)

Eq. A.3b was applied using the raw data (500 Hz) and the slow data (10-min in case of the G2, and $\overline{1\text{min}}^{10\text{min}}$ in case of the CR9000). Notice that in the latter case, the demodulated intensity signal was not band-pass filtered at all. In order to check if the log-normal distribution assumption can be used, the lowest part of Fig. A.2 shows the probability density functions of the 500-Hz demodulated signal and the logarithm of the demodulated signal. Figure A.2 indicates that for this time window the data shows a log-normal distribution. The standard deviation of the demoduladed signal σ_I is 23.33 and the mean intensity is 78.36. So in this case $\sigma_I < \overline{I}$ that indicate that $\sigma^2_{\ln(I)}$ obtained from Mvardirect and Mvarlognorm are expected to be similar.

Data selection

In this study we used the following data:

- LITFASS-2009: from 2 July 2009, day of the year (DOY) 183 until 22 July 2009, DOY 203,
- LITFASS-2009POST: from 26 July 2009, DOY 207 until 4 September, DOY 247.

Data were only selected when the averaged value of the intensity was higher than 75 mV, in order to neglect the weak signal intensity cases which could occur during fog or rain fall.

All the Figures, except for Fig. A.2 and A.6, show the data of the entire experiment.

A.4. Results

A.4.1. Comparing the slow data of the two dataloggers

Figure A.3 shows the analogue processed 10-min output data from the G2 datalogger compared to the $\overline{1\text{min}}^{10\text{min}}$ data from the CR9000 datalogger. On first sight, both dataloggers show quite comparable results, especially for $\overline{V_{\text{out}}}$ and $\overline{C_n^2}$, the important variables. The small differences between the dataloggers could originate from a different time stamp.

But on a closer look, Fig. A.3 shows two large differences in I observed from the two dataloggers. First, the G2 data does not have a continuous range of values, but the data is clustered in bins. The difference between the bins is 2.8 mV. The reason that this resolution problem is not visible for $\overline{V_{\text{out}}}$ and $\overline{C_n^2}$ is that their measured range is larger. It is therefore only slightly visible in the zoom in. For $\overline{V_{\text{out}}}$ and $\overline{C_n^2}$ the entire

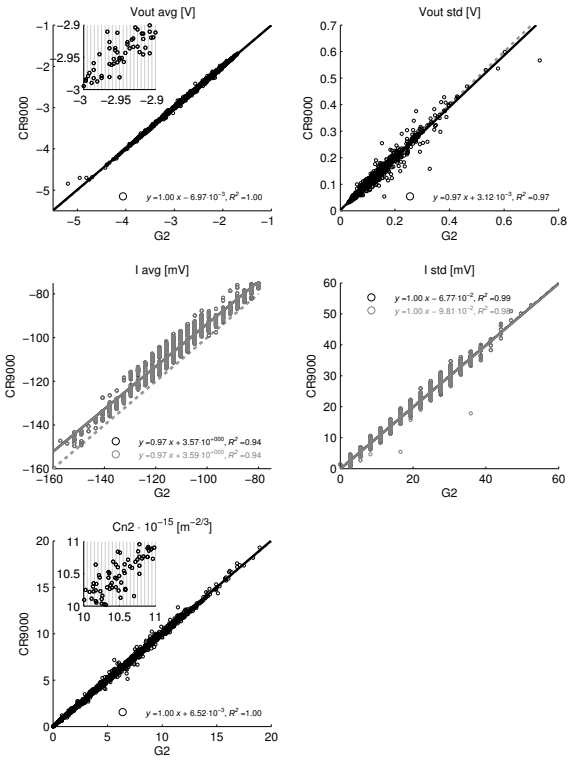

Fig. A.3. The slow data of the G2 datalogger (x-axis, 10-min) versus the slow data of the CR9000 datalogger (y-axis, $\overline{1\text{min}}^{10\text{min}}$) for $\overline{V_{\text{out}}}$, $\sigma_{V_{\text{out}}}$, $\overline{I}$, σ_I and $\overline{C_n^2}$ (all black). For the average and standard deviation of the intensity, also the 500 Hz data are shown (grey).

range of the Analogue Digital Converter (ADC) is used, whereas for $\overline{I}$ and σ_I much less bins are used. For σ_I just 22 of the total number of bins (4096) are used.

Second, the G2 data shows an offset of 3 mV, whereas the slope of the regression line is almost one. With an averaged intensity 100 mV this corresponds to an overestimation of 3 %. An explanation for this difference in the offset is that the G2 itself is not well calibrated. However, in the operational standard use, the averaged intensity signal is only applied as data filter and for that the signal is accurate enough.

The structure parameter itself shows comparable results between the two dataloggers, which means that the internal datalogger (G2) can still be used. However, because the G2 datalogger was only mounted on the WURLAS98005, the following results are based on the data of the CR9000.

A.4.2. Comparing the three different methods to calculate C_n^2

Mvarlognorm versus Mvardirect

Figure A.4 shows C_n^2 calculated via Mvarlognorm (Eq. A.3b, 500 Hz and 10 min) versus C_n^2 calculated via Mvardirect (Eq. A.3a, 500 Hz). Notice, that only the 500 Hz data is high-pass filtered. This means that the correction to exclude absorption fluctuation is

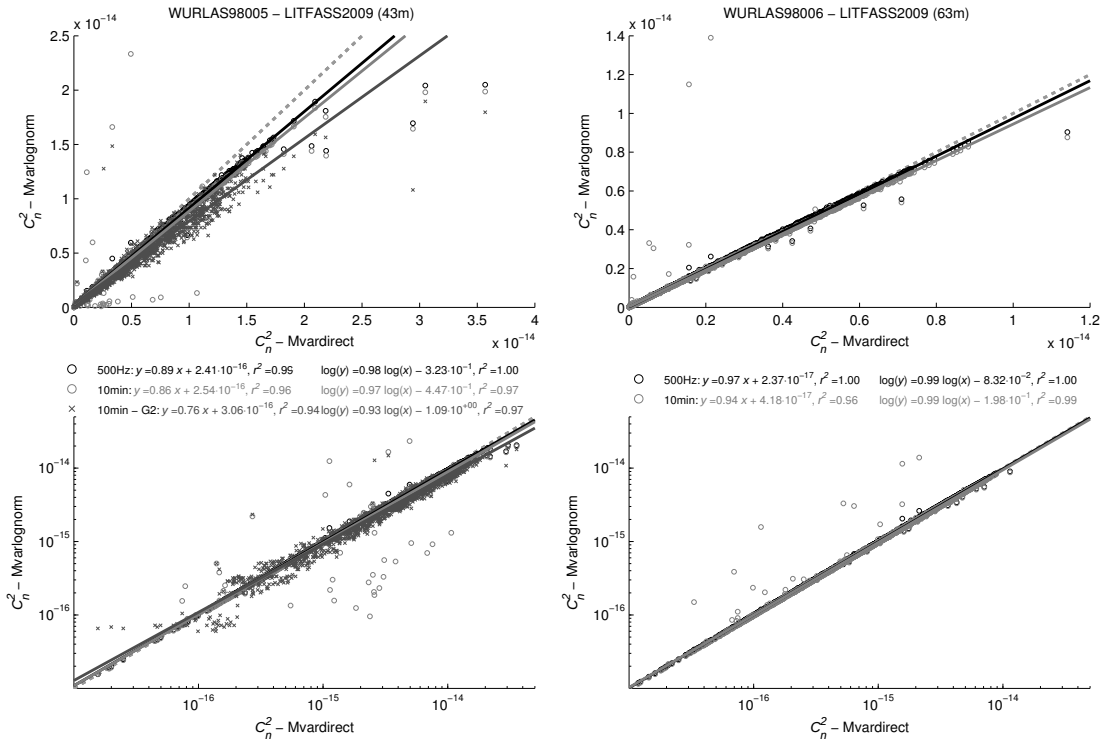

Fig. A.4. C_n^2 calculated via Mvarlognorm versus C_n^2 calculated via Mvardirect for WURLAS98005 (z_{eff} = 43 m, left) and WURLAS98006 (z_{eff} = 63 m, right) at a linlin scale (upper) and a loglog scale (below). With σ_I^2 and $\overline{I}^2$ obtained from the CR9000 slow dataset (grey circles, $\overline{1\text{min}}^{10\text{min}}$, without the band-pass filter), from the CR9000 500-Hz dataset (black circles, including band-pass filter), and in case of the WURLAS98005 from the internal G2 slow dataset (grey crosses, 10 min, without the band-pass filter).

not taken into account for Mvardirect 10min.

From the double linear plots (linlin), we observe that the C_n^2 calculated with Mvarlognorm underestimate Mvardirect for larger structure parameters, whereas for smaller structure parameters the data is more located closer to the 1:1-line. The underestimation is better observed for the data from WURLAS98005 than for WURLAS98006, because the range of C_n^2 is larger due to a lower z_{eff} of the WURLAS98005. The double logarithmic plots (loglog) show that for small structure parameters the two methods are similar.

The underestimation using the lognormal assumption is also found by the intercomparison study of the WURLAS98005 and a BLS900, both installed between Falkenberg and Lindenberg (personal communication: Frank Beyrich, Bram van Kesteren, MOL-RAO, 2012-2013). Within this comparison C_n^2 from the WURLAS98005 was determined from the anologue signal (MVout), however, from the results in the next paragraph, we found that C_n^2 MVout and C_n^2 Mvardirect are similar. The BLS determines C_n^2 via Mvarlognorm. They found an underestimation of the BLS900 compared to the WURLAS98005 of 16% with a regression of 0.84. Further research shows that this underestimation depends on the amount of cross wind along the path.

Table A.3. C_n^2 calculated via Mvarlognorm from slow data (y) versus C_n^2 calculated via Mvarlognorm from raw data (x) obtained with the CR9000.

	y is obtained from $\overline{1\text{min}}^{10\text{min}}$		y is obtained from 1-min	
	equation	r^2	equation	r^2
WURLAS98005	$y = 0.97x + 1.41 \times 10^{-17}$	0.97	$y = 1.00x + 5.12 \times 10^{-19}$	1.00
	$\log y = 0.99 \log x - 1.20 \times 10^{-1}$	1.00	$\log y = 1.00 \log x - 1.88 \times 10^{-3}$	1.00
WURLAS98006	$y = 0.97x + 2.57 \times 10^{-17}$	0.96	$y = 1.00x + 5.26 \times 10^{-20}$	1.00
	$\log y = 0.99 \log x - 1.12 \times 10^{-1}$	0.99	$\log y = 1.00 \log x - 5.53 \times 10^{-4}$	1.00

The slow dataset (grey circles, $\overline{1\text{min}}^{10\text{min}}$) shows a larger underestimation than the raw dataset (black circles, 500 Hz). This could be caused by rounding errors in the second calculation step of the 10-min processed data. First, the CR9000 datalogger processed the 500-Hz data over 1 min (averaged and taking the standard deviation), and afterwards these 1-min data is averaged up to 10 min. In order to investigate, if this is the reason, C_n^2 obtained from the slow data is compared to the raw data for the 1-min averaged intervals (see Table A.3). From the Table we observe that a small underestimation is visible for the 10-min averaged intervals, whereas it is not observed for the 1-min averaged interval. Furthermore, the r^2 improved using the 1-min averaged interval.

For the WURLAS98005 (Fig. A.4 left), we also include C_n^2 obtained via Mvarlognorm using the slow data logged on the G2. The G2 datalogger underestimates $C_{n\ \text{Mvardirect}}^2$ even more than the CR9000 datalogger does. The small overestimation of 3.5 mV in the averaged intensity (see Fig. A.3) contributes to this underestimation. Furthermore, the scatter in C_n^2 is a bit larger when using the G2. This is an effect of the resolution problem in σ_I and $\overline{I}$ (see Fig. A.3).

Mvardirect versus MVout - How is the calibration of the WURLAS during LITFASS-2009?

WURLAS98005 In Fig. A.5 C_n^2 calculated via MVout versus C_n^2 calculated via Mvardirect is plotted as observed by the WURLAS98005. For this instrument, the two methods show comparable results, except of some very large values of $C_{n\ \text{Mvardirect}}^2$ that decrease the slope of the regression to 0.87 (see also last paragraph of this section) with a correlation coefficient of 0.86 (Fig. A.5 left). This means that the calibration was already good during LITFASS-2009 and a recalibration was actually not needed.

Whereas the recalibration was not needed, we have to investigate the effect of the calibration. Table A.4 show the results for the LITFASS-2009POST experiment. It appears that still after the calibrations the two methods shows comparable results, which means that the recalibration was done well.

WURLAS98006 The WURLAS98006, however, does not show comparable results (Fig. A.5 right). C_n^2 calculated via MVout shows a large overestimation (44 %) compared to C_n^2 calculated via Mvardirect. It seems that the degree of overestimation

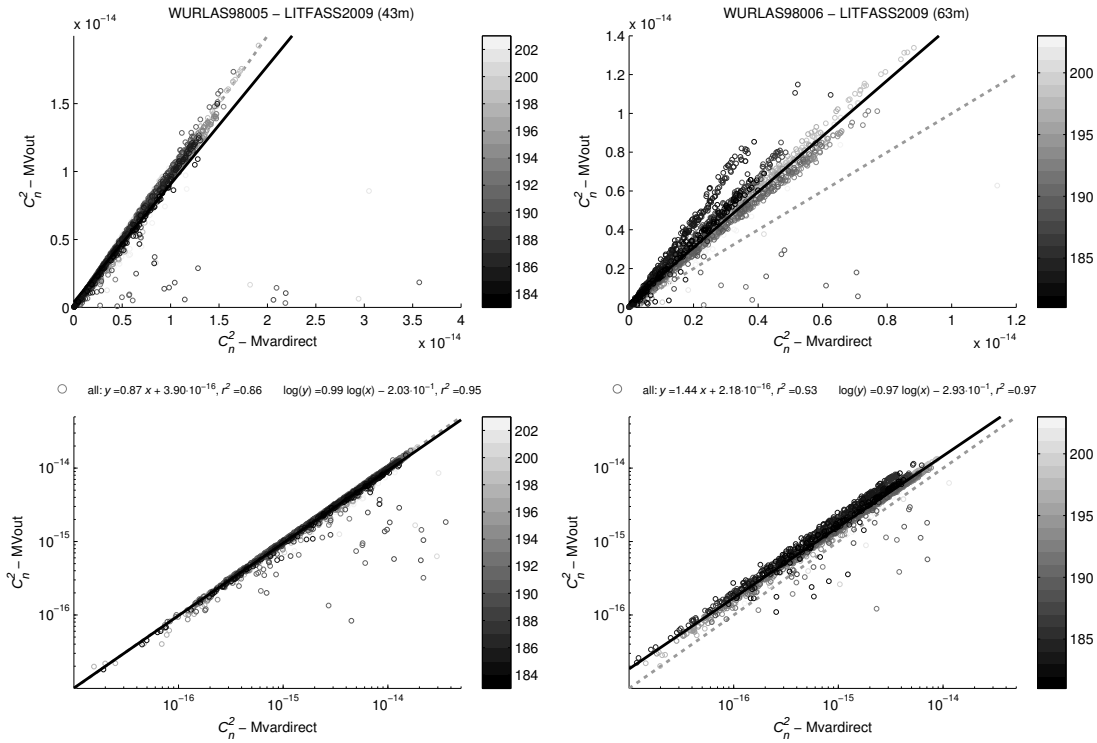

Fig. A.5. C_n^2 calculated via MVout versus C_n^2 calculated via Mvardirect for WURLAS98005 (z_{eff} = 43 m, left) and WURLAS98006 (z_{eff} = 63 m, right) at a linlin scale (upper) and a loglog scale (below). The colour represents the day of the year (DOY) when the measurements were taken.

depends on the day of the measurement. At the beginning of the experiment the overestimation is larger than at the end of the experiment.

One reason can be that the WURLAS98006 is not well calibrated, which will result in an error in the calculation of V_{out}. In order to investigate if the WURLAS98006 is not well calibrated, we study data from the WURLAS98006 observed during the BLLAST experiment done in Lannemezan (France) during June 2011. During BLLAST only the 1-min data and not the raw 500-Hz data were saved on a CR10 datalogger. This makes it only possible to compare $C_{n\ \text{MVout}}^2$ with $C_{n\ \text{Mvarlognorm}}^2$ and not with $C_{n\ \text{Mvardirect}}^2$, and therefore two remarks have to be made:

1. we focus on 1-min data, because we observe that averaging over 10 min could cause

Table A.4. C_n^2 calculated via MVout (y) versus C_n^2 calculated via Mvar (x) obtained during the LITFASS-2009POST experiment (Mvardirect) and during the BLLAST experiment (Mvarlognorm).

	equation	r^2
WURLAS98005 LITFASS-2009POST	$y = 0.98x + 1.34 \times 10^{-16}$	0.96
	$\log y = 1.01 \log x + 2.09 \times 10^{-1}$	0.99
WURLAS98006 BLLAST	$y = 1.09x + 4.12 \times 10^{-16}$	0.96
	$\log y = 1.00 \log x - 1.55 \times 10^{-3}$	1.00

rounding errors (see Sect. A.4.2),

2. we could expect a small overestimation at large values of C_n^2, because we use C_n^2 $_{\text{Mvarlognorm}}$ instead of C_n^2 $_{\text{Mvardirect}}$ (see Sect. A.4.2).

The linear regression through the BLLAST data is given in table A.4. Comparing the two methods, we observe that C_n^2 calculated via MVout overestimates C_n^2 calculated via Mvarlognorm with 10 %, which is smaller than for the Falkenberg data. Notice, that if we had compared the MVout-method with the Mvardirect-method instead of Mvarlognorm the overestimation would be smaller (see remark 2). This effect is even stronger than during LITFASS-2009, because z_{eff} is lower and as a consequence C_n^2 is a factor 10 higher for BLLAST than for LITFASS-2009. So, it seems that the large overestimation of the analogue processed data of the WURLAS98006 during LITFASS-2009 is not caused by a wrong calibration of the WURLAS.

Another reason for the deviation could be that both signals are saved on another module of the CR9000 data logger: V_{out} is saved on the standard module (CR9050), and I is saved on the module CR9052. The module CR9052 can be used to sample several signals simultaneously, so that the raw data I_{MWS} (the intensity signal of the microwave scintillometer) and I_{LAS} could be sampled simultaneously.

Most likely the problem has to be searched in the CR9052 module. There are two reasons for this. First, the same module on the same data logger (CR9052 on CR9000-sn1041) showed also some signs of malfunctioning at beginning of the LITFASS 2012 campaign. Therefore, during this campaign the standard module (CR9050) was used to save I instead (personal communication: Bram van Kesteren, MOL-RAO, 2013).

Second, a comparison of C_n^2 $_{\text{Mvardirect}}$ transformed to a height of 50 m shows that the C_n^2 of the WURLAS98006 is lower than C_n^2 of the WURLAS98005. It seems that this underestimation of the WURLAS98006 depends also on the day of measurement. In order to have a better comparison, we applied a least squared linear regression through the origin between C_n^2 $_{\text{MVout}}$ and C_n^2 $_{\text{Mvardirect}}$ of the WURLAS98006 for each day during daytime conditions (0600 - 1800 UTC). Moreover, we applied least-squared linear regression between C_n^2 $_{\text{50mMvardirect}}$ of the WURLAS98005 and WURLAS98006. The factor and the correlation coefficients are given in Table A.5. For both regressions the correlation is large, and the factors are comparable, which indicates that the malfunctioning of the CR9052 module is the reason for thedeviation between C_n^2 $_{\text{Mvardirect}}$ and C_n^2 $_{\text{MVout}}$.

Exceptionally large values for C_n^2 calculated via Mvardirect

Figure A.5 shows some data points where C_n^2 $_{\text{MVout}}$ is considerably underestimated compared to C_n^2 $_{\text{Mvardirect}}$, which is also observed during BLLAST and the LITFASS-2009POST experiment (figures not shown). In other words, using the 500 Hz data gives extra variability in the intensity. This occurs on different days (colour coding in Fig. A.5), different moments of the day, under stable and unstable conditions, for different values of $\overline{I}$ and σ_I. One possible reason for losing variability is that the analogue band

Table A.5. The factor between C_n^2 MVout and C_n^2 Mvardirect for the WURLAS98006 (z_{eff} = 63 m), and the factor between C_n^2 Mvardirect transferred to 50 m from the WURLAS98006 and the WURLAS98005, for each day during the LITFASS-2009 experiment based on data observed during 0600 and 1800 UTC without rain.

date	doy	C_n^2 MVout vs C_n^2 Mvardirect		C_n^2 WURLAS98005 vs C_n^2 WURLAS98006	
		factor	r^2	factor	r^2
03-07-2009	184	2.21	0.93	2.45	0.32
04-07-2009	185	2.21	0.95	2.29	0.80
05-07-2009	186	1.74	1.00	1.80	0.98
06-07-2009	187	1.68	1.00	1.73	0.98
07-07-2009	188	1.56	0.88	1.52	0.87
08-07-2009	189	1.18	0.60	1.35	0.95
09-07-2009	190	1.39	1.00	1.43	0.99
10-07-2009	191	1.33	0.88	1.40	0.98
11-07-2009	192	1.42	1.00	1.42	0.99
12-07-2009	193	1.35	0.99	1.38	0.99
13-07-2009	194	1.40	0.99	1.42	0.99
14-07-2009	195	1.48	1.00	1.58	0.97
15-07-2009	196	1.50	1.00	1.51	0.98
16-07-2009	197	1.44	0.99	1.48	0.96
17-07-2009	198	1.54	1.00	1.55	0.98
18-07-2009	199	1.47	0.96	-	-
19-07-2009	200	1.45	1.00	1.54	0.99
20-07-2009	201	1.44	0.99	1.49	0.99
21-07-2009	202	1.41	1.00	1.49	0.99

pass filter is too narrow.

In order to search for a possible explanation, we investigate the spectrum and PDF of the demodulated signal intensity of such a data point. Figure A.6 shows the spectrum and the PDF of the most right data point from Fig. A.5 (C_n^2 Mvardirect $= 3.6 \times 10^{-14}$ $\text{m}^{-2/3}$ and C_n^2 Mvardirect $= 1.8 \times 10^{-15}$ $\text{m}^{-2/3}$). Three remarks can be made. First, I does not have a lognormal distribution, but has a distribution with different peaks at low intensities. Second, the spectrum of I has a small slope for low frequencies. Third, the evolution of I in time seems not to be stationary.

Other data points show similar patterns, especially the peaks at smaller intensities. Therefore, we create a filter to check if the PDF of I is log normal distributed[3]. Using this filter improves the results. For the WURLAS98005 the slope increases from 0.87 to 0.98 and the correlation coefficient from 0.86 to 0.99. For the WURLAS98006 the slope increases from 1.44 to 1.47 and the correlation coefficient from 0.89 to 0.96.

[3]The calculations to check if the data is log-normally distributed consist of three steps. First, we determine the maximum difference between the measured distribution and the estimation of the log-normal distribution ($= \frac{1}{x\sqrt{2\pi\sigma^2}}\, e^{-\frac{(\ln x-\mu)^2}{2\sigma^2}}$), i.e., the maximum difference between the red and black lines in Fig. A.2 and A.6. Second, we calculate the ratio of this maximum difference with the maximum of the measured distribution, i.e. the highest peak of the red line. For a log-normal distribution, the maximum difference is small and the ratio will be around 0. Third, we excluded data points with a ratio higher than a threshold value of 0.15.

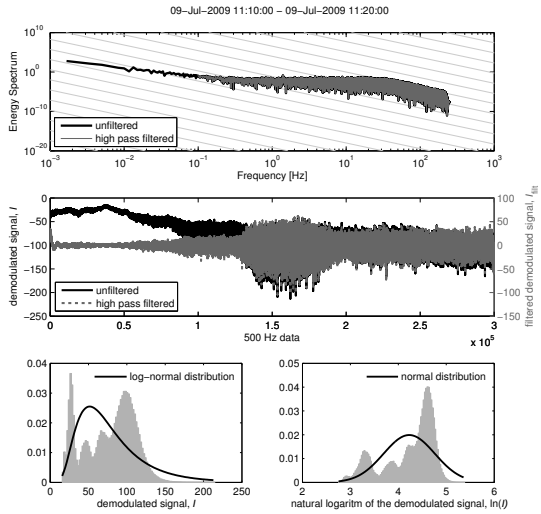

Fig. A.6. Top: Unfiltered and filtered energy spectrum of the 500 Hz data (WURLAS98005) between 1110 UTC and 1120 UTC at 9 July 2009 (doy 190). Middle: the first 10 min plotted for the unfiltered and filtered series. Below: Bar charts of the demodulated signal (left) and the logarithm of the unfiltered demodulated signal (right) including a probability density function of the normal distribution.

A.5. Conclusions

1. The two dataloggers (G2 internal datalogger and the CR9000) give comparable results: V_{out} and C_n^2 are identical. The resolution of the G2 is lower, which is visible for the demodulated intensity measurements. The demodulated intensity of the G2 shows an overestimation with an offset of 3 mV (around 3 %) compared to the CR9000, probably caused by a wrong calibiration of the G2 datalogger.
2. The structure parameters obtained via Mvarlognorm are smaller than those via Mvardirect, especially if C_n^2 is large.
3. If the probability distribution of I is not log normal (under non-stationary conditions), the data of the analogue processed data shows a much smaller structure parameter than the 500 Hz data processed in Matlab. Removing these data points improves the correlation.
4. For the WURLAS98005, the structure parameters obtained via MVout is comparable with those obtained via $\sigma^2_{\ln(I)}$ before and after the recalibration (correlation coefficient of 0.99 and a slope around 1). This means that the instrument was already well calibrated and the recalibration was not needed but did not deteriorate the results.
5. For the WURLAS98006, the structure parameters obtained via MVout are larger than those obtained via Mvardirect. The differences depend on the measurement day. This is a consequence of the malfunctioning of the CR9052 module on the CR9000 datalogger (sn1041). Therefore, if C_n^2 obtained via MVout from the 500 Hz data (datalogger: CR9000-sn1041, module: CR9052) is used during LITFASS-2009 a correction per day has to be applied as given in Table A.5.

A.6. Outlook

During this research some new questions arose:

1. The filter obtained in Matlab has a sharp cut-off, whereas the analogue filter is smoother. It would be of interest to investigate if a much smoother filter would make the results of the analogue processed and the Matlab processed data more similar.
2. Why is C_n^2 calculated via Mvarlognorm (assuming a log normal distribution) smaller than those of the other methods?
3. What causes those non-stationary conditions that result in a deviation from a log-normal distribution?
4. What is the reason for the malfunctioning of the CR9052 module on the CR9000 datalogger during LITFASS-2009 and LITFASS-2012, and why does the correction factor depend on the day of measurement?

Samenvatting

Atmosferische turbulentie en scintillometrie

Atmosferische turbulentie is het belangrijkste mechanisme voor het verticale transport van energie en materie, zoals waterdamp, in de atmosferische grenslaag ("Atmospheric Boundary Layer", ABL). De oppervlaktestromen (fluxen) die gerelateerd zijn aan dit turbulente transport zijn de voelbare (H) en latente warmteflux (LE, verdamping). Hun grootte is onder andere afhankelijk van jaargetijde, de tijd op de dag, en de locatie op aarde. Eén manier om H en LE te meten is door gebruik te maken van scintillometers. Een scintillometersysteem bestaat uit een zender, die elektromagnetische straling uitzendt, en een ontvanger die deze straling opvangt. Voor de scintillometers die in deze studie worden gebruikt is de typische lengte van het pad tussen zender en ontvanger ongeveer 1 tot 5 km. De intensiteit van het elektromagnetische signaal dat door de ontvanger wordt gemeten varieert door fluctuaties in de brekingsindex van lucht (n), die op hun beurt weer veroorzaakt door turbulentie langs het pad. De grootte van de brekingsindexfluctuaties is evenredig met de padgemiddelde structuurparameter voor de brekingsindex (C_n^2), en met C_n^2 kunnen de structuurparameters voor temperatuur (C_T^2) en luchtvochtigheid (C_q^2) worden bepaald. C_T^2 en C_q^2 zijn een maat voor de turbulente temperatuur- en vochtfluctaties in de "inertial subrange" van het turbulente spectrum. De mate waarin C_n^2 afhangt van C_T^2 en C_q^2 is afhankelijk van de golflengte van de straling waarmee de scintillometer uitzendt. Als deze straling in het bereik van zichtbaar licht en infrarood ligt, zoals de "large aperture" scintillometer (LAS, Scintillometer met een grote opening), is C_n^2 voornamelijk gevoelig voor C_T^2. Terwijl C_T^2 en C_q^2 even belangrijk zijn voor scintillometers die geberuiken maken van micro- of radiogolven ("Microwave scintillometer", MWS). Met C_T^2 en C_q^2 worden uiteindelijk de padsgemidddelde H en LE bepaald door het toepassen van de gelijkvormigheidstheorie van Monin en Obukhov ("Monin-Obukhov similarity theory", MOST).

MOST is een theorie die gebaseerd is op dimensie-analyse. MOST biedt een kader waarmee met behulp van universele, empirische, functies de oppervlaktefluxen gekoppeld kunnen worden aan andere turbulente grootheden: structuurparameters in het geval van scintillometrie. MOST is alleen geldig boven homogeen landschap, tijdens starionaire situaties en in de atmosferische oppervlaktelaag ("Atmospheric Surface Layer", ASL). In het algemeen wordt aangenomen dat turbulentie in de ASL voornamelijk wordt veroorzaakt door processen aan het aardoppervlak, en dat andere processen, zoals bij-

voorbeeld "entrainment" en grootschalige advectie, kunnen worden verwaarloosd. De dikte van de ASL varieert sterk al naargelang de tijd van de dag en is ongeveer 10 % van de ABL. Aan het einde van de middag, wanneer de turbulentie het sterks ontwikkeld is, is de ASL het dikst, terwijl hij gedurende de ochtend en de nacht relatief dun is.

De gebiedsgemiddelde fluxen zijn belangrijk voor verschillende meteorologische toepassingen, zoals bijvoorbeeld voor het valideren van numerieke weermodellen en satellietalgoritmen. In de natuur is het landschap vaak heterogeen op een schaal van 1 tot 5 km dat wil zeggen, het bestaat uit verschillende velden die variëren in H en LE. Daarom is het logischer om scintillometrie te gebruiken dan traditionale puntmetingen te gebruiken voor het bepalen fluxen die representatief zijn voor het gehele gebied. Gedurende de laatste twintig jaar is aangetoond dat scintillommeters gebiedsgemiddelde fluxen over een heterogeen landschap kunnen bepalen. Toch zijn er ook nog onopgeloste kwesties die meer onderzoek vereisen. De vier vragen die in dit proefschrift aan bod komen zijn gerelateerd aan de toepassing van MOST (Hoofdstuk 2 en 3) en aan het gedrag van de structuurparameter boven heterogeen landschap (Hoofdstuk 4 en 5). Met andere woorden, de motivatie van dit onderzoek is het beter begrijpen en kwantificeren van het scintillometersignaal en dan met name gericht op de structuurparameter.

De gegevens die we in dit onderzoek analyseren zijn gemeten op drie verschillende locaties. We analyseren alleen de observaties van overdag: onstabiele situaties wanneer turbulentie vooral wordt veroorzaakt door "buoyancy" (drijfvermogen, d.w.z. menging van de lucht door verschil in dichtheid). Omdat MOST alleen geldig is boven homogeen landschap, beantwoorden we de eerste twee MOST-gerelateerde vragen met gegevens die gemeten zijn op een station in relatief homogeneen landschap (Cabauw; Nederland voor hoofdstuk 2, en CASES-99; Leon; Kansas; VS voor hoofdstuk 3). De laatste twee vragen (hoofdstuk 4 en 5) worden beantwoord met gegevens die zijn verzameld gedurende twee experimenten over een relatief heterogeen landschap (LITFASS-2009 en LITFASS-2010; Lindenberg; Duitsland, waarin LITFASS de afkorting is voor "LIndenberg-To-Falkenberg Aircraft Scintillometer Study"). Overigens is het zo dat ondanks het beter willen begrijpen van het scintillometersignaal de voornaamste drijfveer was voor dit onderzoek, we de eerste drie vragen in dit onderzoek met C_T^2 bepaald uit gegevens gemeten door traditionele puntmetingen beantwoorden, d.w.z. via de eddy-covariantiemethode (EC), in plaats van met scintillometers.

De toepassing van MOST

Monin-Obukhovschaling in en boven de oppervlaktelaag

Eén beperking van scintillometrie is dat de achterliggende theorie alleen geldig is voor situaties met zwakke verstrooiing. Het signaal verzadigt namelijk als er sterkere verstrooiing plaats vindt. Verzadiging kan worden voorkomen door de scintillometer hoger boven het aardoppervlak te plaatsen, aangezien C_n^2 afneemt met de hoogte. Dit brengt echter ook een nadeel met zich mee: als de ASL dun is, zal een hoger observatieniveau al gauw boven de ASL liggen, en kan er worden betwist of MOST nog geldig is. Dit

brengt ons tot de eerste onderzoeksvraag die wordt beantwoord in hoofdstuk 2:

Vraag 1 - In welke mate kan de voelbare warmteflux worden bepaald door de temperatuursstructuurparameter gemeten op grotere hoogte boven het aardoppervlak, en dan met name gedurende de ochtend, wanneer het meetniveau boven de ASL zal liggen?

Om deze vraag te beantwoorden, zijn twee concepten om H met C_T^2 te bepalen geïntroduceerd en met elkaar vergeleken. In het eerste concept, MOSTs, schaalt C_T^2 met de oppervlakteflux. In dit concept veronderstellen we dat MOST nog steeds toepasbaar is net boven de ASL. In het tweede concept, MOSTl, schaalt C_T^2 met de lokaal gemeten flux in plaats van met de oppervlakteflux. Dit concept is vergelijkbaar met de lokale schalingshypothese die wordt gebruikt in de stabiele grenslaag (Nieuwstadt, 1984). Om uiteindelijk de oppervlakteflux te bepalen moet er worden gecorrigeerd voor fluxdivergentie in de kolom onder het observatieniveau.

Aan de hand van deze twee MOST-concepten, berekenen we C_T^2 uit de fluxmetingen (m.a.w. MOST in omgekeerde volgorde), en vergelijken we deze met de C_T^2 die rechtstreeks is bepaald uit de sonische wind-/ temperatuurmetingen (sonicmetingen) op het 60-m-niveau van de Cabauwtoren. In de analyse onderscheiden we twee periodes: 's ochtends en 's middags. 's Ochtends ligt het 60-m-niveau boven de ASL en kan MOST worden betwist, terwijl 's middags het 60-m-niveau in de ASL ligt en MOST in principe toegepast kan worden.

's Middags waren de waardes van C_T^2 bepaald met de twee concepten vergelijkbaar met die van C_T^2 rechtstreeks bepaald uit de sonicmetingen. 's Ochtends, daarentegen, is er geen eenduidige voorkeur voor een van de twee concepten. Ten eerste observeren we een piek in C_T^2 wanneer het meetniveau in de entrainmentlaag ligt, wat door geen van beide MOST-concepten wordt ondersteunt. Ten tweede geeft MOSTl weliswaar het juiste verloop in de tijd weer: het moment wanneer de warmteflux nul is valt gelijk met het moment wanneer C_T^2 het kleinst is. Maar aan de andere kant onderschat MOSTl C_T^2 met een factor tien. Ten derde laten de lineaire regressies tussen C_T^2 rechtstreeks bepaald en C_T^2 geschat met de twee concepten zien dat voor MOSTl de helling dichter bij één ligt en voor MOSTs het begingetal dichter bij nul. Ten slotte is de correlatie tussen C_T^2 rechtstreeks bepaald en C_T^2 geschat met de twee concepten voor beide concepten laag en vergelijkbaar. Om al deze redenen concluderen we dat MOST niet toepasbaar is voor de ochtenduren wanneer het observatieniveau zich boven de ASL bevindt.

Afhankelijkheid van regressiemethode, observatieniveau en stabiliteitsbereik

Binnen het kader van MOST moet de universele functie ($f\,(z/L)$, waarbij z is de hoogte en $1/L$ is een maat voor de stabiliteit) die H en C_T^2 met elkaar verbindt, empirisch worden bepaald. In de literatuur is een grote verscheidenheid aan vormen van deze functies te vinden. Een reden voor deze verscheidenheid is dat de locatie, instrumenten en dataverwerking van studie tot studie verschilt. Wij gebruik daarom *één enkele* dataset (CASES-99) om in hoofdstuk 3 de volgende vraag te beantwoorden:

Vraag 2 - In hoeverre wordt de vorm van de universele functie beïnvloed door de keuze van een specifieke regressiebenadering, de opgetreden stabiliteitsrange en de observatie hoogte?

Het voordeel van één dataset is dat we andere oorzaken van variatie uitsluiten, zoals bijvoorbeeld verschillen in de dataverwerking, instrumentatie en het landschap. In deze studie wordt de meest gangbare vorm van $f(z/L)$ voor onstabiele omstandigheden gebruikt, namelijk diegene die wordt beschreven met een machtsfunctie en twee empirische coëfficiënten c_1 en c_2: $f(z/L) = c_1(1 - c_2 z/L)^{-2/3}$.

In het eerste deel van dit onderzoek evalueren we de verschillende regressiebenaderingen. Deze benaderingen verschillen in vier aspecten: het al dan niet logaritmisch transformeren van de data, de wiskundige regressiemethode, het wegen van de data met de meetnauwkeurigheid van elk datapunt, en het aantal regressiecoëfficiënten dat wordt meegenomen in de regressie. De resultaten tonen aan dat het toepassen van deze verschillende benaderingen een invloed heeft op de resulterende regressiecoëfficiënten, en het vermelden van de toegepaste benadering is dus van groot belang. Wij adviseren om een orthogonale regressiemethode te gebruiken, waarbij beide dimensieloze groepen logaritmisch getransformeerd zijn, en de data gewogen is zodat onbetrouwbare metingen een kleinere invloed hebben op de coëefficiënten.

Het verdelen van de dataset in acht klassen voor z en acht klassen voor $1/L$ laat zien dat de hoogte en stabiliteit invloed heeft op de resulterende coëfficiënten. Dit betekent dat de variatie van c_1 en c_2 in de literatuur het gevolg kan zijn van verschillen in meethoogten en stabiliteitsbereiken tussen de verschillende datasets. Bovendien betekent het dat een $f(z/L)$ niet zonder meer kan worden toegepast op een dataset gemeten op een andere hoogte en gedurende een andere stabiliteitsbereik. Tenslotte suggereert de variatie in de coëfficiënten tussen de klassen dat het gebruik van maar twee coefficienten in de similariteitsrelatie onvoldoende kan zijn.

C_s^2 boven heterogeen landschap

Kennis over de variabiliteit van C_s^2 boven heterogeen landschap is belangrijk, omdat MOST, de link tussen C_s^2 en de fluxen, in principe alleen geldig is voor homogene situaties.

Variabiliteit van C_T^2 en C_q^2 waargenomen in de ASL

Of variaties in C_s^2 langs een scintillometer- of vliegtuigpad in het bereik liggen van de lokale variabiliteit van C_s^2, of dat ze moeten worden toegeschreven aan heterogeniteit, is in hoofdstuk 4 de volgende vraag geformuleerd:

Vraag 3 - Wat bepaalt de lokale variabiliteit van de structuurparameter in de atmosferische oppervlaktelaag die gemeten is onder verschillende stabiliteitsbereiken en op verschillende hoogtes?

In dit hoofdstuk richten we ons op de logaritme van de Monin-Obukhovgeschaalde structuurparameter voor temperatuur en luchtvochtigheid (aangeduid als $\log(\widetilde{C_s^2})$) waar

C_s^2 wordt bepaald over tijdvensters variërend van 1-10 min. We gebruiken één maand aan EC-data, verkregen tijdens het LITFASS-2009 experiment op 2,5 m boven een triticaleveld en op 50 m, en 90 m hoogte in de 99-m toren in Falkenberg.

We zien dat de variabiliteit van $\log(\widetilde{C_s^2})$ wordt bepaald door de stabiliteit van de atmosfeer en de breedte van het venster waarover C_s^2 is berekend. Als de instabiliteit groter wordt, is het verschil in $\log(\widetilde{C_s^2})$ tussen stijgende lucht (grote C_s^2) en dalende lucht (kleine C_s^2) groter. De verschillen zijn echter niet voldoende om een bimodale-kansdichtheidsfunctie te creëeren. Als de venstergrootte toeneemt, neemt de variantie van $\log(\widetilde{C_s^2})$ af. De daling wordt ruwweg afgeschat met een eenvoudige lineaire regressie tussen de varianties van $\log(\widetilde{C_s^2})$ en de vensterbreedte. Hieruit blijkt dat voor verschillende stabiliteitsklassen zowel het begingetal als de helling (absoluut gezien) afnemen met toenemende instabiliteit. Voor temperatuur zijn het begingetal en de helling gemeten op de drie hoogtes vergelijkbaar. Voor luchtvochtigheid, daarentegen, zijn het begingetal en helling groter voor 50 m en 90 m dan voor 2,5 m.

Het begingetal en de helling kunnen worden gebruikt om voor een gegeven stabiliteitsbereik de lokale variatie te kwantificeren. Dit kan, op zijn beurt, een indicatie geven of variaties in C_s^2 langs een scintillometer- of vliegtuigpad moet worden toegeschreven aan heterogeniteit.

Een vergelijking van C_T^2 bepaald uit LAS en onbemande vliegtuigmetingen

In het laatste hoofdstuk beantwoorden we de volgende vraag:

Vraag 4 - Tot op welke hoogte zijn de padgemiddelde structuurparameters bepaald met scintillometrie vergelijkbaar met die, die bepaald zijn met een onbemand vliegtuig?

Deze studie borduurt voort op de studie van Beyrich et al. (2012). Voor vijf vluchten op één enkele dag tijdens LITFASS-2009 vergeleken zij C_T^2 bepaald uit metingen van een onbemande vliegtuig (de "meteorological mini aerial vehicle", M^{2}AV) met C_T^2 bepaald uit LAS-metingen. Gebruikmakend van de standaard dataverwerkingsprocedures vonden zij dat C_T^2 bepaald uit M^{2}AV-data systematisch groter is dan C_T^2 bepaald uit LAS-data. In dit hoofdstuk onderzoeken we of we gelijkwaardige verschillen zien tijdens de andere dagen, en of we deze verschillen kunnen verminderen of verklaren als we een uitvoerigere dataverwerkingsprocedure toepassen op zowel de LAS-data als de M^{2}AV-data.

We concluderen dat het verschil dat Beyrich et al. (2012) waarnam ook op de andere dagen van LITFASS-2009 en LITFASS-2010 te zien is. C_T^2 bepaald uit de M^{2}AV-data is groter dan uit de data van de LAS en de sonic. De uitvoerigere dataverwerkingsprocedure verbetert de resultaten niet wezenlijk. Bovendien worden de verschillen tussen beide datasets niet kleiner wanneer de LAS-data exact gesynchroniseerd zijn met de tijdsintervallen van de M^{2}AV-vluchten.

Dit betekent dat uiteindelijk het verschil tussen C_T^2 van de M^{2}AV enerzijds en C_T^2 van de sonic en LAS anderzijds tot nu toe niet kan worden verklaard.

Bedankt, Danke, Thanks!

Op 28 mei 2009 kreeg ik een e-mail van Frank dat ik langs mocht komen voor een sollicitatiegesprek voor deze PhD-baan. Precies vijf jaar later ga ik het proefschrift wat nu voor jullie ligt verdedigen. Hoewel je een PhD zelfstandig doet, heb ik die jaren ook veel hulp gehad van anderen. Soms had ik daarom gevraagd (hopelijk op het juiste moment ;-)), maar soms ook gewoon zonder vragen gekregen. Hier wil ik iedereen graag voor bedanken!

Ten eerste, Frank. Vielen Dank für alle Zeit und Dein Vertrauen in mich. Danke, dass ich immer wieder in Dein Arbeitszimmer hereinlaufen konnte. Ich habe es hoch geschätzt, dass du soviel für mich arrangiert hast, auch wenn es nicht immer in das Muster des DWDs passte. Zum Beispiel die Verwaltungsarbeit rund um die Fortsetzung des DFG-Projekts und dass ich sowohl in Lindenberg als auch in Wageningen arbeiten durfte - ohne Kernzeitverletzung. Aber auch Deine Wissenschaftliche Kenntnisse in Scintillometrie und Bodenschichtmeteorologie waren sehr hilfreich; Du warst zu sprechen, wann immer ich auch ein Diskussion brauchte.

Dan, Arnold. Bedankt voor jouw oneindeloze geduld. Ook als ik weer eens dacht dat het allemaal niks zou worden, wist jij mij dan altijd te stimuleren om toch de tekst aan te passen of nog een Matlab (of toch python?) scriptje te runnen. Moet ik je nu ook nog bedanken voor je oog voor precisie en detail? Nee, want dat vertraagde de boel soms wel enorm, maar, ja, de resultaten en discussie werden er vaak wel veel beter van. Verder wil ik je ook bedanken voor het begrip dat ik misschien na het onderzoek meer richting onderwijs wil en dit stimuleerde door ook over dat soort zaken mee te denken.

Maar ook Bert. Op de zijlijn stond je altijd klaar. Al snel nadat het duidelijk was dat de tweede fase van het project niet door kon gaan, heb jij het voor elkaar gekregen dat ik door de WUR werd betaald door samen met Gerrie effectief andere middelen aan te wenden. Ook aan het einde van mijn PhD, toen Arnold in de VS zat en het boekje af moest komen, was er altijd tijd.

Thanks Jordi. For the motivation talks, and the introduction into the science world. I started my MSc thesis with you and Monica as supervisor. You gave me the possibility to visit the summerschool in Les Houches. I do not know whether I dare to take the plunge if I did not meet Frank there. Maar ik had die sprong natuurlijk niet kunnen nemen als ik niet wist dat deze baan bestond. Oscar bedankt om mij hierop te wijzen. En ook niet als ik niet zo goed was ingewerkt in de scintillometrie. Fred, bedankt voor het geduld en het overbrengen van al jouw kennis gedurende mijn stage, hetgeen heeft

geleid tot het eerste paper.

Verder wil ik ook al mijn collega's bij MAQ bedanken voor de fijne en inspirerende tijd. Ik heb het erg gewaardeerd dat...

- er in de verschillende PhD-kamers waar ik gezeten heb altijd tijd was voor een inhoudelijk of soms minder inhoudelijke discussie,
- ik bij sommigen van jullie kon binnenlopen als ik even weer een beetje moed en relativiteit gebruiken kon,
- ik met anderen zeer prettig heb samengewerkt tijdens veldexperimenten in Lindenberg (LITFASS-2009 en LITFASS-2012),
- er ook collega's waren die net als ik de stress op het werk wilden verminderen door te gaan sporten en te wandelen tijdens de lunch,
- jullie ook op 'exotische' plekken, zoals Cyprus, Boston en Reading probeerden mij thuis te laten voelen.

Weil ich auch in Lindenberg gearbeitet habe, möchte ich mich sehr bei allen Kollegen und Kolleginnen am Obs bedanken. Vielen Dank für die Wissenschaftliche Diskussion über Scintillometrie, Licors und Sonics. Weiterhin vielen Dank Euch allen für die Einladungen zu Euch nach Hause (Mittagessen oder Kaffee und Kuchen, zum Spiele spielen, Sport machen, Fahrrad fahren, und so weiter). Ich habe mich in den letzten fünf Jahren auch in Lindenberg und Umgebung sehr zuhause gefühlt. En Bram, ook al was je al een collega in Nederland, onze intensieve samenwerking begon pas in 2013, toen jij als Postdoc in Lindenberg begon. Onze inhoudelijke discussies (o.a. tijdens rondje windprofiler) vond ik heel inspirerend. Ik hoop dat je voor 28 mei 2014 antwoorden hebt op de vragen die nog open waren na het onderzoek in mijn appendix. Ook nog bedankt dat je zoveel delen van mijn proefschrift wilde doorlezen om het te corrigeren op grammatica en spelling. Voor dat laatste kreeg ik ook nog hulp uit een heel andere hoek, Aimée en Jan, bedankt!

I would also like to thank my colleagues within the two DFG-projects, for the interesting discussions during the project meetings and via e-mail, and all other colleagues in the field for the discussions during conferences, workshops and PhD-schools.

Nu nog het meest informele deel, maar daardoor niet het meest onbelangrijke, van het dankwoord, waar ik al mijn vrienden en familieleden wil bedanken voor de hulp aan de zijlijn. Ten eerste bedankt dat jullie mijn hoogtepunten en dieptepunten gedurende mijn PhD-traject hebben willen meebeleven. Dit zorgde ervoor dat ik alles weer wat beter kon relativeren. Met andere woorden, dat mijn PhD-leven weer meer leek op het verloop van de bodemtemperatuur in de tijd dieper in de bodem, dan die dicht bij het aardoppervlak ;-). Ten tweede bedankt dat jullie hebben laten zien dat een PhD niet het enige is in het leven... De afleiding in de vorm van wandelen (in NL en CH), fietsen, koken, bakken en eten, spelletjes spelen, sporten, gezellig kletsen met een kopje thee in real life of, als de afstand te groot was, via telefoon of Skype heb ik erg gewaardeerd.

In het bijzonder wil ik nog mijn paranimfen bedanken. Sonja, weet je nog hoe prettig het was om na een vermoeide werkdag (vaak een woensdag) toch samen te eten ook al

zeiden we niet veel. Ook mijn plantjes zijn jou goede zorgen erg dankbaar. Anneke, het was fijn om een maatje te hebben op de vakgroep... dezelfde begeleider, beide interesse in het onderwijs, beide betaald door Duitsland.

En dan natuurlijk ook nog expliciet mijn ouders. Ook al zei jij, mam, dat dit niet hoefde, dat moet toch! Bedankt dat jullie mij de laatste vijf jaren gesteund hebben en begrip hadden voor de soms voor jullie onbegrijpelijke wereld van onderzoek en wetenschap. Als ik straks meer richting het onderwijs ga, wordt dat allemaal wat herkenbaarder. Ten tweede, bedankt dat jullie mij hebben geleerd om door te zetten en om uit te gaan van het positieve in situaties en mensen. Dit samen met jullie nuchtere kijk en de vele telefoongesprekken als ik weer wat te onzeker was en te hoge eisen aan mijzelf stelde, hebben mij geholpen om het proefschrift tot een goed einde te brengen.

List of publications

Peer-reviewed papers

- Braam M, Vilà-Guerau de Arellano J, Górska M (2011) Boundary layer characteristics over homogeneous and heterogeneous surfaces simulated by MM5 and DALES. J Appl Meteorol Climatol 50(6):1372–1386
- Beyrich F, Bange J, Hartogensis OK, Raasch S, Braam M, van Dinther D, Gräf D, van Kesteren B, van den Kroonenberg AC, Maronga B, Martin S, Moene AF (2012) Towards a validation of scintillometer measurements: The LITFASS-2009 experiment. Boundary-Layer Meteorol 144:83–112
- Braam M, Bosveld FC, Moene AF (2012) On Monin-Obukhov scaling in and above the atmospheric surface layer: The complexities of elevated scintillometer measurements. Boundary-Layer Meteorol 144:157–177
- Braam M, Moene AF, Beyrich F (2014) Variability of the structure parameters of temperature and humidity observed in the atmospheric surface layer under unstable conditions. Boundary-Layer Meteorol 150:399–422
- Braam M, Moene AF, Beyrich AAM F Holtslag (minor revisions) Similarity relations for C_T^2 in the unstable atmospheric surface layer: Dependence on regression approach, observation height and stability range. Boundary-Layer Meteorol

Other papers

- Braam M (2008) Determination of the surface sensible heat flux from the structure parameter of temperature at 60 m height during day-time. Tech. rep. TR-303, KNMI, the Netherlands
- Braam M, Moene AF, Hartogensis OK, Beyrich F (2012) Validation of C_{n^2} observed from the WURLAS98005 and WURLAS98006 during the LITFASS-2009 experiment. Tech. rep., Meteorology and Air Quality Group, Wageningen University, Wageningen, the Netherlands
- Braam M, Vilà-Guerau de Arellano J, Górska M (2012) Grenslaagprocessen boven homogeen en heterogeen terrein in een mesoschaalmodel en een large eddy model. Meteorologica 1:18–21

Conferences Abstract

- Braam M, Bosveld F, Moene AF (2008) Determination of the Surface Sensible Heat Flux from the Structure Parameter of Temperature at 60 m height. 8th EMS/ 7th ECAC, 29 Sept-3 Oct, Amsterdam
- Braam M, Vilà-Guerau de Arellano J, Górska M (2011) Boundary layer characteristics over homogeneous and heterogeneous surfaces simulated by MM5 and DALES. 11th EMS/ 10th ECAM, 12-16 Sept, Berlin
- Braam M, Moene AF, Beyrich F (2011) Short time variability in the structure parameter of temperature. 11th EMS/ 10th ECAM, 12-16 Sept, Berlin
- Braam M, Moene AF, Beyrich F (2012) Short-time variability in scalar structure parameters. AMS 20th Symposium on Boundary Layers and Turbulence, 9-13 Jul, Boston
- Braam M, Moene AF, Beyrich F (2013) The impact of varying height and stability on Monin-Obukhov similarity functions and evaluation of several fitting methods. 13th EMS/ 11th ECAM, 9-13 Sept, Reading
- Braam M, Moene AF, Beyrich F, Martin S (2013) Validation of the path averaged temperature structure parameter from a LAS system along a heterogeneous path with unmanned aircraft data. Tübingen Atmospheric Physics Symposium "Scintillometers and Applications", 7-9 Oct, Tübingen

Netherlands Research School for the
Socio-Economic and Natural Sciences of the Environment

C E R T I F I C A T E

The Netherlands Research School for the
Socio-Economic and Natural Sciences of the Environment
(SENSE), declares that

Miranda Braam

born on 28 May 1985 in Elburg, The Netherlands

has successfully fulfilled all requirements of the
Educational Programme of SENSE.

Wageningen, 28 May 2014

the Chairman of the SENSE board

Prof. dr. Rik Leemans

the SENSE Director of Education

Dr. Ad van Dommelen

The SENSE Research School has been accredited by the Royal Netherlands Academy of Arts and Sciences (KNAW)

KONINKLIJKE NEDERLANDSE
AKADEMIE VAN WETENSCHAPPEN

The SENSE Research School declares that **Ms. Miranda Braam** has successfully fulfilled all requirements of the Educational PhD Programme of SENSE with a work load of 53 ECTS, including the following activities:

SENSE PhD Courses

- Atmospheric Boundary Layers: Concepts, Observations and Numerical Simulations (2008)
- Environmental Research in Context (2010)
- Autumn School: Biogeochemistry and physics of the lower atmosphere (2010)
- Research Context Activity: Developing and teaching of material based on meteorology for primary (Wetenschapsknooppunt) and secondary schools (Academici voor de Klas) (Wageningen, 2011-2013)
- Bridging the scale gap between atmospheric scales (2012)

Other PhD and Advanced MSc Courses

- PhD competence Assessment (2010)
- Turbulence (2011)
- Techniques for Writing and Presenting a Scientific Paper (2012)
- Career Assessment (2014)

Management and Didactic Skills Training

- Organising the 3rd Scintillometer workshop, Wageningen (2011)
- Teaching assistance in the course "Atmosphere Vegetation Soil Interaction" (2011-2014)

Oral Presentations

- *Boundary-layer characteristics over homogeneous and heterogeneous surfaces simulated by MM5 and DALES*. Buys Ballot Research School Symposium, 27-29 October 2010, Callantsoog, Netherlands
- *Short time variability in the structure parameter of temperature*. European Meteorological Society, 12-16 September 2011, Berlin, Germany
- *Short time variability in C_T^2 measured with sonics during the LITFASS-2009 campaign*. Boundary Layer Turbulence Buys Ballot Research School Symposium, 25 November 2011, Delft, Netherlands
- *Short-time variability in scalar structure parameters*. Conference of the American Meteorological Society, 9-13 July 2012, Boston, United States
- Validation of the path averaged temperature structure parameter from a LAS system along a heterogeneous path with unmanned aircraft data. Tübingen Atmospheric Physics Symposium "Scintillometers and Applications", 7-9 October 2012, Tübingen, Germany
- *The impact of varying height and stability on Monin-Obukhov similarity functions and evaluation of several fitting methods*. European Meteorological Society, 9-13 September 2013, Reading, United Kingdom

SENSE Coordinator PhD Education

Dr. ing. Monique Gulickx

The research described in this thesis was financially supported by the German Research Foundation in the framework of the project: 'Turbulent Structure Parameters over Heterogeneous Terrain - Implications for the Interpretation of Scintillometer Data' (through grants BE2044/3-1 and BE2044/3-3) and by the Meteorology and Air Quality group of Wageningen University.

Financial support from Wageningen University and Deutscher Wetterdienst for printing this thesis is gratefully acknowledged.